EVALUATING MACROMOLECULAR TRANSPORT IN ARTICULAR CARTILAGE TO BETTER UNDERSTAND AND PREDICT TRANSPORT OF ARTHRITIS THERAPEUTICS

A Dissertation

Presented to the Faculty of the Graduate School

of Cornell University

In Partial Fulfillment of the Requirements for the Degree of

Doctor of Philosophy

by

Christopher Dennis DiDomenico

August 2018

EVALUATING MACROMOLECULAR TRANSPORT IN ARTICULAR CARTILAGE TO BETTER UNDERSTAND AND PREDICT TRANSPORT OF ARTHRITIS THERAPEUTICS

Christopher Dennis DiDomenico, Ph. D.

Cornell University 2018

In the United States, joint diseases affect more than 50 million people, a number that is expected to rise in the next few decades. Hallmarks of joint disease often involve degradation of articular cartilage tissue, which leads to patient disability and pain. Articular cartilage cannot heal very effectively on its own, and there is a limited understanding on which therapeutics would be most effective in disease treatment. Because of the inherent complexities of cartilage, it is often difficult to predict how therapeutics will be transported through the tissue, especially for larger molecules.

For proper development of effective therapeutic strategies, a better understanding of transport of larger therapeutics is needed. First, a review of molecular transport in cartilage is presented to better motivate this work (Chapter 1). There are many molecular and environmental factors that affect transport for larger solutes, such as hydrodynamic size and/or molecular weight (Chapter 2), charge (Chapter 3), and the presence of fluid flow within the tissue (convective transport) (Chapter 2 – 4). Additionally, the heterogeneities in composition within the tissue is important and can be used to predict cartilage transport (Chapter 5). Finally, this new macromolecular data informed the development of a predictive framework under which transport of solutes over a wide range of sizes can be accurately predicted (Chapter 6).

BIOGRAPHICAL SKETCH

Christopher DiDomenico received his Bachelor of Science degree from Bucknell University, majoring in Mechanical Engineering. As an undergraduate at Bucknell, Chris worked on a variety of topics, ranging from injury biomechanics to more mechanically-inspired design projects. In his sophomore year, Chris was introduced to injury biomechanics research, which got him interested in a graduate degree in biomedical engineering. Over the next 3 years, Chris worked with Dr. Eric Kennedy on projects that included assessment of facial injury risk from explosive pressure waves and impacts using the FOCUS headform, as well as development and calibration of a drop-tower system to study car accident trauma. Additionally, he also worked on assessing head injury risk from falls onto various playground surfaces. This playground research has currently led to a collaboration with the National Program for Playground Safety at the University of Iowa and will hopefully lead to safer maintenance procedures and protocols for playgrounds around the country. Finally, for his senior research project, Chris worked on development of a steam engine that was sustained by bio-degradable fuels under Dr. Nathan Siegel.

In the fall of 2013, Chris joined Dr. Lawrence Bonassar's lab to work on a project regarding molecular transport in articular cartilage. In the summer of 2014, Chris took part in a clinical experience at the Hospital for Special Surgery (HSS) as a part of Biomedical Engineering Clinical Immersion Program. He shadowed Dr. Susan Goodman, a rheumatologist specializing in administering therapeutics used to treat rheumatoid arthritis (RA). When he returned to Cornell, he used this knowledge and clinical experience to motivate his future experiments looking at how arthritis drugs are

transported through cartilage tissue. Over the next few years, Chris worked closely with AbbVie Inc. to develop new understandings on what drugs could be used to treat osteoarthritis (OA).

Chris is excited to begin consulting for ARCCA Inc., with a focus on understanding large scale injury mechanics that occur during automotive accidents and other traumatic events.

Dedicated to my family, friends, colleagues, and Cassie, who have always supported me and pushed me hard to succeed.

ACKNOWLEDGEMENTS

I would first like to thank my advisor, Dr. Lawrence Bonassar, for his patience and understanding attitude. I would also like to thank my special committee, Drs. Lisa Fortier and Itai Cohen for their guidance and expertise throughout my project.

There are many people to thank along my path to my PhD. I would like to thank all the members of my lab for their support and feedback on my results and data interpretation. Specifically, I would like to thank Lena Bartell, Michelle Delco, Eddie Bonnevie, Jill Middendorf, Alexander Boys, Ben Cohen, Mary Clare McCorry, Vinny Wang, and Aydin Kaghazchi for their input. Attending both lab meeting and cartilage meeting were very helpful over the last few years, and I believe that these meetings were a large part of my success. These meetings helped me with my presentation skills and were the source of my most beneficial criticisms along the way. I would also like to thank Corrine Henak for her help with my modeling work.

For about half of my PhD, I worked with some of the smartest minds on the planet, employees at AbbVie Inc (Andrew Goodearl, Anna Yarilina, Victor Sun, Soumya Mitra, and Annette Schwartz Sterman). They pushed me hard to succeed and taught me a lot about the pharmaceutical industry and how to give insightful presentations. They also forced me to try different techniques and helped form my critical thinking skills, pivotal components to a successful career.

I would like to thank my two of my best friends, Jeff Rosen and Mary Clare McCorry. They had made my time at Cornell exciting and adventurous, as well as giving me valuable job hunting advice and support. It was also fun climbing mountains and hills (both on foot and on bikes) with them. Additionally, Cassandra Benson also played

a key role in my success and helped me when I needed it the most. Lastly, the Philadelphia Flyers also helped distract me from my work when I needed a break.

This work was supported by the National Science Foundation grant (NSF-1536463) and by AbbVie Inc. This work made use of the Cornell Center for Materials Research Shared Facilities which are supported through the NSF MRSEC program (DMR-1719875). This work made use of imaging equipment under grants: NIH S10RR025502, NYSTEM CO29155, and NIH S10OD018516.

TABLE OF CONTENTS

LIST OF FIGURES

Main Figures

Hz. Solid lines denote a radial 1D diffusion curve derived from Fick's 2nd law, while dotted lines denote experimental data. Diffusivities and goodness of fits from each sample are shown.

Figure 5: Transport enhancement vs. strain amplitude at 1 Hz (A) and transport enhancement vs. loading frequency at 2.5% strain (B). Enhancement was found to be linearly correlated with strain amplitude (at 1 Hz) for both neonatal bovine tissue (slope: 0.30) and mature equine tissue (slope: 0.24) ($R2 > 0.93$). The two correlations were forced to have an intercept of 1 and were not statistically different from one another ($p = 0.11$). All strain amplitudes were statistically different from a value of one ($p < 0.05$), except for 0.25% strain. The maximum enhancement was found to be at 1 Hz. All loading frequencies were statistically different from a value of one ($p < 0.05$), except for 0.25 Hz.

Figure 6: Predicted fluid velocities for different strains at 1 Hz (A) and frequencies at 2.5% cyclic strain (B) vs. radial depth into the tissue. Experimental local transport enhancement from neonatal cartilage experiments for different strains at 1 Hz (C) and frequencies at 2.5% strain (D). A normalized radius of 1 corresponds to the sample radial edge. Local diffusivity curves closely followed the curvature of fluid velocity profiles. The highest transport enhancement was found near the edge, near areas of highest fluid flow. Normalized radii of at least 0.925, 0.875, and 0.900 correspond to enhancements greater than 1 for 1.25% 2.5%, and 5.0%, respectively ($p < 0.05$, ANOVA). Normalized radii of at least 0.8750, 0.8750, and 0.9375 correspond to enhancements greater than 1 for 0.25 Hz, 1 Hz, and 2.6 Hz, respectively ($p < 0.05$, ANOVA). All fluid velocity profiles were obtained at steady state conditions (occurred within 10 minutes).

Figure 7: Correlative plot of enhancement ratio and maximum fluid velocity for various loading conditions that were previously analyzed. The best fit line is forced to have an intercept of 1; the correlation was statistically significant ($p < 0.001$). Artifacts from lift-off could have caused transport enhancements from higher loading amplitudes (5%) and frequencies (2.6 Hz) to have data points higher than expected. However, correlations between individual loading regimes were not significantly different from one another.

Figure 8: Schematic of sample preparation and experimental setup (left and center) with the fluid flow induced by the platen being perpendicular to the deep zone (DZ) and the articular surface (AS). A 4-mm diameter sample 2-mm thick was bisected, then a slice was cut from each half to obtain a final sample dimension of 4x2x1.15 mm. Fluorescence image obtained from the Ab (150 kDa) solute using confocal microscopy

(right). Red box (~1000 μm wide, 500 μm tall) indicates the region of interest that was examined for this study.

Figure 9: Representative normalized fluorescence curve for the Ab (150 kDa) solute under passive conditions (blue) compared against the 16-layer diffusion model (solid black) (left). For this sample, average coefficient of variance was 6.4%. All solutes had average coefficient of variances less than 12.5%. Loaded and passive samples had equally good fits overall for all solutes. Average normalized fluorescence curve for Ab (150 kDa) through the articular surface shown (right). Standard deviations are represented by the shaded region for n = 8. For this solute, distinct changes in concavity were observed and therefore profiles could be roughly broken into three distinct regions. The articular surface region is characterized by a sharp decrease in fluorescence for the first 100 μm or so, followed by the plateau region where the fluorescence is relatively constant, followed by the deep region where there is a more rapid drop off of fluorescence.

Figure 10: Passive fluorescence profile comparison of the four differently sized solutes used. Error bars (standard deviation for n = 6-8) for all solutes are shown in shades surrounding average profiles.

Figure 11: Passive fluorescence profile comparison of the four differently sized solutes used (left) along with the multi-layer diffusivities (right). Error bars denote standard deviations for all solutes (n = 7, 8, 7, 6 for DVD, Ab, Fab, scFv, respectively). Fluorescence curves for these solutes were visually similar up until 400 μm, where solute fluorescence diverged according to size. Overall, local diffusivities were heterogeneous throughout the depth of the tissue, and there were three distinct sections of these curves for each solute. On average, diffusivities for the DVD, Ab, Fab, and scFv, were 3.3, 3.4, 5.1, and 6.0 μm2/s from 0-100 μm, but size did not affect diffusivity significantly within this region ($p > 0.05$). Diffusivities increased to a maximum of 16.5, 18.5, 20.5, and 23.4 μm2/s for the DVD, Ab, Fab, and scFv, respectively, between 225-325 μm. Calculated diffusivities at 225 μm, 275 μm, and 325 μm were higher than all other diffusivities in the tissue, for all solutes ($p < 0.05$). Diffusivities then decreased to similar values found within the surface region in the 400-800 μm range (deep region), and had no significant dependence on size ($p > 0.05$). Values obtained from the 0-125 μm range and 400-800 μm range were not different from each other, for any solute ($p > 0.05$).

Figure 12: All four solutes' fluorescence profiles for passive and loaded conditions. Lighter shades of color indicate greater loading amplitude. All cyclic loading was

conducted at 1 Hz for 3 hours. Most enhancement of the fluorescence profiles for all solutes can be found from 0 – 400 μm from the articular surface. Sample sizes: N = 7, 8, 4, 6 for passive, 1.25%, 2.5%, and 5% for DVD solute, respectively. Sample sizes: N = 8, 7, 6, 5 for passive, 1.25%, 2.5%, and 5% for Ab solute, respectively. Sample sizes: N = 7, 6, 7, 7 for passive, 1.25%, 2.5%, and 5% for Fab solute, respectively. Sample sizes: N = 6, 8, 7, 8 for passive, 1.25%, 2.5%, and 5% for scFv solute, respectively.

Figure 13: All four solutes' depth-wise diffusivities for passive and loaded conditions. Lighter shades of color indicate greater loading amplitude. Error bars denote standard deviations with n = 4-8 for all solutes (see Figure 5 for specific sample size information). Loading increased diffusivities most from 0 – 400 μm from the articular surface, with highest diffusivity enhancement occurring between 225-325 μm ($p < 0.05$). For most solutes, no significant transport enhancement was experienced in the first 125 μm of the tissue, at any loading condition ($p > 0.05$). As expected, solutes undergoing higher cyclic amplitudes (i.e. 5%) received more transport enhancement than solutes undergoing less loading, from 125 μm to 325 μm ($p < 0.05$). In general, larger solutes benefited from loading more than smaller solutes, especially within the range 225-325 μm ($p < 0.05$). Almost no loading based enhancement can be observed deeper than 425 μm into the tissue.

Figure 14: Cartilage cylinders were bisected and then sliced to obtain a final sample dimension of 4x2x1.15 mm (A). Samples were loaded in a way that caused fluid flow to be perpendicular to the articular surface (AS) and deep zone (DZ) (B). Representative image from confocal microscopy showing the fluorescence gradient perpendicular to the AS (C). The red box (~1000 μm wide, 500 μm tall) indicates the region of interest that was examined for this study.

Figure 15: Average normalized fluorescence curve for all solutes (pI 4.7, 5.4, 5.9) through the articular surface. Standard deviations are represented by the shaded region for n = 5-7. Fluorescence values trended higher as pI increased within the region 100-300 μm from the articular surface.

Figure 16: Fluorescence curves for all solutes (passive condition) tested (left) and local diffusivities (right). Error bars denote standard deviations with n = 5-7 for all solutes. Overall, local diffusivities were heterogeneous throughout the depth of the tissue. On average, diffusivities for the pI 4.7, pI 5.4, and pI 5.9, were 3.8, 4.5, 4.6 μm2/s at 50 μm, but pI did not affect diffusivity significantly within this region ($p > 0.05$). Diffusivities increased to a maximum of 15.0, 16.9, and 19.0 μm2/s for the pI 4.7, pI 5.4, and pI 5.9 solutes respectively, between 200-275 μm. Calculated diffusivities at 125 μm, 200 μm,

and 275 μm were higher than all other diffusivities in the tissue, for all solutes (*: $p < 0.05$). Diffusivities for pI 5.9 were higher than that of pI 4.7, between 200-375 μm ($p < 0.05$). Diffusivities then decreased to similar values found within the surface region in the 400-800 μm range, and had no significant dependence on pI ($p > 0.05$). Values obtained from 50 μm and 425-800 μm range were not different from each other, for any solute ($p > 0.05$).

Figure 17: Fluorescence curves for pI 5.9 and 5% cyclic loading (left) and local diffusivities for all solutes at 5% cyclic loading (right). Error bars denote standard deviations with n = 5-7 for all solutes. Orange solid line denotes average passive diffusivity levels in the passive condition for all solutes. Cyclic loading at 5% cyclic strain and at 1 Hz increased fluorescence values between 150 and 400 μm. Solutes did not experience any significant differences in diffusivity values or trends at this loading amplitude ($p > 0.05$). Additionally, there were no differences between solute diffusivities at 1.25% or 2.5% (shown in supplement). However, maximal transport enhancement increased for all solutes with increasing loading amplitude, as expected.

Figure 18: During sample preparation (A), cartilage explants were randomly assigned to three groups: 2 mg/ml collagenase, 200 μg/ml trypsin, or healthy controls. With the bottom third of all samples submerged in PBS, drops (~10 μl) of collagenase or trypsin were added to the articular surface of samples. After rinsing with protease inhibitors, samples were cut to obtain slices measuring 4x2x1.15 mm. Degraded and healthy slices were then exposed to a fluorescent antibody solution (B) so that diffusion would occur perpendicularly to the articular surface. After 3 hours of exposure, samples diffusion was examined with confocal microscopy. Compositional analysis was also performed with Fourier transform infrared spectroscopy (FTIR), second harmonic generation (SHG) imaging, biochemistry, and histology. Bulk aggrecan and collagen content were calculated with biochemistry techniques, and was normalized to dry weight for each group ($\overline{N}$) (mg/mg). Using the average relative composition from FTIR and SHG ($\overline{R}$), relative concentrations were scaled point by point by the ratio of $\overline{N}$ and $\overline{R}$.

Figure 19: Fluorescence images allow calculation of fluorescence profiles for all three groups and determination of how degradation affects local solute diffusivities (left). Transport analyses showing the fluorescence curves of all experimental conditions (middle) and their respective local diffusivities throughout the depth of the cartilage (right). Samples with the surfaces degraded by either enzyme (collagenase or trypsin) exhibited higher fluorescence compared to the healthy controls within the first 400 μm from the articular surface. Degradation with either trypsin or collagenase led to higher diffusivities compared to healthy within the first 350 μm (*: $p < 0.05$, repeated-measures

two-way ANOVA), and all groups were statistically similar at depths more than 400 μm (with an average of 4 μm ^{2}/s). Collagenase-treated samples exhibited the highest local diffusivities (70 μm2/s at 250 μm), compared to the trypsin-treated (40 μm2/s at 250 μm) or healthy samples (20 μm2/s at 250 μm), and highest diffusivities at the surface (0 μm) of the tissue (45 μm2/s), compared to the trypsin (10 μm2/s) or healthy (4 μm2/s) groups ($p < 0.05$). Error bars (both shaded and standard) denote standard deviations with $n = 4 - 8$.

Figure 20: Safranin-O histology images (left) demonstrate how trypsin and collagenase degrade the proteoglycans near the surface zone of the cartilage. Absorbance spectra from FTIR analysis for the degraded samples compared to normal healthy controls (middle) at a depth of 100 μm. Collagenase and trypsin both drastically changed the absorbance spectra by altering the carbohydrate peak height near (1140 – 985 cm-1), suggesting collagenase caused greater loss of proteoglycans (including aggrecan) compared to trypsin. Local aggrecan composition (right) was obtained by calculating the depth-dependent aggrecan fitting coefficient by decomposing FTIR absorbance data 152. This coefficient was scaled to the average dry-weight aggrecan concentration obtained from biochemical analysis for each group (21 – 23%) (see Supplementary Figure 1). Degradation with collagenase or trypsin led to significant decreases (up to 40%) in aggrecan content, within the first 210 and 420 μm, respectively ($p < 0.05$). Aggrecan content was statistically similar past 420 μm.

Figure 21: SHG images demonstrate how these enzymes affect the distribution of organized collagen in the tissue (left) and normalized SHG intensity profiles (middle). As anticipated, organized collagen concentrations in trypsin-treated samples did not differ significantly from healthy controls (right), but collagenase-treated samples exhibited significantly lower organized collagen concentrations within the first 50 μm from the articular surface ($p < 0.05$).

Figure 22: Correlations comparing local diffusivities from the transport analysis to the local composition obtained from FTIR and SHG for healthy (A), trypsin-treated (B), and collagenase-treated (C) groups. Lighter shaded data designate points near the articular surface of samples (within 0 – 200 μm). Overall, concentrations of collagen and aggrecan were negatively correlated with local diffusivity in all groups. The slopes of the diffusivity/composition correlations for local aggrecan and collagen content are -78 and -47 for healthy samples, -153 and -138 for trypsin-treated samples, and -293 and -285 for collagenase-treated samples, respectively. Aggrecan and collagen content were more strongly correlated with diffusivity in the degraded groups (trypsin: R^2 = 0.45, 0.74; collagenase: R^2 = 0.86, 0.75), compared to the healthy group (R^2 = 0.31, 0.46). Additionally, aggrecan and collagen correlations for collagenase-treated samples exhibited steeper diffusivity/concentration relationships compared to correlations from the healthy group ($p < 0.05$, ANCOVA). In contrast to both healthy and trypsin-treated samples, points near the articular surface of collagenase-treated samples fell closely to the overall regression lines, highlighting the prohibitive nature that collagen alignment has on macromolecular transport.

Figure 23: Variability in diffusivity is largely predicted by solute molecular weight or hydrodynamic radius. Pooled solute diffusivity data from 31 individual papers, plotted as a function of solute molecular weight (MW) (left) and hydrodynamic radius (right). Data includes spherical (filled points) and "linear" (open points) solutes. All "linear" solute data points were obtained from diffusion studies using variously sized dextran or chondroitin sulfate molecules. All other solutes were classified as spherical. Values for hydrodynamic radii were obtained directly from the cited literature; if this was not cited, an empirical relationship ($r_s = 0.0332MW^{0.463}$) (87), was used to estimate hydrodynamic radius. Spherical solute diffusivity in cartilage was found to be very strongly correlated (black) to both molecular weight and hydrodynamic radius, obtaining an R^2 = 0.81 for both solute metrics. Best fits for linear solutes (gray) were weak ($R^2 < 0.3$), and deviated from spherical solutes, indicating that linear solutes diffuse differently in cartilage tissue. On average, linear solutes had higher diffusivities than spherical solutes of similar size, which may be due to the ability of linear solutes to change conformation as they move through the matrix.

Figure 24: The relationship between solute diffusivity and size does not depend on measurement technique, tissue species, tissue age, or tissue storage method. Pooled solute diffusivity data compared against different experimental techniques (left), tissue species/age (middle), and tissue storage condition (right). Data was grouped into 5 different experimental techniques: computed tomography/nuclear magnetic resonance spectroscopy (CT/NMR), diffusion cell, solute desorption, fluorescence recovery after photobleaching (FRAP), and fluorescence gradient (left). Linear solutes (open points)

were also included for completeness in graph A, but only spherical solutes were included in the best-fit curves (black). Tissue was also separated into tissue types: adult human, mature bovine and equine, and immature bovine cartilage (middle). Finally, data was also separated based on tissue storage condition before experimentation: either fresh or frozen (right). Across all data groupings for spherical solutes, the relationship between diffusivity and size did not differ between groups or from the relationship formed from the pooled data (ANCOVA, using log-transformed data, $p > 0.05$). This strongly supports that diffusivity can be accurately predicted in cartilage regardless of the parameters used in individual experiments.

Figure 25: Mechanistic transport models are inconsistent in predicting solute diffusivity in cartilage. Transport models for solute diffusivity (left) and partition coefficient (right) were compared to aggregate literature data. Diffusivities for all spherical solutes were compared to three prominent models (left): Renkin, Brinkman, and Clague and Phillips (65,72,75). Across this spherical solute data, root mean square (RMS) error [$\mu m^2/s$], coefficient of variance (COV), and R^2 are presented (based on untransformed data). Both the Brinkman and Renkin models did not fit pooled data adequately, assuming an effective pore radius of 7 nm and a Darcy permeability of 1.0 nm^2. The pooled data was well-fit to the Clague and Phillips relation assuming a total volume fraction of 0.25 and an effective fiber radius of 4 nm. However, a simple power-law relationship was found to best-fit the data. Right: The Ogston model was used to predict partition coefficients of spherical solutes assuming a volume fraction and effective fiber radius of aggrecan to be 0.08 and 0.475 nm, respectively. Overall, for neutrally-charged, spherical solutes, the Ogston model was predictive of solute partition coefficient. Partition coefficients for linear solutes (open points), such as dextran, deviated significantly from spherical solutes.

Supplementary Figures:

Figure S1: Passive samples were exposed to the conjugated antibody solution on their cylindrical surface for various amounts of time. Diffusivities were measured in the radial direction; diffusivities asymptotically approached a steady state value after two hours. Due to the experimental setup, there was lag time between cessation of loading and imaging of samples, where additional internal diffusion was taking place. This internal diffusion produced artificially high diffusivities if the length of experiments was not much larger than this lag time (~15 minutes). As a result, experiments needed to be longer than 2 hours to avoid imaging artifacts falsely inflating diffusivity values before the 2-hour time point. Therefore, all data within the manuscript are from experiments that were at least 3 hours in length.

Figure S2: Each fluorescence profile for loaded and unloaded samples were broken down into discrete layers (25 μm bands from 0 – 300 μm from the radial edge, 200 um bands thereafter). A radial multi-layer 1D diffusion model was used to calculate local diffusivities. Layers above were made larger for clarity purposes.

Figure S3: Additionally, a separate group of samples was tested without platens or strain offset to assess passive axial diffusion through the exposed articular surface. Fluorescence profile analysis was carried out perpendicular to the articular surface to obtain a single diffusivity in the axial direction. These diffusivities were compared to radial diffusivities for samples that were also in the free-swelling condition. Passive diffusivity into the articular surface was found to be significantly higher (35-50%) compared to diffusivity in the radial direction for all species types ($p < 0.05$). The antibody had the lowest radial diffusivity in mature equine cartilage (1.9 x 10-8 cm2/s), and the highest in neonatal bovine tissue (4.4 x 10-8 cm2/s). Neonatal bovine tissue had higher diffusivities compared to the other two groups ($p < 0.05$).

Figure S4: All four solutes' fluorescence profiles for passive and loaded conditions. Cyclic loading was conducted for 3 hours at 1 Hz and 1.25% cyclic loading amplitude. Mean values are shown for each solute, with shaded regions denoting standard deviations.

Figure S5: All four solutes' fluorescence profiles for passive and loaded conditions. Cyclic loading was conducted for 3 hours at 1 Hz and 2.5% cyclic loading amplitude. Mean values are shown for each solute, with shaded regions denoting standard deviations.

Figure S6: All four solutes' fluorescence profiles for passive and loaded conditions. Cyclic loading was conducted for 3 hours at 1 Hz and 5% cyclic loading amplitude. Mean values are shown for each solute, with shaded regions denoting standard deviations.

Figure S 7: All three solutes' depth-wise diffusivities for 1.25% (left) and 2.5% (right) cyclic loading. Orange solid line denotes average passive diffusivity levels in the passive condition for all solutes. Error bars denote standard deviations with n = 5-7 for all solutes. Higher loading amplitude lead to higher effective diffusivities, as expected. However, there were no differences in diffusivity between solutes at any loading amplitude.

Figure S 8: Fluorescence profiles for pI 4.7 solute in passive and cyclic loading conditions. Loading was conducted for 3 hours at 1 Hz and at 1.25%, 2.5%, and 5% cyclic loading amplitudes. Mean values are shown for each solute, with shaded regions denoting standard deviations for n = 4-8.

Figure S 9: Fluorescence profiles for pI 5.4 solute in passive and cyclic loading conditions. Loading was conducted for 3 hours at 1 Hz and at 1.25%, 2.5%, and 5% cyclic loading amplitudes. Mean values are shown for each solute, with shaded regions denoting standard deviations for n = 4-8.

Figure S 10: Fluorescence profiles for pI 5.9 solute in passive and cyclic loading conditions. Loading was conducted for 3 hours at 1 Hz and at 1.25%, 2.5%, and 5% cyclic loading amplitudes. Mean values are shown for each solute, with shaded regions denoting standard deviations for n = 4-8.

Figure S 11: Chemiluminescence vs. pI for the three solutes used in this study. Isoelectric point was determined by the maximum chemiluminescence value obtained from electrophoresis.

Figure S12: Graphical depiction of the linear decomposition method to obtain local cartilage composition for a healthy sample at 100 μm from the articular surface. Measured articular cartilage spectra from FTIR were best fit to the addition of a collagen spectra, an aggrecan spectra, and a baseline that accounts for instrument-specific deviations and drift that can occur with different environmental conditions [53]. This linear decomposition method was used to determine local aggrecan content of all samples by scaling the coefficient, c2, to the average dry weight aggrecan content obtained from biochemical analysis for each group (~ 21 – 23%). Error between measured spectra and best fit spectra were consistently less than 15%, for all samples and depths.

Figure S13: Comparison of local collagen content calculated from FTIR (left) and SHG (right). Both methods give similar trends in collagen content as a function of depth. However, data calculated from FTIR decomposition did not exhibit significant differences between groups at any depth. Meanwhile, collagenase-treated data from SHG exhibited significantly lower organized collagen concentrations within the first 50 μm from the articular surface ($p < 0.05$). Thus, SHG is more sensitive to the changes that collagenase imposes on the matrix for this degradation protocol. Likely, longer exposure times to collagenase would have resulted in differences between groups for the FTIR analysis as well.

LIST OF TABLES

LIST OF ABBREVIATIONS

Ab: whole antibody

ANOVA: analysis of variance

COV: coefficient of variance

CT: Computed tomography

D: Diffusion coefficient

DMSO: dimethyl sulfoxide

DVD: dual variable domain

F_{ab}: fragment antigen-bonding

FCD: fixed charge density

FE: finite element

FRAP: Fluorescence recovery after photobleaching

FTIR: Fourier transform infrared

GAG: glycosaminoglycan

HPLC-FLD: high performance liquid chromatography with fluorescence detection

IGF-I: insulin-like growth factor I

IL-1: interleukin-1

K: Partition coefficient

MMP-1: matrix metalloproteinase-1

MRI: Magnetic resonance imaging

NDD: non-descanned detector

NMR: Nuclear magnetic resonance

NSAIDs: non-steroidal anti-inflammatory drugs

OA: osteoarthritis

PBS: Phosphate buffered saline

PFG: patellofemoral groove

pI: Isoelectric point

RA: rheumatoid arthritis

RMS: root mean square

scFv: single-chain variable fragment

SDS-PAGE: sodium dodecyl sulfate polyacrylamide gel electrophoresis

SEC: analytical size-exclusion chromatography

SHG: second harmonic generation

TGF-β: transforming growth factor-β

TIMP-1: tissue inhibitor of metalloproteinase 1

TNF-α: tumor necrosis factor-α

LIST OF SYMBOLS

a	distance from the radial edge of the sample to the middle of the plug
A_1	empirical constant
a_2	empirical constant.
C	solute concentration in the tissue
C_0	initial concentration of solute in the tissue
C_1	initial concentration of the bath
D	diffusivity of the solute in cartilage
D_0	solute diffusivity in free solution
D_{eff}	Effective (combined diffusive and convective) solute diffusivity
$D_{eff}(r)$	Local effective solute diffusivity
D_p	passive solute diffusivity
$D_p(r)$	local passive solute diffusivity
F	Faraday's constant
J	solute flux
J_m	Bessel function of order zero or one
K	partition coefficient of the solute
k_B	Boltzmann's constant
MW	molecular weight of the solute
R	universal gas constant
r	distance from the radial edge of the sample
$r_{f,agg}$	average effective fiber radius of aggrecan in cartilage
$r_{f,t}$	effective fiber radius for all matrix constituents

r_p	effective pore size of the matrix
r_s	hydrodynamic radius of the solute
T	absolute temperature of the solution
t	time sample is exposed to the solute
v	interstitial fluid velocity relative to the solid matrix
z	net charge of the molecule
α_n	nth root of the Bessel function of order zero or one
η	solvent viscosity
θ_{agg}	volume fraction of aggrecan
θ_t	total matrix fiber fraction
κ	Darcy permeability
ψ	electrical potential
ω	solute convection coefficient (also known as the retardation coefficient)

PREFACE

Articular cartilage is a remarkable tissue that lines the ends of long bones, providing a smooth, low-friction surface in synovial joints. This type of cartilage, which is avascular and aneural, relies on the diffusion and transport of nutrients and other factors from synovial fluid to maintain its health. Therefore, disruption of cartilage homeostasis, as with occurrence of joint injury or excessive systemic inflammation, often results in irreversible tissue damage (arthritis). Currently, arthritis is the leading cause of disability in the US, affecting more than 46 million people, with estimated direct costs of $87 billion per year. The two most common forms of the disease are osteoarthritis (OA), which is known to be initiated by multiple biological, genetic, and mechanical factors, and rheumatoid arthritis (RA), an autoimmune disorder that targets tissues in synovial joints. Overall, treatments for these diseases vary in effectiveness. Treatments for OA include steroid injections to reduce pain or injections of viscous polymers to reduce joint friction, but these unfortunately only have limited short-term success. Eventually, most people affected with severe OA need to receive joint replacements, which is a costly and painful procedure for the patient. Because of the lack of long-term options, there has been a great interest to develop new OA therapies.

Inhibition of inflammatory pathways has been promising as a therapeutic strategy for arthritis treatment, as inflammation plays a key role in both OA and RA. To date, this strategy has been significantly more successful in treating rheumatoid arthritis. Several strategies for inhibiting inflammation, including antibody-based strategies, such as Humira®, have proven very effective at abating both the symptoms of RA and associated

joint degeneration. As such, there is much interest in determining whether such antibody-based approaches would also be effective in preventing cartilage degeneration in OA. Because of the inherent complexities of cartilage, transport of these large molecules is often hard to predict and is not currently fully characterized. Furthermore, these antibody molecules are similar in size to the native pore size of the tissue, which may lead to severely hindered transport properties. Thus, the purpose of this research is to fully describe antibody transport in articular cartilage, to aid development of new arthritis therapeutic strategies. Additionally, this research also synthesizes this new antibody transport data with existing data for smaller molecules, to formulate a predictive framework from which to predict transport of a wide variety of therapeutics targeting cartilage. We will begin with assessing what is currently known about molecular transport in cartilage, including all relevant background information for the reader, and end with a comprehensive synthesis of data collected from these studies with historical data.

CHAPTER 1

Molecular Transport in Articular Cartilage: What Have We Learned in the Past 50 Years?[1]

Abstract

Developing therapeutic molecules to target chondrocytes and inflammatory factors within arthritic cartilage is an active area of investigation. The extensive work conducted over the past half century enables accurate prediction and reliable optimization of transport of a wide variety of molecules into cartilage. In this review, we summarize the factors that can be used to tune transport kinetics of therapeutics. Overall, the most crucial factor when designing new therapeutic molecules is solute size. Diffusivity and partition coefficient both decrease with solute size as indicated by molecular weight or hydrodynamic radius. Surprisingly, despite an effective pore size of about 6 nm, even very large molecules (~ 16 nm) can diffuse through the cartilage matrix. Additionally, altering solute charge/shape or applying physiologic loading to cartilage can be used to predictably improve solute transport. This knowledge can be used to accurately predict and improve transport of solutes in adult human cartilage and enable the development of arthritis therapeutics with the most desirable transport kinetics.

[1]C. DiDomenico, M. Lintz, and L. J. Bonassar, "Molecular transport in cartilage: What has a half century taught us?," *Nat. Rev. Rheumatol*., In press.

Introduction

Treatment of osteoarthritis (OA) necessitates transport of therapeutic molecules into cartilage[1–3] to reach the numerous degradative enzymes and cytokines produced by chondrocytes[4–7]. The use of large therapeutic molecules, such as antibodies (150 kDa), has been very successful in other arthritic diseases, such as rheumatoid arthritis (RA), where large quantities of degradative cytokines are produced in the synovium[7–11]. Because of the vascularized nature of the synovium, efficacious anti-inflammatory drugs that are administered intravenously can quell cytokine production and halt RA disease progression[10]. However, sufficient transport of these drugs into cartilage is difficult, because of its highly anisotropic, dense, and avascular nature[12]. Thus, understanding how molecular transport occurs within cartilage is critical to the successful development and implementation of future OA therapies.

Current therapies for arthritis include intra-articular injection of steroids and oral administration of non-steroidal anti-inflammatory drugs (NSAIDs)[1,12–14], which are both about 500 Da and 0.5 nm in hydrodynamic size (FIG. 1). These drugs have limited long-term efficacy for treatment of OA[13–17] and there has been interest to investigate the administration of larger therapeutics[1,3,18–20], which include growth factors and antibodies that range from 7 – 200 kDa and 1 – 6 nm in hydrodynamic radii. Regardless of their size, all of these solutes need to penetrate the dense cartilage in the joint to exert therapeutic effects on chondrocytes[2,3]. While smaller molecules are assumed to fully penetrate the tissue quickly, the transport mechanics of larger molecules are much less clear, because of the highly complex nature of cartilage.

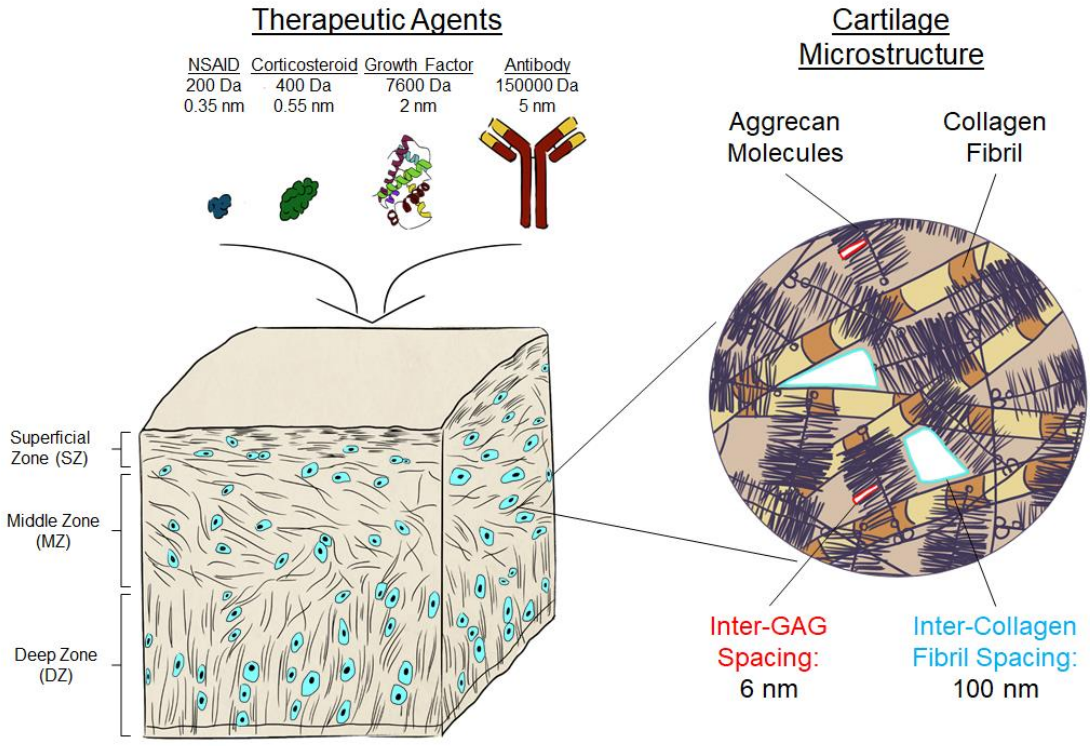

Figure 1| **Molecules used for arthritis therapy range from ~ 200 Da – 150 kDa and 0.35 – 5 nm in hydrodynamic size.** Some of the most common agents are: nonsteroidal anti-inflammatory drugs (NSAIDs), corticosteroids, growth factors, and antibodies. All of these molecules need to reach chondrocytes, which are embedded in a dense, heterogeneous matrix that varies in composition with depth. This matrix is thought to have a hierarchy of pore sizes from ~ 6 nm between glycosaminoglycan (GAG) chains to ~ 50 – 100 nm between collagen fibrils[21]. Notably, larger solutes, such as antibodies, are about the same size as the smaller pores in cartilage. The breadth of sizes of potential therapeutics and heterogeneity of articular cartilage results in a highly complex molecular transport problem.

Cartilage is a unique, complex tissue that is predominantly water (~75%), with two main solid components, type II collagen and aggrecan, a highly negatively charged macromolecule[22,23]. The fibrillar collagen II changes from highly aligned along the surface layers of the cartilage, to a more perpendicular alignment deeper in the tissue[24]. The concentration of aggrecan and collagen II also increase as a function of depth from

the articular surface[22,23,25], which causes the local fixed charge density (FCD) of the tissue to increase as well[22,23]. Together, these solid matrix components contribute to a heterogeneous, highly dense, negatively charged tissue, with an effective pore size of ~ 6 nm[21,22], which is similar to that of some proposed therapeutics (FIG. 1). Because of the poroelastic mechanical response of cartilage[26–28], fluid flow induced from mechanical loading helps expel waste products and transports nutrients (salt, glucose, etc.) and larger (> 10 kDa) growth factors into the tissue from the synovial fluid[25,29–32]. Thus, transport of molecules in this tissue is subject to many different factors, and it is important to understand how smaller nutrients, as well as very large potential therapeutic molecules, are affected by these heterogeneities.

In this review, we firstly describe the experimental techniques that have been used to examine molecular transport in articular cartilage. We then describe several major factors that can be utilized to help predict and improve transport. We end by discussing how *in vivo* conditions influence molecular transport in cartilage and potential implications for the design of therapeutics.

Techniques for examining transport

The primary means for studying transport in cartilage are *in vitro* experimental techniques (summarized below and in FIG. 2). Some studies have focused on understanding bulk-tissue transport mechanics, while others quantified mechanics that vary spatially within the sample. Both are important for the complete understanding of transport within cartilage. Ultimately, these experimental techniques mainly focus on

quantifying two metrics: diffusivity and solute partition coefficient. Diffusivity (*D*) is a metric that quantifies solute mobility (movement speed) in the tissue, whereas the partition coefficient (*K*) measures the equilibrium concentration of the solute in the cartilage compared to the concentration in the surrounding bath (i.e. synovial fluid). These metrics reveal important transport information that can be used to inform therapeutic design.

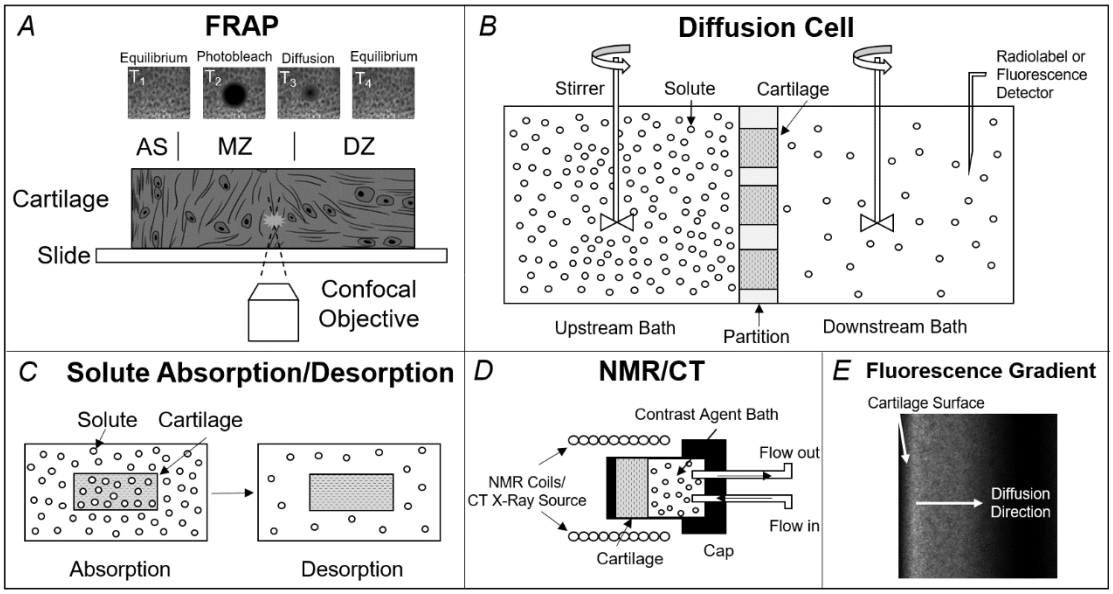

Figure 2| **Graphical depiction of experimental techniques used to determine solute diffusivity and partition coefficient.** Fluorescence recovery after photobleaching (FRAP) (A) uses transient changes in local fluorescence to determine local solute diffusivities in the region of interest (AS: articular surface, MZ: middle zone, DZ: deep zone). In diffusion cell (B) experiments, cartilage is placed in between two baths, with one filled with the solute that is tagged by a fluorophore or radiolabel. By monitoring how much solute permeates through the sample into the other bath over time, solute diffusivity can be calculated. Solute desorption (C) allows a known amount of solute to fully exude from the sample in a set time, which enables calculation of partition coefficient and diffusivity. This technique is one of the most commonly used techniques to examine solute partition coefficient. Nuclear magnetic resonance and computed tomography (NMR/CT) (D) and fluorescence gradient (E) techniques rely on visualization of local solute signal within the cartilage sample, and can be used to determine either local or bulk diffusivities.

Nuclear magnetic resonance spectroscopy and computed tomography

Nuclear magnetic resonance (NMR) spectroscopy can be used to quantify and track solute movement in cartilage. In this method, cartilage is exposed to large magnetic fields and the relaxation spectra of desired NMR-active solutes are measured (FIG. 2). Solute concentrations can be calculated by examining the relative intensity of the local NMR spectra obtained from the sample. Additionally, temporal changes of the obtained NMR spectra elucidate how fast a solute is moving within the cartilage and can be used to predict solute diffusivities[33–35]. NMR spectra are very well known and predictable for small solutes, but interpretation of these spectra becomes more challenging with increasing molecular complexity. However, small contrast agents have been attached to larger solutes to visualize macromolecular transport in cartilage[35].

Computed tomography (CT) is a way to visualize contrast agent penetration into cartilage by utilizing the ability of such agents to absorb X-ray radiation. CT scans rely on reconstructions of data taken from many different angles to produce 3D images of a region of interest[36]. The experimental setup for using CT to measure solute transport is similar to that used for NMR spectroscopy (FIG. 2), where the sample is subjected to X-ray exposure from many angles while a side of the cartilage sample is exposed to the contrast agent bath. As the solute penetrates the sample, X-ray absorption changes, which allows the calculation of concentration and hence diffusivity. Since this method causes significant X-ray exposure, CT imaging has only been used to measure cartilage

transport *ex vivo*[36–40]. This method can be used for calculating bulk or local transport mechanics.

Solute absorption/desorption

This method focuses on quantifying a volume of solute that diffuses into and/or out of a cartilage sample *ex vivo,* and does not attempt to track solute movement within the sample itself. Solutes can be labeled with a variety of molecules (predominantly fluorophores or radiolabels) to identify and track their movement with appropriate detection techniques. In solute absorption experiments, samples are exposed to the solute bath for a set amount of time, usually until equilibrium[21,25,32,41–46]. Since the initial concentration of the bath and time exposed are known, one can deduce how much infiltrated the sample and therefore calculate bulk diffusivities and partition coefficients. This is often followed by allowing the solute in the sample to "desorb" into another bath (FIG. 2) so that an additional metric of diffusivity can be obtained[32,45,54–57,46–53]. Additionally, samples can be cyclically loaded during either the absorption or desorption steps to elucidate the effect of convection on a solute[29,40,42,48,58–60]. Most times, diffusivities from absorbance tests and desorption tests are similar, but comparing these two metrics can discern if the solute is binding to the cartilage matrix. This method can also be used to test diffusivities in different layers of cartilage, if the sample is sliced into discrete sections as a function of depth. However, slicing the cartilage in this way may damage the collagen network and therefore skew diffusivity measurements[45].

Diffusion cell

Diffusion cells measure the rate at which solutes diffuse through cartilage tissue. In this method, experimental setups include an upstream bath and a downstream bath, with cartilage acting as a permeable membrane between the two[31,32,46,54–57,61] (FIG. 2). The solute of interest is added to one of the baths, which are usually stirred to promote well-mixed boundary conditions on both sides of the cartilage. Solutes can be labeled with either fluorophores or radiolabels to identify and track their movement. Because of their nature, diffusion cells only can measure diffusivity of a solute through the cartilage tissue, and cannot be used to accurately calculate partition coefficients. Thus, this method is often paired with solute desorption techniques to obtain both metrics. As with solute desorption, diffusion cells can also be used to test diffusivities in different layers of cartilage.

Fluorescence gradient

Transport in samples can also be measured by quantifying solute fluorescence within the sample itself[58,61–64]. After solute exposure (which may not be to equilibrium) in a bath, samples are bisected to measure a spatial fluorescence gradient in the cartilage sample using appropriate microscopic techniques[62] (FIG. 2). This fluorescence gradient is commonly fit to a 1D diffusion model to calculate bulk solute diffusivities[62,65]. This technique can also be used to measure local diffusivities, which can help quantify how solutes move through different regions of the tissue[65]. Changes in local sample fluorescence can also be examined after mechanical loading to quantify convective transport[58,62]. If samples have equilibrated, local fluorescence can be analyzed to distinguish if the solute partition coefficient varies as a function of position within the

cartilage. Or simply, average sample fluorescence can be related to solute concentration to quantify a bulk partition coefficient[29]. However, in contrast to solute absorption/desorption methods, one must be careful to avoid cartilage autofluorescence and background signal from matrix constituents, as well as other transient imaging artifacts[62,65].

Fluorescence recovery after photobleaching

Fluorescence recovery after photobleaching (FRAP) enables calculation of local transport metrics for fluorescently tagged solutes. Most commonly, this technique involves exposing the tissue to a solute until equilibrium. Then, the sample is imaged using a confocal microscope where high intensity laser light photobleaches a small area on the sample[63,64,66,67] (FIG. 2). Over time, the fluorescence at the photobleached area (usually circular) recovers due to diffusion of the fluorescently tagged solute. Based on the time of recovery, diffusivities can be obtained for discrete regions of the cartilage. Determination of any direction-dependent diffusion can be examined by comparing times for fluorescence recovery along two perpendicular axes of the circular photobleached area[64]. Ultimately, FRAP is a very accurate way to obtain local diffusivities of a solute. However, because of the local nature of FRAP, obtaining large-scale bulk diffusivities is not usually feasible.

Factors that affect transport

Because of the complex nature of cartilage, there are several factors that can drastically affect solute transport kinetics. These include solute size, solute charge and shape, cartilage composition, and application of mechanical loading to the tissue. The

extensive work conducted over the past half century enables accurate prediction and reliable optimization of transport of a wide variety of molecules that vary in size from 7 Da to 500 kDa and 0.1 nm to 16 nm. This knowledge allows researchers to design therapeutics that are best able to penetrate and be retained within the cartilage matrix.

Transport depends on solute size

The framework in which we understand molecular transport in cartilage involves the movement of molecules of varying size through the network of pores in the tissue. We would expect solute size to have a significant impact on transport because of the tortuosity of the pores within cartilage as well as a small effective tissue pore size[57]. Based on theories of transport in porous media[68–71], it is expected that diffusivity decreases for larger solutes. In particular, diffusivity should drop dramatically as solutes approach the size of the pores in the tissue. Examining the significant cohort of data that this field has generated over the past 50 years[25,29,45–47,49–55,31,57,60–63,65,67,72–74,32,75,34,35,37–40] demonstrates this inverse relationship between diffusivity and solute size across a broad range of solute radii (0.1 – 16 nm) and molecular weights (10 Da – 500 kDa) (Table 1). This cohort of data also shows that the relationship between molecular size and diffusivity is robust for all the measurement techniques described above. Further, such effects are similar across a variety of tissue species (human, bovine, equine) and developmental stages (neonatal to adult). Notably, linear molecules with flexible molecular structures (i.e. dextrans), which are commonly used as surrogates for macromolecules, exhibit higher diffusivities compared to similarly-sized spherical molecules (Table 1).

As with diffusivity, molecular size would be expected to influence the partition coefficient of solutes in cartilage[32,68,76]. Based on literature data, partition coefficients for both spherical and linear solutes decrease rapidly with solute hydrodynamic radius (r_s) (Table 1). However, linear solutes consistently have higher partition coefficients than similarly-sized spherical solutes. With respect to partition coefficients and diffusivities, the disparity between spherical and linear solute data suggests that linear solutes exhibit fundamentally different transport mechanics in cartilage[77].

Table 1: **Summary of solutes that have been used to examine transport in cartilage (data from references:[25,29,45–47,49–55,31,57,60–63,65,67,72–74,32,75,34,35,37–40]).**

Spherical Solutes	**Molecular Weight (Da)**	**Hydrodynamic Radius (nm)**	**Diffusivity ($\mu m^2/s$)**	**Partition Coefficient**
Small ions and sugars	7 – 350	0.08 – 0.5	1200 – 180	1 – 0.9
Peptides	140 – 760	0.3 – 0.7	500 – 120	~ 0.75
Radiocontrast agents	500 – 1,500	0.6 – 1	200 – 90	~ 0.5
Growth factors and smaller proteins	7,600 – 80,000	2 – 4.5	26 – 12	~ 0.1
Antibodies	25,000 – 200,000	2.5 – 7.6	16 – 2	0.05 – 0.01
Linear Solutes	**Molecular Weight (Da)**	**Hydrodynamic Radius (nm)**	**Diffusivity ($\mu m^2/s$)**	**Partition Coefficient**
Dextrans	3,000 – 500,000	1.75 – 16	400 – 8	1.75 – 0.02
Chondroitin sulfate	~ 20,000	~ 3.25	~ 90	~ 0.25

Based on common formulations used to predict transport in porous media[68,70,71], diffusion of molecules greater than the effective pore size of the tissue should not be possible. However, there is evidence that even extremely large (> 200 kDa, r_s > 7 nm) molecules diffuse through the dense cartilage matrix[63,65]. Such data is likely surprising, especially since the effective pore size of healthy articular cartilage is estimated to be about 6 nm [22]. These data suggest that there is a hierarchal system of pores within cartilage. Because inter-GAG spacing is about 5 nm, this implies that these large molecules move around aggrecan molecules and through spaces between collagen fibrils, which are about 50 – 100 nm in size[21,78] (FIG. 1). Such observations raise the possibility of even larger therapeutics being relevant to arthritis therapy.

Spatially-dependent transport mechanics

Above, we confirmed that solute size is highly dependent on both diffusivity and partition coefficient in cartilage tissue. While these relationships are very useful, it is important to note that not all solutes exhibit uniform diffusivities throughout the heterogeneous tissue, especially larger solutes.

In general, small uncharged solutes (< 1 kDa, r_s: 0.2 – 0.5 nm), such as glucose and urea, generally exhibit uniform diffusion kinetics throughout the tissue because their size is significantly smaller than the effective pore size within the tissue[22]. However, the local transport properties of larger molecules (> 3 kDa) are much more complicated. Leddy et al[63] studied the effects of dextran size (3 kDa – 500 kDa) on local transport kinetics in cartilage by means of FRAP. The smallest (3 kDa, r_s ~ 1.75 nm) and largest (500 kDa,

r_s ~ 15.3 nm) dextrans had highest diffusivities in the surface zone and statistically similar diffusivities elsewhere. The 40 kDa (r_s ~ 5.7 nm) and 70 kDa (r_s ~ 7.4 nm) dextrans had the opposite trends; they had lowest diffusivities in the surface region and highest diffusivities in the middle and deep regions. This is consistent with another study[65], where local diffusivities of various antibodies were highest just past the surface zone, within 150 μm – 350 μm, for solutes sized 25 (r_s ~ 2.35 nm), 50 (r_s ~ 3.25 nm), 150 (r_s ~ 5.45 nm), and 200 kDa (r_s ~ 7.59 nm). These data support that sufficiently small and very large molecules diffuse fastest through the surface zone of the cartilage, whereas molecules between these molecular weights will diffuse fastest just past the articular surface. This reinforces that size-based thresholds exist within cartilage that can drastically affect diffusive behavior.

Additionally, larger molecules can exhibit significantly different diffusive behaviors in terms of diffusional anisotropy. Leddy et al[64] found that diffusivity along the primary collagen fiber orientation of a 500 kDa dextran molecule was about 1.5 times greater than perpendicular to the fiber direction. There was no such anisotropy apparent in the other zones of the cartilage or for a 3 kDa dextran. Thus, larger solutes are more readily affected by changes in composition and orientation of the collagen within the tissue.

Solute size summary

There is a strong inverse relationship between transport and solute size across a large range of solute radii (0.1 – 16 nm) and molecular weights (10 Da – 500 kDa) (Table 1). Ultimately, increasing solute size has a large negative impact on both diffusivity and

partition coefficient. In terms of local transport mechanics, large (> 3 kDa, r_s > 1.75 nm) solutes are more likely to exhibit heterogeneous diffusion through the thickness of the tissue and are more likely to be diffusively hindered by the collagenous surface region of the cartilage. These data can inform the development of successful arthritis therapeutics.

Increasing solute charge aids transport

Cartilage tissue has a very strong net negative charge that increases near the underlying subchondral bone[22,23]. Because the negative charges within cartilage are fixed, the tissue acts as a selective membrane that obeys Donnan equilibrium[79]. Thus, solute charge sometimes has a large effect on transport throughout the tissue because of electrostatic interactions with the matrix. Solute charge is usually quantified using isoelectric focusing which determines the isoelectric point of a molecule (pI), the pH at which the molecule has no charge.

A significant amount of research has been conducted on the transport of charged molecules in cartilage. Maroudas et al[21] has shown that small cations, such as Na^+ and K^+, have partition coefficients 2 – 4 times higher, on average, than negatively charged ions, such as Cl^- (K ~ 0.6). Partition coefficients of cations generally increase with higher tissue GAG content, while partition coefficients of anions generally decrease[32]. Consistently, Byun et al[55] found that that the partition coefficient of a positively charged peptide inhibitor (~ 500 Da, pI ~11) was between 2 and 5. When GAGs were removed from the tissue with enzymatic degradation in this study, partition coefficients dropped

to about 1. On the other hand, diffusivity is not significantly dependent on solute charge for small charged molecules.

Even large (> 10 kDa) positively charged molecules can utilize electrostatic interactions to increase partitioning into cartilage. Bajpayee et al[61] has shown that neutrally charged (pI: 7) 66 kDa avidin had a partition coefficient of 0.5 and positively charged, 66 kDa avidin (pI: 10.5 and net charge: +20) had a partition coefficient of 6. However, these equally sized solutes had similar diffusivities, suggesting that solute charge does not play a significant role in macromolecular solute mobility. Additionally, retention of the positive avidin in cartilage was superior (> 40%) compared to the neutrally charged version.

Notably, solute charge was shown to alter local diffusion mechanics for antibody molecules (150 kDa) within 125 – 300 μm from the articular surface of the cartilage[75]. In this region, a 5.9 pI antibody exhibited a 20% increase in diffusivity compared to that of a pI 4.7 molecule. This research supports that solute charge also influences local transport mechanics, which might not be apparent in bulk diffusivity measurements.

Charge summary

Increasing positive solute charge is associated with higher local diffusivities, and higher partition coefficients. Positively charged solutes also are retained in the cartilage tissue for longer periods of time. Thus, relying on reversible binding of positively charged solutes can be used to increase effectiveness of future drug therapies. These effects are

ultimately linked to strong electrostatic interactions between the solute and the negatively charged cartilage matrix.

Solute shape changes transport behavior

Larger molecules can exhibit different shapes that can affect mobility in porous tissues. Solutes such as glucose and antibodies, are generally spherical in shape[80]. Some solutes, such as dextran, consist of long sugar chains that contribute to a more linear (and intrinsically more flexible) molecular structure[80]. This flexibility allows these solutes to change their conformation as they diffuse through a porous medium to an ellipsoidal conformation (i.e. a random coil) or a flexible chain conformation (reptational behavior)[80,81]. To date, very few studies have investigated the effects of solute shape in cartilage, but there are several models that describe diffusion in other porous media[77,82–87]. These models predict the diffusivity of the linear molecule based its size relative to the pores of the media through which it is diffusing[81,88].

Several studies have directly compared transport of linear and spherical molecules in porous media. Using FRAP, Pluen et al[82] demonstrated that flexible macromolecules (DNA chains) better diffused through agarose gels compared to similarly-sized rigid molecules (polymer beads). Across the literature, flexible molecules exhibited 20 – 30% greater diffusivity than their spherical molecule counterparts in various gels[82,89]. This is likely because flexible molecules can change conformation while moving through the tortuous pore network, while their generally rigid, spherical counterparts cannot. This behavior also explains why partition coefficients of these molecules are generally higher

than spherical solutes[90,91]. Although these studies were done in gels, the trends are accurate for cartilage as well (Table 1). Ultimately, linear molecules are likely not good predictors of transport characteristics of similarly-sized proteins or small molecules.

Cartilage composition alters transport

Several studies have demonstrated that the local and bulk composition of cartilage (which can change with animal species and age) can affect solute transport[46,51,62–65,92]. In one study, Evans et al [92] investigated several such relationships by correlating solute diffusivities to several cartilage tissue properties. GAG weight fraction was negatively correlated with solute diffusivities of various 500 Da fluorophores and 10 kDa dextran. Additionally, these diffusivities were positively correlated to fluid volume fraction. Another accurate predictor of solute diffusivity is tissue permeability[32], a metric that is closely tied to the above tissue properties. Such a relationship between permeability and diffusivity exists because both depend on friction inside the tissue pores as well as the cartilage tortuosity[32].

The relationship between composition and solute diffusivity becomes more complicated when considering local diffusion mechanics. Because cartilage has a depth dependent permeability and water content[25], intuition suggests that solutes should diffuse fastest near the surface and slowest deeper towards the subchondral bone. This trend is generally true, but some very large solutes have lowest diffusivities near the surface[63,65]. This deviation is likely caused from hindrance of these large molecules diffusing perpendicularly to the highly aligned collagen in this zone[64]. Additionally, some larger

(> 1 kDa) solutes exhibit depth-dependent[32] partition coefficients which are proportional to tissue permeability[21,46]. Ultimately, the heterogeneity of cartilage influences local diffusion and partitioning of larger solutes (> 1 kDa) to a greater degree than smaller ones.

Diseased or damaged tissue can drastically affect tissue properties and therefore have significant effects imposed on transport[50,93,94]. Torzilli et al[45] demonstrated the effects of degrading GAGs on the diffusivities of three uncharged solutes of different molecular sizes (glucose, inulin, and dextran). After degradation, diffusivities of both inulin and dextran increased by about 2-fold, but there was no such change in diffusivity for the smaller glucose molecule. It is thought that removing GAGs from the tissue increases diffusivities of these larger molecules because it drastically increases the effective pore size of the tissue. These results further support that the composition of the cartilage has a greater effect on larger molecules.

Cartilage composition summary

The heterogeneities of cartilage can drastically affect solute transport properties. Ultimately, transport is fastest where the matrix density and FCD of the tissue is lowest (i.e. near the surface). However, larger solutes can deviate from these expected relations and are more readily influenced by these heterogeneities. Further study into the relationship between compositional heterogeneities and transport can enable therapies that are targeted to specific regions of the cartilage structure.

Physiologic loading increases transport

Convection of solutes occurs via fluid flows that are induced by cyclic mechanical loading or sliding[95], which can enhance transport of some solutes. These flows induce frictional interactions between the solvent, solute, and matrix[96,97]. How far fluid moves inside of cartilage during a loading cycle and overall fluid velocity depends heavily on the loading frequency and loading amplitude applied, because of the poroelastic nature of cartilage[22]. In general, increasing loading amplitude and frequency increases fluid velocity but decreases fluid penetration depth[22,62]. Both factors influence local and bulk transport kinetics within cartilage[29,62,65,98]. In some cases, the calculation of the Peclet number can quantify what impact convective and diffusive contributions have in an experimental system with applied loading[58].

Many studies have investigated the effects of various loading conditions (0.01 Hz - 3 Hz, 0.1 - 10% amplitude) on solute transport[29,42,100–104,48,58,59,62,65,73,98,99]. Ultimately, transport contributions from convection for smaller solutes (< 1 kDa, 1 nm) are relatively small (< 50%), because diffusion of these molecules occurs quickly. For instance, Evans et al[58,98] investigated the effects of cyclic loading on a relatively small (~ 400 Da) glucose-like molecule over a range of amplitudes and frequencies (5 – 50%, 0.0006 – 0.1 Hz). They demonstrated that loading with 10% or 20% cyclic amplitude at 0.1 Hz augmented desorption kinetics (< 50%), but other loading conditions produced minimal effects.

Convection has been shown to have a much greater effect (> 100%) on solutes that are large (> 1 kDa)[29,31,48,62,65,73,98]. For instance, loading cartilage disks at 10% cyclic strain at 0.2 Hz led to dramatic enhancement of partition coefficients of variously-sized molecules (400 Da – 70 kDa)[29]. These enhancements were greater in larger molecules than in smaller ones (i.e. 9 for 70 kDa dextran, 2.5 for 3 kDa dextran, but no enhancement for fluorescein). In another study, convective contributions from cyclic loading for a 150 kDa antibody were found to be maximal at 1 Hz and 5% cyclic strain, for a variety of cartilage tissue obtained from different animal species[62]. In this study, bulk solute transport in the radial direction in loaded samples was 2-3 times higher than transport in passive samples. Additionally, areas of local transport enhancement were highest near the sample periphery (and near the articular surface[65]), where fluid velocity was highest. These data support the idea that obtaining the best combination of fluid velocity and fluid penetration depth is important to maximizing solute transport enhancement[62].

On the other hand, static compression without a cyclic component, has been shown to decrease both diffusivities and partition coefficients of solutes, regardless of solute size or molecular weight[46,47,92]. Additionally, both transport metrics are inversely related to the amount of static compression applied to the sample[46,47,92]. Static compression effectively increases the density of cartilage and decreases effective pore size, leading to slower transport mechanics, especially for larger solutes.

Convective transport summary

Cyclic mechanical loading of cartilage leads to a significant enhancement (up to 10-fold) of solute transport at physiologic strain amplitudes (1 – 10%) and frequencies (0.1 – 1 Hz). These enhancements from convection and mechanical loading are greater for larger solutes. However, static compression of cartilage leads to a slowing of transport kinetics. These data support that joint movement is very important for sufficient penetration of arthritis therapeutics *in vivo.*

Solute transport considerations *in vivo*

The solute, cartilage, and external transport factors discussed thus far have been shown to translate accurately to more clinically relevant preclinical and animal models[44,105–110]. Magnetic resonance imaging (MRI) techniques have also been used in several prominent human and animal models involving transport of nutrients and growth factors within the joint space[34,37,111,112]. However, when solutes are introduced to the joint space *in vivo*, several new transport factors come into play. Two of the most critically important factors i*n vivo* are solute residence time within the joint space and solute retention within the cartilage. This section aims to briefly summarize how solute-specific variables affect these factors.

The joint ultrastructure allows the body to effectively replace the synovial fluid that lubricates and hydrates the cartilage tissue several times per day, which is important for joint health[113]. The joint space is surrounded by the highly vascularized synovial membrane, which includes wide intercellular gaps, no basement membrane, and a highly efficient lymphatic drainage system[113]. Additionally, inflammation of the

synovium in OA and RA increases the permeability of this membrane[113]. Thus, in most instances, the synovial membrane is extremely permeable to most solutes. Because of this inherent permeability, it is difficult to maintain clinically relevant and efficacious concentrations of therapeutics in the joint space for extended periods of time[1,113].

Concentrations of therapeutic solutes within the joint space have residence times ranging from 1-48 hours, depending on several key factors, the most important of which is solute size[1,114,115]. Corticosteroids and orally administered anti-inflammatory drugs (< 700 Da) that are clinically used to treat pain and inflammation in arthritic joints have been estimated to have a mean joint residence time of around 1-3 hours[1,2,115]. Larger molecules, such as albumin (66 kDa) and hyaluronic acid (> 1 MDa) have joint residence times of about 11 and 24 hours, respectively[2]. Even though these larger molecules have higher residence times in the joint, larger molecules typically have lower concentration ratios between blood serum and synovial fluid, necessitating intra-articular injections to obtain clinically-relevant concentration levels[1]. Furthermore, larger solutes unfortunately have much slower transport kinetics in cartilage, which makes obtaining efficacious amounts of the drug within the tissue difficult.

There are several ways to increase solute residence times. One way is to develop highly positively-charged solutes that would either irreversibly or reversibly bind to the cartilage matrix[113]. Another strategy is to incorporate the drug within microspheres of sufficient size (often several μm in diameter)[1,116]. These microspheres act as drug carriers and slowly release the drug into the joint space as they are degraded by

naturally-occurring enzymes. Research supports that microspheres or solutes larger than 200 nm cannot easily be removed from the joint space and therefore have very long residence times ($\geq$ 48 hours)[113,116,117]. However, even the biggest microspheres are eventually phagocytosed and removed by native macrophages in the synovial fluid.

As cartilage tissue degrades, as in many joint diseases, the composition and structure of the tissue changes[118,119]. These changes include removal of GAGs and an eventual disruption of the collagen orientation at the articular surface[119,120]. These changes have implications for transport of therapeutics. It is likely, especially with larger therapeutics, that these cartilage changes will cause faster transport mechanics and enable a higher concentration of solutes within the cartilage tissue[45,121]. However, this increased tissue permeability may lead to shorter solute retention times within the tissue, which may negatively affect therapeutic efficacy. Given these challenges, there are competing interests when developing arthritic therapeutics. Thus, it is likely that researchers will need to consider many factors when designing and applying new therapies so that penetration into the cartilage tissue and retention within the joint space are optimized.

Future directions

Many decades of work in this field has led to a much greater understanding of transport in cartilage. However, several significant questions remain. Why more flexible, linear molecules diffuse through cartilage tissue at a higher rate compared to more spherical molecules is unclear. Despite having large frictional forces exerted on them by pore walls, it is possible that linear molecules make up for this by being able to diffuse into smaller pores than more rigid molecules. While further understanding the diffusion

mechanics of linear solutes in cartilage would be helpful, it is important to understand that the diffusivities measured for such molecules are poor predictors of comparably-sized proteins.

Even solutes larger than the effective pore size of cartilage can diffuse through the entire depth of the tissue. This raises some interesting opportunities for macromolecular therapeutic design. For instance, nanoparticles ($r_s \geq 3$ nm) have been used to deliver customizable effects to cancer cells[122], but these particles have never been used to target cartilage chondrocytes directly. Likewise, delivery of antibodies using microspheres and delivery of large ($r_s \sim 25$ nm) viral vectors to modify diseased chondrocytes remains unstudied for arthritis therapy[1,116]. Even though these macromolecules would diffuse slowly through cartilage, they could be modified to maximize joint residence times, which could make their development more feasible.

Currently, few studies[45,50,93,94] address solute transport in light of cartilage degradation or damage. There is also relatively little known[64,65,67,123] on how local composition affects local solute transport in both healthy and degraded cartilage tissue. We argue that developing a robust relationship or transport model for predicting solute diffusivities as a function of cartilage composition (both locally, and bulk) would be very helpful and hold great clinical significance. If combined with non-invasive imaging techniques (i.e. MRI) to estimate cartilage composition, this transport relationship could enable patient-specific tailoring of therapeutics, and likely lead to increased treatment success.

Conclusion

Even though cartilage tissue is avascular, transport of solutes through this porous tissue is multi-faceted. The intrinsic heterogeneities of the tissue, such as collagen orientation and composition, drive solute transport mechanics that can be spatially-dependent and change significantly with solute properties. When joint homeostasis is disrupted, either by injury or genetic factors, this can often lead to long-term degradation of the joint space. Use of cartilage-targeted therapeutics to help restore joint homeostasis is under investigation, and understanding how such molecules diffuse into cartilage is critical for successful implementation. Ultimately, solute size is an excellent predictor of transport, and even solutes larger than the effective pore size can diffuse into the tissue. Additionally, altering solute shape or charge, and applying physiologic loading conditions to cartilage can be used to predictably augment transport of therapeutics into cartilage. This knowledge further enables researchers and clinicians to optimize kinetics of arthritis therapeutics into articular cartilage.

REFERENCES

1. Evans, C. H., Kraus, V. B. & Setton, L. A. Progress in intra-articular therapy. *Nat. Rev. Rheumatol.* **10,** 11–22 (2013).
2. Evans, C. H. Drug delivery to chondrocytes. *Osteoarthritis and Cartilage* **24,** 1–3 (2016).
3. Bajpayee, A. G. & Grodzinsky, A. J. Cartilage-targeting drug delivery: can electrostatic interactions help? *Nat. Rev. Rheumatol.* **13,** 183–193 (2017).
4. Moos, V., Fickert, S., Müller, B., Weber, U. & Sieper, J. Immunohistological analysis of cytokine expression in human osteoarthritic and healthy cartilage. *J. Rheumatol.* **26,** 870–879 (1999).
5. Fernandes, J. C., Martel-Pelletier, J. & Pelletier, J.-P. The role of cytokines in osteoarthritis pathophysiology. *Biorheology* **39,** 237–46 (2002).
6. Scanzello, C. R. *et al.* Local cytokine profiles in knee osteoarthritis: elevated synovial fluid interleukin-15 differentiates early from end-stage disease. *Osteoarthr. Cartil.* **17,** 1040–1048 (2009).
7. Hampel, U. *et al.* Chemokine and cytokine levels in osteoarthritis and rheumatoid arthritis synovial fluid. *J. Immunol. Methods* **396,** 134–139 (2013).
8. Marc Feldmann, Fionula M. Brennan, A. & Ravinder N. Maini. Role of Cytokines in Rheumatoid Arthritis. *Annu. Rev. Immunol.* **14,** 397–440 (1996).
9. Steiner, G. *et al.* Cytokine production by synovial T cells in rheumatoid arthritis. *Rheumatology* **38,** 202–213 (1999).
10. Feldmann, M. & Maini, R. N. Anti -TNFα Therapy of Rheumatoid Arthritis: What Have We Learned? *Annu Rev Immunol* **19,** 163–96 (2001).

11. McInnes, I. B., McInnes, I. B., Schett, G. & Schett, G. Cytokines in the pathogenesis of rheumatoid arthritis. *Nat. Rev. Immunol.* **7,** 429–42 (2007).

12. Gerwin, N., Hops, C. & Lucke, A. Intraarticular drug delivery in osteoarthritis. *Adv. Drug Deliv. Rev.* **58,** 226–242 (2006).

13. McAlindon, T. E. *et al.* OARSI guidelines for the non-surgical management of knee osteoarthritis. *Osteoarthr. Cartil.* **22,** 363–388 (2014).

14. da Costa, B. R. *et al.* Effectiveness of non-steroidal anti-inflammatory drugs for the treatment of pain in knee and hip osteoarthritis: a network meta-analysis. *Lancet* **390,** e21–e33 (2017).

15. McCabe, P. S., Maricar, N., Parkes, M. J., Felson, D. T. & O'Neill, T. W. The efficacy of intra-articular steroids in hip osteoarthritis: a systematic review. *Osteoarthritis and Cartilage* **24,** 1509–1517 (2016).

16. Raynauld, J.-P. *et al.* Safety and efficacy of long-term intraarticular steroid injections in osteoarthritis of the knee: A randomized, double-blind, placebo-controlled trial. *Arthritis Rheum.* **48,** 370–377 (2003).

17. Garg, N., Perry, L. & Deodhar, A. Intra-articular and soft tissue injections, a systematic review of relative efficacy of various corticosteroids. *Clin. Rheumatol.* **33,** 1695–1706 (2014).

18. Carubbi, F. *et al.* Safety and efficacy of intra-articular anti-tumor necrosis factor α agents compared to corticosteroids in a treat-to-target strategy in patients with inflammatory arthritis and monoarthritis flare. *Int. J. Immunopathol. Pharmacol.* **29,** 252–266 (2016).

19. Urech, D. M. *et al.* Anti-inflammatory and cartilage-protecting effects of an intra-

articularly injected anti-TNF{alpha} single-chain Fv antibody (ESBA105) designed for local therapeutic use. *Ann. Rheum. Dis.* **69,** 443–449 (2010).

20. Hunter, D. J. Are there promising biologic therapies for osteoarthritis? *Curr. Rheumatol. Rep.* **10,** 19–25 (2008).
21. Maroudas, A. Biophysical chemistry of cartilaginous tissues with special reference to solute and fluid transport. *Biorheology`* **12,** 233–248 (1975).
22. Mow, V. C., Holmes, M. H. & Michael Lai, W. Fluid transport and mechanical properties of articular cartilage: A review. *J. Biomech.* **17,** 377–394 (1984).
23. Poole, A. R. *et al.* Composition and structure of articular cartilage: a template for tissue repair. *Clin. Orthop. Relat. Res.* **1,** S26–S33 (2001).
24. Hwang, W. S. *et al.* Collagen fibril structure of normal, aging, and osteoarthritic cartilage. *J. Pathol.* **167,** 425–433 (1992).
25. Maroudas, A. Physicochemical Properties of Cartilage in the Light of Ion Exchange Theory. *Biophys. J.* **8,** 575–595 (1968).
26. Kim, Y. J., Bonassar, L. J. & Grodzinsky, A. J. The role of cartilage streaming potential, fluid flow and pressure in the stimulation of chondrocyte biosynthesis during dynamic compression. *J. Biomech.* **28,** 1055–1066 (1995).
27. Zhu, W., Mow, V. C., Koob, T. J. & Eyre, D. R. Viscoelastic shear properties of articular cartilage and the effects of glycosidase treatments. *J. Orthop. Res.* **11,** 771–781 (1993).
28. Fortin, M., Soulhat, J., Shirazi-Adl, a, Hunziker, E. B. & Buschmann, M. D. Unconfined compression of articular cartilage: nonlinear behavior and comparison with a fibril-reinforced biphasic model. *J. Biomech. Eng.* **122,** 189–

195 (2000).

29. Albro, M. B. *et al.* Dynamic loading of immature epiphyseal cartilage pumps nutrients out of vascular canals. *J. Biomech.* **44,** 1654–1659 (2011).

30. Sophia Fox, A. J., Bedi, A. & Rodeo, S. A. The Basic Science of Articular Cartilage: Structure, Composition and Function. *Orthopaedics* **1,** 461–468 (2009).

31. Garcia, A. M., Frank, E. H., Grimshaw, P. E. & Grodzinsky, A. J. Contributions of Fluid Convection and Electrical Migration to Transport in Cartilage: Relevance to Loading. *Arch. Biochem. Biophys.* **333,** 317–325 (1996).

32. Maroudas, A. Distribution and diffusion of solutes in articular cartilage. *Biophys. J.* **10,** 365–379 (1970).

33. Yin, Y., Zhao, C., Kuroki, S. & Ando, I. Diffusion of rodlike polypeptides with different main-chain lengths in the thermotropic liquid crystalline state as studied by the field-gradient 1H NMR method. *Macromolecules* **35,** 2335–2338 (2002).

34. Burstein, D., Gray, M. L., Hartman, A. L., Gipe, R. & Foy, B. D. Diffusion of small solutes in cartilage as measured by nuclear magnetic resonance (NMR) spectroscopy and imaging. *J. Orthop. Res.* **11,** 465–478 (1993).

35. Foy, B. D. & Blake, J. Diffusion of paramagnetically labeled proteins in cartilage: enhancement of the 1-D NMR imaging technique. *J. Magn. Reson.* **148,** 126–134 (2001).

36. Honkanen, J. T. J. *et al.* Cationic Contrast Agent Diffusion Differs Between Cartilage and Meniscus. *Ann. Biomed. Eng.* **44,** 2913–2921 (2016).

37. Kulmala, K. A. M. *et al.* Diffusion coefficients of articular cartilage for different

CT and MRI contrast agents. *Med. Eng. Phys.* **32,** 878–882 (2010).

38. Silvast, T. S., Jurvelin, J. S., Tiitu, V., Quinn, T. M. & Töyräs, J. Bath Concentration of Anionic Contrast Agents Does Not Affect Their Diffusion and Distribution in Articular Cartilage In Vitro. *Cartilage* **4,** 42–51 (2013).

39. Arbabi, V., Pouran, B., Weinans, H. & Zadpoor, A. A. Transport of Neutral Solute Across Articular Cartilage: The Role of Zonal Diffusivities. *J. Biomech. Eng.* **137,** 071001 (2015).

40. Kokkonen, H. T., Chin, H. C., Töyräs, J., Jurvelin, J. S. & Quinn, T. M. Solute Transport of Negatively Charged Contrast Agents Across Articular Surface of Injured Cartilage. *Ann. Biomed. Eng.* **45,** 973–981 (2017).

41. Bonassar, L. J., Grodzinsky, a J., Srinivasan, a, Davila, S. G. & Trippel, S. B. Mechanical and physicochemical regulation of the action of insulin-like growth factor-I on articular cartilage. *Arch. Biochem. Biophys.* **379,** 57–63 (2000).

42. Bonassar, L. J. *et al.* The effect of dynamic compression on the response of articular cartilage to insulin-like growth factor-I. *J. Orthop. Res.* **19,** 11–17 (2001).

43. Buschmann, M. D. *et al.* Stimulation of aggrecan synthesis in cartilage explants by cyclic loading is localized to regions of high interstitial fluid flow. *Arch. Biochem. Biophys.* **366,** 1–7 (1999).

44. Allen, K. D., Adams, S. B. & Setton, L. A. Evaluating intra-articular drug delivery for the treatment of osteoarthritis in a rat model. *Tissue Eng. Part B. Rev.* **16,** 81–92 (2010).

45. Torzilli, P. A., Arduino, J. M., Gregory, J. D. & Bansal, M. Effect of proteoglycan

removal on solute mobility in articular cartilage. *J. Biomech.* **30,** 895–902 (1997).

46. Nimer, E., Schneiderman, R. & Maroudas, A. Diffusion and partition of solutes in cartilage under static load. *Biophys. Chem.* **106,** 125–146 (2003).

47. Quinn, T. M., Kocian, P. & Meister, J. J. Static compression is associated with decreased diffusivity of dextrans in cartilage explants. *Arch. Biochem. Biophys.* **384,** 327–334 (2000).

48. Albro, M. B., Li, R., Banerjee, R. E., Hung, C. T. & Ateshian, G. A. Validation of theoretical framework explaining active solute uptake in dynamically loaded porous media. *J. Biomech.* **43,** 2267–2273 (2010).

49. Quinn, T. M., Morel, V. & Meister, J. J. Static compression of articular cartilage can reduce solute diffusivity and partitioning: Implications for the chondrocyte biological response. *J. Biomech.* **34,** 1463–1469 (2001).

50. Chin, H. C., Moeini, M. & Quinn, T. M. Solute transport across the articular surface of injured cartilage. *Arch. Biochem. Biophys.* **535,** 241–247 (2013).

51. Torzilli, P. A., Grande, D. A. & Arduino, J. M. Diffusive properties of immature articular cartilage. *J. Biomed. Mater. Res.* **40,** 132–138 (1998).

52. Torzilli, P. A., Adams, T. C. & Mis, R. J. Transient solute diffusion in articular cartilage. *J. Biomech.* **20,** 203–214 (1987).

53. Allhands, R. V, Torzilli, P. A. & Kallfelz, F. A. Measurement of diffusion of uncharged molecules in articular cartilage. *Cornell Vet.* **74,** 111–123 (1984).

54. Garcia, A. M. *et al.* Transport and binding of insulin-like growth factor I through articular cartilage. *Arch. Biochem. Biophys.* **415,** 69–79 (2003).

55. Byun, S. *et al.* Transport and equilibrium uptake of a peptide inhibitor of PACE4

into articular cartilage is dominated by electrostatic interactions. *Arch. Biochem. Biophys.* **499,** 32–39 (2010).

56. Maroudas, A. & Bullough, P. Permeability of articular cartilage. *Nature* **219,** 1260–1261 (1968).

57. Maroudas, A. Transport of solutes through cartilage: permeability to large molecules. *J. Anat.* **122,** 335–347 (1976).

58. Evans, R. C. & Quinn, T. M. Dynamic compression augments interstitial transport of a glucose-like solute in articular cartilage. *Biophys. J.* **91,** 1541–1547 (2006).

59. O'Hara, B. P., Urban, J. P. & Maroudas, a. Influence of cyclic loading on the nutrition of articular cartilage. *Ann. Rheum. Dis.* **49,** 536–539 (1990).

60. Shafieyan, Y., Khosravi, N., Moeini, M. & Quinn, T. M. Diffusion of MRI and CT contrast agents in articular cartilage under static compression. *Biophys. J.* **107,** 485–492 (2014).

61. Bajpayee, A. G., Wong, C. R., Bawendi, M. G., Frank, E. H. & Grodzinsky, A. J. Avidin as a model for charge driven transport into cartilage and drug delivery for treating early stage post-traumatic osteoarthritis. *Biomaterials* **35,** 538–549 (2014).

62. DiDomenico, C. D., Xiang Wang, Z. & Bonassar, L. J. Cyclic Mechanical Loading Enhances Transport of Antibodies Into Articular Cartilage. *J. Biomech. Eng.* **139,** 011012 (2016).

63. Leddy, H. A. & Guilak, F. Site-specific molecular diffusion in articular cartilage measured using fluorescence recovery after photobleaching. *Ann. Biomed. Eng.*

31, 753–760 (2003).

64. Leddy, H. A., Haider, M. A. & Guilak, F. Diffusional anisotropy in collagenous tissues: fluorescence imaging of continuous point photobleaching. *Biophys. J.* **91,** 311–316 (2006).

65. DiDomenico, C. D. *et al.* The Effect of Antibody Size and Mechanical Loading on Solute Diffusion Through the Articular Surface of Cartilage. *J. Biomech. Eng.* **139,** 091005 (2017).

66. Travascio, F. & Gu, W. Y. Simultaneous measurement of anisotropic solute diffusivity and binding reaction rates in biological tissues by FRAP. *Ann. Biomed. Eng.* **39,** 53–65 (2011).

67. Fetter, N. L., Leddy, H. A., Guilak, F. & Nunley, J. A. Composition and transport properties of human ankle and knee cartilage. *J. Orthop. Res.* **24,** 211–219 (2006).

68. Ogston, A. G. The spaces in a uniform random suspension of fibres. *Trans. Faraday Soc.* **54,** 1754 (1958).

69. Clague, D. S. & Phillips, R. J. Hindered diffusion of spherical macromolecules through dilute fibrous media. *Phys. Fluids* **8,** 1720–1731 (1996).

70. Amsden, B. Solute Diffusion within Hydrogels. Mechanisms and Models. *Macromolecules* **31,** 8382–8395 (1998).

71. Renkin, E. M. Filtration, diffusion, and molecular sieving through porous cellulose membranes. *J. Gen. Physiol.* **38,** 225–243 (1954).

72. Schneiderman, R. *et al.* Insulin-like growth factor-I and its complexes in normal human articular cartilage: studies of partition and diffusion. *Arch. Biochem.*

Biophys. **324,** 159–172 (1995).

73. Garcia, A. M., Lark, M. W., Trippel, S. B. & Grodzinsky, A. J. Transport of tissue inhibitor of metalloproteinases-1 through cartilage: Contributions of fluid flow and electrical migration. *J. Orthop. Res.* **16,** 734–742 (1998).

74. DiDomenico, C. *et al.* Cyclic Mechanical Loading Enhances Transport of Antibodies Through Articular Cartilage. in *Orthopaedic Research Society* (2016).

75. DiDomenico, C. *et al.* Antibody Charge Affects Depth-Dependent Diffusion in Healthy Articular Cartilage. in *Orthopaedic Research Society* (2017).

76. Ogston, A. G., Preston, B. N. & Wells, J. D. On the Transport of Compact Particles Through Solutions of Chain-Polymers. *Proc. R. Soc. A Math. Phys. Eng. Sci.* **333,** 297–316 (1973).

77. Deen, W. M. Hindered transport of large molecules in liquid-filled pores. *AIChE J.* **33,** 1409–1425 (1987).

78. Levick, J. R. Flow Through Interstitium and Other Fibrous Matrices. *Q. J. Exp. Physiol.* **72,** 409–437 (1987).

79. Helfferich, F. G. *Ion Exchange*. (Courier Corporation, 1962).

80. Fredrickson, G. H. The theory of polymer dynamics. *Curr. Opin. Solid State Mater. Sci.* **1,** 812–816 (1996).

81. Gennes, P.-G. de. in 324 (Cornell University Press, 1979).

82. Pluen, A., Netti, P. A., Jain, R. K. & Berk, D. A. Diffusion of macromolecules in agarose gels: comparison of linear and globular configurations. *Biophys. J.* **77,** 542–52 (1999).

83. Deen, W. M., Bohrer, M. P. & Epstein, N. B. Effects of molecular size and configuration on diffusion in microporous membranes. *AIChE J.* **27,** 952–959 (1981).

84. Baumgärtner, A. & Muthukumar, M. A trapped polymer chain in random porous media. *J. Chem. Phys.* **87,** 3082 (1987).

85. Shen, H., Hu, Y. & Saltzman, W. M. DNA diffusion in mucus: effect of size, topology of DNAs, and transfection reagents. *Biophys. J.* **91,** 639–644 (2006).

86. Yamakov, V. & Milchev, A. Diffusion of a polymer chain in porous media. *Phys. Rev. E* **55,** 1704–1712 (1997).

87. Pajević, S., Bansil, R. & Koňák, Č. Diffusion of Linear Polymer Chains in Methyl Methacrylate Gels. *Macromolecules* **26,** 305–312 (1993).

88. Doi, M. & Edwards, S. F. *The theory of polymer dynamics*. *Oxford University Press* (1988).

89. Tong, J. & Anderson, J. L. Partitioning and Diffusion of Proteins and Linear Polymers in Polyacrylamide Gels. *Biophys. J.* **70,** 1505–1513 (1996).

90. Davidson, M. G., Suter, U. W. & Deen, W. M. Equilibrium Partitioning of Flexible Macromolecules between Bulk Solution and Cylindrical Pores. *Macromolecules* **20,** 1141–1146 (1987).

91. Truskey, G. A., Yuan, F. & Katz, D. F. *Transport Phenomena in Biological Systems*. (Pearson Education, 2010).

92. Evans, R. C. & Quinn, T. M. Solute diffusivity correlates with mechanical properties and matrix density of compressed articular cartilage. *Arch. Biochem. Biophys.* **442,** 1–10 (2005).

93. Moeini, M. *et al.* Decreased solute adsorption onto cracked surfaces of mechanically injured articular cartilage: Towards the design of cartilage-specific functional contrast agents. *Biochim. Biophys. Acta - Gen. Subj.* **1840,** 605–614 (2014).

94. Decker, S. G. A., Moeini, M., Chin, H. C., Rosenzweig, D. H. & Quinn, T. M. Adsorption and distribution of fluorescent solutes near the articular surface of mechanically injured cartilage. *Biophys. J.* **105,** 2427–2436 (2013).

95. Graham, B. T., Moore, A. C., Burris, D. L. & Price, C. Sliding enhances fluid and solute transport into buried articular cartilage contacts. *Osteoarthr. Cartil.* **25,** 2100–2107 (2017).

96. Ateshian, G. A. & Weiss, J. A. in *Computer Models in Biomechanics* 231–249 (Springer Science+Business Media Dordrecht, 2013). doi:10.1007/978-94-007-5464-5_17

97. Yao, H. & Gu, W. Y. Convection and diffusion in charged hydrated soft tissues: A mixture theory approach. *Biomech. Model. Mechanobiol.* **6,** 63–72 (2007).

98. Evans, R. C. & Quinn, T. M. Solute convection in dynamically compressed cartilage. *J. Biomech.* **39,** 1048–1055 (2006).

99. Gardiner, B. *et al.* Solute transport in cartilage undergoing cyclic deformation. *Comput. Methods Biomech. Biomed. Engin.* **10,** 265–278 (2007).

100. Ferguson, S. J., Ito, K. & Nolte, L. P. Fluid flow and convective transport of solutes within the intervertebral disc. *J. Biomech.* **37,** 213–221 (2004).

101. Quinn, T. M., Studer, C., Grodzinsky, A. J. & Meister, J. J. Preservation and analysis of nonequilibrium solute concentration distributions within

mechanically compressed cartilage explants. *J. Biochem. Biophys. Methods* **52,** 83–95 (2002).

102. Zhang, L., Gardiner, B. S., Smith, D. W., Pivonka, P. & Grodzinsky, A. The effect of cyclic deformation and solute binding on solute transport in cartilage. *Arch. Biochem. Biophys.* **457,** 47–56 (2007).

103. Hung, C. T. Modeling of Neutral Solute Transport in a Dynamically Loaded Porous Permeable Gel: Implications for Articular Cartilage Biosynthesis and Tissue Engineering. *J. Biomech. Eng.* **125,** 602 (2003).

104. Entezari, V. *et al.* Effect of mechanical convection on the partitioning of an anionic iodinated contrast agent in intact patellar cartilage. *J. Orthop. Res.* **32,** 1333–1340 (2014).

105. Chevalier, X. *et al.* Safety study of intraarticular injection of interleukin 1 receptor antagonist in patients with painful knee osteoarthritis: A multicenter study. *J. Rheumatol.* **32,** (2005).

106. Chevalier, X. *et al.* Intraarticular injection of anakinra in osteoarthritis of the knee: A multicenter, randomized, double-blind, placebo-controlled study. *Arthritis Care Res.* **61,** 344–352 (2009).

107. Bajpayee, A. G., Scheu, M., Grodzinsky, A. J. & Porter, R. M. A rabbit model demonstrates the influence of cartilage thickness on intra-articular drug delivery and retention within cartilage. *J. Orthop. Res.* **33,** 660–667 (2015).

108. Ghosh, P. & Guidolin, D. Potential mechanism of action of intra-articular hyaluronan therapy in osteoarthritis: Are the effects molecular weight dependent? *Semin. Arthritis Rheum.* **32,** 10–37 (2002).

109. Winalski, C. S. *et al.* Enhancement of joint fluid with intravenously administered gadopentetate dimeglumine: technique, rationale, and implications. - PubMed - NCBI. *Radiology* **187,** 179–185 (1993).

110. Bajpayee, A. G., Quadir, M. A., Hammond, P. T. & Grodzinsky, A. J. Charge based intra-cartilage delivery of single dose dexamethasone using Avidin nano-carriers suppresses cytokine-induced catabolism long term. *Osteoarthr. Cartil.* **24,** 71–81 (2016).

111. Burstein, D. *et al.* Protocol issues for delayed Gd(DTPA)2--enhanced MRI (dGEMRIC) for clinical evaluation of articular cartilage. *Magn. Reson. Med.* **45,** 36–41 (2001).

112. Hawezi, Z. K., Lammentausta, E., Svensson, J., Dahlberg, L. E. & Tiderius, C. J. In vivo transport of Gd-DTPA2- in human knee cartilage assessed by depth-wise dGEMRIC analysis. *J. Magn. Reson. Imaging* **34,** 1352–1358 (2011).

113. Edwards, S. H. R. Intra-articular drug delivery: The challenge to extend drug residence time within the joint. *Vet. J.* **190,** 15–21 (2011).

114. Chevalier, X., Eymard, F. & Richette, P. Biologic agents in osteoarthritis: hopes and disappointments. *Nat. Rev. Rheumatol.* **9,** 400–410 (2013).

115. Owen, S., Francis, H. & Roberts, M. Disappearance kinetics of solutes from synovial fluid after intra- articular injection. *Br. J. Clin. Pharmacol.* **38,** 349–355 (1994).

116. Champion, J. A., Walker, A. & Mitragotri, S. Role of Particle Size in Phagocytosis of Polymeric Microspheres. *Pharm. Res.* **25,** 1815–1821 (2008).

117. Horisawa, E. *et al.* Size-dependency of DL-lactide/glycolide copolymer

particulates for intra-articular delivery system on phagocytosis in rat synovium. *Pharm. Res.* **19,** 132–9 (2002).

118. Maroudas, A., Bayliss, M. T. & Venn, M. F. Further studies on the composition of human femoral head cartilage. *Ann Rheum Dis* **39,** 514–523 (1980).

119. Venn, M. & Maroudas, A. Chemical composition and swelling of normal and osteoarthrotic femoral head cartilage. I. Chemical composition. *Ann. Rheum. Dis.* **36,** 121–9 (1977).

120. Saarakkala, S. *et al.* Depth-wise progression of osteoarthritis in human articular cartilage: investigation of composition, structure and biomechanics. *Osteoarthr. Cartil.* **18,** 73–81 (2010).

121. Manning, H. B. *et al.* Detection of cartilage matrix degradation by autofluorescence lifetime. *Matrix Biol.* **32,** 32–38 (2013).

122. Kim, S. E. *et al.* Ultrasmall nanoparticles induce ferroptosis in nutrient-deprived cancer cells and suppress tumour growth. *Nat. Nanotechnol.* **11,** 977–985 (2016).

123. DiDomenico, C. & Bonassar, L. Local Solute Transport Kinetics are Strongly Correlated to Local Cartilage Composition. in *Orthopaedic Research Society* (2018).

CHAPTER 2

Cyclic Mechanical Loading Enhances Transport of Antibodies into Articular Cartilage[2]

Abstract

The goal of this study was to characterize antibody penetration through cartilage tissue under mechanical loading. Mechanical stimulation aids in the penetration of some proteins, but this effect has not been characterized molecules such as antibodies (> 100 kDa), which may hold some clinical value for treating osteoarthritis. For each experiment, fresh articular cartilage plugs were obtained and exposed to fluorescently labeled antibodies while under cyclic mechanical load in unconfined compression for several hours. Penetration of these antibodies was quantified using confocal microscopy and finite element simulations were conducted to predict fluid flow patterns within loaded samples. Transport enhancement followed a linear trend with strain amplitude (0.25% to 5%) and a non-linear trend with frequency (0.25-2.60 Hz), with maximum enhancement found to be at 5% cyclic strain and 1 Hz, respectively. Regions of highest enhancement of transport within the tissue were associated with the regions of highest interstitial fluid velocity, as predicted from finite element simulations. Overall, cyclic compression enhanced antibody transport by 2 to 3-fold. To our knowledge, this is the first study to test how mechanical stimulation affects the diffusion of antibodies in cartilage and suggest further study into other important factors regarding macromolecular transport.

[2]C. DiDomenico, Z. X. Wang, and L. J. Bonassar, "Cyclic Mechanical Loading Enhances Transport of Antibodies into Articular Cartilage," J. Biomech. Eng., vol. 139, no. 1, pp. 11012-11012–7, 2016.

Introduction

Both rheumatoid arthritis (RA) and osteoarthritis (OA) are thought to be initiated by the release of inflammatory cytokines that degrade and inflame the joint tissues [1,2]. Inhibition of these inflammatory pathways has been of great interest as a therapeutic strategy for disease treatment for RA. Antibody based strategies inhibiting tumor necrosis factor-α (TNF-α), have proven especially effective at reducing both the symptoms of RA and associated joint degeneration. Interestingly, TNF-α is also known to play a role in OA [3], and there is interest in determining whether such RA antibody-based approaches would also be effective in treating OA.

Pathophysiologically, RA and OA are very different. Primary contributors of inflammation and degradation are found in different joint tissues in both diseases. In RA, the synoviocytes in the well-vascularized synovial lining surrounding the joint capsule are the main contributors to the release of inflammatory cytokines that infiltrate the synovial fluid, cartilage, and surrounding bone [4,5]. Consequently, intravenous injection of antibodies easily reaches the source of inflammation and greatly reduces the activity of inflammatory factors, significantly decreasing future degradation and joint pain. However, in OA, chondrocytes located in the avascular articular cartilage produce a significant amount of these inflammatory cytokines, and are thus are a more challenging target for therapy [2,3]. Therapeutics, especially smaller ones, injected directly into the joint have relatively short intra-articular half-lives (ranging from 1 hour for aspirin [180 Da] to several hours for albumin [66 kDa]), which may be another important consideration for future OA therapy [6–8].

A main factor limiting the potential utility of antibody-based approaches for OA treatment is the limited ability of such large molecules (molecular weight [MW] > 100 kDa) to penetrate the dense avascular cartilage extracellular matrix, with pore sizes as low as 10 nm [9]. Other factors, such as the high fixed charge density of the tissue may also limit macromolecular transport through phenomena such charge-meditated partitioning and binding [10]. However, it has been shown that convective fluid flows, such as those induced by mechanical loading, can enhance transport of macromolecules into cartilage, including relatively large molecules such as TIMP-1 (MW: 23 kDa), albumin (MW: 66 kDa), IGF-I (MW: 7.6 kDa), and transferrin (MW: 80 kDa) [11–14]. These studies have demonstrated that the magnitude of convective enhancement of transport increases with the size of the solute of interest, giving credence to the idea that such methods could be used to enhance the transport of very large, complex molecules such as antibodies. This loading-based enhancement has also been shown that physical activity can enhance the uptake of smaller molecules such as MRI contrast agents into cartilage [15]. However, it has never been explored whether loading-induced compressive flows can enhance the transport of antibodies into cartilage.

Therefore, the goal of this study is to investigate the use of cyclic mechanical loading to enhance the transport of antibodies into cartilage tissue. Specifically, we investigate how transport due to cyclic compression changes with frequency and amplitude of loading and the extent to which regions of enhanced transport in the tissue correlate with regions of enhanced fluid flow.

Methods

Cartilage Harvest and Preparation

For each experiment, fresh, full-thickness cylindrical articular cartilage plugs (n = 12-24) were harvested using biopsy punches under sterile conditions from one of three tissue sources to be compared: patellofemoral groove (PFG) of 1-3 day old bovids (~25 experiments from ~20 different animals) (Gold Medal Packing, Rome, NY); PFG cartilage from skeletally mature equines (6 experiments from 2 different animals) (Cornell Veterinary School, Ithaca, NY); or hock joint cartilage from skeletally mature bovids (2 experiment from 1 animal) (Articular Engineering, Northbrook, IL). For all sources, samples were randomly distributed to experimental groups based on location within the joint to prevent tissue composition variation skewing experimental results. For all tissue, all plugs had the articular surface intact and were sliced to be nominally 1.15 mm thick and 4 mm diameter, except for the mature bovine cartilage (0.5 mm thick). Superficial, middle, and deep zones were represented in all samples tested. These plugs were randomly assigned to two different groups (loaded and passive) and were placed into individual wells in 24-well plates with the articular surface facing upwards. An impermeable platen array was placed on top of each well plate, applying a 15% axial strain to all samples, to keep samples in place and to combat the effects of swelling and limit diffusion in the axial direction. For each well, 350 μl of fluorescently labeled (Alexa Fluor 633) goat-anti-mouse antibodies (MW: 150 kDa) (Life Technologies, Grand Island, NY) at a concentration of ~1 μM (50 μg/ml) in PBS (Corning, NY) was added. With this setup, only the outside cylindrical (radial) surface was exposed to the

antibody solution. Both mature and immature animals were chosen so that one could determine if experimental trends differed between young and mature tissue.

Mechanical Compression

Each group was placed into a 37°C incubator where the loaded group underwent unconfined cyclic axial compression with a custom-built, displacement-controlled bioreactor that maintained sterile conditions, as described previously [16]. On top of the 15% axial offset, singular sinusoidal strain amplitudes (0.25%, 1.25%, 2.5%, or 5.0%) were applied to the loaded samples at a singular frequency (0.25 Hz, 0.5 Hz, 1 Hz, 1.7 Hz, or 2.6 Hz) for 3-4 hours. The passive group served as a control, with only a 15% offset strain. Through preliminary experiments, diffusive resistance from any stagnant film layer that may have formed on the passive group samples during testing was insignificant, which is consistent with literature regarding samples of similar size [17].

Transport Analysis

After loading, all plugs were bisected axially and the cut surface on one half was assessed on an inverted confocal microscope stage (LSM 510, Zeiss, Oberkochen, Germany) to characterize the radial antibody penetration (Figure 1). Laser power (λ: 635 nm, ~15 mW) was set so that the total fluorescence intensity of the 8-bit image was roughly Gaussian and so that no pixels were saturated (pixel dwell time: ~0.5 ms). The pinhole was set to obtain a representative 30 μm thickness for each sample with a spatial resolution of 1.35 μm/pixel. A 10x objective with a numerical aperture of 0.3 (Zeiss,

Oberkochen, Germany) and a working distance of about 3 mm was used for all samples. A total of 12 tiles were taken to fully capture the sample under these imaging conditions.

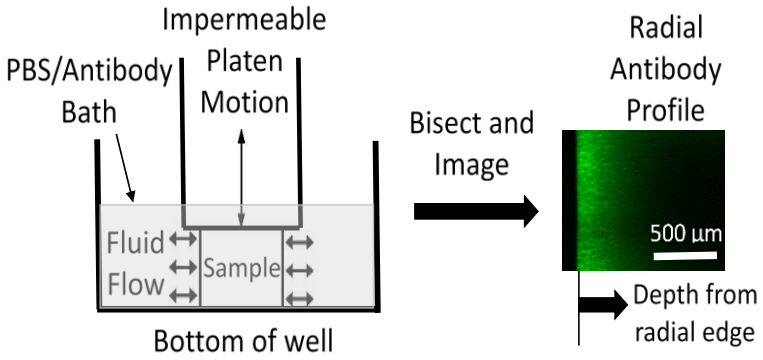

Figure 3: Schematic of experimental procedure. The left shows the experimental setup of an individual well and the right shows a radial fluorescence profile of an individual sample. Cylindrical samples are bisected and that cut surface is imaged under the confocal microscope. Only the middle 50% of the sample is shown in the confocal image.

Radial penetration was defined as diffusion perpendicular to the circumferential surface of the plug that was in contact with the antibody bath. Experiments focused on radial penetration because permeability is more homogeneous in that direction (when compared to through the articular surface) and this allowed better control of the loading conditions [18]. However, using the procedure described below, passive axial penetration through the articular surface was examined to understand the directional dependence of diffusion through cartilage in different species in the free-swelling condition.

This experiment was modeled as 1D radial diffusion, under the assumption that antibodies only penetrated radially into the sample's exposed cylindrical surface.

Background fluorescence was calculated from a 1000 μm^2 area sufficiently far away from the sample and subtracted from the sample fluorescence. Although minimal at this wavelength and laser power, autofluorescence of each sample was calculated from a 1000 μm^2 area in the middle of the sample (where no solute was found on the time scale of the experiment) and subtracted from the total sample fluorescence. For all samples, column-wise pixel averages of the sample image data were obtained. These summations were constrained to the middle 50% of the sample to avoid edge effects from the bottom and top of the sample. Limiting to the middle of the sample also helped avoid any transport artifacts if the loading platen did not maintain contact with the sample throughout the loading cycle. Then, average fluorescence intensity profiles, from both radial edges of the cut surface to the center, were fitted to a radial 1D diffusion membrane absorption model derived from Fick's 2nd law [19]:

$$\frac{C - C_0}{C_1 - C_0} = 1 - \frac{2}{a}\sum_{n=1}^{\infty} \frac{e^{(-D\alpha_n^2 t)} J_0(r\alpha_n)}{\alpha_n J_1(a\alpha_n)} \quad (1)$$

where C is the solute concentration in the tissue, C_0 and C_1 are the initial concentrations of the tissue and bath, respectively, D is the solute diffusivity, t is the time exposed to the solute, a is the distance from the radial edge of the sample to the middle of the plug, J_m is the Bessel function of order zero or one, α_n is the nth root of the Bessel function of order zero or one, and r is the distance from the radial edge of the sample. In these experiments, C_0 was assumed to be 0 and C_1 was the concentration of the bath. The solute fluorescence/concentration relationship was found by taking different dilutions of the solute and observing them under a confocal microscope (LSM 510, Zeiss, Oberkochen, Germany). The fluorescence of the antibody was found to be linearly

correlated ($R^2 > 0.95$) to solute concentration in the range of dilute concentrations (1-2 μM) used for these experiments (data not shown), and thus fluorescence values was substituted for concentration values into Eq. 1, without affecting the initially unknown variable of interest, *D*. After normalizing the fluorescence curves to the maximum value, the above equation was fit to the fluorescence profile data and diffusivities that resulted in the lowest root-mean-squared (RMS) error for the entire curve fit were used for each sample. The diffusivities from each radial edge of a sample were averaged together to obtain the final measurement.

Because it took approximately 15-30 minutes to remove and image all of the samples, a test was conducted to verify that experiments were long enough to negate any potential artifacts of additional sample diffusion during sample preparation and imaging. It was determined that passive diffusivities (D_p) were insensitive to bath exposure time for experiments that lasted longer than 2 hours (Figure S1) and as such, all further studies focused on times greater than 2 hours.

Eq. 1 is a simplification of the solution to the advection-diffusion equation, and all convective effects are captured by the variable D_{eff}, the "effective" diffusivity [20–22]. Because direct sample pairing was not possible for this study, for every experiment, each effective diffusivity was divided by the average experimental D_p, then further averaged [23] to obtain an average "transport enhancement" for every loaded sample (defined as D_{eff}/D_p).

Local Diffusivity Analysis

Once an average diffusivity was obtained for a sample, fluorescence profile data were broken down into discrete "layers" (25 μm segments from 0-300 μm from the radial edge; 200 μm segments thereafter, for a total of 20 layers). Using a RMS error minimization procedure for each layer (assuming continuity between layers, and implementing boundary conditions and geometry used from Eq. 1), fluorescence data within that particular layer was analyzed with a transient radial 1D multi-layer diffusion model adapted from Carr et al [24], enabling the calculation of local diffusivities within a sample (either D_p or D_{eff}) at t = 3-4 hours (Figure S2). Collectively, these calculations enabled the determination of radial diffusivity functions, and radially dependent diffusivities of loaded samples ($D_{eff}(r)$) were compared across experiments to passive controls ($D_p(r)$) to obtain information about how transport enhancement of the solute changed throughout the radial depth of the tissue.

FE Modeling

Finite element modeling was performed to obtain predictions of the fluid flow patterns throughout cartilage plug under cyclic loading using a biphasic model in FEBio [25]. Assuming a neo-Hookean solid (solid volume fraction = 0.2, modulus = 0.7 MPa, Poisson ratio = 0.2) with Holmes-Mow permeability ($P_0 = 1 \times 10^{-14}$ m^4/Ns, M = 1.5, α = 2) throughout the entire plug (made of ~100 rectangular prism elements), maximum fluid velocity profiles in the radial direction were obtained for various bouts of loading of the plug (diameter=4 mm, thickness=1.15 mm) in unconfined compression [26]. At steady state conditions (achieved on the order of 10 minutes), velocity profiles were

obtained for 5%, 2.5%, and 1.25% sinusoidal amplitude at 1 Hz, as well as 2.5% sinusoidal amplitude at 0.25 Hz and 2.6 Hz. In all cases, waveforms were superimposed on a 15% static compression with constant exterior fluid pressure [26]. Although previously shown for other loading conditions [27], this model was used to investigate how fluid velocity changed as a function of radial depth for the loading conditions used in this study. The results of these models were then compared to experimental measurements of the radial profile of local transport enhancement.

Solute Characterization

Before experiments were conducted, size exclusion chromatography (SEC) (Agilent 1200 HPLC, GE Healthcare, Pittsburgh, PA, US) was used to determine that the conjugated goat-anti-mouse antibodies were not aggregating in solution on the time scale of the experiments (> 91% monomer). Additionally, high performance liquid chromatography with fluorescence detection (HPLC-FLD) (Agilent 1200 HPLC, GE Healthcare, Pittsburgh, PA, US) confirmed that there were non-detectable amounts of free conjugate (Alexa Fluor 633 label) in the conjugated antibody solution before experiments were conducted.

Statistical Analysis

For each strain amplitude and applied frequency, a one-way ANOVA was performed to determine the effect of mechanical loading, with subsequent Tukey post-hoc tests for pairwise comparisons. This method was also performed to determine where samples exhibited local transport enhancement and differences between radial and axial

diffusivities and species. Additionally, the effect of loading amplitude on transport enhancement and the relationship between fluid velocity and transport enhancement were assessed by linear regression analysis. An ANCOVA determined any differences between transport enhancement correlations for different cartilage species as well as differences between correlations for different loading conditions.

Results

The one-dimensional Fickian diffusion relationship fit well to both the loaded and passive radial fluorescence curves ($R^2 > 0.95$, coefficient of variance < 15%) (Figure 2). Low residual error between this model and data from loaded sample indicated that convective and diffusive contributions can be combined into an "effective diffusivity," (D_{eff}) a term used previously in other studies [20–22]. For example, in neonatal bovine tissue, 5% dynamic strain at 1 Hz for 3 hours resulted in $D_{eff} = 10 \times 10^{-8}$ cm^2/s, a 2.4-fold increase over passive diffusion. Under free-swelling conditions, axial penetration of antibodies (through the articular surface) was higher than radial penetration for all species (Figure S3).

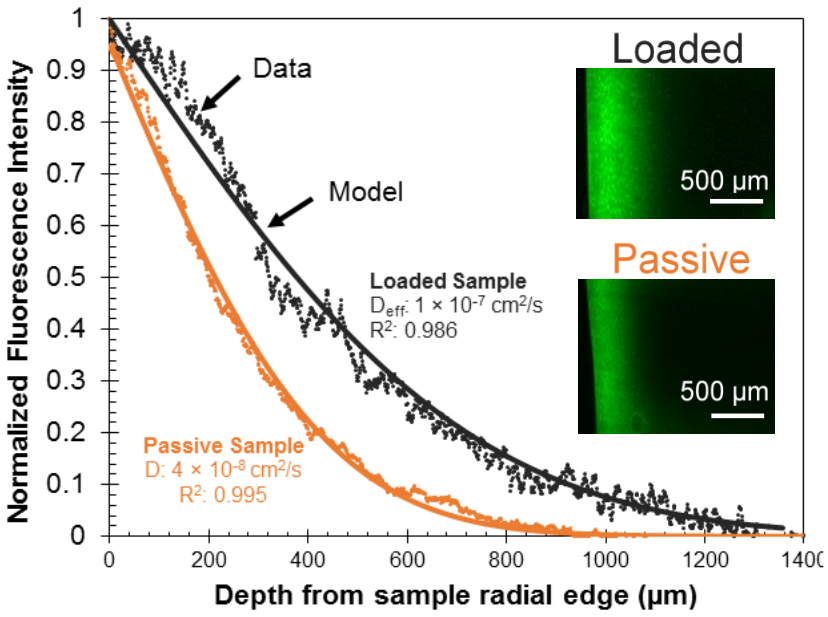

Figure 4: Normalized fluorescence intensity vs radial depth from the sample edge for a representative middle portion of loaded and passive sample exposed to the antibody solution for 3 hours. The loaded sample was exposed to loading at 5% cyclic strain at 1 Hz. Solid lines denote a radial 1D diffusion curve derived from Fick's 2nd law, while dotted lines denote experimental data. Diffusivities and goodness of fits from each sample are shown.

Increasing the strain amplitude of the applied loading at 1 Hz significantly increased radial antibody transport into cartilage, with enhancement up to 2.4 at 5% strain (Figure 3). For passive samples, D_p ranged from 2.8 to 6.0 × 10^{-8} cm^2/s, while D_{eff} for 1 Hz (≥ 1.25% strain) loaded samples ranged from 6.8 to 15.4 × 10^{-8} cm^2/s. The convective transport enhancement (at 1 Hz) were linearly related to strain amplitude for both mature equine and neonatal bovine tissue ($R^2 > 0.92$, $p < 0.05$) and these correlations were determined not to be statistically different from one another ($p = 0.11$). Due to tissue thinness, adult bovine tissue was not tested under loading.

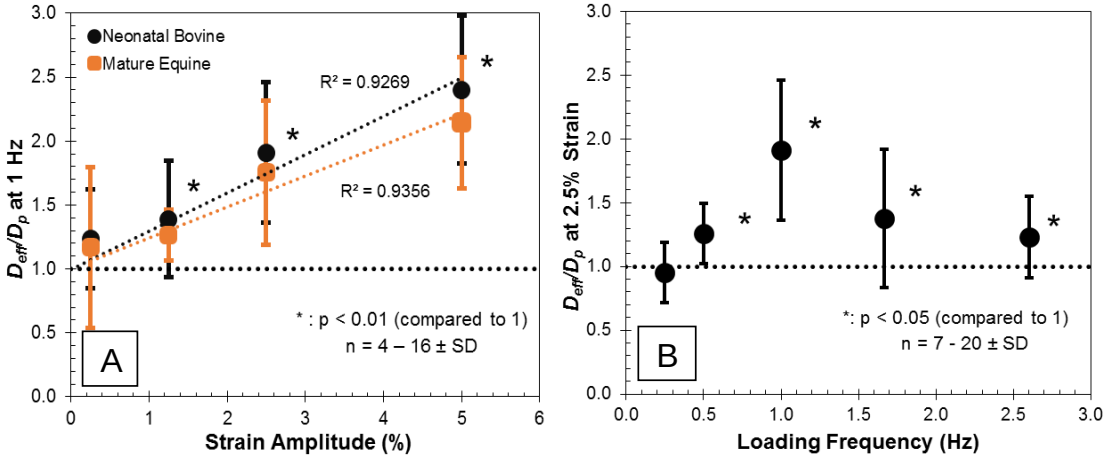

Figure 5: Transport enhancement vs. strain amplitude at 1 Hz (A) and transport enhancement vs. loading frequency at 2.5% strain (B). Enhancement was found to be linearly correlated with strain amplitude (at 1 Hz) for both neonatal bovine tissue (slope: 0.30) and mature equine tissue (slope: 0.24) ($R^2 > 0.93$). The two correlations were forced to have an intercept of 1 and were not statistically different from one another ($p = 0.11$). All strain amplitudes were statistically different from a value of one ($p < 0.05$), except for 0.25% strain. The maximum enhancement was found to be at 1 Hz. All loading frequencies were statistically different from a value of one ($p < 0.05$), except for 0.25 Hz.

The relationship between transport enhancement and applied loading frequency showed a non-linear trend at a strain amplitude of 2.5% (Figure 3). Transport enhancements were significantly higher than 1 ($p < 0.05$), except for the loading frequency of 0.25 Hz, which showed no enhancement. The maximum transport enhancement was 1.9 at 1 Hz. The average transport enhancement at the highest frequency tested (2.6 Hz) was 1.2.

To understand the relationship between fluid flow and local transport enhancement, simulations were performed to map the radial profiles of fluid flow during compression and further data analysis was performed to map the regions of transport enhancement in

cartilage samples. Fluid flow predictions from FE simulations of samples loaded at 1 Hz showed regions of high fluid flow near the radial edges of samples, where the normalized radius (r/r_0) is close to 1 (Figure 4). Increasing strain amplitude increased the predicted maximal fluid velocity at the radial edge of cartilage samples from ~3.5 µm/s at 1.25% to ~7 µm/s at 5%. For simulations of all amplitudes, fluid exchange was confined to the outer 15% of the sample. Simulations also showed that changing the frequency at 2.5% strain increased fluid maximum fluid velocity from <2 µm/s at 0.25 Hz to ~7 µm/s at 2.6 Hz. Changing the frequency of stimulation also had a great effect on the region of the tissue in which fluid exchange occurred. At 2.6 Hz, fluid maximal fluid velocity dropped to 0 within 10% of the radius of the tissue, compared to 30% penetration at 0.25 Hz loading.

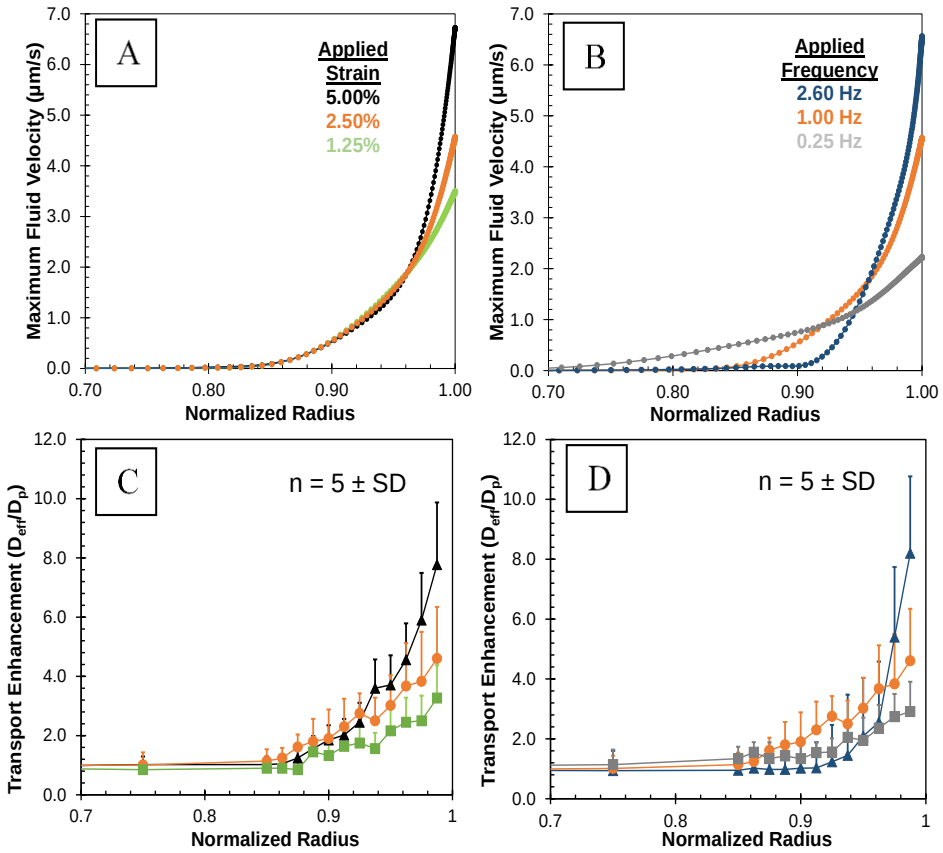

Figure 6: Predicted fluid velocities for different strains at 1 Hz (A) and frequencies at 2.5% cyclic strain (B) vs. radial depth into the tissue. Experimental local transport enhancement from neonatal cartilage experiments for different strains at 1 Hz (C) and frequencies at 2.5% strain (D). A normalized radius of 1 corresponds to the sample radial edge. Local diffusivity curves closely followed the curvature of fluid velocity profiles. The highest transport enhancement was found near the edge, near areas of highest fluid flow. Normalized radii of at least 0.925, 0.875, and 0.900 correspond to enhancements greater than 1 for 1.25% 2.5%, and 5.0%, respectively ($p < 0.05$, ANOVA). Normalized radii of at least 0.8750, 0.8750, and 0.9375 correspond to enhancements greater than 1 for 0.25 Hz, 1 Hz, and 2.6 Hz, respectively ($p < 0.05$, ANOVA). All fluid velocity profiles were obtained at steady state conditions (occurred within 10 minutes).

Fitting Eq. 1 to discrete regions of the fluorescence curves of loaded and unloaded samples enabled the calculation of $D_p(r)$, $D_{eff}(r)$, and $(D_{eff}/D_p)(r)$ (Figure 4). Local diffusion curve fits had and average $R^2 > 80\%$ and an average coefficient of variance of < 20%. This analysis revealed that transport enhancement was also confined to a narrow region of the tissue near the radial edge, with spatial patterns of enhancement varying with amplitude and frequency of loading. For loading at 1 Hz, transport enhancement at the radial edge was as high as ~8 at 5% amplitude and ~4 at 1.25% amplitude, and in all cases there was no enhancement (i.e. $D_{eff}/D_p = 1$) 15% in from the radial edge of the tissue. For loading at 2.5% amplitude, transport enhancement at the radial edge was as high as 9 at 2.6 Hz and 2.5 at 0.25 Hz. At 2.6 Hz, the region of transport enhancement penetrated about 8% from the radial edge, while at 0.25 Hz, D_{eff}/D_p remained as high at 1.15 at 25% from the radial edge.

Discrete radial regions of highest enhancement and fluid flow from neonatal experiments were found near the sample radial edge (Figure 4). The regions of tissue

with highest enhancement transport (i.e. $r/r_0 > 0.9$) were the same as those with highest predicted fluid velocity. Linear regression found a positive relationship between transport enhancement and maximum fluid velocities predicted by the FE models ($R^2 = 0.85$, $p < 0.001$) (Figure 5).

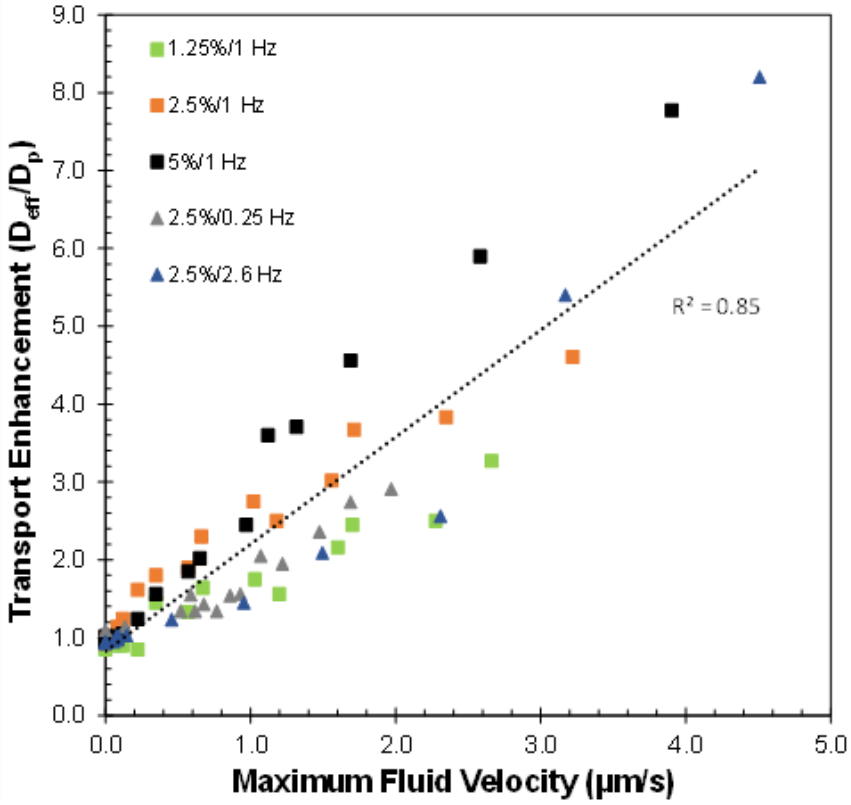

Figure 7: Correlative plot of enhancement ratio and maximum fluid velocity for various loading conditions that were previously analyzed. The best fit line is forced to have an intercept of 1; the correlation was statistically significant ($p < 0.001$). Artifacts from lift-off could have caused transport enhancements from higher loading amplitudes (5%) and frequencies (2.6 Hz) to have data points higher than expected. However, correlations between individual loading regimes were not significantly different from one another.

Discussion

The objective of this study was to investigate the role of mechanical loading on the transport of antibodies into articular cartilage *in vitro* [28]. This study showed that cyclic mechanical loading enhanced antibody transport up to 2.4-fold for the whole sample

and up to 8-fold locally in regions of high fluid flow near the radial edge. This 2.4-fold enhancement led to loaded samples having approximately 200 μm deeper penetration when the fluorescence (and thus, concentration) was half of the maximum for a given loaded and passive sample. Additionally, at a radial depth of 500 μm, loaded samples had approximately two to three-fold greater concentration of antibodies compared to passive samples. Given the molecular weight (MW: 150 kDa) and hydrodynamic radius (~5.29 nm [29]) of the antibody used, the obtained average passive diffusivity (~4×10^{-8} cm^2/s) is consistent with literature values and with the idea that diffusivity is inversely proportional to solute molecular weight and size [10,29,30]. Additionally, it has been shown that mechanically aided transport with similar loading for molecules such as IGF-I (MW: 7.6 kDa) had enhanced transport by a factor of two over passive controls [13], which is consistent with the level of enhancement noted here.

The novel technique used in these experiments enabled the determination of both local and global diffusivities of a fluorescent antibody within articular cartilage. This method allows more information to be drawn from a solute of interest, and does not rely on the system reaching equilibrium, such as in other studies [31,32]. To date, local diffusivities of solutes in cartilage have not been examined extensively and could be important to understand how some solutes move through complex, heterogeneous physiological tissues, such as cartilage and tendon.

To determine whether similar transport enhancement trends were exhibited in both mature and neonatal tissue, data from mature equine were compared to neonatal bovine

cartilage. Mature equine cartilage (which was found to have comparable properties to human tissue for both permeability and aggregate modulus [33,34]) followed the same enhancement trends as the neonatal cartilage when exposed to different loading amplitudes (Figure 3). For all species, diffusion through the articular surface was 35-50% higher than radial penetration under free-swelling conditions (Figure S3). Collectively, these data suggest that while the magnitude of diffusion is different between mature and neonatal tissue, enhancement of transport due to loading and directional dependence of transport are quite similar. As such, neonatal bovine tissue appears to be a valuable model system for studying transport *in vitro*.

Previous studies suggest convective enhancement of nutrients plays a role in cell metabolism in regions of high fluid flow [12,26]. To determine whether fluid flow is an important contributor to the enhancement of transport of this antibody, we compared the spatial pattern of enhancement to patterns of fluid flow predicted by FE models [26,35]. These models have established that as the frequency or amplitude of loading increases, the maximum fluid velocity at the radial edge increases (Figure 4). However, increasing strain amplitude has a smaller effect on fluid penetration depth than increasing loading frequency. These fluid flow and fluid penetration relationships with loading are representative of the poroelastic tissue response of cartilage [36–38]. Both a high fluid flow (to initially convect the solute into the tissue) and deep fluid penetration (to push solute inward) are needed for high levels of loading-based enhancement throughout the tissue. It was found that loading the samples at 1 Hz achieved both high fluid flow at the edges and deep fluid penetration (Figure 4), likely leading to the highest overall transport

enhancement (Figure 3) and the linear increase in enhancement for amplitudes at 1 Hz (Figure 3), which is consistent with other studies [39]. Overall, it was found that the regions of highest transport enhancement (and thus effective diffusivities) were found near the radial edge of the plug, in regions of fluid flow predicted by FE models (Figure 4). Additionally, local fluid velocities correlated positively (R^2 = 0.81) with local enhancement (and thus effective diffusivities) (Figure 5). This relationship strongly links fluid flow with increased solute transport in cartilage, and seems to indicate a proportionality between fluid flow and local solute transport. However, this relationship and FE model does not explain *mechanistically* how fluid flow contributes to increased transport, but it does help give a basic understanding on how fluid flow affects local diffusivity measurements within the sample and that faster fluid flow correlates to increased local transport. Indeed, previous work has shown that frictional drag between the solid matrix and interstitial fluid help explain more of mechanistic understanding on how loading induces increased transport of solutes [40].

Besides increased fluid flow near the sample edges, there could be other phenomenon occurring that enhance transport of various solutes and prevent molecules from being expelled from outward fluid flow during loading. It is possible that the collapse of pores during the downstroke of loading entraps large molecules and keeps them inside the cartilage matrix to be convected deeper into the tissue on subsequent cycles [41]. Compressing the tissue to a higher degree (i.e. 5%, instead of 2.5%) could cause increased compression of these pores, leading to higher amounts of temporary entrapment and/or entanglement of these large molecules within the tissue (thus

increasing transport) [41]. This phenomenon could explain why mechanical loading enhances transport of larger molecules more so than smaller ones [11,32,42,43]. Likely, there is an interplay with all aforementioned phenomenon that result in increased penetration of the antibody used with loading.

Given these positive results, there are some remaining questions and limitations. Due to the poroelastic response of cartilage, platen separation during its upstroke most likely occurred at most loading conditions, leading to harmonic distortion of the load applied to the cartilage [13,44]. To avoid any fluid flow artifacts that were created by this platen separation, image analysis took place in the middle portion of the samples, sufficiently far away from the articular surface. Additionally, loading conditions *in vivo* are significantly different compared to conditions in these experiments. Solute penetration would occur perpendicular to the articular surface, instead of radially through the deeper zones of the tissue. However, it was found that diffusivity into the articular surface was higher than that in the radial direction (Figure S3), which was likely attributed to the increased permeability in that layer of the tissue compared to the deeper zones noted in this study [45]. As a result, using diffusivity in the radial direction in the deeper zone of the tissue would likely be an underestimation of how much solute would penetrate the cartilage *in vivo* through the articular surface. Additionally, compaction of the superficial zone of cartilage in vivo may negatively affect diffusion through the tissue, which was not addressed in this study. Even though samples within loaded and passive groups were initially compressed by 15%, which could cause decreased diffusivities of

solute [46,47], this will not affect the relationship between passive and loaded conditions, which was the predominant message of this study.

Ultimately, loading increased antibody transport in only a couple of hours. Since *in vivo* intra-articular half-lives of similarly sized solutes are about 6-10 hours [6], exercising the joint could have a significant impact on antibody diffusion into the cartilage matrix within this time frame, as has been shown with smaller solutes [15]. Additionally, OA cartilage would exhibit some form of proteoglycan loss near the articular surface, resulting in higher permeabilities than the healthy cartilage used in these experiments [48]. This increased permeability of OA cartilage would most likely help the penetration and utility of OA antibody treatments as well. Interestingly, maximal enhancement was found at 1 Hz, which corresponds well with to the frequency of the walking gait cycle, which is consistent with previous studies noting enhancement of molecular transport as a result of extended periods of walking [15]. Notably, partition coefficients of large molecules such as antibodies in cartilage are quite low (e.g. 0.01) [10], and the current study only measured relative (not absolute) concentrations of antibody within the tissue. Similarly, recent clinical trials of antibodies that block IL-1 have met with limited success, possibly due to limited penetration of these molecules within cartilage [49]. As a result, it remains to be seen whether the 2 to 3-fold enhancement noted in this study would result in therapeutic concentrations of antibodies in cartilage.

Overall, this study showed that antibodies can penetrate the dense healthy cartilage matrix and mechanical loading enhanced antibody transport to a large degree. Transport

enhancement of the antibody used was linearly correlated with applied strain amplitude and had a non-linear relationship with applied loading frequency. Regions of highest enhancement of transport were associated with the regions of highest interstitial fluid velocity, as predicted from FE simulations. These data suggest that the enhancement from dynamic compression is largely due to enhanced convective flows at the radial edges of the tissue. To our knowledge, this is the first study to test how mechanical stimulation affects the diffusion of antibodies in cartilage and suggest further study into other important factors regarding macromolecular transport.

Supplementary Materials:

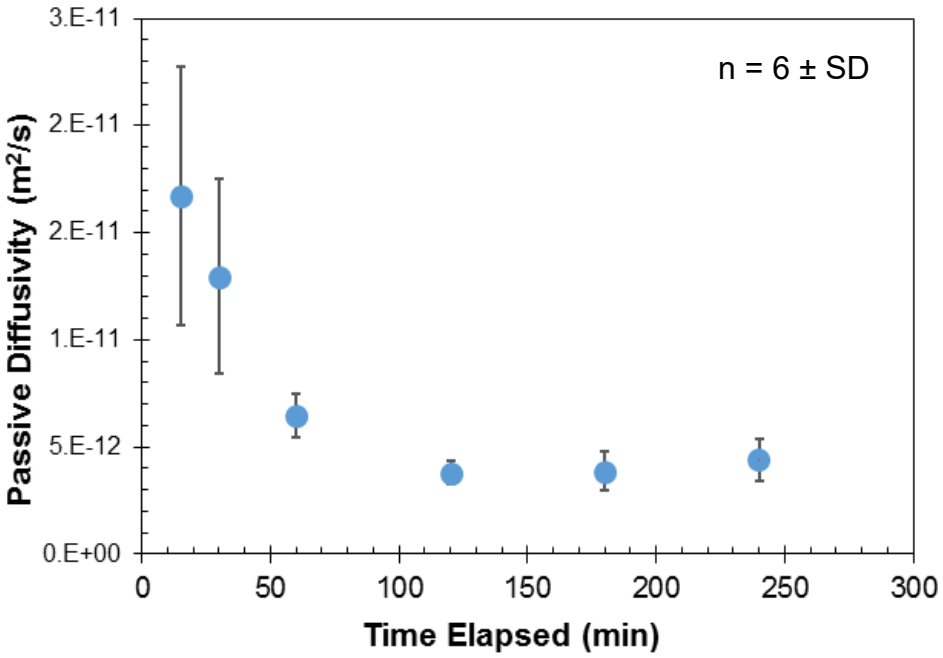

Figure S1: Passive samples were exposed to the conjugated antibody solution on their cylindrical surface for various amounts of time. Diffusivities were measured in the radial direction; diffusivities asymptotically approached a steady state value after two hours. Due to the experimental setup, there was lag time between cessation of loading and imaging of samples, where additional internal diffusion was taking place. This internal diffusion produced artificially high diffusivities if the length of experiments was not much larger than this lag time (~15 minutes). As a result, experiments needed to be longer than 2 hours to avoid imaging artifacts falsely inflating diffusivity values before the 2-hour time point. Therefore, all data within the manuscript are from experiments that were at least 3 hours in length.

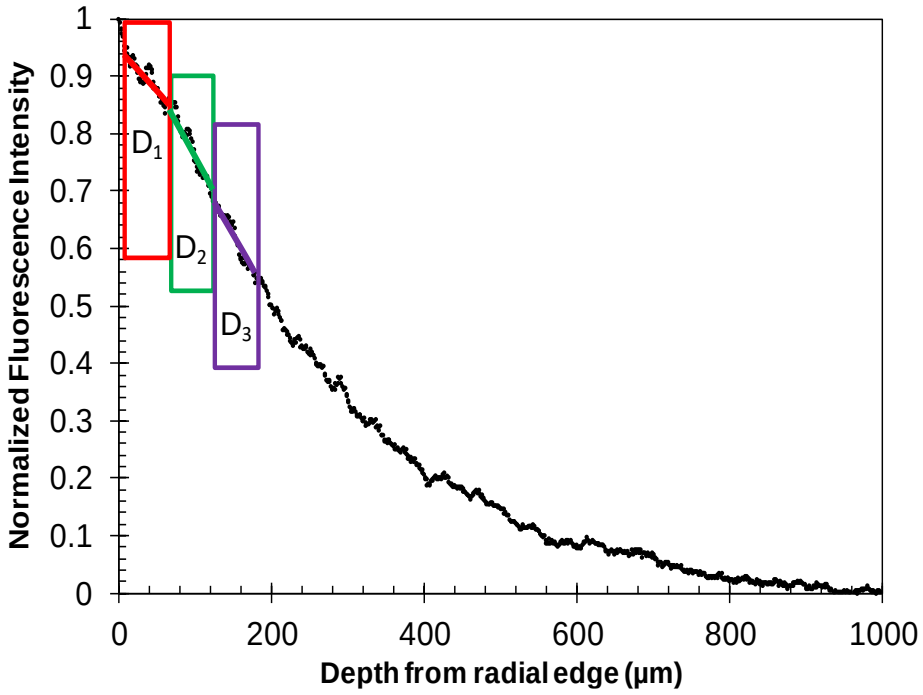

Figure S2: Each fluorescence profile for loaded and unloaded samples were broken down into discrete layers (25 μm bands from 0 – 300 μm from the radial edge, 200 um bands thereafter). A radial multi-layer 1D diffusion model was used to calculate local diffusivities. Layers above were made larger for clarity purposes.

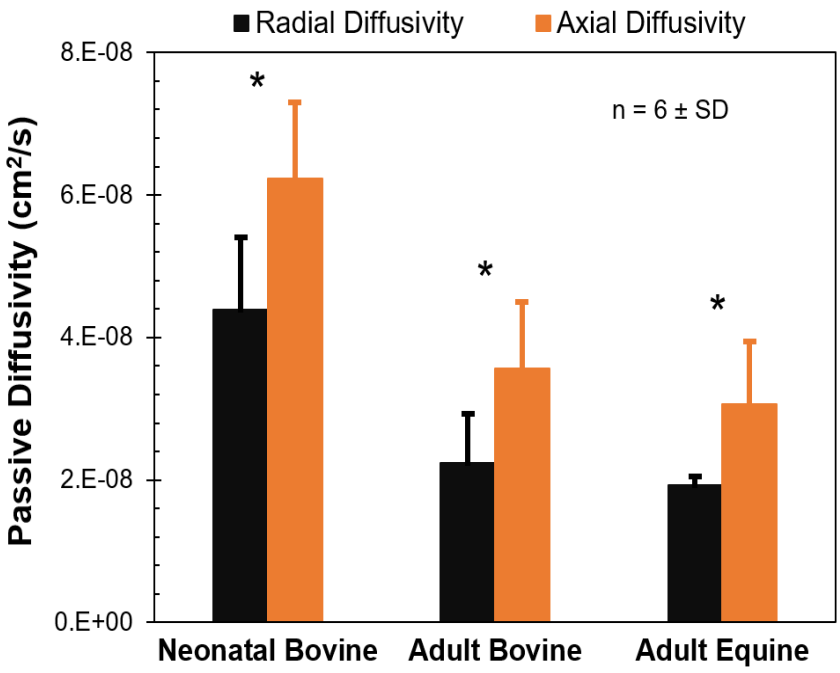

Figure S3: Additionally, a separate group of samples was tested without platens or strain offset to assess passive axial diffusion through the exposed articular surface. Fluorescence profile analysis was carried out perpendicular to the articular surface to obtain a single diffusivity in the axial direction. These diffusivities were compared to radial diffusivities for samples that were also in the free-swelling condition. Passive diffusivity into the articular surface was found to be significantly higher (35-50%) compared to diffusivity in the radial direction for all species types ($p < 0.05$). The antibody had the lowest radial diffusivity in mature equine cartilage (1.9×10^{-8} cm^2/s), and the highest in neonatal bovine tissue (4.4×10^{-8} cm^2/s). Neonatal bovine tissue had higher diffusivities compared to the other two groups ($p < 0.05$).

REFERENCES

1. Shimizu, Y. & Ohta, M. Influence of plaque stiffness on deformation and blood flow patterns in models of stenosis. *Biorheology* **52,** 171–182 (2015).
2. Martel-Pelletier, J. Pathophysiology of osteoarthritis. *Osteoarthritis Cartilage* **12 Suppl A,** S31–S33 (2004).
3. Moos, V., Fickert, S., Müller, B., Weber, U. & Sieper, J. Immunohistological analysis of cytokine expression in human osteoarthritic and healthy cartilage. *J. Rheumatol.* **26,** 870–879 (1999).
4. Steiner, G. *et al.* Cytokine production by synovial T cells in rheumatoid arthritis. *Rheumatology* **38,** 202–213 (1999).
5. Feldmann, M., Brennan, F. M. & Maini, R. N. Role of cytokines in rheumatoid arthritis. *Annu. Rev. Immunol.* **14,** 397–440 (1996).
6. Owen, S., Francis, H. & Roberts, M. Disappearance kinetics of solutes from synovial fluid after intra- articular injection. *Br. J. Clin. Pharmacol.* **38,** 349–355 (1994).
7. Gerwin, N., Hops, C. & Lucke, A. Intraarticular drug delivery in osteoarthritis. *Adv. Drug Deliv. Rev.* **58,** 226–242 (2006).
8. Allen, K. D., Adams, S. B. & Setton, L. A. Evaluating intra-articular drug delivery for the treatment of osteoarthritis in a rat model. *Tissue Eng. Part B. Rev.* **16,** 81–92 (2010).
9. Maroudas, A. Biophysical chemistry of cartilaginous tissues with special reference to solute and fluid transport. *Biorheology`* **12,** 233–248 (1975).
10. Maroudas, A. Transport of solutes through cartilage: permeability to large

molecules. *J. Anat.* **122,** 335–347 (1976).

11. Garcia, A. M., Lark, M. W., Trippel, S. B. & Grodzinsky, A. J. Transport of tissue inhibitor of metalloproteinases-1 through cartilage: Contributions of fluid flow and electrical migration. *J. Orthop. Res.* **16,** 734–742 (1998).
12. Garcia, A. M., Frank, E. H., Grimshaw, P. E. & Grodzinsky, A. J. Contributions of Fluid Convection and Electrical Migration to Transport in Cartilage: Relevance to Loading. *Arch. Biochem. Biophys.* **333,** 317–325 (1996).
13. Bonassar, L. J. *et al.* The effect of dynamic compression on the response of articular cartilage to insulin-like growth factor-I. *J. Orthop. Res.* **19,** 11–17 (2001).
14. Albro, M. B. *et al.* Dynamic loading of immature epiphyseal cartilage pumps nutrients out of vascular canals. *J. Biomech.* **44,** 1654–1659 (2011).
15. Winalski, C. S. *et al.* Enhancement of joint fluid with intravenously administered gadopentetate dimeglumine: technique, rationale, and implications. - PubMed - NCBI. *Radiology* **187,** 179–185 (1993).
16. Ballyns, J. J. & Bonassar, L. J. Dynamic compressive loading of image-guided tissue engineered meniscal constructs. *J. Biomech.* **44,** 509–516 (2011).
17. Maroudas, A. Physicochemical Properties of Cartilage in the Light of Ion Exchange Theory. *Biophys. J.* **8,** 575–595 (1968).
18. Schinagl, R. M., Gurskis, D., Chen, A. C. & Sah, R. L. Depth-dependent confined compression modulus of full-thickness bovine articular cartilage. *J. Orthop. Res.* **15,** 499–506 (1997).
19. Crank, J. *The mathematics of diffusion*. *Oxford University Press* (Clarendon

Press, 1975). doi:10.1016/0306-4549(77)90072-X

20. Fannjiang, A. & Papanicolaou, G. Convection-enhanced diffusion for random flows. *J. Stat. Phys.* **88,** 1033–1076 (1997).

21. Lebrun, L. & Junter, G. A. Diffusion of dextran through microporous membrane filters. *J. Memb. Sci.* **88,** 253–261 (1994).

22. Scherer, P. W., Shendalman, L. H. & Greene, N. M. Simultaneous diffusion and convection in single breath lung washout. *Bull. Math. Biophys.* **34,** 393–412 (1972).

23. Taylor, J. R., Semon, M. D. & Pribram, J. K. *POST-USE REVIEW:* An Introduction to Error Analysis: The Study of Uncertainties in Physical Measurements. *American Journal of Physics* **51,** (University Science Books, 1983).

24. Carr, E. J. & Turner, I. W. A semi-analytical solution for multilayer diffusion in a composite medium consisting of a large number of layers. *Appl. Math. Model.* **40,** 7034–7050 (2015).

25. Maas, S. A., Ellis, B. J., Ateshian, G. A. & Weiss, J. A. FEBio: Finite Elements for Biomechanics. *J. Biomech. Eng.* **134,** 011005 (2012).

26. Mow, V. C., Holmes, M. H. & Michael Lai, W. Fluid transport and mechanical properties of articular cartilage: A review. *J. Biomech.* **17,** 377–394 (1984).

27. Armstrong, C. & Lai, W. I. An Analysis of the Unconfined Compression of Articular Cartilage. *J. Biomech. Eng.* **106,** 165–173 (1984).

28. Eckstein, F., Hudelmaier, M. & Putz, R. The effects of exercise on human articular cartilage. *J. Anat.* **208,** 491–512 (2006).

29. Armstrong, J. K., Wenby, R. B., Meiselman, H. J. & Fisher, T. C. The hydrodynamic radii of macromolecules and their effect on red blood cell aggregation. *Biophys. J.* **87,** 4259–70 (2004).

30. Maroudas, A. Distribution and diffusion of solutes in articular cartilage. *Biophys. J.* **10,** 365–379 (1970).

31. Bonassar, L. J., Grodzinsky, a J., Srinivasan, a, Davila, S. G. & Trippel, S. B. Mechanical and physicochemical regulation of the action of insulin-like growth factor-I on articular cartilage. *Arch. Biochem. Biophys.* **379,** 57–63 (2000).

32. O'Hara, B. P., Urban, J. P. & Maroudas, a. Influence of cyclic loading on the nutrition of articular cartilage. *Ann. Rheum. Dis.* **49,** 536–539 (1990).

33. Athanasiou, K. A. *et al.* Biomechanical properties of hip cartilage in experimental animal models. *Clin. Orthop. Relat. Res.* **316,** 254–266 (1995).

34. Athanasiou, K. A., Rosenwasser, M. P., Buckwalter, J. A., Malinin, T. I. & Mow, V. C. Interspecies comparisons of in situ intrinsic mechanical properties of distal femoral cartilage. *J. Orthop. Res.* **9,** 330–340 (1991).

35. Buschmann, M. D. *et al.* Stimulation of aggrecan synthesis in cartilage explants by cyclic loading is localized to regions of high interstitial fluid flow. *Arch. Biochem. Biophys.* **366,** 1–7 (1999).

36. Park, S., Hung, C. T. & Ateshian, G. A. Mechanical response of bovine articular cartilage under dynamic unconfined compression loading at physiological stress levels. *Osteoarthr. Cartil.* **12,** 65–73 (2004).

37. Ateshian, G. a, Maas, S. & Weiss, J. a. Multiphasic finite element framework for modeling hydrated mixtures with multiple neutral and charged solutes. *J.*

Biomech. Eng. **135,** 111001 (2013).

38. Chahine, N. O. *et al.* Effect of dynamic loading on the transport of solutes into agarose hydrogels. *Biophys. J.* **97,** 968–975 (2009).

39. Hung, C. T. Modeling of Neutral Solute Transport in a Dynamically Loaded Porous Permeable Gel: Implications for Articular Cartilage Biosynthesis and Tissue Engineering. *J. Biomech. Eng.* **125,** 602 (2003).

40. Yao, H. & Gu, W. Y. Convection and diffusion in charged hydrated soft tissues: A mixture theory approach. *Biomech. Model. Mechanobiol.* **6,** 63–72 (2007).

41. Zhang, L., Gardiner, B. S., Smith, D. W., Pivonka, P. & Grodzinsky, A. The effect of cyclic deformation and solute binding on solute transport in cartilage. *Arch. Biochem. Biophys.* **457,** 47–56 (2007).

42. Leddy, H. A. & Guilak, F. Site-specific molecular diffusion in articular cartilage measured using fluorescence recovery after photobleaching. *Ann. Biomed. Eng.* **31,** 753–760 (2003).

43. Evans, R. C. & Quinn, T. M. Solute convection in dynamically compressed cartilage. *J. Biomech.* **39,** 1048–1055 (2006).

44. Fortin, M., Soulhat, J., Shirazi-Adl, a, Hunziker, E. B. & Buschmann, M. D. Unconfined compression of articular cartilage: nonlinear behavior and comparison with a fibril-reinforced biphasic model. *J. Biomech. Eng.* **122,** 189–195 (2000).

45. Chen, A. C., Bae, W. C., Schinagl, R. M. & Sah, R. L. Depth-and strain-dependent mechanical and electromechanical properties of full-thickness bovine articular cartilage in con"ned compression. *J. Biomech.* **34,** 1–12 (2001).

46. Quinn, T. M., Kocian, P. & Meister, J. J. Static compression is associated with decreased diffusivity of dextrans in cartilage explants. *Arch. Biochem. Biophys.* **384,** 327–334 (2000).

47. Evans, R. C. & Quinn, T. M. Solute diffusivity correlates with mechanical properties and matrix density of compressed articular cartilage. *Arch. Biochem. Biophys.* **442,** 1–10 (2005).

48. Hayes, W. C. & Mockros, L. F. Viscoelastic properties of human articular cartilage. *J. Appl. Physiol.* **31,** 562–568 (1971).

49. Evans, C. H., Kraus, V. B. & Setton, L. A. Progress in intra-articular therapy. *Nat. Rev. Rheumatol.* **10,** 11–22 (2013).

CHAPTER 3

The Effect of Antibody Size and Mechanical Loading on Solute Diffusion Through the Articular Surface of Cartilage[3]

Abstract

Because of the heterogeneous nature of articular cartilage tissue, penetration of potential therapeutic molecules for osteoarthritis (OA) through the articular surface is complex, with many factors that affect transport of these solutes within the tissue. Therefore, the goal of this study is to investigate how the size of antibody variants, as well as application of cyclic mechanical loading, affect solute transport within healthy cartilage tissue. Penetration of fluorescently-tagged solutes was quantified using confocal microscopy. For all solutes tested, fluorescence curves were obtained through the articular surface. On average, diffusivities for the solutes of sizes 200 kDa, 150 kDa, 50 kDa, and 25 kDa were 3.3, 3.4, 5.1, and 6.0 $\mu m^2/s$ from 0-100 μm from the articular surface. Diffusivities went up to a maximum of 16.5, 18.5, 20.5, and 23.4 $\mu m^2/s$ for the 200 kDa, 150 kDa, 50 kDa, and 25 kDa molecules, respectively, from 225-325 μm from the surface. Overall, the effect of loading was very significant, with maximal transport enhancement for each solute ranging from 2.2 to 3.4-fold near 275 μm. Ultimately, solutes of this size do not diffuse uniformly, nor are convected uniformly, through the depth of the cartilage tissue. This research potentially holds great clinical significance to discover ways of further optimizing transport into cartilage and lead to effective antibody-based treatments for OA.

[3]C. DiDomenico, A. Goodearl, A. Yarilina, V. Sun, S. Mitra, A. S. Sterman, and L. J. Bonassar, "The Effect of Antibody Size and Mechanical Loading on Solute Diffusion through the Articular Surface of Cartilage Chris D. DiDomenico," *J. Biomech. Eng.*, vol. 14853, no. 607, pp. 1–34, Jul. 2017.

Introduction

The progression of osteoarthritis (OA) is known to be influenced by the release of inflammatory cytokines that cause widespread joint degeneration [1]. As a result, inhibition of inflammatory cytokines and mediators has been a matter of great interest for development of arthritis therapies. Other effective inhibitory treatments for various diseases utilize antibodies or antibody fragments to bind to the target of interest and stop its effects. For example, antibody based strategies inhibiting tumor necrosis factor-α (TNF-α) have been effective in stopping joint degeneration in rheumatoid arthritis (RA), and are some of the highest grossing drugs (Humira, Enbrel, Remicade etc.) on the market [2–4]. Because of the systemic nature of RA, subcutaneous injection of therapeutic antibodies is able to quell the production of inflammatory factors and reduce joint degradation and systemic symptoms. TNF-α and interleukin-1 (IL-1α and β) are also known to play a part in OA, but using antibody based therapy for OA remains a challenge for several reasons [5–7]. In OA, a significant amount of degradative and inflammatory cytokines, including TNF-α and IL-1, are localized to the chondrocytes within the avascular cartilage tissue. As such, access of large molecules like antibodies to target cytokines is difficult, especially since synovial clearance times for drugs are on the order of hours [2,5–10]. Additionally, because of the heterogeneous nature of cartilage tissue, penetration of drugs through the articular surface is complex and there are many factors that affect transport of these large therapeutic molecules within the cartilage matrix.

The structure and composition of cartilage is paramount to understanding how molecular transport occurs through the articular surface. Overall, articular cartilage has an avascular extracellular matrix that by wet weight, is mostly water (75%), glycosaminoglycans (10-12%), and collagen type-II (13-15%) [11,12]. Glycosaminoglycans (GAGs) are responsible for a very small tissue pore size (~10 nm) [13] and also contribute a high fixed charge density of the tissue [11,12]. Importantly, concentrations of both GAGs and collagen type-II generally increase as a function of depth from the articular surface and cause decreasing tissue pore size and increasing fixed charged density [11,12,14]. Collagen fiber orientation changes from being parallel and densely packed at the surface to more perpendicular further into the tissue [15]. Additionally, near the articular surface, there are other proteins, such as decorin and biglycan, that could influence solute interactions [12]. Collectively, the depth-dependence of cartilage structure and composition, combined with known effects of solute size on transport through porous media [16–18], may give rise to a complex molecular transport problem. Research suggests that there could be some distinct size-related solute diffusion behavior for the different "zones" of cartilage for dextrans [19]. Understanding how the composition of cartilage as a function of depth affects diffusion of large (25-200 kDa) therapeutic antibody molecules could shed light on how to better design these molecules to penetrate cartilage more readily and ultimately be more effective in preventing future joint degeneration.

Transport of large macromolecules through cartilage is also known to be affected by mechanical loading. Multiple studies report that mechanical loading causes increased

fluid flow within cartilage and leads to increased molecular transport for relatively large molecules such as insulin-like growth factor I (IGF-I) (MW: 7.6 kDa), tissue inhibitor of metalloproteinase 1 (TIMP-1) (MW: 23 kDa), transforming growth factor-β (TGF-β) (MW: 25 kDa), and albumin (MW: 66 kDa) [20–23]. Mechanical loading has been identified as an important influence in enhancement of penetration of antibodies radially through the deeper zones of the tissue [24]. Also, axial penetration of solutes through the articular surface is highly relevant to the transport of intra-articular therapeutics but little is known about how the depth dependent nature of cartilage affects this phenomenon. Further, understanding this loading enhancement for large molecules, as well as antibodies, could be beneficial in developing exercise regimens for arthritis patients that utilize optimal loading conditions for penetration of the solute of interest [25].

Therefore, the goal of this study is to investigate how various antibodies variants of different size (antibodies and antibody fragments) penetrate perpendicular to the articular surface. Additionally, the effects of cyclic loading at different amplitudes at 1 Hz will be investigated to study how convective flows perpendicular to the articular surface affect transport into cartilage.

Methods

Cartilage Harvest and Preparation

For each experiment, fresh, full-thickness (2 mm) articular cartilage plugs (4 mm diameter) were harvested using biopsy punches under sterile conditions from the patellofemoral groove (PFG) of 1-3 day old bovids (~10 experiments from ~20 different

animals) (Gold Medal Packing, Rome, NY). These plugs were bisected axially, and one 2x4x1.15 mm slice of tissue was obtained from each bisected half, for a total of 20-24 slices for each experiment (Figure 1). All slices represented full-thickness (nominally 2 mm thick) cartilage with the articular surface, middle zone, and deep zone intact. All slices were randomly distributed to experimental groups based on location within the joint to prevent variation in tissue composition skewing experimental results. These slices were randomly assigned to two different groups (loaded and passive) and were placed into individual wells in 24-well plates. Samples were placed in wells such that one of the cut surfaces (2x4 mm surface) was flat on the bottom of the well and the articular surface and deep zones were exposed to media on the lateral faces (Figure 1). An impermeable platen array was placed on top of each well plate, compressing all sample thicknesses approximately 15%, from 1.15 mm to 1.0 mm. This arrangement kept the samples in place and reduced the effects of swelling and limited diffusion perpendicular to the cut surfaces of the samples. For each well, 350 μl of one of 4 fluorescently labeled (Alexa Fluor 633) antibody variants (AbbVie Inc, Worcester, MA) were added at a concentration of ~1-5 μM in PBS (Corning, NY). These antibody variants were the following: a 200 kDa dual variable domain (DVD) antibody, a 150 kDa whole antibody (Ab), a 50 kDa fragment antigen-bonding (F_{ab}) fragment, and a 25 kDa single-chain variable fragment (scFv). All variants were derived from the same 150 kDa whole antibody. With this setup, the solute of interest could freely diffuse perpendicular to the articular surface and the deep zone, but only diffusion through the articular surface was analyzed.

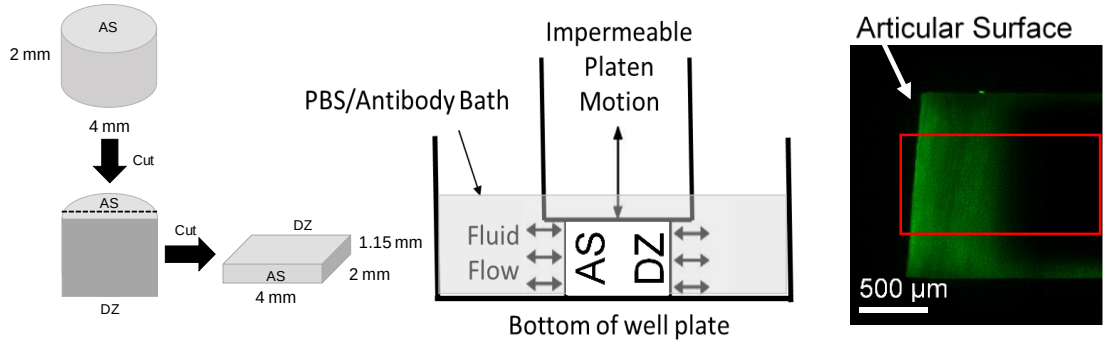

Figure 8: Schematic of sample preparation and experimental setup (left and center) with the fluid flow induced by the platen being perpendicular to the deep zone (DZ) and the articular surface (AS). A 4-mm diameter sample 2-mm thick was bisected, then a slice was cut from each half to obtain a final sample dimension of 4x2x1.15 mm. Fluorescence image obtained from the Ab (150 kDa) solute using confocal microscopy (right). Red box (~1000 µm wide, 500 µm tall) indicates the region of interest that was examined for this study.

Fluorescent labeling of antibodies

Each antibody or fragment was labeled using the Alexa Fluor-633 protein labeling kit (Thermo Fisher, A20170) using the protocol supplied by the manufacturer. Briefly, the pH of the protein solution was adjusted by adding 1/10 volume of 1M sodium bicarbonate (pH 8.5). Amine reactive dye (Thermo Fisher, Cat: A20170) was dissolved in dimethyl sulfoxide (DMSO) to a concentration of 50 mM immediately before conjugation. The dye and pH-adjusted protein were mixed at a 9:1 molar ratio and incubated at room temperature for 2h under constant rotation. Separation of free dye from protein was carried out using PD-10 desalting columns (GE Healthcare Cat: 17-0851-01). Labeled protein was analyzed by analytical size-exclusion chromatography (SEC) and sodium dodecyl sulfate polyacrylamide gel electrophoresis (SDS-PAGE) to ensure minimal change in aggregation during conjugation. Protein concentration and degree of label was determined via absorbance readings at 280 nm and 632 nm.

Disassociation of the label from the antibodies was not deemed significant, as confirmed by independent experiments comparing diffusion from free label and the conjugated antibodies [24].

Mechanical Compression

Each group was placed into a 37°C incubator where the loaded group underwent unconfined cyclic compression with a custom-built, displacement-controlled bioreactor that maintained sterile conditions, as described previously [24,26]. Superimposed on the 15% static strain offset, singular sinusoidal strain amplitudes (0.25%, 1.25%, 2.5%, or 5.0%) were applied to the loaded samples at a singular frequency of 1 Hz for 3 hours. The time-frame of this experiment was verified to be long enough to negate any potential artifacts due to lag between end of loading and imaging in a previous paper [24]. The passive group served as a control, with only a 15% offset strain.

Transport Analysis

After loading, all slices were bisected along the long axis from the articular surface to deep zone, resulting in two slices of 2x2x1.15 mm. This new cut surface was assessed on an inverted confocal microscope stage (LSM 510, Zeiss, Oberkochen, Germany) to characterize the antibody penetration perpendicular to the articular surface (Figure 1). Laser power (λ: 635 nm, ~15 mW) was set so that the total fluorescence (with an emission λ of approximately 640 nm) intensity of the 8-bit image was roughly Gaussian and so that no pixels were saturated (pixel dwell time: ~0.5 ms). The pinhole was set to obtain a representative 30 μm optical section for each sample with a spatial resolution

of 1.35 μm/pixel. A 10x objective with a numerical aperture of 0.3 (Zeiss, Oberkochen, Germany) and a working distance of about 3 mm was used for all samples. A total of 6 tiles were taken to fully capture the sample under these imaging conditions.

This experiment was modeled as 1D diffusion, and steps were taken to negate any edge artifacts and any other unwanted effects in the image analysis. Background fluorescence was calculated from a 1000 μm^2 square area sufficiently far away from the sample and subtracted from the sample fluorescence. Although minimal (< 1% of overall signal intensity) at this wavelength and laser power, autofluorescence of each sample was calculated from a 1000 μm^2 area in the middle of the sample (where no solute was found on the time scale of the experiment) and subtracted from the total sample fluorescence. For all samples, column-wise pixel averages of the sample image data were obtained from the articular surface to 1000 μm deep into the tissue. This depth was chosen for image analysis because it captured the full penetration of all solutes, and limited potential artifacts arising from vasculature that may have been present deeper in this immature tissue. These averages were constrained to the middle 50% of the sample to avoid edge effects from the bottom and top of the sample. Limiting to the middle of the sample also helped avoid any transport artifacts if the loading platen did not maintain contact with the sample throughout the loading cycle. Although there is diffusional anisotropy evident in cartilage [27], the dimensions of the sample and application of the platen prohibited the effects of unwanted diffusion from biasing the results.

The solute fluorescence/concentration relationship was found by taking different dilutions of the solute and observing them under a confocal microscope (LSM 510, Zeiss, Oberkochen, Germany). The fluorescence of the antibody was found to be linearly correlated ($R^2 > 0.95$) to solute concentration in the range of dilute concentrations (1-5 μM) used for these experiments (data not shown), and thus fluorescence values and concentration values could be interchanged to determine how the diffusivity of the solute changes with depth from the articular surface. After normalizing the fluorescence curves to the maximum value, fluorescence profile data were broken down into discrete "layers," spaced 50 μm apart, for a total of 16 layers per sample.

Using a RMS error minimization procedure for each layer, fluorescence data within that particular layer was analyzed with a transient 1D multi-layer diffusion model from Carr et al [28], enabling the calculation of local diffusivities within a sample as a function of depth. This model used a semi-analytical method based on the Laplace transform and an orthogonal eigenfunction expansion to solve the transient slab diffusion equation in 1D for many layers [28]. Fluorescence data were gathered up to 1000 μm from the surface and fluorescence values were normalized to the value at the articular surface. The model was fit to the average depth-wise fluorescence values obtained from the image analysis. A concentration value of one was input at x=0 (the articular surface). Since fluorescence in the center of all samples was negligible, the concentration of the sample was assumed zero at x=1000 μm. Concentration continuity was assumed between the 16 layers, so concentrations from one edge of a layer to the edge of the subsequent layer were

assumed the same. Each layer was assumed homogeneous. All samples were analyzed assuming a solute exposure time of three hours. Both loaded and passive samples had the same initial and boundary conditions.

The model, which only describes transport, was used to investigate how solute diffusivity is affected locally within the heterogeneous cartilage matrix. For cyclically loaded samples, this model yields an "effective diffusivity" [24,29], which includes contributions from both convection and passive diffusion. In passive samples, our local diffusivity measurement only includes diffusion, which we call passive diffusivity. A measure of transport enhancement can be calculated by taking the ratio of these two metrics, which has been highly correlated to local peak fluid flow in a previous study [24]. Because of this relationship with fluid flow, comparing effective diffusivities to passive diffusivities is a good local assessment of how convection affects solute transport. While there are several metrics of quantifying convective contributions of transport [30,31], this method enables easy and accurate comparisons between samples across a range of loading conditions. Decoupling the convective and diffusive contributions was not viable with this model and experimental design. These local diffusivity functions were then compared to obtain information about how loading affected transport of the solute throughout the tissue depth. This model enabled accurate calculation of passive local diffusivity in static samples and an effective local diffusivity in loaded samples.

Statistical Analysis

A repeated-measures three-way ANOVA was performed to determine the effect of solute size, loading amplitude, and depth (the repeated-measure) from the articular surface on local diffusivities, with subsequent Tukey post-hoc tests for pairwise comparisons. All statistics were carried out in Minitab 17 Statistical Software (State College, PA).

Results

Using the experimental setup described above, fluorescence images were obtained and analyzed using custom Matlab software to obtain fluorescence as a function of depth within the region of interest (Figure 1). For all solutes tested, the shape of the fluorescence curves suggest that diffusive behavior is heterogeneous through the depth of the tissue. Indeed, fitting these fluorescence profiles to a 1D diffusion curve with only one overall diffusion coefficient produced a poor fit ($R^2 < 0.5$, data not shown). As such, we used a recently developed slab diffusion model for many layers in series to assess the suitability for this system and to identify distinct diffusive regions within the cartilage depth [28]. Overall, having the multi-layer model contain 16 layers gave the best blend of low error and computation time. Larger layers resulted in unacceptable amounts of error between the model and data; whereas, smaller layers did not resolve any further distinguishing diffusive characteristics. Thus, this experimental setup captures all the most important diffusive effects that are evident as a function of tissue depth for these solutes. The one dimensional multi-layer diffusion model fit well to loaded and passive fluorescence curves of all solutes (coefficient of variances < 12.5%) (Figure 9).

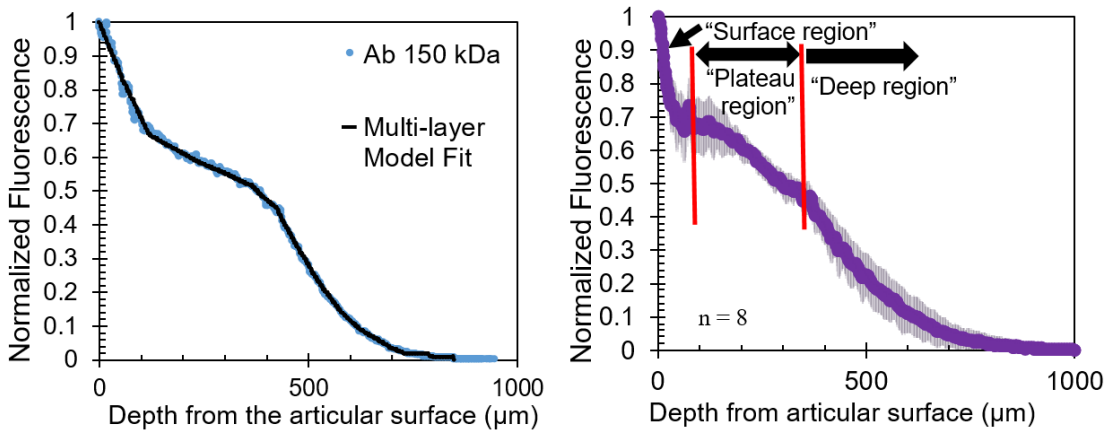

Figure 9: Representative normalized fluorescence curve for the Ab (150 kDa) solute under passive conditions (blue) compared against the 16-layer diffusion model (solid black) (left). For this sample, average coefficient of variance was 6.4%. All solutes had average coefficient of variances less than 12.5%. Loaded and passive samples had equally good fits overall for all solutes. Average normalized fluorescence curve for Ab (150 kDa) through the articular surface shown (right). Standard deviations are represented by the shaded region for n = 8. For this solute, distinct changes in concavity were observed and therefore profiles could be roughly broken into three distinct regions. The articular surface region is characterized by a sharp decrease in fluorescence for the first 100 μm or so, followed by the plateau region where the fluorescence is relatively constant, followed by the deep region where there is a more rapid drop off of fluorescence.

Qualitative analysis of solute fluorescence curves

For all solutes tested, fluorescence curves were obtained from the articular surface to a depth of 1000 μm (Figure 9 and Figure 10). All solutes exhibited diffusive behavior that appeared to vary in three distinct regions: herein defined as the "surface region," "plateau region," and the "deep region" (Figure 9 and Figure 10). For all solutes, the surface region exhibited a sharp decrease in fluorescence for the first 100 μm into the tissue, followed by the plateau region where the fluorescence decreased more slowly from approximately 100 – 350 μm, followed by the deep region where there was a more rapid drop off of fluorescence. All solutes did not penetrate more than 1000 μm in the

3-hour diffusion experiments. Larger molecules, such as the DVD and Ab, seemed to have more abrupt transitions between these three regions than the smaller solutes in this study (Figure 10). To better understand and quantify these regions, local diffusivities were obtained by examining the fluorescence curves for each solute.

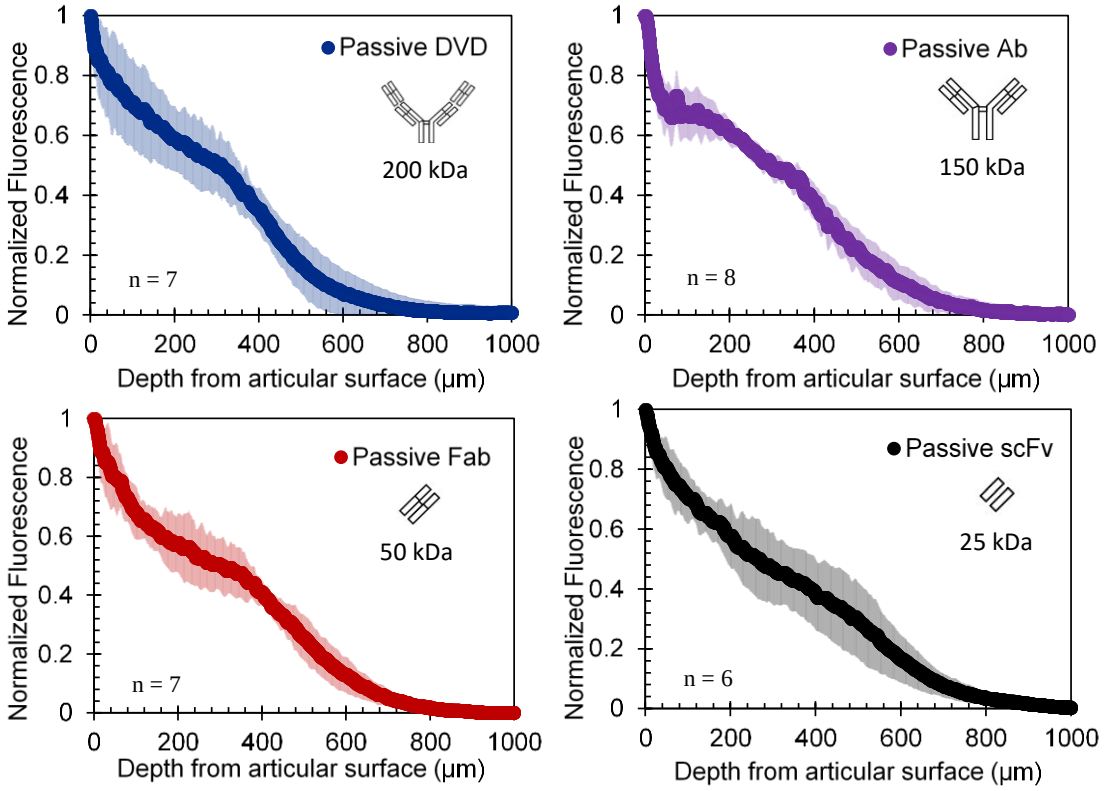

Figure 10: Passive fluorescence profile comparison of the four differently sized solutes used. Error bars (standard deviation for n = 6-8) for all solutes are shown in shades surrounding average profiles.

Effect of size and tissue depth on local passive diffusivities

Overall, fluorescence profiles for solutes were similar up until approximately 350 μm deep (up until the "deep region"), where the solutes diverge according to their size (i.e. smaller ones penetrate further in the tissue) (Figure 11). Fluorescence curves were broken up into 16 layers and a multi-layer 1D diffusion model was used to determine

local diffusivities as a function of depth for the passive solute condition (Figure 11). Overall, local diffusivities were heterogeneous throughout the depth of the tissue, and there were three distinct sections of these curves for each solute. On average, diffusivities for the DVD (200 kDa), Ab (150 kDa), Fab (50 kDa), and scFv (25 kDa), were 3.3, 3.4, 5.1, and 6.0 $\mu m^2/s$ from 0-100 μm (surface region). However, the size of the solute did not affect diffusivity significantly within this region ($p > 0.05$). Diffusivities increased to a maximum of 16.5, 18.5, 20.5, and 23.4 $\mu m^2/s$ for the DVD, Ab, Fab, and scFv, respectively, between 225-325 μm. These data are consistent with previous reports that diffusivity is inversely proportional to molecular weight, even for very large solutes [16]. Calculated diffusivities at 225 μm, 275 μm, and 325 μm were higher than all other diffusivities in the tissue, for all solutes ($p < 0.05$). At 275 μm, the 25 kDa and 50 kDa solute had higher diffusivities than the 150 kDa and 200 kDa antibodies ($p < 0.05$). For all solutes, diffusivities then decreased to statistically similar values found within the surface region in the 400-800 μm range (deep region), and had no significant dependence on size ($p > 0.05$). However, smaller molecules, such as the F_{ab} and scFv, had deeper overall fluorescence penetration into the tissue, because of higher trending diffusivities compared to the larger solutes within this "deep region" (Figure 11). For example, at 575 μm, scFv fluorescence intensity and average local diffusivity were about 2 times that of the DVD solute.

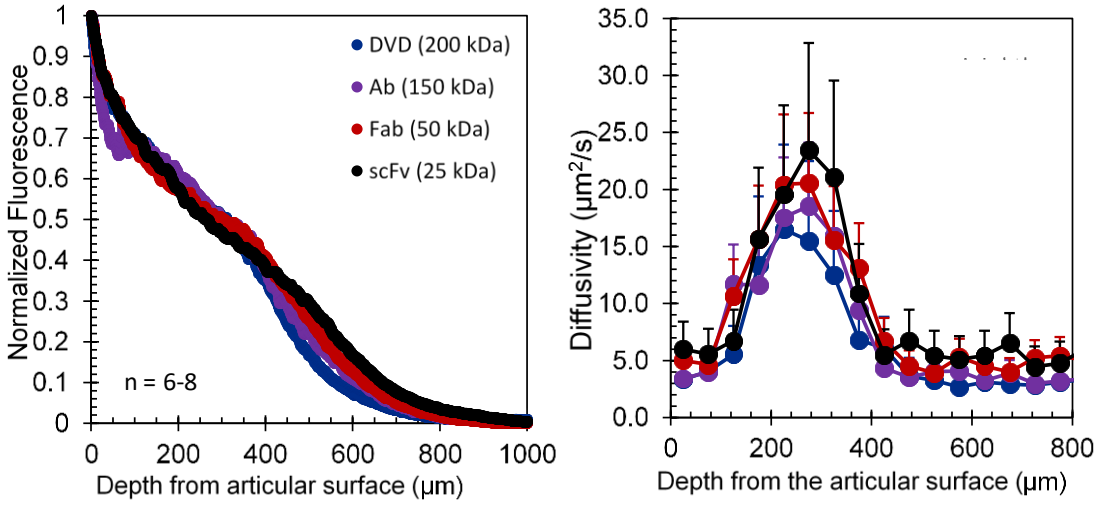

Figure 11: Passive fluorescence profile comparison of the four differently sized solutes used (left) along with the multi-layer diffusivities (right). Error bars denote standard deviations for all solutes (n = 7, 8, 7, 6 for DVD, Ab, Fab, scFv, respectively). Fluorescence curves for these solutes were visually similar up until 400 μm, where solute fluorescence diverged according to size. Overall, local diffusivities were heterogeneous throughout the depth of the tissue, and there were three distinct sections of these curves for each solute. On average, diffusivities for the DVD, Ab, Fab, and scFv, were 3.3, 3.4, 5.1, and 6.0 $\mu m^2/s$ from 0-100 μm, but size did not affect diffusivity significantly within this region ($p > 0.05$). Diffusivities increased to a maximum of 16.5, 18.5, 20.5, and 23.4 $\mu m^2/s$ for the DVD, Ab, Fab, and scFv, respectively, between 225-325 μm. Calculated diffusivities at 225 μm, 275 μm, and 325 μm were higher than all other diffusivities in the tissue, for all solutes ($p < 0.05$). Diffusivities then decreased to similar values found within the surface region in the 400-800 μm range (deep region), and had no significant dependence on size ($p > 0.05$). Values obtained from the 0-125 μm range and 400-800 μm range were not different from each other, for any solute ($p > 0.05$).

Effect of loading on solute transport

To examine how these solutes were affected by loading conditions for three hours at 1 Hz, fluorescence profiles were obtained at 1.25%, 2.5%, and 5% cyclic strain (Figure 12 and Figure S4-3). This loading approximates the strains and amplitudes experienced in articular cartilage in humans from walking (1 Hz, 1.25%) to vigorous exercising (5%)

[32]. Local effective diffusivities were determined for the loaded conditions (Figure 13). Overall, most enhancement of the fluorescence profiles for all solutes was seen from 0 – 400 μm from the articular surface, with highest transport enhancement (compared to respective passive diffusivities) occurring between 175-325 μm ($p < 0.05$). For most solutes, no significant transport enhancement was experienced in the first 125 μm of the tissue, at any loading condition ($p > 0.05$). As expected, solutes undergoing higher cyclic amplitudes (i.e. 5%) received more transport enhancement than ones undergoing less loading, from 175 μm to 325 μm ($p < 0.05$). Compared to passive controls, any loading condition applied maximally enhanced diffusivities from 1.5 to 3.4-fold near 275 μm, but ultimately, local enhancement depended greatly on location within the tissue, solute size, and loading amplitude (Figure 13). For example, the DVD solute experienced a 3.4-fold maximal enhancement at 275 μm compared to passive controls at 5% amplitude, but only experienced a 1.4-fold enhancement at 75 μm. However, the scFv solute experienced a 2.2-fold maximal enhancement (also at 275 μm) at 5% amplitude, with a 1.3-fold enhancement at 75 μm. In general, larger solutes benefited from loading more than smaller ones, especially within the range 225-325 μm ($p < 0.05$). Overall, no loading-based enhancement can be observed deeper than 425 μm into the tissue for any solute ($p > 0.05$).

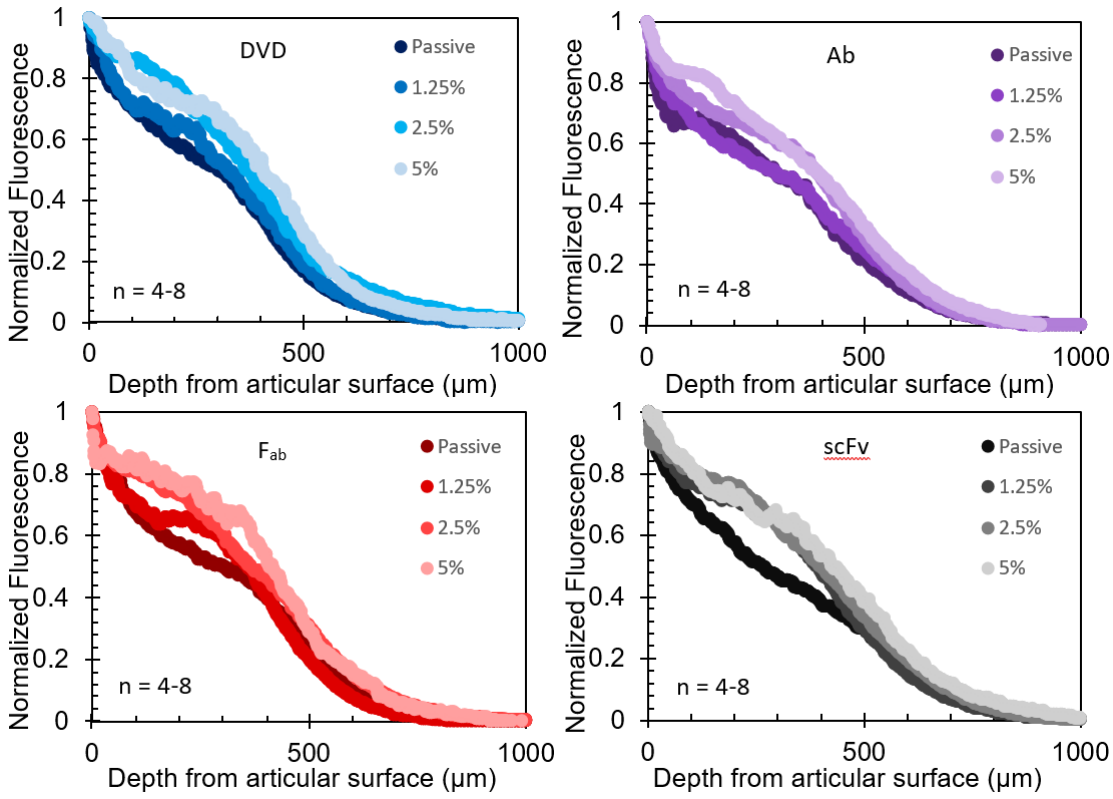

Figure 12: All four solutes' fluorescence profiles for passive and loaded conditions. Lighter shades of color indicate greater loading amplitude. All cyclic loading was conducted at 1 Hz for 3 hours. Most enhancement of the fluorescence profiles for all solutes can be found from 0 – 400 μm from the articular surface. Sample sizes: N = 7, 8, 4, 6 for passive, 1.25%, 2.5%, and 5% for DVD solute, respectively. Sample sizes: N = 8, 7, 6, 5 for passive, 1.25%, 2.5%, and 5% for Ab solute, respectively. Sample sizes: N = 7, 6, 7, 7 for passive, 1.25%, 2.5%, and 5% for Fab solute, respectively. Sample sizes: N = 6, 8, 7, 8 for passive, 1.25%, 2.5%, and 5% for scFv solute, respectively.

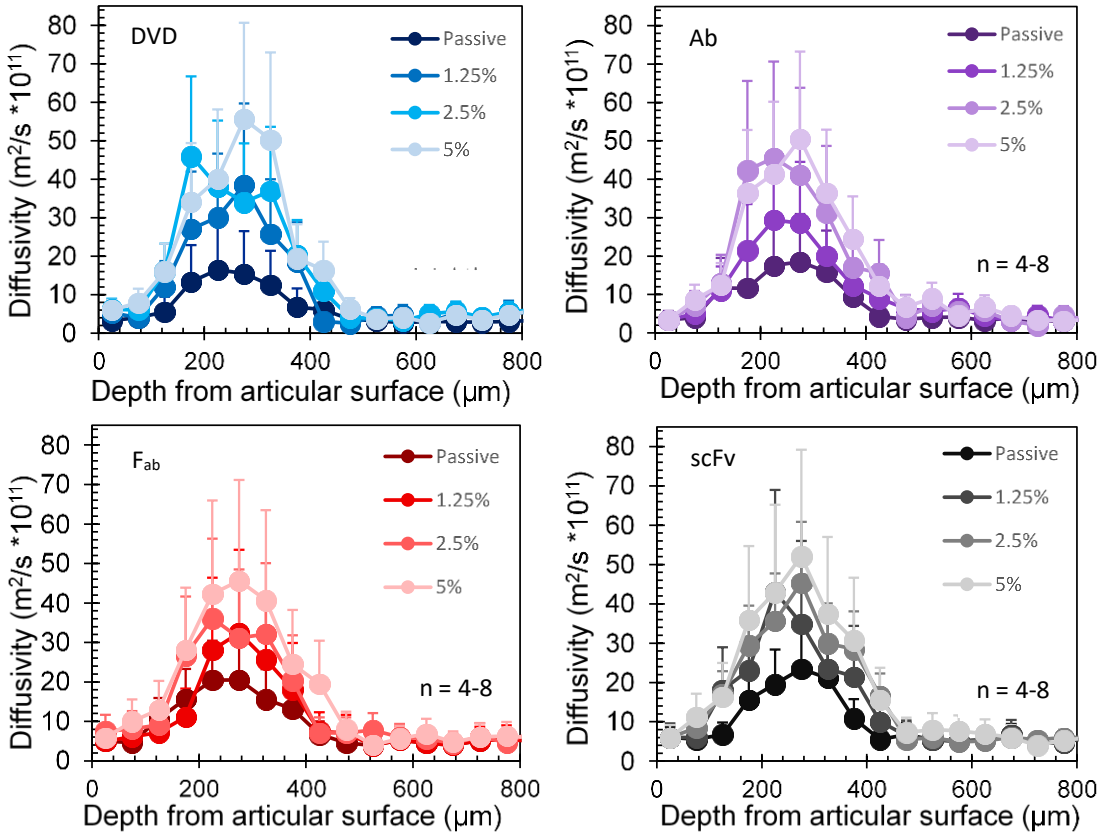

Figure 13: All four solutes' depth-wise diffusivities for passive and loaded conditions. Lighter shades of color indicate greater loading amplitude. Error bars denote standard deviations with n = 4-8 for all solutes (see Figure 5 for specific sample size information). Loading increased diffusivities most from 0 – 400 μm from the articular surface, with highest diffusivity enhancement occurring between 225-325 μm ($p < 0.05$). For most solutes, no significant transport enhancement was experienced in the first 125 μm of the tissue, at any loading condition ($p > 0.05$). As expected, solutes undergoing higher cyclic amplitudes (i.e. 5%) received more transport enhancement than solutes undergoing less loading, from 125 μm to 325 μm ($p < 0.05$). In general, larger solutes benefited from loading more than smaller solutes, especially within the range 225-325 μm ($p < 0.05$). Almost no loading based enhancement can be observed deeper than 425 μm into the tissue.

Discussion

The objectives of this study were two-fold: to determine how the depth-dependent cartilage structure affects antibody penetration through the articular surface; and to

investigate how mechanical loading affects transport through the surface. This study showed that diffusion of 25 – 200 kDa antibody variants was greatly affected by the depth dependent structure of cartilage. For each solute, similar diffusivities were observed near the surface (0-100 μm) and in the deeper zones (> 400 μm), but all exhibited highest diffusivities within the region 150 – 350 μm from the surface. On average, diffusivities within this region were about 300-400% more than diffusivities found elsewhere. Additionally, cyclic mechanical loading enhanced transport of antibody variants 1.5 to 3.4-fold within the region 150-350 μm from the articular surface. Overall, loading had some positive effect on transport up to 375 μm, but did not affect transport past that depth. Previous work has established that enhancement of full-length antibodies through cartilage is approximately 2-3 fold [24], which is consistent with the level of enhancement noted herein and elsewhere [20]. Additionally, diffusivities obtained from the articular surface and deeper regions are consistent with literature values for similarly-sized solutes [16,19,33].

This novel technique enables the determination of local diffusivities for any fluorescently labeled solute in porous media. The cartilage samples were cut in a way that preserved the depth dependent nature of the cartilage. As *in vivo*, solutes in this study diffuse perpendicularly through the articular surface, which is crucial to understand the local diffusive mechanics that would be present within the joint tissue. The multi-layer model enabled quantification of local diffusivities and effective diffusivities for experiments involving passive diffusion and convective transport, respectively. The determination of local diffusivities with a relatively small (~ 50 μm)

resolution remains largely unstudied for different types of cartilage and may prove useful for other applications, such as tendon or ligament research. Although the model used describes transport only, including multi-phasic mixture theories would enable the prediction of local deformations and flows and be useful for future studies that incorporate more complex loading conditions.

Neonatal bovine cartilage was chosen for this study for multiple reasons. This tissue is easy to obtain and to manipulate, and is overall very consistent in terms of physical properties [34]. Additionally, mature equine cartilage (which has comparable permeability to mature human tissue [35,36]) has similar levels of enhancement due to mechanical loading when compared to neonatal bovine tissue [24]. Because mature and neonatal cartilages have similar compositional trends as a function of depth [35,37], implications of this study likely can be applied to healthy human tissue.

While it is well known that cartilage can be discretized into three zones (superficial, middle, and deep) based on cell density, collagen content and organization, and aggrecan content [11,38,39], the effect of such variations on local macromolecular transport is not well understood. Ultimately, it is hypothesized that varying pore size due to both collagen content/organization and aggrecan content affects local diffusivities of solutes of this size [19,27]. Overall, our data support the idea that there are distinct diffusive regions within cartilage for large (25 – 200 kDa) solutes and that local composition has a strong influence on local diffusive behavior. Specifically, we noted that diffusivity is highest approximately 275 μm below the surface ("plateau region"), where collagen and

proteoglycan concentrations are low, and collagen organization is low [37,39]. Diffusivity is lowest and steady deeper in the tissue ("deep region") where such concentrations are highest and steady [37]. However, one would also expect the highest diffusivities to occur near the articular surface ("surface region") because permeability, a strong correlate to diffusivity of a solute [37,40], is highest there. However, diffusivities were low (comparable to the deep region) at the surface, where proteoglycan and collagen concentrations are relatively low [37]. Together, this supports that these sized molecules have a hard time diffusing through the highly organized collagen at the articular surface zone of the cartilage as well as the denser deep zone. Some studies have shown that diffusivities perpendicular to the collagen orientation (which would be the case for diffusion through the articular surface) may be hindered for larger solutes [27]. Most similar to this study, it has been shown that large dextrans (40 kDa and 70 kDa) had lowest diffusivities in the superficial zone compared to deeper in the tissue, while small (3 kDa) and very large (500 kDa) had highest respective diffusivities within this region [19]. Along with results contained herein, this supports that there are size-based thresholds that dramatically influence diffusion behavior as a function of depth in cartilage tissue. Collectively, data from our studies and others suggest that both matrix composition and organization are important determinants of local diffusivity.

Another interesting result comes from the comparing passive diffusion curves between solutes (Figure 11). For example, one would expect a 25 kDa solute to penetrate and diffuse much better than a larger 200 kDa solute, especially in dense tissue. Although this is ultimately true, it is surprising that the 25 kDa solute only had about a 50% greater

diffusivity up until 375 μm, but then had a 100% greater diffusivity deeper than 375 μm. Near the articular surface, with large enough pore sizes, all solutes within 25 kDa – 200 kDa can occupy the same space and diffuse approximately at the same rate. However, as pore size decreases from increasing matrix density, larger solutes seem to be hindered more significantly compared to smaller ones, resulting in a more drastic decrease in diffusivity as depth increases. Together, these data suggest that larger solutes are more readily affected by changes in matrix density in cartilage [41].

In terms of loading-based enhancement, all solutes experienced some level of increased transport from the loading conditions tested. Higher amplitude loading led to higher effective diffusivities within the first 375 μm, with most enhancement (2.2 to 3.4-fold, depending on the solute) occurring near 275 μm (Figure 13). Bigger solutes benefited from loading more than smaller ones up to 375 μm, which supports the idea that bigger solutes experience a larger effect from mechanical stimulation [20,30]. Additionally, previous work indicated that local transport was highly correlated with fluid flow [24]. Interestingly, all four solutes undergoing 5% cyclic strain had approximately a maximum 50 $\mu m^2/s$ local effective diffusivity, independent of size. This provides further evidence that at high amplitudes, convection dominates transport of solutes within this size range, which is supported by a previous study [24].

Fluid flow is an integral part of why large solutes are able to be convected into dense porous tissues such as cartilage [42–44]. Frictional interactions between the solute of interest and tissue matrix has been shown to be very important in the modeling of these

processes [42,45]. Consistent with another study [24], there was no transport enhancement deeper than 425 μm from the articular surface, which implies that there was no fluid flow further into the tissue**.** Besides fluid flow, other researchers have proposed that large solutes can become temporarily entrapped within smaller pores as the pores are compressed on the downstroke of mechanical loading, and then convected deeper into the matrix with future loading cycles [46]. Higher loading amplitudes could increase the compression of these pores, and help higher loading magnitudes retain and convect solutes more than lower loading regimes [46]. This phenomenon could also explain why mechanical loading enhances transport of larger molecules more so than smaller ones [20,30]. In our study, peak effective diffusivities under loading were quite similar (48-55 $\mu m^2/s$), suggesting that drag coefficients are similar across this wide range of antibody sizes.

There are some limitations to this study. The applied mechanical loading to samples is not in a direction consistent with loading conditions found *in vivo* [47]. Loading samples in the way described in the methods was designed to produce 1D flows perpendicular to the articular surface. As such, both diffusion and convection occurred in 1D perpendicular to the surface. This 1D approach elucidates contributions of flow that are important to transport through the articular surface. More complicated models of flow can be coupled with this data to further understand these important phenomena. Nevertheless, it is likely that fluid flow, which has been shown as a significant correlate to solute transport enhancement in cartilage [24,30,31], would have similar impacts *in vivo***.** Because cartilage is poroelastic, there was likely significant platen separation during the

upstroke of the loading cycle at the amplitudes and frequency tested. Tests conducted on a loading frame with a load cell confirmed that total harmonic distortion of 10-35% were present. However, image analysis was performed in the middle 50% of the sample to avoid any edge artifacts near the surface that was in contact with the loading platen. Additionally, loading and passive samples underwent 15% pre-strain, which could cause decreased diffusivities of the solute of interest [48,49]. Upon further investigation, diffusivities of samples undergoing this pre-strain did experience lower local diffusivities throughout the tissue compared to non-strained samples, but these differences were not significant. Most importantly, there were no differences in trends in local diffusivity between samples that experienced pre-strain and those that did not**.** This study does not look at how these solutes behave under equilibrium conditions, which could have elucidated how the solutes are partitioned locally within the tissue after long-term exposure. There is reason to believe that partitioning effects for these molecules are significant and represent yet another important factor that could influence therapeutic development in the future [50]. Although we have not explicitly measured antibody binding, fluorescence profiles for all solutes in this paper were similar to a non-reactive antibody in a previous paper [24], as well as other large solutes in cartilage [50]. Finally, this study did not form an explicit relationship between tissue composition and structure and correlate them to local diffusivity measurements. Using spectroscopic techniques, such as Fourier transform infrared (FTIR) spectroscopy, can help confirm that the local tissue composition is indeed playing a role in the diffusive characteristics of these solutes.

Ultimately, two main points can be gathered from this study. Firstly, the effect of loading on large solutes through the articular surface is very significant, and this potentially holds great clinical significance for the development of exercise regimens in conjunction with antibody therapy [25]. Because diseased OA cartilage has a lower proteoglycan content and is more permeable than healthy tissue [51], it is possible that antibody therapy could be even more effective than predicted when coupled with sufficient mechanical loading [51]. Since the surface and middle zones of osteoarthritic cartilage produce many degradative cytokines [7], targeting these zones with therapeutics could prove to be most beneficial. Fortunately, our study supports that even the largest of antibodies are able to penetrate up to 400 μm fairly easily over 3 hours, which is on the order of *in vivo* synovial clearance times of solutes of this size [9]. Additionally, loading at 1 Hz, which corresponds to the frequency of the walking gait cycle, seems to be optimal for loading based enhancement of antibodies [24]. Another important point of this study was that the depth-dependent structure of cartilage greatly affects the diffusion of antibodies. For all solutes 25-200 kDa in size, local diffusivities were highest around 275 μm from the articular surface, while 300-400% lower near the articular surface and in the deeper zones. Additionally, smaller solutes were able to penetrate deeper into the tissue than bigger ones. Research into how other factors, such as solute charge, could unveil ways to further optimize transport into cartilage and lead to effective antibody-based treatments for OA.

Supplementary Material:

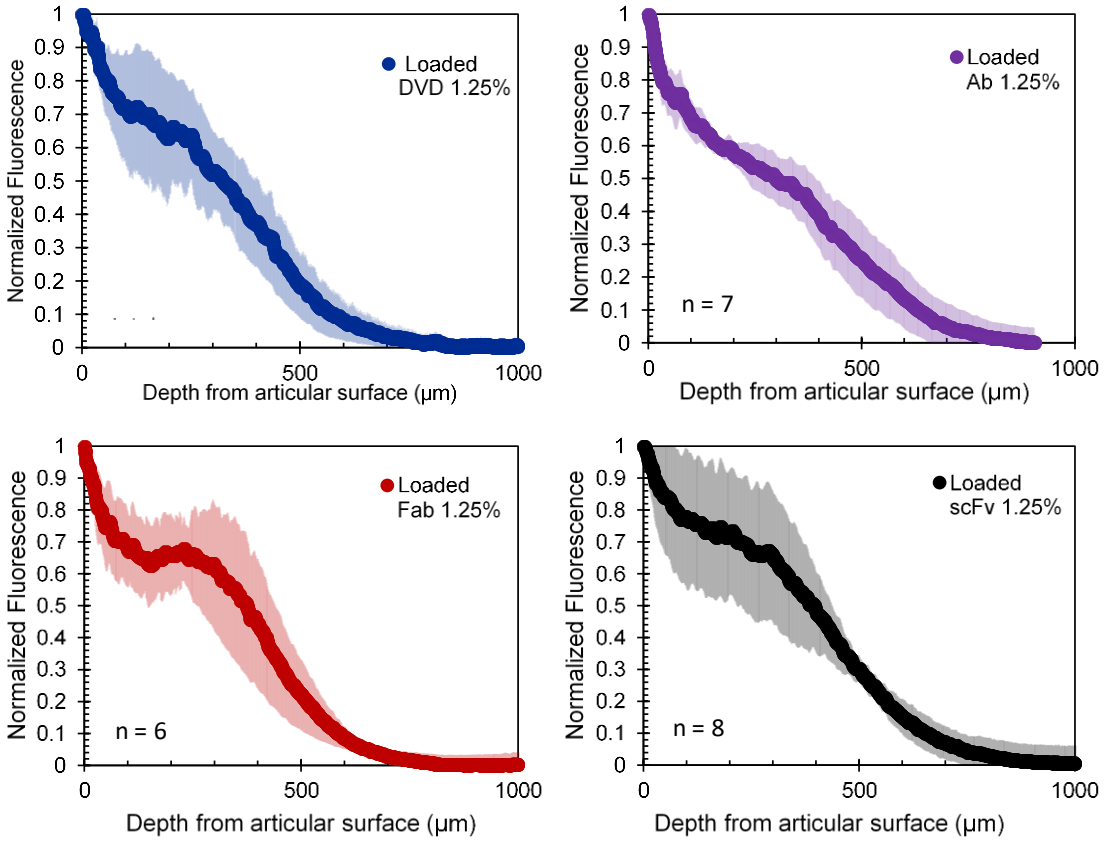

Figure S4: All four solutes' fluorescence profiles for passive and loaded conditions. Cyclic loading was conducted for 3 hours at 1 Hz and 1.25% cyclic loading amplitude. Mean values are shown for each solute, with shaded regions denoting standard deviations.

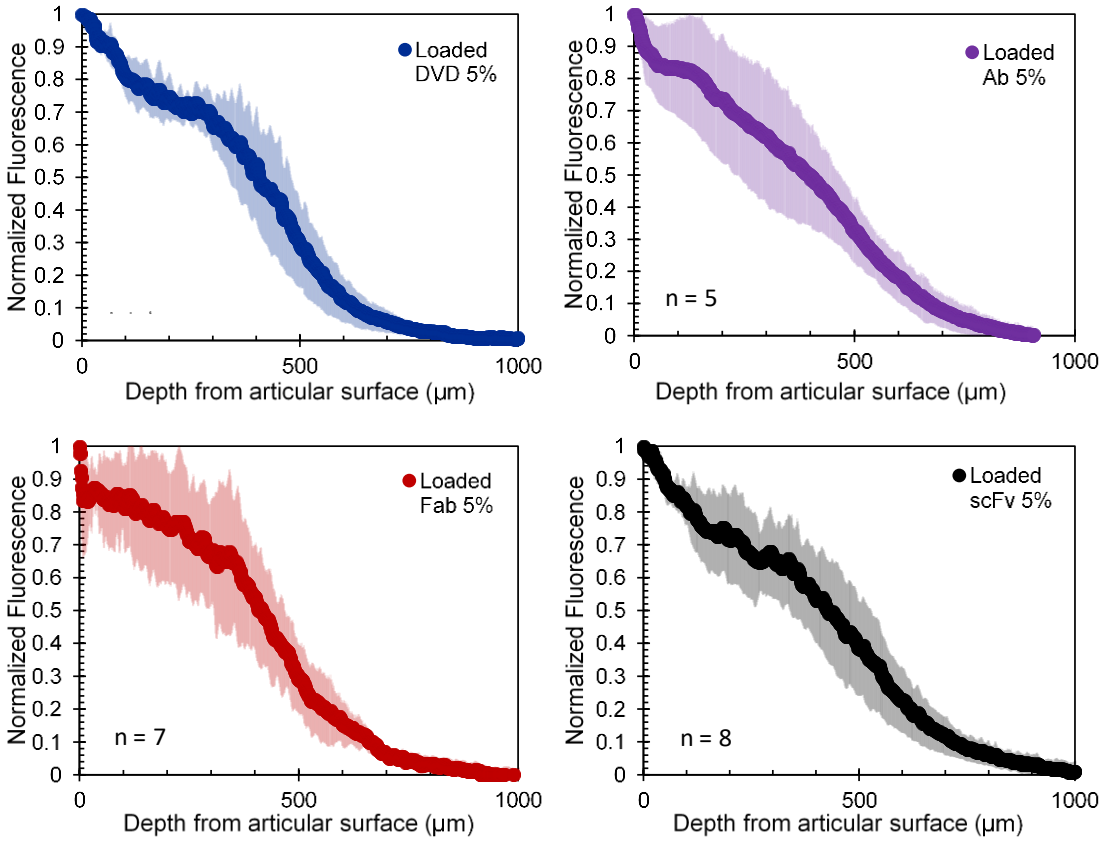

Figure S5: All four solutes' fluorescence profiles for passive and loaded conditions. Cyclic loading was conducted for 3 hours at 1 Hz and 2.5% cyclic loading amplitude. Mean values are shown for each solute, with shaded regions denoting standard deviations.

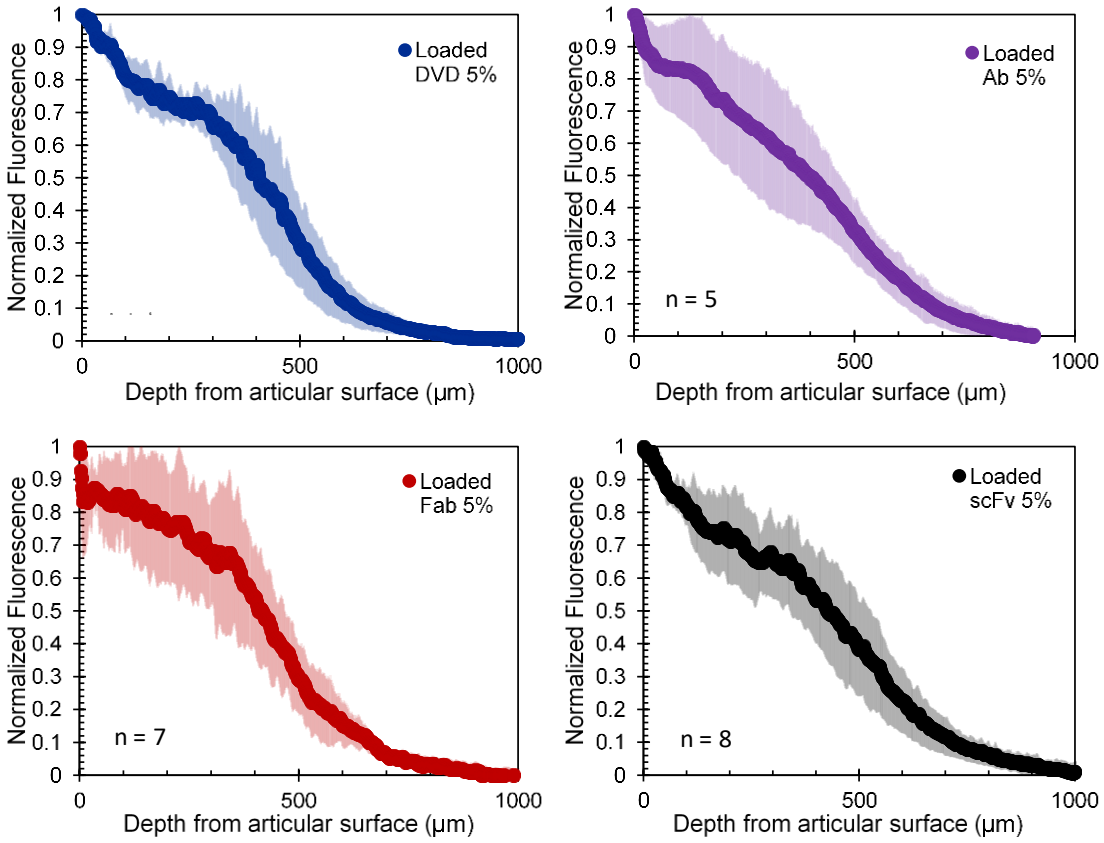

Figure S6: All four solutes' fluorescence profiles for passive and loaded conditions. Cyclic loading was conducted for 3 hours at 1 Hz and 5% cyclic loading amplitude. Mean values are shown for each solute, with shaded regions denoting standard deviations.

REFERENCES

1. Shimizu, Y. & Ohta, M. Influence of plaque stiffness on deformation and blood flow patterns in models of stenosis. *Biorheology* **52,** 171–182 (2015).
2. Bang, L. M. & Keating, G. M. A Review of its Use in Rheumatoid Arthritis. *Biodrugs* **18,** 121–139 (2004).
3. Nestorov, I. Clinical pharmacokinetics of TNF antagonists: How do they differ? *Semin. Arthritis Rheum.* **34,** 12–18 (2005).
4. Feldmann, M. & Maini, R. N. Anti -TNFα Therapy of Rheumatoid Arthritis: What Have We Learned? *Annu Rev Immunol* **19,** 163–96 (2001).
5. Goldring, M. B. Anticytokine therapy for osteoarthritis. *Expert Opin. Biol. Ther.* **1,** 817–829 (2001).
6. Allen, K. D., Adams, S. B. & Setton, L. A. Evaluating intra-articular drug delivery for the treatment of osteoarthritis in a rat model. *Tissue Eng. Part B. Rev.* **16,** 81–92 (2010).
7. Moos, V., Fickert, S., Müller, B., Weber, U. & Sieper, J. Immunohistological analysis of cytokine expression in human osteoarthritic and healthy cartilage. *J. Rheumatol.* **26,** 870–879 (1999).
8. Martel-Pelletier, J. Pathophysiology of osteoarthritis. *Osteoarthritis Cartilage* **12 Suppl A,** S31–S33 (2004).
9. Owen, S., Francis, H. & Roberts, M. Disappearance kinetics of solutes from synovial fluid after intra- articular injection. *Br. J. Clin. Pharmacol.* **38,** 349–355 (1994).
10. Gerwin, N., Hops, C. & Lucke, A. Intraarticular drug delivery in osteoarthritis.

Adv. Drug Deliv. Rev. **58,** 226–242 (2006).

11. Mow, V. C., Holmes, M. H. & Michael Lai, W. Fluid transport and mechanical properties of articular cartilage: A review. *J. Biomech.* **17,** 377–394 (1984).
12. Poole, A. R. *et al.* Composition and structure of articular cartilage: a template for tissue repair. *Clin. Orthop. Relat. Res.* **1,** S26–S33 (2001).
13. Maroudas, A. Biophysical chemistry of cartilaginous tissues with special reference to solute and fluid transport. *Biorheology`* **12,** 233–248 (1975).
14. Maroudas, A. & Bullough, P. Permeability of articular cartilage. *Nature* **219,** 1260–1261 (1968).
15. Hwang, W. S. *et al.* Collagen fibril structure of normal, aging, and osteoarthritic cartilage. *J. Pathol.* **167,** 425–433 (1992).
16. Maroudas, A. Distribution and diffusion of solutes in articular cartilage. *Biophys. J.* **10,** 365–379 (1970).
17. Torzilli, P. A., Arduino, J. M., Gregory, J. D. & Bansal, M. Effect of proteoglycan removal on solute mobility in articular cartilage. *J. Biomech.* **30,** 895–902 (1997).
18. Zhang, L. & Szeri, A. Z. Transport of neutral solute in articular cartilage: Effect of microstructure anisotropy. *J. Biomech.* **41,** 430–437 (2005).
19. Leddy, H. A. & Guilak, F. Site-specific molecular diffusion in articular cartilage measured using fluorescence recovery after photobleaching. *Ann. Biomed. Eng.* **31,** 753–760 (2003).
20. Bonassar, L. J. *et al.* The effect of dynamic compression on the response of articular cartilage to insulin-like growth factor-I. *J. Orthop. Res.* **19,** 11–17 (2001).

21. Garcia, A. M., Lark, M. W., Trippel, S. B. & Grodzinsky, A. J. Transport of tissue inhibitor of metalloproteinases-1 through cartilage: Contributions of fluid flow and electrical migration. *J. Orthop. Res.* **16,** 734–742 (1998).

22. Lima, E. G. *et al.* The beneficial effect of delayed compressive loading on tissue-engineered cartilage constructs cultured with TGF-β3. *Osteoarthr. Cartil.* **15,** 1025–1033 (2007).

23. O'Hara, B. P., Urban, J. P. & Maroudas, a. Influence of cyclic loading on the nutrition of articular cartilage. *Ann. Rheum. Dis.* **49,** 536–539 (1990).

24. DiDomenico, C. D., Xiang Wang, Z. & Bonassar, L. J. Cyclic Mechanical Loading Enhances Transport of Antibodies Into Articular Cartilage. *J. Biomech. Eng.* **139,** 011012 (2016).

25. Winalski, C. S. *et al.* Enhancement of joint fluid with intravenously administered gadopentetate dimeglumine: technique, rationale, and implications. - PubMed - NCBI. *Radiology* **187,** 179–185 (1993).

26. Ballyns, J. J. & Bonassar, L. J. Dynamic compressive loading of image-guided tissue engineered meniscal constructs. *J. Biomech.* **44,** 509–516 (2011).

27. Leddy, H. A., Haider, M. A. & Guilak, F. Diffusional anisotropy in collagenous tissues: fluorescence imaging of continuous point photobleaching. *Biophys. J.* **91,** 311–316 (2006).

28. Carr, E. J. & Turner, I. W. A semi-analytical solution for multilayer diffusion in a composite medium consisting of a large number of layers. *Appl. Math. Model.* **40,** 7034–7050 (2015).

29. Fannjiang, A. & Papanicolaou, G. Convection-enhanced diffusion for random

flows. *J. Stat. Phys.* **88,** 1033–1076 (1997).

30. Garcia, A. M., Frank, E. H., Grimshaw, P. E. & Grodzinsky, A. J. Contributions of Fluid Convection and Electrical Migration to Transport in Cartilage: Relevance to Loading. *Arch. Biochem. Biophys.* **333,** 317–325 (1996).

31. Evans, R. C. & Quinn, T. M. Solute convection in dynamically compressed cartilage. *J. Biomech.* **39,** 1048–1055 (2006).

32. Eckstein, F., Hudelmaier, M. & Putz, R. The effects of exercise on human articular cartilage. *J. Anat.* **208,** 491–512 (2006).

33. Maroudas, A. Transport of solutes through cartilage: permeability to large molecules. *J. Anat.* **122,** 335–347 (1976).

34. Klein, T. J., Chaudhry, M., Bae, W. C. & Sah, R. L. Depth-dependent biomechanical and biochemical properties of fetal, newborn, and tissue-engineered articular cartilage. *J. Biomech.* **40,** 182–190 (2007).

35. Athanasiou, K. A. *et al.* Biomechanical properties of hip cartilage in experimental animal models. *Clin. Orthop. Relat. Res.* **316,** 254–266 (1995).

36. Athanasiou, K. A., Rosenwasser, M. P., Buckwalter, J. A., Malinin, T. I. & Mow, V. C. Interspecies comparisons of in situ intrinsic mechanical properties of distal femoral cartilage. *J. Orthop. Res.* **9,** 330–340 (1991).

37. Silverberg, J. L. *et al.* Structure-function relations and rigidity percolation in the shear properties of articular cartilage. *Biophys. J.* **107,** 1721–1730 (2014).

38. Wilson, W., Huyghe, J. M. & Van Donkelaar, C. C. Depth-dependent compressive equilibrium properties of articular cartilage explained by its composition. *Biomech. Model. Mechanobiol.* **6,** 43–53 (2007).

39. Sophia Fox, A. J., Bedi, A. & Rodeo, S. A. The Basic Science of Articular Cartilage: Structure, Composition and Function. *Orthopaedics* **1,** 461–468 (2009).

40. Maroudas, A. Physicochemical Properties of Cartilage in the Light of Ion Exchange Theory. *Biophys. J.* **8,** 575–595 (1968).

41. Kulmala, K. A. M. *et al.* Diffusion coefficients of articular cartilage for different CT and MRI contrast agents. *Med. Eng. Phys.* **32,** 878–882 (2010).

42. Hung, C. T. Modeling of Neutral Solute Transport in a Dynamically Loaded Porous Permeable Gel: Implications for Articular Cartilage Biosynthesis and Tissue Engineering. *J. Biomech. Eng.* **125,** 602 (2003).

43. Albro, M. B. *et al.* Dynamic loading of immature epiphyseal cartilage pumps nutrients out of vascular canals. *J. Biomech.* **44,** 1654–1659 (2011).

44. Buschmann, M. D. *et al.* Stimulation of aggrecan synthesis in cartilage explants by cyclic loading is localized to regions of high interstitial fluid flow. *Arch. Biochem. Biophys.* **366,** 1–7 (1999).

45. Ateshian, G. A. & Weiss, J. A. in *Computer Models in Biomechanics* 231–249 (Springer Science+Business Media Dordrecht, 2013). doi:10.1007/978-94-007-5464-5_17

46. Zhang, L., Gardiner, B. S., Smith, D. W., Pivonka, P. & Grodzinsky, A. The effect of cyclic deformation and solute binding on solute transport in cartilage. *Arch. Biochem. Biophys.* **457,** 47–56 (2007).

47. Besier, T. F., Gold, G. E., Beaupré, G. S. & Delp, S. L. A modeling framework to estimate patellofemoral joint cartilage stress in vivo. *Med. Sci. Sports Exerc.*

37, 1924–1930 (2005).

48. Quinn, T. M., Kocian, P. & Meister, J. J. Static compression is associated with decreased diffusivity of dextrans in cartilage explants. *Arch. Biochem. Biophys.* **384,** 327–334 (2000).

49. Evans, R. C. & Quinn, T. M. Solute diffusivity correlates with mechanical properties and matrix density of compressed articular cartilage. *Arch. Biochem. Biophys.* **442,** 1–10 (2005).

50. Bajpayee, A. G., Wong, C. R., Bawendi, M. G., Frank, E. H. & Grodzinsky, A. J. Avidin as a model for charge driven transport into cartilage and drug delivery for treating early stage post-traumatic osteoarthritis. *Biomaterials* **35,** 538–549 (2014).

51. Hayes, W. C. & Mockros, L. F. Viscoelastic properties of human articular cartilage. *J. Appl. Physiol.* **31,** 562–568 (1971).

CHAPTER 4

The Effect of Charge and Mechanical Loading on Antibody Diffusion through the Articular Surface of Cartilage[4]

Abstract

Molecular transport of osteoarthritis (OA) therapeutics within articular cartilage is influenced by many factors, such as solute charge, that have yet to be fully understood. This study characterizes how solute charge influences local diffusion and convective transport of antibodies within the heterogeneous cartilage matrix. Three fluorescently-tagged solutes of varying pI (4.7-5.9) were tested in either cyclic or passive cartilage loading conditions. In each case, local diffusivities were calculated based on local fluorescence in the cartilage sample, as observed by confocal microscopy. In agreement with past research, local solute diffusivities within the heterogeneous cartilage matrix were highest around 200-275 μm from the articular surface, but 3-4 times lower at the articular surface and in the deeper zones of the tissue. Transport of all 150 kDa solutes was significantly increased by the application of mechanical loading at 1 Hz, but local transport enhancement was not significantly affected by changes in solute isoelectric point. More positively charged solutes (higher pI) had significantly higher local diffusivities 200-275 μm from the tissue surface, but no other differences were observed. This implies that there are certain regions of cartilage that are more sensitive to changes in solute charge than others, which could be useful for future development of OA therapeutics.

[4]This work has been submitted for publication: C. DiDomenico and L. J. Bonassar, "The Effect of Charge and Mechanical Loading on Antibody Diffusion Through the Articular Surface of Cartilage."
Submitted to the *Journal of Biomechanical Engineering*.

Introduction

To date, there is no clear, effective treatment of osteoarthritis (OA). This wide-spread, debilitating disease is known to be influenced by inflammatory cytokines excreted by native chondrocytes within articular cartilage [1–3]. As such, it is hypothesized that therapeutic agents, such as antibodies, can be used to inhibit these inflammatory processes, provided they can diffuse sufficiently through the dense, avascular cartilage matrix and reach the source cells. Use of antibody therapy has been very successful in other diseases [4,5] and these drugs have many tunable properties, such as charge and molecular weight modification [6]. However, the ability of these large molecules to target these chondrocytes is difficult, especially since synovial clearance times for drugs are on the order of hours [1,3,4,7–10]. Additionally, because of the heterogeneous structure and composition of cartilage, there are many factors that could affect transport of these large molecules.

The composition and structure of cartilage has implications for molecular transport. By dry weight, articular cartilage consists mainly of glycosaminoglycans (40%), and collagen type-II (60%) [11,12]. As a result of the glycosaminoglycans (GAGs), cartilage has a very small pore size (~10 nm) [13] and a very high negative charge density [11,12]. Increasing concentrations of collagen II and GAGs lead to decreasing pore size and increasing negative charge density deeper in the tissue [11,12,14]. Additionally, orientation of collagen fibers changes from the surface to the deeper zone, starting as parallel to the surface and becoming perpendicular near the underlying bone [15]. Recent work indicates that these structural and compositional changes cause large molecules to exhibit

spatially-dependent diffusive characteristics in cartilage that change with molecular weight (25-200 kDa) [16]. There is evidence that more positively charged solutes diffuse more easily into articular cartilage because of attractive electrostatic interactions with the negatively charged matrix [17]. Because therapeutic antibodies can easily be tuned to have different isoelectric points without loss of effective binding to their target *in vivo* [6], this could be an effective way to obtain faster diffusion kinetics into cartilage. However, little is known about how these attractive forces affect larger solutes (> 100 kDa), such as antibodies, and how solute charge affects local diffusion through cartilage.

Because of the poroelastic nature of cartilage, mechanical stimulation of the tissue leads to convective movement that could increase transport of these large therapeutic molecules over passive diffusion alone. As such, mechanical loading has enhanced molecular transport for molecules such as insulin-like growth factor I (IGF-I) (MW: 7.6 kDa), tissue inhibitor of metalloproteinase 1 (TIMP-1) (MW: 23 kDa), transforming growth factor-β (TGF-β) (MW: 25 kDa), and albumin (MW: 66 kDa) [18–21]. Understanding this loading enhancement for large, charged molecules could lead to specialized physical therapy regimens that are tailored to the characteristics of the solute (MW, charge, etc.) administered [22].

Therefore, the goals of this study are to: 1) investigate how charged antibodies of differing isoelectric points (pI) penetrate cartilage through the articular surface and 2) determine the effect of cyclic loading on the transport of charged antibodies through cartilage.

Methods

Cartilage Harvest and Preparation

As described previously [16,23], fresh, 2 mm thick cartilage (with articular surface, middle, and deeper tissue intact) was harvested from the patellofemoral groove of 1-3 day old bovids (8 experiments from ~12 different animals) (Gold Medal Packing, Rome, NY). From this tissue, 12-20 2x4x1.15 mm slices of tissue were obtained (Figure 1). These slices were randomly assigned to two different loading groups (cyclic and passive). Samples were placed in wells in 24-well plates so that the articular surface and deep zones were exposed to media on the lateral faces (Figure 1). An impermeable platen array was placed on top of each 24-well plate, compressing all sample thicknesses approximately 15%, from 1.15 mm to 1.0 mm. This arrangement reduced the effects of tissue swelling and limited diffusion perpendicular to the cut surfaces of the sample, while allowing the solute to freely diffuse perpendicular to the articular surface. Then, 350 μl of one of 3 fluorescently labeled (Alexa Fluor 633) antibody variants (AbbVie Inc, Worcester, MA) were added to each well at a concentration of ~2.5 μM in phosphate buffered saline (PBS) (Corning, NY). These antibodies varied in isoelectric point (pI 4.7, 5.2, 5.9), and were derived from the same 150 kDa antibody [16]. Isoelectric point was determined from capillary electrophoresis, where the location of the maximum chemiluminescence was reported to be the pI of the molecule (Supplemental Figure S5). Fluorescent labeling and quality control tests were performed, as previously reported [16].

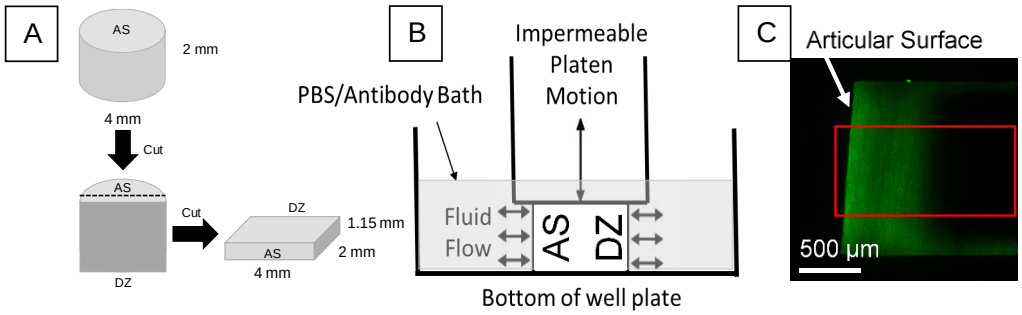

Figure 14: Cartilage cylinders were bisected and then sliced to obtain a final sample dimension of 4x2x1.15 mm (A). Samples were loaded in a way that caused fluid flow to be perpendicular to the articular surface (AS) and deep zone (DZ) (B). Representative image from confocal microscopy showing the fluorescence gradient perpendicular to the AS (C). The red box (~1000 µm wide, 500 µm tall) indicates the region of interest that was examined for this study.

Cyclic Mechanical Compression

Each loading group was placed into a 37°C incubator where the cyclic loading group underwent unconfined cyclic compression with a custom-built, displacement-controlled bioreactor that maintained sterile conditions, as described previously [23,24]. Superimposed on the 15% static strain offset, singular sinusoidal strain amplitudes (1.25%, 2.5%, or 5.0%) were applied to the cyclic loading samples at a frequency of 1 Hz for 3 hours. The time-frame (i.e. 3 hours) of this experiment was verified to be long enough to negate any potential artifacts due to lag between end of loading and imaging [16,23]. The passive group served as a control, with only a 15% offset strain.

Transport Analysis

As previously described [16,23], after loading, all slices were bisected along the short axis from the articular surface to deep zone, resulting in two slices of 2x2x1.15 mm. This new cut surface was assessed on an inverted confocal microscope stage (LSM 710, Zeiss, Germany) to characterize the antibody penetration perpendicular to the articular surface (Figure 1). Then, 30 μm-thick optical sections for each sample were obtained, as previously described [16,23].

This experiment was modeled as a 1-dimensional diffusion problem, as previously described [16,23]. Background fluorescence and autofluorescence were mitigated using previously described method [16,23]. Using custom Matlab code, column-wise pixel averages of sample image data were obtained from the articular surface to 1000 μm deep into the tissue. These averages were constrained to the middle 50% of the sample (see Figure 1) to avoid edge effects and any loading artifacts due to platen/sample separation during the loading cycle. Sample geometry and application of the platen also mitigated the effects of diffusion that was not perpendicular to the articular surface [16,23].

Because of the linear relationship between fluorescence and concentration [23], local fluorescence values can be used to determine how the diffusivity of the solute changed with depth. After normalizing the fluorescence curves to the maximum value, local fluorescence data were broken down into discrete "layers," spaced 75 μm apart, for a total of 13 layers per sample. This layer resolution captured all major features from the fluorescence curves while maintaining a low coefficient of variance (< 15%). Using a RMS error minimization procedure for each layer, fluorescence data within that

particular layer was analyzed with a transient 1D multi-layer diffusion model from Carr et al [25], as described previously [16,23]. Collectively, these calculations enabled the determination for local diffusivities of both cyclic loading and passive samples for all experimental conditions.

Statistical Analysis

A repeated-measures, three-way ANOVA was performed to determine the effect of solute charge, loading amplitude, and depth (the repeated-measure) from the articular surface on local diffusivities, with subsequent Tukey post-hoc tests for pairwise comparisons. All statistics were carried out in Minitab 17 Statistical Software (State College, PA).

Results

Qualitative analysis of solute fluorescence curves

Fluorescent intensity curves as a function of depth were calculated from sample images, for each experimental condition (cyclic and passive). The shape of all fluorescence curves suggest that diffusive behavior is heterogeneous through the depth of the tissue and appeared to vary in three distinct regions, as previously described (Figure 2) [16]. Near the surface (0-100 μm), there was a rapid decrease in fluorescence, followed by a region (100 – 400 μm) of fluorescence that decreased more slowly, followed by another section (> 400 μm) with a more rapid fluorescence decrease. Fluorescence values trended higher (10-15%) for higher pI within the range 200-350 μm from the surface.

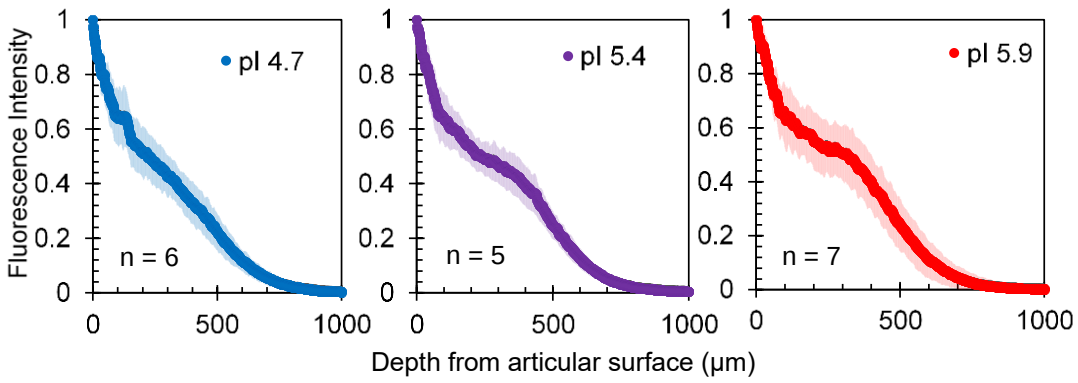

Figure 15: Average normalized fluorescence curve for all solutes (pI 4.7, 5.4, 5.9) through the articular surface. Standard deviations are represented by the shaded region for n = 5-7. Fluorescence values trended higher as pI increased within the region 100-300 μm from the articular surface.

Effect of charge and tissue depth on local passive diffusivities

The aforementioned transport model calculated passive local diffusivities in static samples and effective local diffusivities (combining diffusive and convective phenomena) [23,26] in cyclic loading samples, with a low coefficient of variance (< 15%). Diffusivity calculated at 50 μm from the articular surface was about 4 $\mu m^2/s$ and did not vary with isoelectric point ($p > 0.05$). Between 200-300 μm deep, diffusivities increased to a maximum of 19.0, 16.8, and 15.0, $\mu m^2/s$ for solutes with an isoelectric point of 4.7, 5.4, and 5.9, respectively ($p < 0.05$) (Figure 3). In this region, negative charge inhibited antibody diffusion, with the pI 4.7 antibody having a diffusivity 20-30% lower than that of the pI 5.9 antibody at 200, 275, and 350 μm ($p < 0.05$). Deeper in the tissue (500-1000 μm), diffusivities were similar to those found at 50 μm and had no dependence on isoelectric point ($p > 0.05$). Fluorescence of all solutes did not penetrate further than 800 μm into the tissue within the timeframe of the experiment.

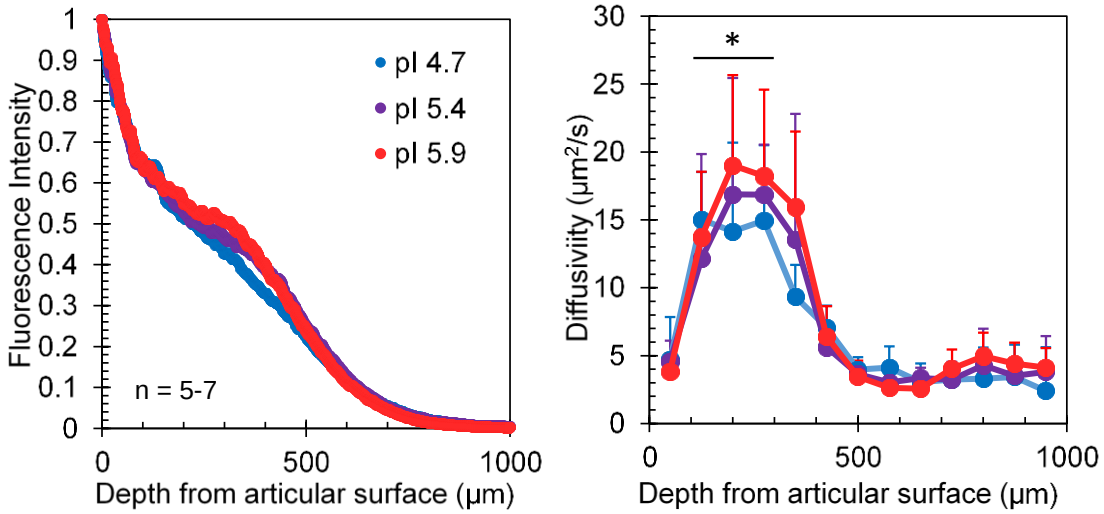

Figure 16: Fluorescence curves for all solutes (passive condition) tested (left) and local diffusivities (right). Error bars denote standard deviations with n = 5-7 for all solutes. Overall, local diffusivities were heterogeneous throughout the depth of the tissue. On average, diffusivities for the pI 4.7, pI 5.4, and pI 5.9, were 3.8, 4.5, 4.6 $\mu m^2/s$ at 50 μm, but pI did not affect diffusivity significantly within this region ($p > 0.05$). Diffusivities increased to a maximum of 15.0, 16.9, and 19.0 $\mu m^2/s$ for the pI 4.7, pI 5.4, and pI 5.9 solutes respectively, between 200-275 μm. Calculated diffusivities at 125 μm, 200 μm, and 275 μm were higher than all other diffusivities in the tissue, for all solutes (*: $p < 0.05$). Diffusivities for pI 5.9 were higher than that of pI 4.7, between 200-375 μm ($p < 0.05$). Diffusivities then decreased to similar values found within the surface region in the 400-800 μm range, and had no significant dependence on pI ($p > 0.05$). Values obtained from 50 μm and 425-800 μm range were not different from each other, for any solute ($p > 0.05$).

Effect of loading on solute transport

To examine how these solutes were affected by cyclic loading, effective local diffusivities were obtained after samples underwent 1.25%, 2.5%, and 5% cyclic strain at 1 Hz (Figure 4 and Figure S1). These loading conditions were chosen to estimate the possible *in vivo* strains in human knee cartilage [27]. Overall, highest diffusivity enhancement was 2 to 3-fold compared to passive diffusivities, occurring between 225-350 μm ($p < 0.05$). Comparing effective diffusivities to passive diffusivities has been

shown to be a good assessment of convective contributions in cyclically loaded samples [16,23]. At all cyclic loading conditions, no significant transport enhancement (ratio of effective diffusivities to passive diffusivities) was evident until 125 μm ($p > 0.05$) (Figure 4). As expected, solutes undergoing higher cyclic amplitudes (i.e. 5%) demonstrated higher transport enhancement than ones undergoing less loading, from 125 μm to 325 μm ($p < 0.05$) (Figure S1). For all solutes, maximal loading enhancement (at 5% cyclic strain) was 2.5 to 3.1-fold at 200 μm. Loading had no effect on diffusivity deeper than 425 μm into the tissue ($p > 0.05$). Fluorescence curves for all loading conditions were not visibly different compared to their respective solute passive curves after 500 μm (Figures S2-S4).

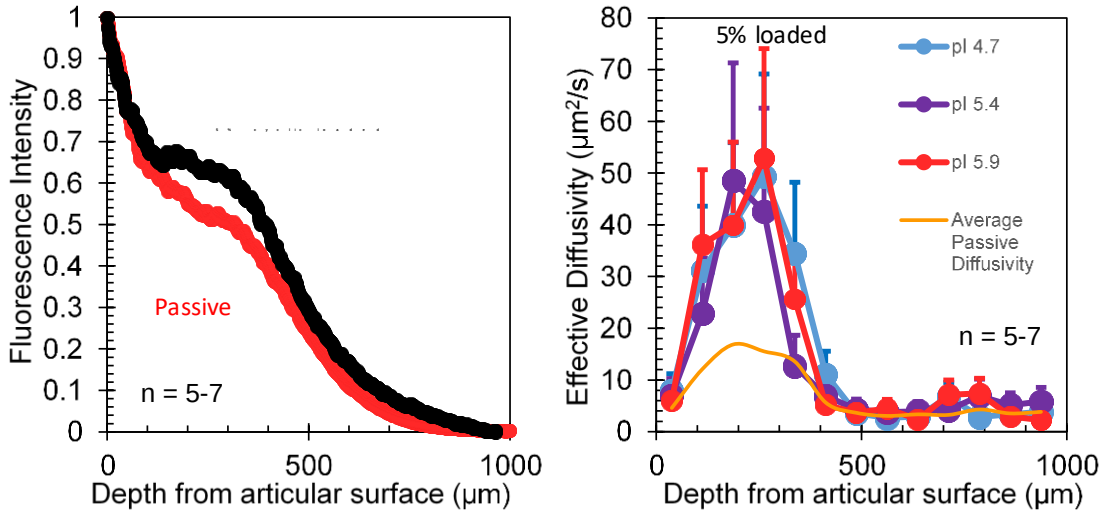

Figure 17: Fluorescence curves for pI 5.9 and 5% cyclic loading (left) and local diffusivities for all solutes at 5% cyclic loading (right). Error bars denote standard deviations with n = 5-7 for all solutes. Orange solid line denotes average passive diffusivity levels in the passive condition for all solutes. Cyclic loading at 5% cyclic strain and at 1 Hz increased fluorescence values between 150 and 400 μm. Solutes did not experience any significant differences in diffusivity values or trends at this loading amplitude ($p > 0.05$). Additionally, there were no differences between solute

diffusivities at 1.25% or 2.5% (shown in supplement). However, maximal transport enhancement increased for all solutes with increasing loading amplitude, as expected.

Discussion

This study examined how antibody charge affects diffusion through the articular surface of cartilage and investigated how transport of these charged molecules is affected by mechanical loading of the tissue. Using a previously-validated technique and methods [16,23], this study showed that diffusion of pI 4.7-5.9 antibody variants was heterogeneous through the depth of cartilage. For each solute, local diffusivities were 250% higher 200-300 μm from the articular surface, as compared to any other depth. Elsewhere in the tissue, diffusivities were at lower, similar values. Additionally, cyclic loading enhanced diffusivities 1.5 to 3-fold within this same region, but did not significantly enhance transport elsewhere. These depth-dependent diffusivities and loading-based enhancement trends are consistent with other studies looking at variously-sized solutes [16,18,23,28–30].

Because articular cartilage is heterogeneous [11,31,32], it is hypothesized that varying pore size due to both collagen content/organization and aggrecan content affects the diffusion characteristics of solutes, especially larger ones [29,33]. Overall, our data are consistent with the idea that local variations in composition are reflected in variations in local diffusion of these large (150 kDa), charged solutes. Local solute diffusivities were lowest where collagen and aggrecan concentrations are highest (> 400 μm deep) [34]. Additionally, diffusivities were highest around 200 μm, where constituent

concentrations and collagen organization are relatively low [34], which is consistent with work published on solutes with a range of molecular weights (25-200 kDa) [16].

High matrix permeability near the articular surface [34,35] implies that solutes should diffuse fastest in this region. As noted elsewhere [16], local diffusivities were low at the surface (i.e. at 50 μm), even though collagen and aggrecan concentrations are relatively low [34]. However, this instead suggests that the densely packed, highly aligned collagen within the surface region affects diffusion of these large, charged solutes [33]. Another study showed that diffusion of large 40 and 70 kDa dextran molecules, but not small 3 kDa dextran, were hindered significantly in the surface region but not in the middle region of articular cartilage [29]. Thus, composition and collagen organization are likely important determinants of local diffusivity, especially for larger, charged solutes.

The antibody with a pI of 5.9 had the highest local diffusivities. Since the cartilage matrix is highly negatively charged [11], this is consistent with attractive electrostatic interactions between the solute and matrix. However, these increased diffusivities were only found from 200-350 μm from the articular surface for the pI 5.9 solute. These data show that local diffusion and solute charge interactions are strongest in areas of the cartilage that are low in matrix content and collagen organization, just past the articular surface region (near 200 μm). Although not seen within the pI range tested in this study, it is possible that diffusion of more positively charged molecules would be elevated in the more negatively charged regions of the cartilage deeper in the tissue (> 500 μm) [11].

Overall, these data support the notion that large, more positively-charged molecules are more mobile in cartilage tissue [17,36], particularly in the sub-surface region.

Ultimately, local transport enhancement due to mechanical loading was consistent with studies that used similar loading conditions [16,23]. For all solutes, loading-based enhancement occurred within 400 μm and was highest around 200 μm (1.5 to 3.1-fold, depending on solute and loading condition). Previously, fluid flow has been highly correlated to solute transport enhancement [23]. As such, all solutes had approximately the same maximum effective diffusivity (at around 200 μm) for every loading condition tested. Thus, at these loading conditions, it is unlikely that small changes (i.e. pI range of 1.2) in solute charge have any effect on transport enhancement *in vivo*.

There are some limitations to this study. The loading direction used was chosen because of its production of generally predictable fluid flow patterns into the articular surface. Although the loading is not in a direction consistent with that in vivo [37], this method produced fluid flow perpendicular to the tissue surface, as predicted by models of joint loading [38,39]. It is possible that a larger range of pI or longer experiments are needed to capture other differences that would appear between solutes. Because of the varying fixed charged density of the tissue, partition coefficients likely change as a function of depth in the tissue and could be another important molecular transport factor [36]. Examination of how partition coefficient changes as a function of depth could be especially important for more highly-charged solutes. Finally, determination of explicit

correlations between local composition and/or collagen content/organization and local diffusivity would have been helpful, but was outside the scope of this study.

Ultimately, negatively-charged antibodies penetrated ~800 μm into healthy cartilage in three hours, which is on the scale of the residence time of similarly-sized molecules within the joint *in vivo* [10]. Transport of all 150 kDa solutes (pI 4.7-5.9) were significantly increased by the application of 1 Hz mechanical loading, but local transport enhancement was not significantly affected by changes in solute isoelectric point. In agreement with past research, local solute diffusivities within the heterogeneous cartilage matrix were highest around 200-275 μm from the articular surface, but 300-400% lower at the articular surface and in the deeper zones [16]. Significantly, more positively charged solutes (higher pI) had significantly higher local diffusivities within the range 200-275 μm, but no other differences were observed. This implies that there are certain regions of cartilage that are more sensitive to changes in solute charge than others. These data support that solute charge is yet another important factor that should be considered in the future development of arthritis therapeutics.

Supplementary Material

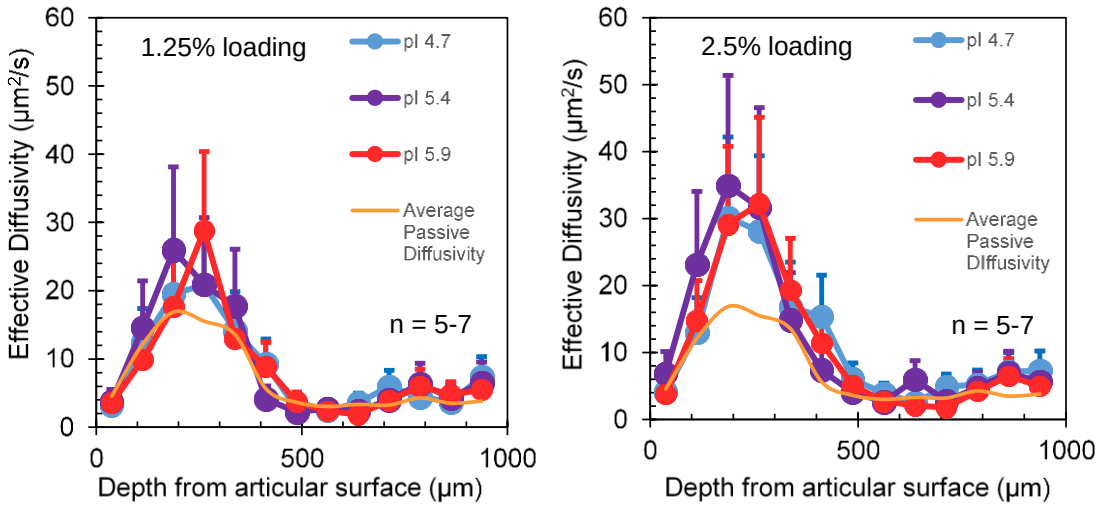

Figure S7: All three solutes' depth-wise diffusivities for 1.25% (left) and 2.5% (right) cyclic loading. Orange solid line denotes average passive diffusivity levels in the passive condition for all solutes. Error bars denote standard deviations with n = 5-7 for all solutes. Higher loading amplitude lead to higher effective diffusivities, as expected. However, there were no differences in diffusivity between solutes at any loading amplitude.

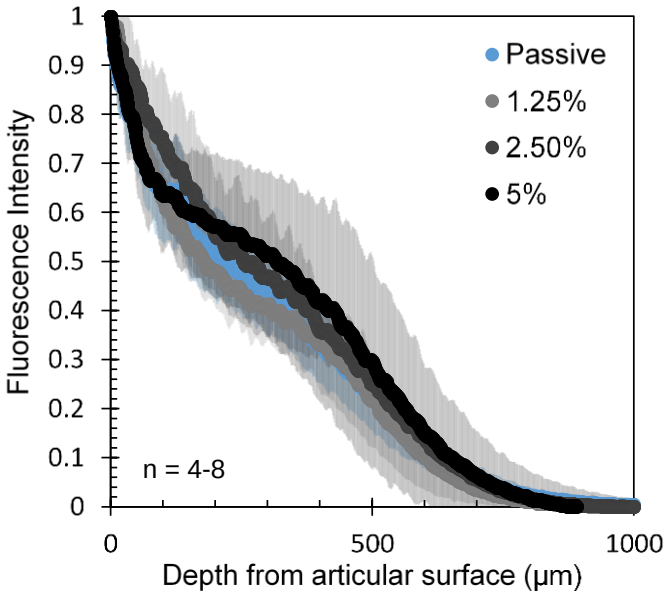

Figure S8: Fluorescence profiles for pI 4.7 solute in passive and cyclic loading conditions. Loading was conducted for 3 hours at 1 Hz and at 1.25%, 2.5%, and 5% cyclic loading amplitudes. Mean values are shown for each solute, with shaded regions denoting standard deviations for n = 4-8.

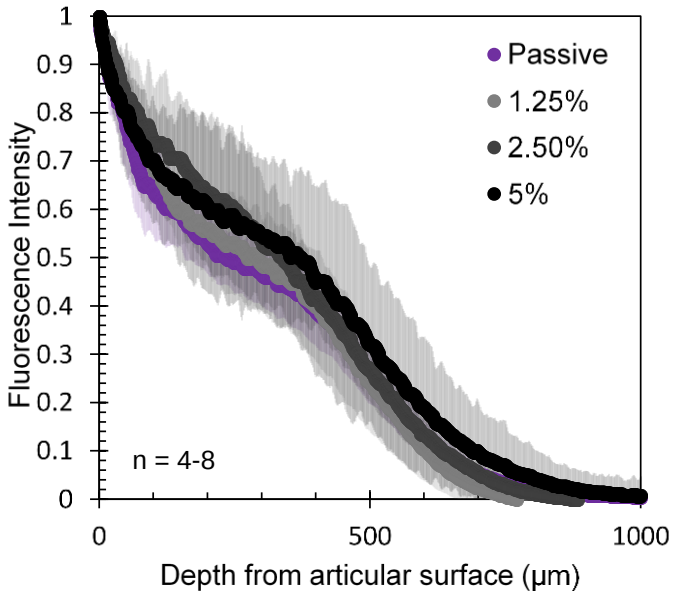

Figure S9: Fluorescence profiles for pI 5.4 solute in passive and cyclic loading conditions. Loading was conducted for 3 hours at 1 Hz and at 1.25%, 2.5%, and 5% cyclic loading amplitudes. Mean values are shown for each solute, with shaded regions denoting standard deviations for n = 4-8.

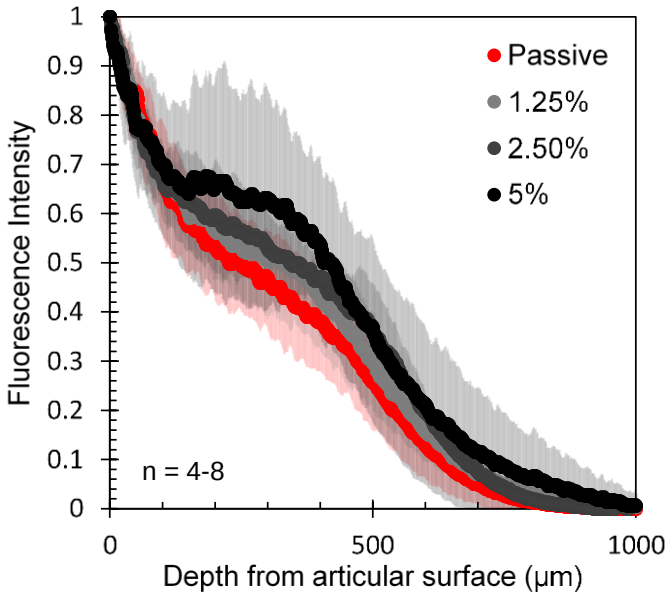

Figure S10: Fluorescence profiles for pI 5.9 solute in passive and cyclic loading conditions. Loading was conducted for 3 hours at 1 Hz and at 1.25%, 2.5%, and 5% cyclic loading amplitudes. Mean values are shown for each solute, with shaded regions denoting standard deviations for n = 4-8.

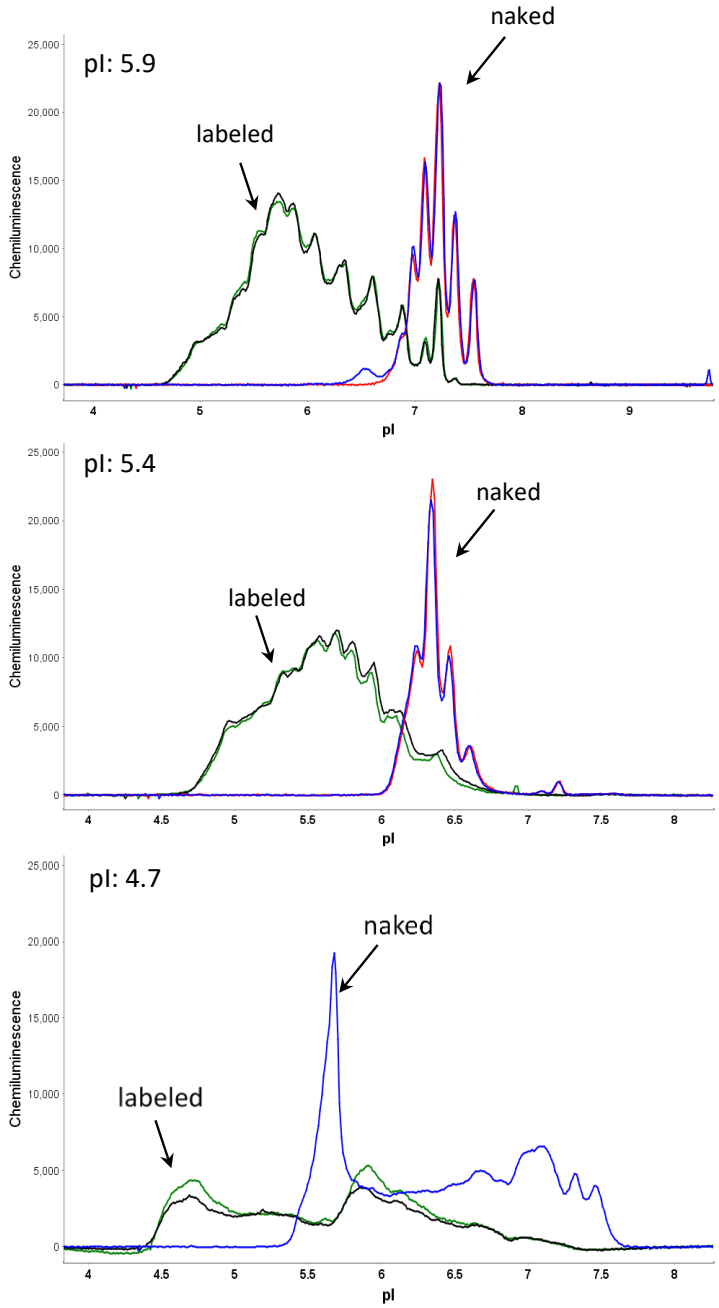

Figure S11**:** Chemiluminescence vs. pI for the three solutes used in this study. Isoelectric point was determined by the maximum chemiluminescence value obtained from electrophoresis.

REFERENCES

1. Moos, V., Fickert, S., Müller, B., Weber, U. & Sieper, J. Immunohistological analysis of cytokine expression in human osteoarthritic and healthy cartilage. *J. Rheumatol.* **26,** 870–879 (1999).
2. Evans, C. H., Kraus, V. B. & Setton, L. A. Progress in intra-articular therapy. *Nat. Rev. Rheumatol.* **10,** 11–22 (2013).
3. Gerwin, N., Hops, C. & Lucke, A. Intraarticular drug delivery in osteoarthritis. *Adv. Drug Deliv. Rev.* **58,** 226–242 (2006).
4. Bang, L. M. & Keating, G. M. A Review of its Use in Rheumatoid Arthritis. *Biodrugs* **18,** 121–139 (2004).
5. Chan, C. E. Z., Chan, a H. Y., Hanson, B. J. & Ooi, E. E. The use of antibodies in the treatment of infectious diseases. *Singapore Med. J.* **50,** 663–72; quiz 673 (2009).
6. Khawli, L. A. *et al.* Charge variants in IgG1: Isolation, characterization, in vitro binding properties and pharmacokinetics in rats. *MAbs* **2,** 613–624 (2010).
7. Goldring, M. B. Anticytokine therapy for osteoarthritis. *Expert Opin. Biol. Ther.* **1,** 817–829 (2001).
8. Allen, K. D., Adams, S. B. & Setton, L. A. Evaluating intra-articular drug delivery for the treatment of osteoarthritis in a rat model. *Tissue Eng. Part B. Rev.* **16,** 81–92 (2010).
9. Martel-Pelletier, J. Pathophysiology of osteoarthritis. *Osteoarthritis Cartilage* **12 Suppl A,** S31–S33 (2004).
10. Owen, S., Francis, H. & Roberts, M. Disappearance kinetics of solutes from

synovial fluid after intra- articular injection. *Br. J. Clin. Pharmacol.* **38,** 349–355 (1994).

11. Mow, V. C., Holmes, M. H. & Michael Lai, W. Fluid transport and mechanical properties of articular cartilage: A review. *J. Biomech.* **17,** 377–394 (1984).
12. Poole, A. R. *et al.* Composition and structure of articular cartilage: a template for tissue repair. *Clin. Orthop. Relat. Res.* **1,** S26–S33 (2001).
13. Maroudas, A. Biophysical chemistry of cartilaginous tissues with special reference to solute and fluid transport. *Biorheology`* **12,** 233–248 (1975).
14. Maroudas, A. & Bullough, P. Permeability of articular cartilage. *Nature* **219,** 1260–1261 (1968).
15. Hwang, W. S. *et al.* Collagen fibril structure of normal, aging, and osteoarthritic cartilage. *J. Pathol.* **167,** 425–433 (1992).
16. DiDomenico, C. D. *et al.* The Effect of Antibody Size and Mechanical Loading on Solute Diffusion Through the Articular Surface of Cartilage. *J. Biomech. Eng.* **139,** 091005 (2017).
17. Bajpayee, A. G. & Grodzinsky, A. J. Cartilage-targeting drug delivery: can electrostatic interactions help? *Nat. Rev. Rheumatol.* **13,** 183–193 (2017).
18. Bonassar, L. J. *et al.* The effect of dynamic compression on the response of articular cartilage to insulin-like growth factor-I. *J. Orthop. Res.* **19,** 11–17 (2001).
19. Garcia, A. M., Lark, M. W., Trippel, S. B. & Grodzinsky, A. J. Transport of tissue inhibitor of metalloproteinases-1 through cartilage: Contributions of fluid flow and electrical migration. *J. Orthop. Res.* **16,** 734–742 (1998).

20. Lima, E. G. *et al.* The beneficial effect of delayed compressive loading on tissue-engineered cartilage constructs cultured with TGF-β3. *Osteoarthr. Cartil.* **15,** 1025–1033 (2007).

21. O'Hara, B. P., Urban, J. P. & Maroudas, a. Influence of cyclic loading on the nutrition of articular cartilage. *Ann. Rheum. Dis.* **49,** 536–539 (1990).

22. Winalski, C. S. *et al.* Enhancement of joint fluid with intravenously administered gadopentetate dimeglumine: technique, rationale, and implications. - PubMed - NCBI. *Radiology* **187,** 179–185 (1993).

23. DiDomenico, C. D., Xiang Wang, Z. & Bonassar, L. J. Cyclic Mechanical Loading Enhances Transport of Antibodies Into Articular Cartilage. *J. Biomech. Eng.* **139,** 011012 (2016).

24. Ballyns, J. J. & Bonassar, L. J. Dynamic compressive loading of image-guided tissue engineered meniscal constructs. *J. Biomech.* **44,** 509–516 (2011).

25. Carr, E. J. & Turner, I. W. A semi-analytical solution for multilayer diffusion in a composite medium consisting of a large number of layers. *Appl. Math. Model.* **40,** 7034–7050 (2015).

26. Fannjiang, A. & Papanicolaou, G. Convection-enhanced diffusion for random flows. *J. Stat. Phys.* **88,** 1033–1076 (1997).

27. Eckstein, F., Hudelmaier, M. & Putz, R. The effects of exercise on human articular cartilage. *J. Anat.* **208,** 491–512 (2006).

28. Maroudas, A. Transport of solutes through cartilage: permeability to large molecules. *J. Anat.* **122,** 335–347 (1976).

29. Leddy, H. A. & Guilak, F. Site-specific molecular diffusion in articular cartilage

measured using fluorescence recovery after photobleaching. *Ann. Biomed. Eng.* **31,** 753–760 (2003).

30. Maroudas, A. Distribution and diffusion of solutes in articular cartilage. *Biophys. J.* **10,** 365–379 (1970).

31. Wilson, W., Huyghe, J. M. & Van Donkelaar, C. C. Depth-dependent compressive equilibrium properties of articular cartilage explained by its composition. *Biomech. Model. Mechanobiol.* **6,** 43–53 (2007).

32. Sophia Fox, A. J., Bedi, A. & Rodeo, S. A. The Basic Science of Articular Cartilage: Structure, Composition and Function. *Orthopaedics* **1,** 461–468 (2009).

33. Leddy, H. A., Haider, M. A. & Guilak, F. Diffusional anisotropy in collagenous tissues: fluorescence imaging of continuous point photobleaching. *Biophys. J.* **91,** 311–316 (2006).

34. Silverberg, J. L. *et al.* Structure-function relations and rigidity percolation in the shear properties of articular cartilage. *Biophys. J.* **107,** 1721–1730 (2014).

35. Maroudas, A. Physicochemical Properties of Cartilage in the Light of Ion Exchange Theory. *Biophys. J.* **8,** 575–595 (1968).

36. Bajpayee, A. G., Wong, C. R., Bawendi, M. G., Frank, E. H. & Grodzinsky, A. J. Avidin as a model for charge driven transport into cartilage and drug delivery for treating early stage post-traumatic osteoarthritis. *Biomaterials* **35,** 538–549 (2014).

37. Besier, T. F., Gold, G. E., Beaupré, G. S. & Delp, S. L. A modeling framework to estimate patellofemoral joint cartilage stress in vivo. *Med. Sci. Sports Exerc.*

37, 1924–1930 (2005).

38. Li, L. P., Cheung, J. T. M. & Herzog, W. Three-dimensional fibril-reinforced finite element model of articular cartilage. *Med. Biol. Eng. Comput.* **47,** 607–615 (2009).

39. Ferguson, S. J., Bryant, J. T., Ganz, R. & Ito, K. The acetabular labrum seal: A poroelastic finite element model. *Clin. Biomech.* **15,** 463–468 (2000).

CHAPTER 5

Measurement of Local Diffusion and Composition in Degraded Articular Cartilage Reveals the Unique Role of Surface Structure in Controlling Macromolecular Transport[5]

Abstract

Developing effective therapeutics for osteoarthritis (OA) necessitates that such molecules can reach and target chondrocytes within articular cartilage. However, predicting how well very large therapeutic molecules diffuse through cartilage is often difficult, and the relationship between local transport mechanics for these molecules and tissue heterogeneities in the tissue is still unclear. In this study, a 150 kDa antibody diffused through the articular surface of healthy and enzymatically degraded cartilage, which enabled the calculation of local diffusion mechanics in tissue with large compositional variations. Local cartilage composition and structure was quantified with Fourier transform infrared (FTIR) spectroscopy and second harmonic generation (SHG) imaging techniques. Overall, both local concentrations of aggrecan and collagen were correlated to local diffusivities for both healthy and surface-degraded samples ($0.3 > R^2 < 0.9$). However, samples that underwent surface degradation by collagenase exhibited stronger correlations ($R^2 > 0.75$) compared to healthy samples ($R^2 < 0.46$), suggesting that the highly aligned collagen at the surface of cartilage acts as a barrier to macromolecular transport.

[5]This work is to be submitted for publication: C. DiDomenico, A. Kaghazchi, and L. J. Bonassar, "Measurement of local diffusion and composition in degraded articular cartilage reveals the unique role of surface structure in controlling macromolecular transport."
To be submitted to the *Journal of Biomechanics*.

Introduction

One of the most prominent types of joint disease is osteoarthritis (OA), for which a clear, effective treatment remains elusive. Recent research supports that chondrocytes within articular cartilage play a large role in joint disease initiation and progression by producing inflammatory cytokines such as such as interleukin-1 (IL-1) and tumor necrosis factor-alpha (TNF-α) [1–5]. The use of antibodies (150 kDa) to bind to and inhibit these factors has been very successful in other diseases, such as rheumatoid arthritis (RA) [6,7]. However, there is concern that these drugs will have trouble diffusing through the avascular articular cartilage to target source cells *in vivo*, especially since synovial fluid clearance times are on the order of hours [1,3,5,8,9]. As such, macromolecular transport into the inherently complex cartilage tissue is an active area of investigation.

There are well-known depth-dependent variations in composition and structure within articular cartilage, which is comprised of mainly of type-II collagen and aggrecan [10,11]. Aggrecan, a large negatively charged proteoglycan, is responsible for a very small matrix pore size [12] and an increasing matrix density deeper in the tissue [10,11,13]. Near the surface, collagen fibers are dense and highly aligned, but fiber organization changes throughout the depth of the tissue [14]. The highly heterogeneous nature of this tissue has many implications for molecular diffusion. Several studies have shown that there are depth-dependent diffusive mechanics for a wide range of large solutes [15–17]. However, these studies lack explicit correlations between local matrix composition and local diffusivity. Developing such relationships for larger therapeutics would be helpful in

healthy tissue, but it is also important to consider how disease or degradation of cartilage affects these relationships.

This clinical progression of many types of arthritis manifests itself by a loss in aggrecan and collagen density [14,18–23], which have important implications for bulk drug transport [24–26]. To mimic *in vivo* degradation, matrix metalloproteinase-1 (MMP-1) [27–29] and other inflammatory cytokines, such as IL-1 [29,30] and TNF-α [30,31], have been used to investigate the effects of degradation on cartilage structure and solute diffusion mechanics. These studies have demonstrated decreases in bulk and local mechanical properties [32–37] and increases to solute diffusion [24,25]. Specifically, Torzilli reported an inverse dependence of solute diffusivity on local aggrecan content for inulin and 70 kDa dextran molecules [24]. Interestingly, diffusion of even larger molecules (e.g. antibodies, 150 kDa) exhibit unexpectedly slow diffusion through the superficial region [17], which is relatively low in aggrecan content [38]. As such, it is hypothesized that these molecules are heavily affected by collagen structure, but this relationship has not been fully elucidated.

Therefore, the overarching goal of this study is to investigate the relationship between local cartilage structure and composition and its effect on local antibody diffusion mechanics. Specifically, this study aims to elucidate the role of the surface layer of cartilage with regards to its effect on macromolecular diffusion through the articular surface.

Methods

Cartilage Harvest, Preparation, and Cartilage Surface Degradation

As described previously [17], fresh, sterile, 2 mm full-thickness cartilage was harvested from the patellofemoral groove of 1-3 day old bovine calves (~10 experiments/animals) (Gold Medal Packing, Rome, NY). These plugs (~16 per experiment) were rinsed in sterile phosphate buffered saline (PBS) (Corning, NY) and randomly assigned to two groups: undegraded (healthy) and surface-degraded (n = 8 per group). Surface-degraded samples had a drop (~10 μl) of either two different enzymes applied to the articular surface for 30 minutes at 37°C (Figure 18): 2 mg/mL of bacterial collagenase (Worthington, type II collagenase, Lakewood, NJ), to degrade both proteoglycans and collagen [37,39], or 200 μg/mL of trypsin (Cellgro, 0.25% trypsin EDTA, Manassas, VA), to degrade only proteoglycans [28,37]. Sufficient surface tension of the drop prevented accidental degradation of the sides of the cartilage plugs. After degradation, samples were serially rinsed with protease inhibitors in 1x PBS for 10 minutes.

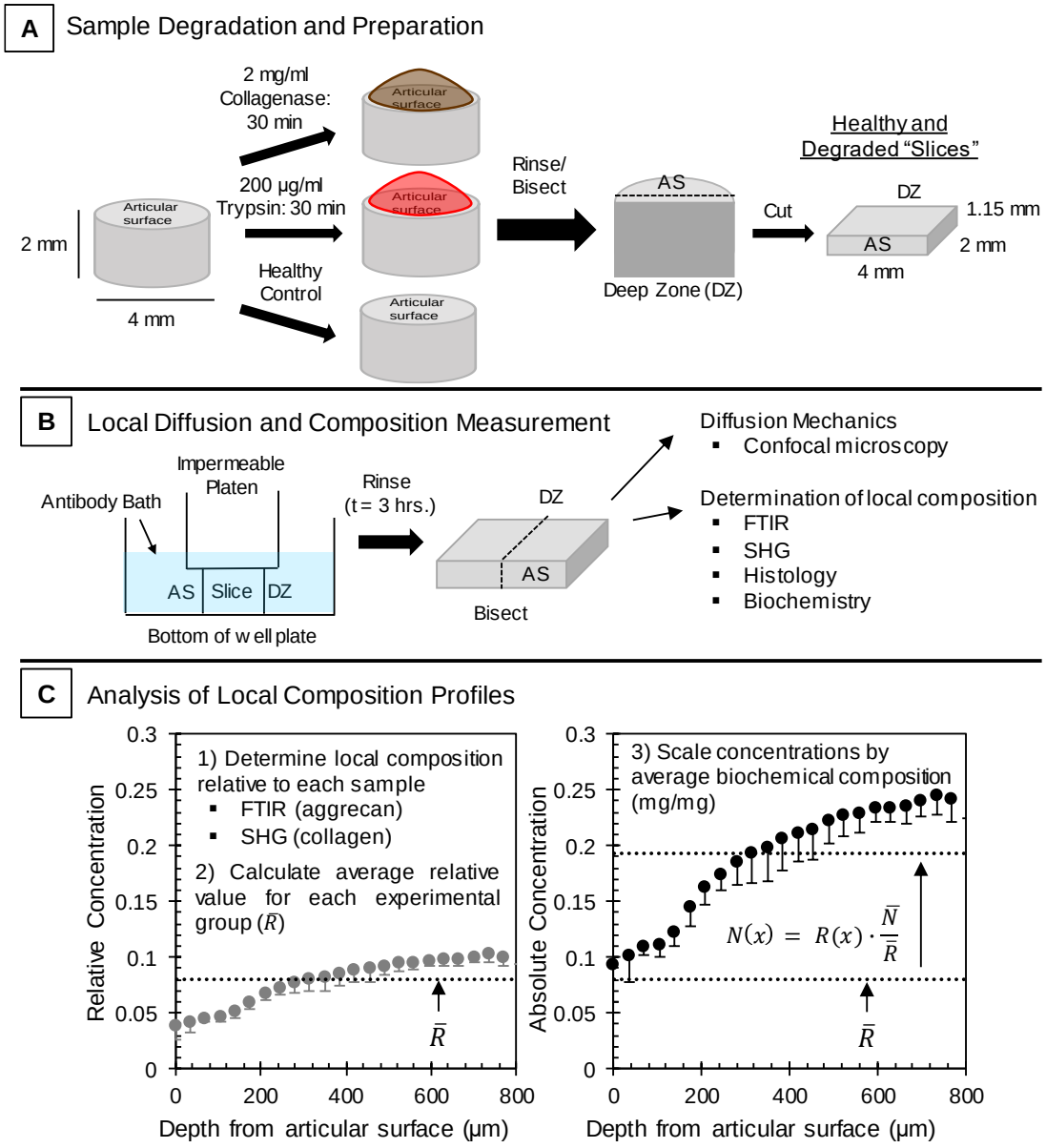

Figure 18: During sample preparation (A), cartilage explants were randomly assigned to three groups: 2 mg/ml collagenase, 200 µg/ml trypsin, or healthy controls. With the bottom third of all samples submerged in PBS, drops (~10 µl) of collagenase or trypsin were added to the articular surface of samples. After rinsing with protease inhibitors, samples were cut to obtain slices measuring 4x2x1.15 mm. Degraded and healthy slices were then exposed to a fluorescent antibody solution (B) so that diffusion would occur perpendicularly to the articular surface. After 3 hours of exposure, samples diffusion was examined with confocal microscopy. Compositional analysis was also performed with Fourier transform infrared spectroscopy (FTIR), second harmonic generation (SHG) imaging, biochemistry, and histology. Bulk aggrecan and collagen content were calculated with biochemistry techniques, and was normalized to dry weight for each

group ($\bar{\boldsymbol{N}}$) (mg/mg). Using the average relative composition from FTIR and SHG ($\bar{\boldsymbol{R}}$), relative concentrations were scaled point by point by the ratio of $\bar{\boldsymbol{N}}$ and $\bar{\boldsymbol{R}}$.

Solute Transport Setup

For all samples, 2x4x1.15 mm slices of tissue were obtained [17] and placed in two 24-well plates (one for healthy and one for degraded) such that the articular surface and deep zones were exposed to media on lateral faces (Figure 18). To limit unwanted diffusion and tissue swelling [17,40], an impermeable platen array was placed on top of each 24-well plate, compressing all samples ~ 15%. As in another study [17], 350 μl of a chemically-stable [17,40], fluorescently-labeled (Alexa Fluor 633) antibody (150 kDa) solution (AbbVie Inc, Worcester, MA) was added to each well at a concentration of ~ 2.5 μM in PBS. Samples were exposed to this solution for 3 hours [17,40].

Solute Transport Analysis (1-D Spatial Diffusion Model)

After solute exposure, all slices were bisected perpendicular to the articular surface [17]. This cut surface of one of these slices (2x2x1.15 mm) was assessed on a confocal microscope stage (LSM 710, Zeiss, Germany) to characterize antibody penetration perpendicular to the articular surface (Figure 18). Confocal microscope and laser settings were similar to those described previously [17,40]. Column-wise pixel averages of sample image data (hereby defined as fluorescence profiles) were obtained from the articular surface to 1000 μm deep into the tissue. The sample geometry, averaging technique, and cutting procedure in these experiments mitigated the effects of diffusion in directions that were not perpendicular to the articular surface and other imaging

artifacts [17,40]. These fluorescence profiles can be used in place of concentration profiles to inform local solute diffusion mechanics [17,40].

Fluorescence profiles (normalized to the fluorescence value at x = 0 μm) were broken down into discrete "layers," spaced 35 μm apart, for a total of 28 layers per sample (from 0 – 1000 μm). Using a root mean square (RMS) error minimization procedure for each layer, fluorescence data within that particular layer was fit to the appropriate local solution of a multi-layer, transient slab diffusion equation in 1D [41], as utilized in previous studies [17,40]. The transport model was used to calculate how solute diffusivity is affected locally throughout the depth in both healthy and degraded samples (Figure 19). Model assumptions and boundary conditions were the same as previously described [17,40].

Analysis of Gross Sample Composition (Biochemistry)

Using the same bisected half of cartilage used for confocal imaging, biochemical analyses were performed, as previously described [42]. These samples were weighed, refrozen, lyophilized, and weighed again. Samples were then digested with 1.25 mg/mL papain solution (Sigma-Aldrich, St. Louis, MO) overnight at 60°C and analyzed for sulfated glycosaminoglycan (GAG) content through a 1,9-dimethylmethylene blue assay [43] and for collagen through a hydroxyproline assay [44]. Biochemical properties were normalized to the dry weight of the samples and averaged within healthy and degraded groups.

Analysis of Spatial Aggrecan Sample Composition (Histology)

The other 2x2x1.15 mm section of cartilage was then fixed in formalin, embedded in paraffin, and sectioned into 4-μm thick sections on glass slides. Samples were dewaxed in serial xylene baths and rehydrated in serial washes of ethyl alcohol [38]. These samples were then stained with Safranin-O for 11 minutes and dehydrated to visualize aggrecan within the tissue (Figure 20).

Analysis of Spatial Aggrecan Content (Fourier Transform Infrared Spectroscopy)

As reported previously [38], 4-um thick sections of all samples were also placed on 2-mm-thick, 25 mm diameter infrared transparent BaF^2 disks (Spectral Systems, Hopewell Junction, NY). Sections were dewaxed and rehydrated as described above. In transmission mode, a Hyperion 2000 Fourier transform infrared imaging (FTIR) microscope (Bruker, Billerica, MA) obtained sample absorbance spectra (average of 32 background-corrected scans between 600 and 4000 cm^{-1}) with a resolution of 4 cm^{-1} using a 15x objective [38]. These absorbance spectra were collected at equally spaced intervals (35 μm) over a rectangular region of 25 x 120 mm^2, from the articular surface to the deep zone. Using a previously validated method [38], spectra were fit to a linear combination of a pure type II collagen spectrum [45], a pure aggrecan spectrum [45], and a linear baseline over a spectral window from 900 to 1725 cm^{-1} [38]. The resulting depth-wise, pure-compound aggrecan coefficient, which is proportional to molecular concentration [38], was scaled to the results of the biochemical analysis by a single multiplicative factor. This factor was equal to the average group-specific aggrecan content from biochemistry (~ 22% of the dry weight) divided by the average pure-

compound aggrecan coefficient for each sample. Using this factor enabled the calculation of absolute, group-specific, depth-wise concentrations of aggrecan (Figure 20).

Analysis of Spatial Collagen Content (Second Harmonic Generation Imaging)

Although the FTIR method enabled calculation of the spatial collagen content, this method could not quantify disruption of the organization of the collagen matrix in degraded samples. As such, second harmonic generation (SHG) imaging was used to obtain a better overall picture of how this degradation protocol affected the concentration of *organized* collagen through the depth of the tissue [46]. Using the bisected sample halves used for histology, an upright confocal microscope capable of SHG imaging (LSM 880, Zeiss, Germany) was used to image 13-μm thick, deparaffinized sections of all samples. A 20x water-immersion objective with a numerical aperture of 0.17 captured a ~1.5 μm optical slice of each sample with a resolution of 0.35 μm/pixel. A circular polarizer was used to prevent changes in collagen orientation from affecting SHG intensity. With a laser excitation wavelength of 880 nm, a non-descanned detector (NDD) was used to capture SHG intensity profiles from the articular surface to the deep zone of the tissue (0-1000 um) with a 430 – 455 nm wavelength filter in place to mitigate autofluorescence of the collagen and other matrix constituents. Column-wise pixel averages of SHG image data were then obtained and converted to organized collagen concentration by taking the square root of each averaged pixel value [46]. This depth-wise collagen concentration map for each sample was normalized to group-specific gross

collagen content (~ 52% of the dry weight) obtained from biochemistry, which resulted in absolute, organized collagen concentrations for all samples (Figure 21).

Statistical Analysis

Repeated-measures two-way analysis of variance (ANOVA) was performed to determine the effect of degradation and depth (the repeated-measure) from the articular surface on local diffusivities and local composition, with subsequent Tukey post-hoc tests for pairwise comparisons. Linear regression was performed to assess the relationship between local diffusivities and composition. Analysis of covariance (ANCOVA) was used to compare relationships between diffusivity and composition. All statistics were carried out in Minitab 17 Statistical Software (State College, PA).

Results

Transport Analysis

For healthy and degraded samples, the shape of the fluorescence profiles obtained from confocal images suggest that diffusion behavior is highly heterogeneous throughout the depth of the tissue, consistent with previous studies [16,17,40]. Degrading with collagenase or trypsin increased local fluorescence values up to 50% higher than healthy controls within 0 – 400 μm and changed the shape of the fluorescence profiles in this region, but no differences between groups were found past that depth. Increases in local fluorescence were observed in areas of lower aggrecan in all samples (Figure 19), supporting that aggrecan content and local transport mechanics are highly related.

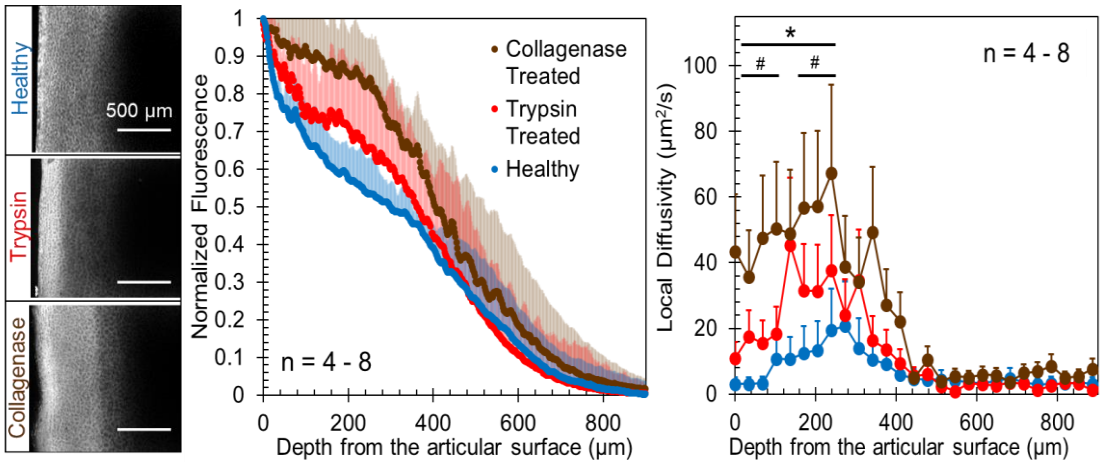

Figure 19: Fluorescence images allow calculation of fluorescence profiles for all three groups and determination of how degradation affects local solute diffusivities (left). Transport analyses showing the fluorescence curves of all experimental conditions (middle) and their respective local diffusivities throughout the depth of the cartilage (right). Samples with the surfaces degraded by either enzyme (collagenase or trypsin) exhibited higher fluorescence compared to the healthy controls within the first 400 μm from the articular surface. Degradation with either trypsin or collagenase led to higher diffusivities compared to healthy within the first 350 μm (*: $p < 0.05$, repeated-measures two-way ANOVA), and all groups were statistically similar at depths more than 400 μm (with an average of 4 $\mu m^2/s$). Collagenase-treated samples exhibited the highest local diffusivities (70 $\mu m^2/s$ at 250 μm), compared to the trypsin-treated (40 $\mu m^2/s$ at 250 μm) or healthy samples (20 $\mu m^2/s$ at 250 μm), and highest diffusivities at the surface (0 μm) of the tissue (45 $\mu m^2/s$), compared to the trypsin (10 $\mu m^2/s$) or healthy (4 $\mu m^2/s$) groups ($p < 0.05$). Error bars (both shaded and standard) denote standard deviations with n = 4 - 8.

Using a validated multi-layer diffusion model with 28 layers [17], all samples exhibited heterogeneous diffusivities through the depth of the tissue (Figure 19). Healthy samples exhibited a maximum local diffusivity of 20 $\mu m^2/s$ at 250 μm from surface ($p < 0.05$, repeated-measures two-way ANOVA), whereas values near the articular surface (0-100 μm) and deeper zones (> 400 μm) were about 4 $\mu m^2/s$ (Figure 19). Degradation with either trypsin or collagenase led to higher diffusivities within the first 350 μm ($p < 0.05$), and all groups were statistically similar at depths more than 400 μm. Collagenase-

treated samples exhibited the highest local diffusivities (70 $\mu m^2/s$ at 250 μm), compared to the trypsin-treated (40 $\mu m^2/s$ at 250 μm) or healthy samples, and highest diffusivities at the surface (0 μm) of the tissue (45 $\mu m^2/s$), compared to the trypsin (10 $\mu m^2/s$) or healthy (4 $\mu m^2/s$) groups ($p < 0.05$).

FTIR Analysis (Local Aggrecan Composition)

A previously established [38], linear decomposition analysis was conducted to analyze how aggrecan content varied as function of depth in cartilage. Linearly decomposed spectra closely fit the actual FTIR absorbance spectra at all tissue depths, with average errors between 10-15%. Overall, the biochemistry-scaled aggrecan composition of both healthy and degraded samples varies as a function of depth (Figure 20), as previously reported [38]. Degradation with collagenase or trypsin led to significant decreases (up to 40%) in aggrecan content, within the first 210 and 420 μm, respectively ($p < 0.05$) (Figure 20). Consistently, there were visible decreases in Safranin-O histological staining intensity in the first 0 – 250 μm from the articular surface in samples that were treated with trypsin and collagenase. At 100 μm, the FTIR absorbance spectra for degraded samples exhibited lower absorbance values near wavenumbers (~1140 – 985 cm^{-1}) associated with carbohydrate content [45,47,48], consistent with these samples containing lower amounts of proteoglycan (aggrecan) near the surface. Absorbances near the amide I (1720 – 1590 cm^{-1}) and amide III (1590 – 1492 cm^{-1}) regions [48] were similar for all groups and depths, suggesting that that the gross amount of collagen content was unchanged across all sample groups.

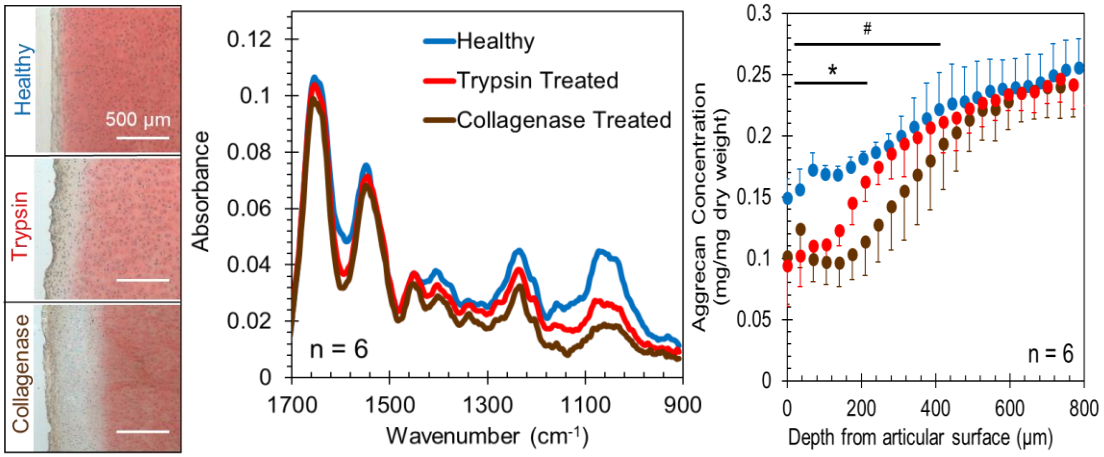

Figure 20*:* Safranin-O histology images (left) demonstrate how trypsin and collagenase degrade the proteoglycans near the surface zone of the cartilage. Absorbance spectra from FTIR analysis for the degraded samples compared to normal healthy controls (middle) at a depth of 100 μm. Collagenase and trypsin both drastically changed the absorbance spectra by altering the carbohydrate peak height near (1140 – 985 cm^{-1}), suggesting collagenase caused greater loss of proteoglycans (including aggrecan) compared to trypsin. Local aggrecan composition (right) was obtained by calculating the depth-dependent aggrecan fitting coefficient by decomposing FTIR absorbance data [38]. This coefficient was scaled to the average dry-weight aggrecan concentration obtained from biochemical analysis for each group (21 – 23%) (see Supplementary Figure 1). Degradation with collagenase or trypsin led to significant decreases (up to 40%) in aggrecan content, within the first 210 and 420 μm, respectively ($p < 0.05$). Aggrecan content was statistically similar past 420 μm.

SHG Analysis (Local Collagen Composition)

Since FTIR could not identify the effects of collagenase on collagen organization, SHG imaging was used to assess local composition of *organized* collagen, scaled to biochemistry data [46]. Overall, organized collagen concentration for the healthy group mirrored compositional trends in collagen reported elsewhere [38,48]. As anticipated, organized collagen concentrations in trypsin-treated samples did not differ significantly from healthy controls, but collagenase-treated samples exhibited significantly lower

organized collagen concentrations within the first 50 μm from the articular surface ($p < 0.05$) (Figure 21).

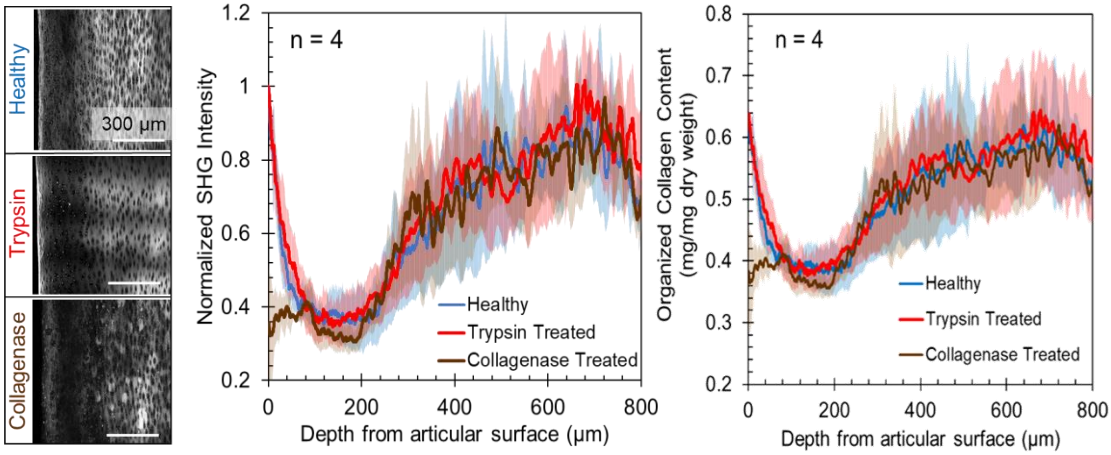

Figure 21: SHG images demonstrate how these enzymes affect the distribution of organized collagen in the tissue (left) and normalized SHG intensity profiles (middle). As anticipated, organized collagen concentrations in trypsin-treated samples did not differ significantly from healthy controls (right), but collagenase-treated samples exhibited significantly lower organized collagen concentrations within the first 50 μm from the articular surface ($p < 0.05$).

Correlation Analysis

Local diffusivities were compared to local collagen content obtained from SHG and local aggrecan content obtained from FTIR analyses. Overall, concentrations of collagen and aggrecan were negatively correlated with local diffusivity in all groups (Figure 22). Aggrecan and collagen correlations for collagenase-treated samples differed from correlations from the healthy group ($p < 0.05$, ANCOVA). Additionally, aggrecan and collagen content were more strongly correlated with diffusivity in the degraded groups (trypsin: $R^2 = 0.45, 0.74$; collagenase: $R^2 = 0.86, 0.75$), compared to the healthy group ($R^2 = 0.31, 0.46$). The relationship between local diffusivity and matrix density (addition of aggrecan and organized collagen content for each depth) was

different between all groups ($p < 0.05$, ANCOVA), with the collagenase-treated group exhibiting the steepest slope and strongest correlation ($R^2 = 0.84$).

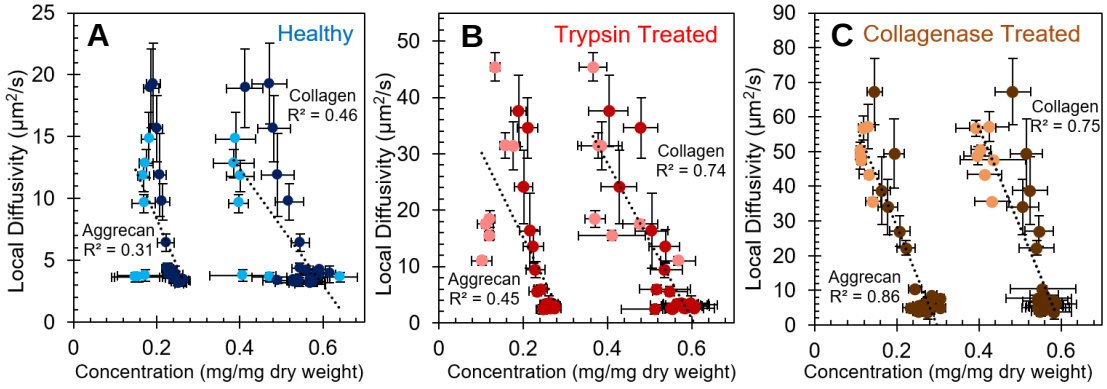

Figure 22: Correlations comparing local diffusivities from the transport analysis to the local composition obtained from FTIR and SHG for healthy (A), trypsin-treated (B), and collagenase-treated (C) groups. Lighter shaded data designate points near the articular surface of samples (within 0 – 200 μm). Overall, concentrations of collagen and aggrecan were negatively correlated with local diffusivity in all groups. The slopes of the diffusivity/composition correlations for local aggrecan and collagen content are -78 and -47 for healthy samples, -153 and -138 for trypsin-treated samples, and -293 and -285 for collagenase-treated samples, respectively. Aggrecan and collagen content were more strongly correlated with diffusivity in the degraded groups (trypsin: $R^2 = 0.45$, 0.74; collagenase: $R^2 = 0.86$, 0.75), compared to the healthy group ($R^2 = 0.31$, 0.46). Additionally, aggrecan and collagen correlations for collagenase-treated samples exhibited steeper diffusivity/concentration relationships compared to correlations from the healthy group ($p < 0.05$, ANCOVA). In contrast to both healthy and trypsin-treated samples, points near the articular surface of collagenase-treated samples fell closely to the overall regression lines, highlighting the prohibitive nature that collagen alignment has on macromolecular transport.

Discussion

The goal of this study was to investigate how the spatial diffusion mechanics of an antibody relate to local cartilage structure and composition in healthy and degraded samples. Consistent with previous research [17], diffusion kinetics of this antibody are highly heterogeneous. These spatially-dependent diffusivities were found to be related

to local structure and composition ($0.3 < R^2 < 0.9$). When the collagen structure near the articular surface of samples was disrupted with collagenase, correlations increased in strength ($R^2 > 0.75$) and these samples exhibited much higher (up to an order of magnitude) local diffusivities at the surface. Ultimately, this study reveals that the aligned surface collagen of healthy cartilage dominates diffusive hindrance of large therapeutics.

This study used two enzymes to target the two main constituents of articular cartilage: trypsin and collagenase. In cartilage, trypsin cleaves sulfated GAG chains from aggrecan (and other smaller proteoglycans) [24,49], thus allowing them to diffuse out of the tissue. In addition to removing proteoglycans [39,50], collagenase denatures the triple helix of collagen II, cleaving the collagen molecule into smaller fragments and degrading intermolecular crosslinks that enable formation of organized fibrils [39]. Use of FTIR showed that collagenase and trypsin both decrease local concentrations of aggrecan (a proteoglycan). Unexpectedly, FTIR did not demonstrate differences for absolute collagen concentrations between healthy and collagenase-treated groups (Supplementary Figure 2). However, use of SHG images revealed lower amounts of organized collagen at the surface of collagenase-treated samples within the first 50 μm. Thus, collagenase did not have enough time to remove significant amounts of collagen protein from the matrix, but was able to disrupt collagen organization by fragmenting collagen fibrils [39]. This study therefore elucidates the relationship the role of the collagen structure and aggrecan depletion on macromolecular transport.

Making local measurements revealed that enzymatic treatment had the most profound effect on the diffusivity of the surface region. Application of trypsin or collagenase resulted in higher local diffusivities (up to 10-fold compared to healthy) at depths up to 400 μm from the tissue surface. Although both trypsin and collagenase treatments increased sample diffusivities, collagenase-treated samples exhibited significantly higher diffusivities than trypsin treated within 0 – 100 μm (Figure 2). Because both enzymes degraded aggrecan similarly in this region, the higher local diffusivities in collagenase-treated samples are likely due to disruption of the highly aligned collagen at the surface.

Correlations between local composition and diffusivity also point to the importance of the surface layer on macromolecular transport. Across all depths, healthy samples had the weakest correlations between aggrecan content and local diffusivity ($R^2 < 0.46$), whereas these correlations for collagenase-treated samples were stronger ($R^2 > 0.75$). In general, correlations were weakened in healthy samples by regions in the top 200 μm (light points in Figure 5), which had much lower diffusivity than would be predicted by relationships formed from the middle and deep regions of samples (dark points in Figure 5). Importantly, the surface and deeper zone points within collagenase-treated samples formed strong, uniform relationships between local diffusivity and composition (Figure 5c). Furthermore, if the surface points (within 0 – 200 um) were removed from the aggrecan correlation for the trypsin-treated group, the resulting abbreviated regression exhibits similar slope (m = -356) to that of the collagenase-degraded group (m = -293). Because the only major change between these two groups are differences in collagen

structure within this region (see Figure 3 and Figure 4), this further supports the conclusions that an intact collagenous surface zone acts as a selective barrier to large solutes and that aggrecan content is a strong predictor of diffusivity in degraded cartilage and in the deeper zones of healthy cartilage.

Although the highly aligned collagen layer at the surface has major implications for macromolecular transport, there is strong evidence that aggrecan concentration is more important for transport deeper in the tissue, where collagen content was similar for all groups. Compared to healthy samples at 150 μm, aggrecan content was ~ 43% lower for collagenase-treated samples and 25% lower for trypsin-treated samples, whereas diffusivities were ~ 4 and 3 times higher in this region, respectively. Thus, even a small decrease in aggrecan content can lead to a significant increase in local diffusivity for large solutes. These data are consistent with data from smaller molecules (inulin and 70 kDa dextran) [24]. Ultimately, both the surface layer and aggrecan content are critical factors in determining macromolecular transport throughout the depth of cartilage.

While this study uses a well-established and validated experimental procedure for antibody diffusion [17,40], using these degradative enzymes raise some unanswered questions. Although desired, it is currently unknown how to degrade only the collagen matrix without affecting aggrecan in cartilage [?]. As such, the correlations obtained for collagenase-treated samples intrinsically include effects from degrading both constituents of cartilage. However, we argue that this type of degradation is more clinically relevant, since natural degradation *in vivo* would be similar to collagenase

degradation [39]. There is also reason to believe that the local partition coefficient is being significantly affected by degradation of the aggrecan in the tissue. Fluorescence images show large bands of increased fluorescence that match up well with areas of lower aggrecan content from histology (Figure 2). Thus, it is likely that these areas are experiencing higher local partition coefficients, but these were not calculated in this study. These experiments were not conducted on mature cartilage tissue. However, because the structure and heterogeneities of articular cartilage are similar across species and age [11,51] [?], the composition and diffusivity relationships are likely transferrable to other types of cartilage, including adult human tissue.

With the application of FTIR and SHG techniques on well-established diffusion protocols [17,40], this is the first study to directly examine the relationship between local structure/composition and local diffusion mechanics of a large therapeutic antibody (150 kDa) in cartilage. Overall, both local concentrations of aggrecan and collagen were highly correlated to local diffusivities and the highly aligned collagen at the articular surface was found to hinder transport of antibodies into the tissue. These relationships are relevant to both healthy and diseased human cartilage. With the application of *in vivo* techniques to determine local cartilage composition, such as magnetic resonance imaging (MRI), these data can be used to help inform and develop targeted therapies that are based on patient-specific cartilage composition.

Supplementary Material:

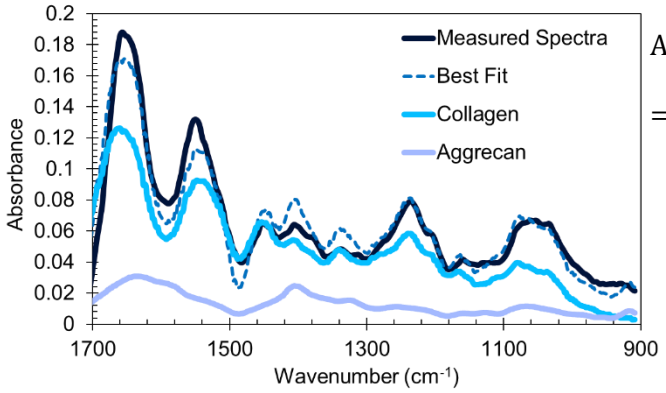

$$\text{AC spectra} = c_1 \times (\text{Pure collagen II spectra}) + \boldsymbol{c_2} \times (\text{Pure aggrecan spectra}) + [c_3 \times (\text{wavenumber}) + c_4]$$

Figure S12: Graphical depiction of the linear decomposition method to obtain local cartilage composition for a healthy sample at 100 μm from the articular surface. Measured articular cartilage spectra from FTIR were best fit to the addition of a collagen spectra, an aggrecan spectra, and a baseline that accounts for instrument-specific deviations and drift that can occur with different environmental conditions [52]. This linear decomposition method was used to determine local aggrecan content of all samples by scaling the coefficient, c_2, to the average dry weight aggrecan content obtained from biochemical analysis for each group (~ 21 – 23%). Error between measured spectra and best fit spectra were consistently less than 15%, for all samples and depths.

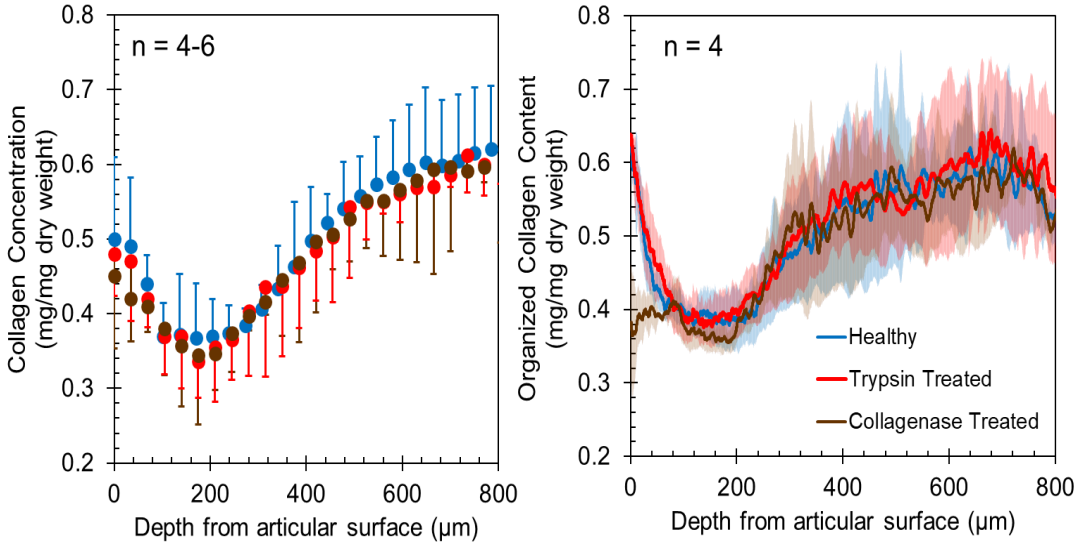

Figure S13: Comparison of local collagen content calculated from FTIR (left) and SHG (right). Both methods give similar trends in collagen content as a function of depth. However, data calculated from FTIR decomposition did not exhibit significant differences between groups at any depth. Meanwhile, collagenase-treated data from SHG exhibited significantly lower organized collagen concentrations within the first 50 μm from the articular surface ($p < 0.05$). Thus, SHG is more sensitive to the changes that collagenase imposes on the matrix for this degradation protocol. Likely, longer exposure times to collagenase would have resulted in differences between groups for the FTIR analysis as well.

REFERENCES

1. Moos, V., Fickert, S., Müller, B., Weber, U. & Sieper, J. Immunohistological analysis of cytokine expression in human osteoarthritic and healthy cartilage. *J. Rheumatol.* **26,** 870–879 (1999).
2. Evans, C. H., Kraus, V. B. & Setton, L. A. Progress in intra-articular therapy. *Nat. Rev. Rheumatol.* **10,** 11–22 (2013).
3. Gerwin, N., Hops, C. & Lucke, A. Intraarticular drug delivery in osteoarthritis. *Adv. Drug Deliv. Rev.* **58,** 226–242 (2006).
4. Shimizu, Y. & Ohta, M. Influence of plaque stiffness on deformation and blood flow patterns in models of stenosis. *Biorheology* **52,** 171–182 (2015).
5. Martel-Pelletier, J. Pathophysiology of osteoarthritis. *Osteoarthritis Cartilage* **12 Suppl A,** S31–S33 (2004).
6. Feldmann, M. & Maini, R. N. Anti -TNFα Therapy of Rheumatoid Arthritis: What Have We Learned? *Annu Rev Immunol* **19,** 163–96 (2001).
7. Chan, C. E. Z., Chan, a H. Y., Hanson, B. J. & Ooi, E. E. The use of antibodies in the treatment of infectious diseases. *Singapore Med. J.* **50,** 663–72; quiz 673 (2009).
8. Goldring, M. B. Anticytokine therapy for osteoarthritis. *Expert Opin. Biol. Ther.* **1,** 817–829 (2001).
9. Allen, K. D., Adams, S. B. & Setton, L. A. Evaluating intra-articular drug delivery for the treatment of osteoarthritis in a rat model. *Tissue Eng. Part B. Rev.* **16,** 81–92 (2010).
10. Mow, V. C., Holmes, M. H. & Michael Lai, W. Fluid transport and mechanical

properties of articular cartilage: A review. *J. Biomech.* **17,** 377–394 (1984).

11. Poole, A. R. *et al.* Composition and structure of articular cartilage: a template for tissue repair. *Clin. Orthop. Relat. Res.* **1,** S26–S33 (2001).
12. Maroudas, A. Biophysical chemistry of cartilaginous tissues with special reference to solute and fluid transport. *Biorheology`* **12,** 233–248 (1975).
13. Maroudas, A. & Bullough, P. Permeability of articular cartilage. *Nature* **219,** 1260–1261 (1968).
14. Hwang, W. S. *et al.* Collagen fibril structure of normal, aging, and osteoarthritic cartilage. *J. Pathol.* **167,** 425–433 (1992).
15. Leddy, H. A., Haider, M. A. & Guilak, F. Diffusional anisotropy in collagenous tissues: fluorescence imaging of continuous point photobleaching. *Biophys. J.* **91,** 311–316 (2006).
16. Leddy, H. A. & Guilak, F. Site-specific molecular diffusion in articular cartilage measured using fluorescence recovery after photobleaching. *Ann. Biomed. Eng.* **31,** 753–760 (2003).
17. DiDomenico, C. D. *et al.* The Effect of Antibody Size and Mechanical Loading on Solute Diffusion Through the Articular Surface of Cartilage. *J. Biomech. Eng.* **139,** 091005 (2017).
18. Treppo, S. *et al.* Comparison of biomechanical and biochemical properties of cartilage from human knee and ankle pairs. *J Orthop Res* **18,** 739–748 (2000).
19. Bank, R. A. *et al.* A simplified measurement of degraded collagen in tissues: Application in healthy, fibrillated and osteoarthritic cartilage. *Matrix Biol.* **16,** 233–243 (1997).

20. Bank, R. A., Soudry, M., Maroudas, A., Mizrahi, J. & Tekoppele, J. M. The increased swelling and instantaneous deformation of osteoarthritic cartilage is highly correlated with collagen degradation. *Arthritis Rheum.* **43,** 2202–2210 (2000).

21. Venn, M. & Maroudas, A. Chemical composition and swelling of normal and osteoarthrotic femoral head cartilage. I. Chemical composition. *Ann. Rheum. Dis.* **36,** 121–9 (1977).

22. Sun, H. B. Mechanical loading, cartilage degradation, and arthritis. *Ann. N. Y. Acad. Sci.* **1211,** 37–50 (2010).

23. Martel-Pelletier, J. *et al.* Excess of metalloproteases over tissue inhibitor of metalloprotease may contribute to cartilage degradation in osteoarthritis and rheumatoid arthritis. *Lab Invest* **70,** 807–815 (1994).

24. Torzilli, P. A., Arduino, J. M., Gregory, J. D. & Bansal, M. Effect of proteoglycan removal on solute mobility in articular cartilage. *J. Biomech.* **30,** 895–902 (1997).

25. Lotke, P. A. & Granda, J. L. Alterations in the permeability of articular cartilage by proteolytic enzymes. *Arthritis Rheum.* **15,** 302–308 (1972).

26. Clark, R. A. A Critical Comparison of Two Long-term Zooplankton Time Series from the Central-west North Sea. *J. Plankton Res.* **23,** 27–39 (2001).

27. Case, J. P. *et al.* Transin/stromelysin expression in the synovium of rats with experimental erosive arthritis. In situ localization and kinetics of expression of the transformation-associated metalloproteinase in euthymic and athymic Lewis rats. *J. Clin. Invest.* **84,** 1731–1740 (1989).

28. Nguyen, Q., Murphy, G., Roughley, P. J. & Mort, J. S. Degradation of

proteoglycan aggregate by a cartilage metalloproteinase. Evidence for the involvement of stromelysin in the generation of link protein heterogeneity in situ. *Biochem. J.* **259,** 61–7 (1989).

29. Pelletier, J. P., Martel???Pelletier, J. & Malemud, C. J. Canine osteoarthritis: Effects of endogenous neutral metalloproteoglycanases on articular cartilage proteoglycans. *J. Orthop. Res.* **6,** 379–388 (1988).

30. Chin, J. R., Murphy, G. & Werb, Z. Stromelysin, a connective tissue-degrading metalloendopeptidase secreted by stimulated rabbit synovial fibroblasts in parallel with collagenase: Biosynthesis, isolation, characterization, and substrates. *J. Biol. Chem.* **260,** 12367–12376 (1985).

31. MacNaul, K. L., Chartrain, N., Lark, M., Tocci, M. J. & Hutchinson, N. I. Discoordinate expression of stromelysin, collagenase, and tissue inhibitor of metalloproteinases-1 in rheumatoid human synovial fibroblasts: Synergistic effects of interleukin-1 and tumor necrosis factor-?? on stromelysin expression. *J. Biol. Chem.* **265,** 17238–17245 (1990).

32. Williamson, A. K., Chen, A. C., Masuda, K., Thonar, E. J. M. A. & Sah, R. L. Tensile mechanical properties of bovine articular cartilage: Variations with growth and relationships to collagen network components. *J. Orthop. Res.* **21,** 872–880 (2003).

33. Elliott, D. M., Narmoneva, D. A. & Setton, L. A. Direct Measurement of the Poisson's Ratio of Human Patella Cartilage in Tension. *J. Biomech. Eng.* **124,** 223–228 (2002).

34. Wilson, W., Van Donkelaar, C. C., Van Rietbergen, B., Ito, K. & Huiskes, R.

Stresses in the local collagen network of articular cartilage: A poroviscoelastic fibril-reinforced finite element study. *J. Biomech.* **37,** 357–366 (2004).

35. Hayes, W. C. & Bodine, A. J. Flow-independent viscoelastic properties of articular cartilage matrix. *J. Biomech.* **11,** 407–419 (1978).

36. Zhu, W., Mow, V. C., Koob, T. J. & Eyre, D. R. Viscoelastic shear properties of articular cartilage and the effects of glycosidase treatments. *J. Orthop. Res.* **11,** 771–781 (1993).

37. Griffin, D. J. *et al.* Effects of enzymatic treatments on the depth-dependent viscoelastic shear properties of articular cartilage. *J. Orthop. Res.* **32,** 1652–1657 (2014).

38. Silverberg, J. L. *et al.* Structure-function relations and rigidity percolation in the shear properties of articular cartilage. *Biophys. J.* **107,** 1721–1730 (2014).

39. Billinghurst, R. C. Enhanced cleavage of type II collagen by collagenase in osteoarthritic articular cartilage. *J Clin Invest* **99,** 1534–1545 (1997).

40. DiDomenico, C. D., Xiang Wang, Z. & Bonassar, L. J. Cyclic Mechanical Loading Enhances Transport of Antibodies Into Articular Cartilage. *J. Biomech. Eng.* **139,** 011012 (2016).

41. Carr, E. J. & Turner, I. W. A semi-analytical solution for multilayer diffusion in a composite medium consisting of a large number of layers. *Appl. Math. Model.* **40,** 7034–7050 (2015).

42. Ballyns, J. J. *et al.* Image-guided tissue engineering of anatomically shaped implants via MRI and micro-CT using injection molding. *Tissue Eng. Part A* **14,** 1195–1202 (2008).

43. Enobakhare, B. O., Bader, D. L. & Lee, D. a. Quantification of sulfated glycosaminoglycans in chondrocyte/alginate cultures, by use of 1,9-dimethylmethylene blue. *Anal. Biochem.* **243,** 189–191 (1996).

44. Neuman, R. E. & Logan, M. A. The determination of hydroxyproline. *J. Biol. Chem.* **184,** 299–306 (1950).

45. Camacho, N. P., West, P., Torzilli, P. A. & Mendelsohn, R. FTIR microscopic imaging of collagen and proteoglycan in bovine cartilage. *Biopolym. - Biospectroscopy Sect.* **62,** 1–8 (2001).

46. Chen, X., Nadiarynkh, O., Plotnikov, S. & Campagnola, P. J. Second harmonic generation microscopy for quantitative analysis of collagen fibrillar structure. *Nat. Protoc.* **7,** 654–669 (2012).

47. Saarakkala, S. & Julkunen, P. Specificity of Fourier Transform Infrared (FTIR) Microspectroscopy to Estimate Depth-Wise Proteoglycan Content in Normal and Osteoarthritic Human Articular Cartilage. *Cartilage* **1,** 262–269 (2010).

48. Khanarian, N. T. *et al.* FTIR-I compositional mapping of the cartilage-to-bone interface as a function of tissue region and age. *J. Bone Miner. Res.* **29,** 2643–2652 (2014).

49. Xia, Y. *et al.* Self-Diffusion Monitors Degraded Cartilage. *Arch. Biochem. Biophys.* **323,** 323–328 (1995).

50. Fosang, A. J., Last, K., Knäuper, V., Murphy, G. & Neame, P. J. Degradation of cartilage aggrecan by collagenase-3 (MMP-13). *FEBS Lett.* **380,** 17–20 (1996).

51. Klein, T. J., Chaudhry, M., Bae, W. C. & Sah, R. L. Depth-dependent biomechanical and biochemical properties of fetal, newborn, and tissue-

engineered articular cartilage. *J. Biomech.* **40,** 182–190 (2007).

52. Smith, B. *Fundamentals of Fourier transform infrared spectroscopy*. (CRC Press, 2011).

CHAPTER 6

Assessing Transport of Therapeutics in Articular Cartilage: A Review of Experimental Data from the Last Half Century[6]

Abstract

Objective: For the last half century, transport of nutrients and therapeutics in articular cartilage has been studied with various *in vitro* systems that attempt to model *in vivo* conditions. However, experimental technique, tissue species, and tissue storage condition (fresh/frozen) vary widely and there is debate on the most appropriate model system. Additionally, there is still no clear overarching framework with which to predict solute transport properties based on molecular characteristics. This review aims to develop such a framework, and to assess whether experimental procedure affects trends in transport data.

Methods: Solute data from 31 published papers that investigated transport in healthy articular cartilage were obtained and analyzed for trends.

Results: Here, we show that diffusivity of spherical and globular solutes in cartilage can be predicted by molecular weight and hydrodynamic radius via a power-law relationship. This relationship is robust for many solutes, spanning 5 orders of magnitude in molecular weight and was not affected by variations in cartilage species, age, condition (fresh/frozen), and experimental technique. Traditional models of transport in porous media exhibited mixed effectiveness at predicting diffusivity in cartilage, but were good in predicting solute partition coefficient.

Conclusion: Ultimately, these robust relationships can be used to accurately predict and improve transport of solutes in adult human cartilage and enable the development of better optimized arthritis therapeutics.

[6]This work has been submitted for publication: C. DiDomenico and L. J. Bonassar, "Assessing Transport of Therapeutics in Articular Cartilage: A Review of Experimental Data from the Last Half Century."
Submitted to the *Osteoarthritis and Cartilage*.

Introduction

During arthritis, cartilage homeostasis is disrupted from various inflammatory factors that are produced from joint tissues[1–5]. For instance, there is evidence that diseased chondrocytes within cartilage produce inflammatory cytokines and play a significant role in osteoarthritis (OA) progression[1,6–8]. Thus, effective treatment of OA necessitates penetration of therapeutic molecules into cartilage to reach target chondrocytes[9–11]. Small non-steroidal anti-inflammatory drugs (NSAIDs) and steroids (~ 0.5 nm in size) are currently used to treat OA[9,12–14], but there is interest in developing larger therapeutics (up to 6 nm in size)[15]. Use of large therapeutic antibodies have been effective in other arthritic diseases, including rheumatoid arthritis (RA)[4], but remains understudied for treatment of OA. Because of the wide variation in size of potential therapeutics (0.5 – 6 nm in hydrodynamic radii), understanding how molecular transport occurs within highly heterogeneous cartilage is important to the design of future therapies.

Articular cartilage is a highly dense, avascular tissue that relies on diffusion of nutrients and growth factors to maintain equilibrium with the surrounding synovial fluid in the joint space. It is comprised of two main solid components, type-II collagen (18%) and aggrecan (8%)[16,17]. In this tissue, large collagen fibrils (~ 50 nm in diameter)[18] are highly aligned along the surface and transition to a more perpendicular alignment to the subchondral bone in the deep region[19]. Because of the negatively-charged glycosaminoglycans (GAGs) attached to aggrecan, articular cartilage is highly charged and has a very small effective pore size[16–18,20]. Additionally, the concentrations of these

components vary spatially within the tissue and lead to many different heterogeneities that affect solute transport.

The first body of work that investigated molecular transport in cartilage dates to over 50 years ago [20,21]. Studies conducted by Maroudas et al[20–23] primarily investigated diffusion kinetics of smaller ions and sugars, which are important to the homeostasis of cartilage *in vivo*[16]. As our understanding of smaller solutes grew, others investigated kinetics of small proteins and growth factors[24–26], which are also found naturally in the joint space. Near the turn of the 21st century, the focus of the field turned to dextrans, linear polysaccharides that have been used as surrogates for larger molecules because of their customizability[27]. Consequently, dextrans were used to investigate how transport was affected by large changes in hydrodynamic size or molecular weight (3 kDa – 500 kDa)[28–30]. Despite their therapeutic potential, transport of large antibodies (25 – 200 kDa) has only recently been comprehensively examined[15,31,32]. Ultimately, the diversity of molecules studied for transport in cartilage is remarkable, and there are dozens of studies that have contributed to the knowledge in this field. However, despite this work, there is no clear framework from which to predict transport of these molecules, which range widely in size and shape. Developing such a framework can be very useful in deciding which molecules are most appropriate for use as arthritis therapies.

In this review, we first describe techniques used to measure transport in porous media such as cartilage. We then consolidate transport data from 31 individual studies on 47

unique solutes spanning 7 Da – 500 kDa and 0.1 – 16 nm (summarized in Supplementary Table S1). Analysis of such data demonstrate that diffusivity of spherical solutes is strongly predicted (R^2 = 0.81) by molecular weight and hydrodynamic radius with a power-law relationship. This relationship is insensitive to the specific experimental procedure used and tissue age or species. Further, we review the extent to which such trends in data can be explained by steric hindrance or frictional drag of molecules moving through the cartilage matrix. We end on a discussion of future work that should be done to further strengthen the findings from this review and how such findings can inform design of therapeutics.

Experimental techniques used to measure transport

For the last half-century, transport fundamentals have been studied with *in vitro* systems that attempt to maintain a high degree of physiologic relevance to *in vivo* conditions. Even though these systems measure transport in different ways, all result in quantification of diffusivities and/or partition coefficients (Table 2). All such methods require measuring solute concentration in cartilage, either in bulk tissue or locally. For example, computed tomography (CT)[33–37] uses radio-opaque tracers to measure and spatially map solutes. Nuclear magnetic resonance (NMR) spectroscopy[26,38,39] relies on molecular vibrations and relaxations to measure and track local solutes. Other methods, such as solute desorption techniques[18,21,23,24,30,40–43] or diffusion cells[20,22,23,25,43–46], rely on quantifying a volume of solute that diffuses through a sample over a given time, often using fluorescent or radioactive labels. Additionally, there are methods that track local fluorescence of a labeled solute within cartilage, such as fluorescence recovery after photobleaching (FRAP)[32,47], and fluorescence gradient techniques[28,29,32,46–48].

Table 2: Summary of how experimental techniques have been used to quantify transport. All of these methods rely on visualizing a solute in cartilage, either by using contrast agents, NMR-active solutes, or attaching fluorophores or radiolabels to the solute of interest. In general, most of these techniques have been used to measure average, bulk transport properties, except for FRAP. To date, local transport properties have not been extensively studied, but can be measured using most techniques (denoted with at *).

Experimental Technique	Method of Visualizing Solute	Have been used to measure bulk transport?		Have been used to measure local transport?	
		Diffusivity	Partition Coefficient	Diffusivity	Partition Coefficient
Computed Tomography	Radioactive contrast agent	Yes	Yes	Yes	Yes
Nuclear Magnetic Resonance	NMR-active solute	Yes	–	*	–
Diffusion Cell	Radiolabel or fluorophore	Yes	–	*	–
Solute Absorption and Desorption	Radiolabel or fluorophore	Yes	Yes	*	*
Fluorescence Recovery after Photobleaching	Fluorophore	–	–	Yes	–
Fluorescence Gradient	Fluorophore	Yes	Yes	Yes	*

Before the turn of the 21st century, widespread use of diffusion cells and solute absorption/desorption protocols have enabled a much better understanding of transport on a large (bulk) scale. Even today, they remain popular and are very robust in their ability to study transport. Recently, other techniques, such as FRAP and fluorescence gradient protocols, were developed that enabled the study of transport on a more local scale (< 100 μm) (Table 2). These techniques rely on high-resolution microscopic

techniques to visualize fluorescently-tagged molecules in cartilage. Other more clinically-motivated techniques, such as CT, have also been used to study local transport. Because of its very high resolution, the continued use of CT for solute transport is very promising.

Characterizing transport mechanics

Extracting trends from 50 years of work in this field requires an understanding of how molecular transport is analyzed in porous tissues, such as cartilage. Molecular transport is a complex phenomenon that is governed by three main contributions: stagnant liquid film generation at the cartilage-fluid interface; the solute partition coefficient; and the mobility of the solute inside cartilage[23]. For the techniques described above, contributions of transport due to stagnant film generation can be neglected due to stirring of the solute bath or by using thick tissue samples[23]. Additionally, because of joint movement and tissue thickness (~ 1 mm), stagnant film generation is likely negligible *in vivo*. As such, this review will only focus on analysis of solute mobility and partition coefficient.

Solute mobility

Three main phenomena dominate solute mobility: diffusion, how fast a molecule will move along a concentration gradient; convection, the movement of solutes induced by interstitial fluid flow; and electrochemical migration[49–53], movement induced by charge-based interactions between the solute and matrix. Mobility (i.e. transport) of solutes can therefore be accurately described by the addition of diffusive, convective, and

electrochemical flux[49,54,55]. Assuming Fickian diffusion and incompressible fluid flow, the total solute flux into cartilage can be defined as[54,55]:

$$\vec{J} = j_{diffusion} + j_{convection} + j_{electrochemical} = -D\nabla C + \omega\vec{v}C - \frac{DCzF}{RT}\nabla\psi \quad (Eq.\,1)$$

where J is the solute flux, D is the solute diffusivity, C is the concentration of the solute, ω is the solute convection coefficient (also known as the retardation coefficient), v is the interstitial fluid velocity relative to the solid matrix, z is the net charge of the molecule, F is Faraday's constant, R is the universal gas constant, T is the absolute temperature of the solution, and ψ is the electrical potential. The diffusivity and convection coefficient quantify the diffusive speed of the molecule and the ratio of solute convective velocity to interstitial fluid velocity, respectively. These metrics can be measured as an average for the entire tissue, or measured locally[32]. If electrochemical gradients are not considered, both the convection and diffusion coefficient can intrinsically include steric, hydrodynamic, and physiochemical effects of the solute in cartilage[49]. Overall, there are many potential solutions to Eq. 1, with and without convection and electrochemical gradients considered[56,57]. Because the vast majority of research has focused on quantifying solute diffusion, this review will focus on synthesizing diffusion data in the absence of significant contributions from convection or electrochemical gradients.

Partition coefficient

Partition coefficient, which is the equilibrium concentration of the solute in the cartilage compared to the concentration of the solute in the surrounding bath, usually varies

between 0 and 1, but it can be higher than unity in some cases[22,45,46]. The partition coefficient of a solute depends on the volume accessible to the solute in the tissue matrix, and the affinity of the matrix for the solute[22]. Because of the small pore network of cartilage, some solutes are can only occupy a portion of the total available pores, which causes the partition coefficient to be less than unity. Electrostatic forces between charged solutes and the negatively charged matrix also can drastically affect partitioning. The partition coefficient can be measured for the whole tissue or it can be measured locally within the cartilage[22,43,58].

Assessing frameworks for solute transport in cartilage

Even though there has been no explicit framework developed for cartilage, several empirical relations have been proposed to describe how diffusivity changes with molecular weight or solute size in other porous media. Diffusivity has been described with the relation[55,59,60]:

$$\boldsymbol{D = A_1 (MW)^{-a_2}} \qquad (\boldsymbol{Eq.\,2})$$

where A_1 is an empirical constant, MW is the molecular weight of the solute, and a_2 is an empirical constant. These constants depend on many tissue and solute factors[55]. Additionally, diffusivities have been shown to follow a similar relationship with hydrodynamic radius[61]. To date, these relationships were developed from observing solutes of varying size/MW diffuse through membrane filters[60,61] and various tissues[59,62], but these relations have not been extensively tested for solutes in cartilage. Thus, we will examine solute diffusivity and partition coefficient with respect to the relationship in Eq. 2.

Solute diffusivity depends on molecular weight and hydrodynamic radius

The combined effort of this field over 50 years has generated a significant cohort of data that can be used to assess the relationship between molecular size and solute transport in cartilage. Diffusivity data collected from the literature (from 31 studies and 47 unique solutes) were examined across a range of molecular weights and hydrodynamic radii (Figure 23). Data was also divided up into two solute groups: "linear" and "spherical." Dextran and chondroitin sulfate have demonstrated the ability to change from a random coil conformation to a more chain-like (linear) conformation in solution[63], and were classified as linear. All other solutes were classified as spherical, with chemical compositions that dictate a more rigid structure in solution. Ultimately, across spherical solute data, the relationship between solute diffusivity and molecular weight (7 Da – 200 kDa) or hydrodynamic radius (0.1 to 7 nm) was well described ($R^2 = 0.81$) by a power-law relationship stated in Eq. 2. Diffusivities of linear solutes, such as dextran, were not well described ($R^2 = 0.07 – 0.25$) by a power-law and deviated significantly from spherical solutes (ANCOVA, $p < 0.05$). The disparity between spherical and linear solute data suggests that linear solutes exhibit fundamentally different transport mechanics in cartilage[64]. As such, all future data analyses will investigate linear and spherical solutes separately.

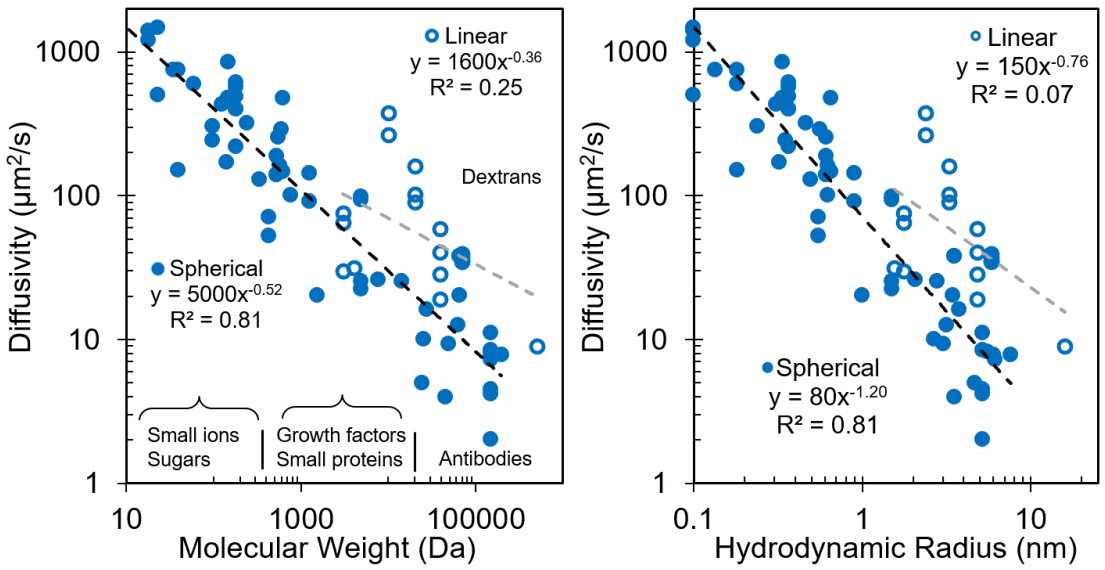

Figure 23: Variability in diffusivity is largely predicted by solute molecular weight or hydrodynamic radius. Pooled solute diffusivity data from 31 individual papers, plotted as a function of solute molecular weight (MW) (left) and hydrodynamic radius (right). Data includes spherical (filled points) and "linear" (open points) solutes. All "linear" solute data points were obtained from diffusion studies using variously sized dextran or chondroitin sulfate molecules. All other solutes were classified as spherical. Values for hydrodynamic radii were obtained directly from the cited literature; if this was not cited, an empirical relationship ($\boldsymbol{r_s = 0.0332MW^{0.463}}$)[65], was used to estimate hydrodynamic radius. Spherical solute diffusivity in cartilage was found to be very strongly correlated (black) to both molecular weight and hydrodynamic radius, obtaining an $R^2 = 0.81$ for both solute metrics. Best fits for linear solutes (gray) were weak ($R^2 < 0.3$), and deviated from spherical solutes, indicating that linear solutes diffuse differently in cartilage tissue. On average, linear solutes had higher diffusivities than spherical solutes of similar size, which may be due to the ability of linear solutes to change conformation as they move through the matrix.

There has been a wide variety of techniques and tissues sources used to study solute transport in cartilage. As such, there is considerable debate about the appropriateness of these tissue sources and techniques. To assess whether these techniques and tissue sources function similarly, we evaluated the relationship between diffusivity and

molecular weight or size with respect to experimental technique. Spherical solute data was grouped into experimental techniques: computed tomography/nuclear magnetic resonance spectroscopy (CT/NMR), diffusion cell, solute desorption, and fluorescence gradient (Figure 24A). Tissue was also separated into tissue types: adult human, mature bovine and equine, and immature bovine cartilage (Figure 24B). Finally, data was also separated based on tissue storage condition before experimentation: fresh or frozen (Figure 24C). Ultimately, there were no differences in relationship between spherical solute size and diffusivity across all data groupings (ANCOVA, using log-transformed data, $p > 0.05$). These trends strongly support that diffusivity for spherical solutes can be accurately predicted in cartilage regardless of tissue age and species or experimental technique. These data were also compared to several mechanistic transport models, presented below.

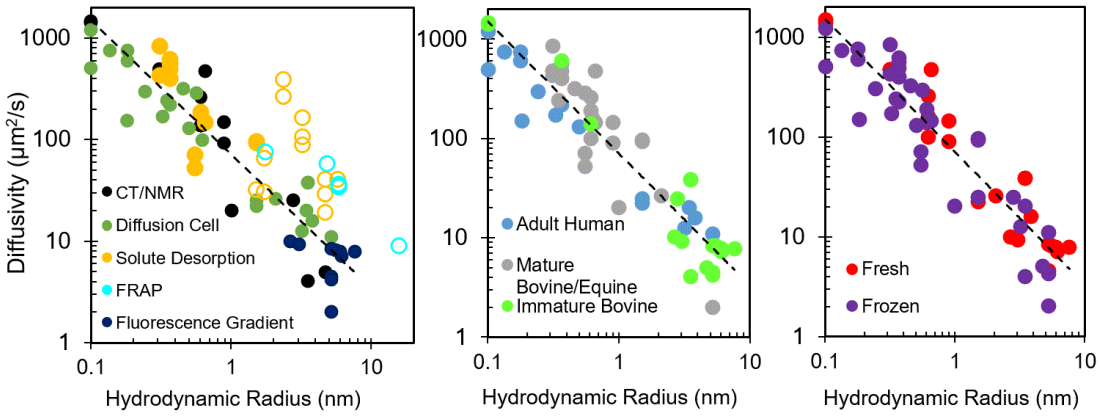

Figure 24**: The relationship between solute diffusivity and size does not depend on measurement technique, tissue species, tissue age, or tissue storage method.** Pooled solute diffusivity data compared against different experimental techniques (left), tissue species/age (middle), and tissue storage condition (right). Data was grouped into 5 different experimental techniques: computed tomography/nuclear magnetic resonance spectroscopy (CT/NMR), diffusion cell, solute desorption, fluorescence recovery after photobleaching (FRAP), and fluorescence gradient (left). Linear solutes (open points) were also included for completeness in graph A, but only spherical solutes were included in the best-fit curves (black). Tissue was also separated into tissue types: adult human, mature bovine and equine, and immature bovine cartilage (middle). Finally, data was also separated based on tissue storage condition before experimentation: either fresh or frozen (right). Across all data groupings for spherical solutes, the relationship between diffusivity and size did not differ between groups or from the relationship formed from the pooled data (ANCOVA, using log-transformed data, $p > 0.05$). This strongly supports that diffusivity can be accurately predicted in cartilage regardless of the parameters used in individual experiments.

Models exhibit mixed effectiveness in predicting solute transport

Mechanistic models have been used to predict transport of solutes in various porous media, such as soil and hydrogels. However, there is limited assessment of these models for their ability to describe transport in cartilage, and this assessment has been limited to narrow ranges of solute size[43]. Additionally, the appropriateness of such models to predict transport for larger therapeutics, such as antibodies or growth factors, is unclear. We examined three prominent transport models with varying assumptions. Due to the formulation of these models, they are only appropriate for spherical molecules, and not linear solutes. These models assume that diffusivity of spherical solutes in cartilage can be approximated by multiplying the solute diffusivity in water by frictional (hydrodynamic) or steric hindrance factors[55]. Additionally, they rely on the assumption that solute diffusivity decreases as the size of the diffusing solute approaches the size of the pores in the matrix. One prominent relation, was developed by Renkin et al[66]:

$$D = (1 - \lambda)^2 \cdot (1 - 2.1\lambda + 2.1\lambda^3 - 0.95\lambda^5) * D_0 \approx \left(1 - \frac{r_s}{r_p}\right)^4 * D_0 \qquad (Eq. 3)$$

where λ is defined as r_s/r_p, r_s is the hydrodynamic radius of the solute, r_p is the effective pore size of the matrix, D is the diffusivity of the solute in cartilage and D_0 is the solute diffusivity in free solution. Typical effective pore radii for this tissue range from 4-10 nm, with highest values near the articular surface[16,21]. The solute diffusivity in free solution of a dilute, spherical (and most linear[67,68]) solute in solution can be calculated using the Stokes-Einstein equation[69,70]:

$$D_0 = \frac{k_B T}{6\pi\eta r_s} \qquad (Eq. 4)$$

where k_B is Boltzmann's constant, T is the absolute temperature of the solution, and η is the solvent viscosity. In Eq. 3, the first term represents exclusion of solute from the membrane pores based on geometrical considerations and the second term represents hydrodynamic drag on the solute molecules due to the pores[71].

The Brinkman model, based on hydrodynamic theory[72], relates solute diffusivity to solute hydrodynamic radius and the Darcy permeability of the cartilage tissue [73]:

$$D = \frac{1}{1 + \frac{r_s}{\sqrt{\kappa}} + \frac{r_s^2}{3\kappa}} * D_0 \qquad (Eq. 5)$$

where κ is the Darcy permeability of cartilage (~ 1 nm^2 [74,75]), an intrinsic property of the tissue that quantifies how easily interstitial fluid flow can occur. The Darcy permeability can also be thought of as a surrogate for pore size in the matrix, with smaller values representing a smaller pore size.

For spherical solutes across a broad range (0.1 – 7.6 nm) of hydrodynamic sizes, both the Brinkman and Renkin models fit pooled data poorly, assuming an effective pore radius of 7 nm and a Darcy permeability of 1.0 nm^2 (Figure 25), which were chosen to represent averages reported in the literature. For the Renkin model, the root-mean-squared error (RMSE) including all data points was 328 $\mu m^2/s$, and the coefficient of variance (COV) was 116%. For the Brinkman model, RMSE was 287 $\mu m^2/s$, and the COV was 101%. If model parameters were optimized to minimize error across all collected data, values for the effective pore radius was 3.6 nm and Darcy permeability was 0.4 nm^2. Using these optimized parameters did not reduce RMSE significantly (< 20%), and so the use of average literature values was deemed appropriate. With these literature-based parameters, models generally overestimated *D* for smaller solutes (r_s < 0.5 nm) and underestimated *D* for larger (r_s > 5 nm) solutes. These two popular models are thus not ideal for predicting solute diffusivity in cartilage.

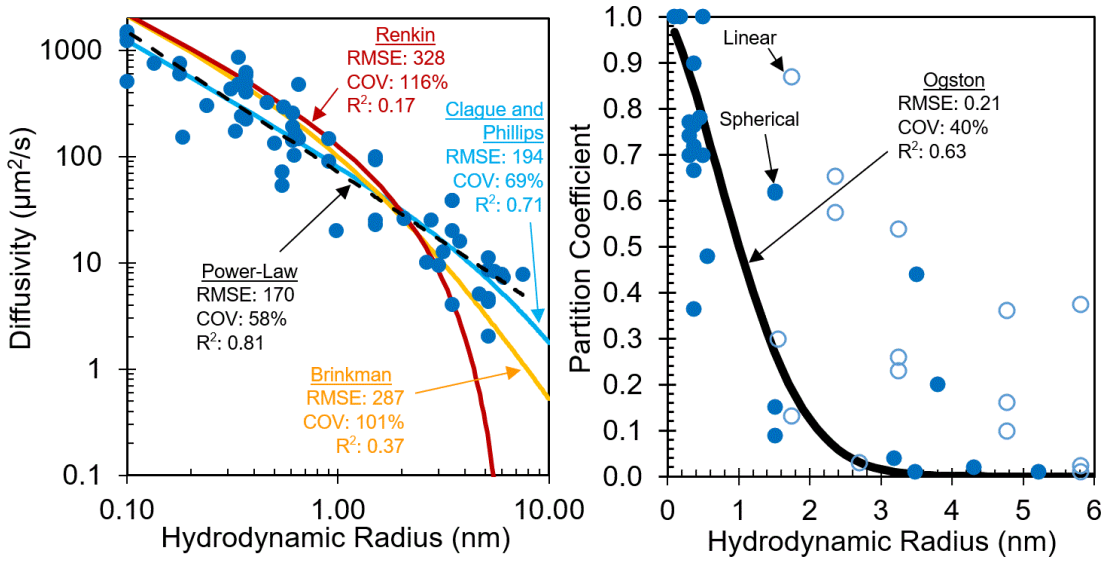

Figure 25: Mechanistic transport models are inconsistent in predicting solute diffusivity in cartilage. Transport models for solute diffusivity (left) and partition coefficient (right) were compared to aggregate literature data. Diffusivities for all spherical solutes were compared to three prominent models (left): Renkin, Brinkman, and Clague and Phillips[66,73,76]. Across this spherical solute data, root mean square (RMS) error [$\mu m^2/s$], coefficient of variance (COV), and R^2 are presented (based on untransformed data). Both the Brinkman and Renkin models did not fit pooled data adequately, assuming an effective pore radius of 7 nm and a Darcy permeability of 1.0 nm^2. The pooled data was well-fit to the Clague and Phillips relation assuming a total volume fraction of 0.25 and an effective fiber radius of 4 nm. However, a simple power-law relationship was found to best-fit the data. Right: The Ogston model was used to predict partition coefficients of spherical solutes assuming a volume fraction and effective fiber radius of aggrecan to be 0.08 and 0.475 nm, respectively. Overall, for neutrally-charged, spherical solutes, the Ogston model was predictive of solute partition coefficient. Partition coefficients for linear solutes (open points), such as dextran, deviated significantly from spherical solutes.

Ultimately, one of the only known transport relations that was accurate over the entire range of pooled spherical solute data was a model developed for stiff hydrogels by Clague and Phillips [76]. The first term of this relation accounts for the steric exclusion of

the solute from the cartilage matrix, while the second term accounts for hydrodynamic drag imparted on the solute[76]:

$$\boldsymbol{D = \left(1 + \frac{2}{3}\alpha\right)^{-1} * exp\left(-\pi\theta_t^{\,0.174\, ln\left(59.6\frac{r_{f,t}}{r_s}\right)}\right) * D_0\,;\ \alpha = \theta * \left(\frac{r_s + r_{f,t}}{r_{f,t}}\right)^2} \quad (\boldsymbol{Eq.6})$$

where θ_t is total matrix fiber fraction (typically ranging from 0.20-0.35 in healthy articular cartilage[77,78]), and $r_{f,t}$ is the effective fiber radius for all matrix constituents. The individual effective fiber radii of the GAGs, aggrecan core protein, and collagen in cartilage have been reported to be 0.55 nm, 0.4 nm, and 11-50 nm, respectively[77,79,80]. Thus, the effective fiber radius of all combined constituents in cartilage has been estimated to be between 2-6 nm[77]. The pooled data from the literature was moderately well-fit to this relation assuming a total volume fraction of 0.25 and an effective fiber radius of 4 nm (Figure 25). For this model, the RMSE was 194 $\mu m^2/s$, COV was 69%, and R^2 was 0.71. If model parameters were optimized to minimize error, values for the effective fiber radius was 3.68 nm and fiber volume fraction of cartilage was 0.20, which is consistent with assumed literature values. Due to the complexity of molecular transport, many more transport models exist[63,72], but they were not found to better predict the pooled data.

The fact that a simple, empirical power-law relationship better predicted solute diffusivity compared to mechanistic transport models is notable. Additionally, these mechanistic models were inconsistent in predicting diffusivity. The Clague and Phillips model includes both steric and hydrodynamic solute/matrix interactions, which is likely

why this model outperformed the Brinkman (hydrodynamic) and Renkin (steric) models. However, all current transport models were developed specifically for hydrogels with only one fiber species, which may not be appropriate for cartilage. These models also do not attempt to account for charge or osmotic interactions between the solute and matrix. With the exception of the Clague and Phillips model, we urge caution in using these models to estimate diffusivity of most solutes in cartilage, and argue that cartilage-specific models that include both steric and hydrodynamic solute/matrix effects be developed in the future.

Partitioning depends on solute size

As with diffusivity, molecular size would be expected to influence partitioning of solute in cartilage. To assess such effects, solute partition coefficients were collected from a host of studies across a range of solute sizes (Figure 25). Because we only wanted to analyze data as a function of solute size, data for charged ions (such as Na^+) and other significantly charged (5 > isoelectric point, pI > 8) solutes were not included in this analysis (Figure 25). Overall, partition coefficients for both spherical and linear solutes decreased exponentially with solute hydrodynamic radius (Figure 25). However, linear solutes consistently had higher partition coefficients than similarly-sized spherical solutes. With respect to partition coefficients and diffusivities, it is apparent that linear solutes and spherical solutes exhibit vastly different transport mechanics in cartilage tissue. This literature data was also compared to a mechanistic model, presented below.

Ogston partitioning model is accurate

One popular relation, based on steric exclusion theory[81], was derived by Ogston[80,82] to describe partitioning of spherical solutes in cartilage by linear rod-like macromolecules (most commonly assumed to be sulfated GAGs or the entire aggrecan molecule)[43,55]. Literature data was compared to the Ogston model[43] that considers partitioning of solutes from the entire aggrecan molecule:

$$K = \frac{\exp\left(-\theta_{agg}\left(1+\frac{r_s}{r_{f,agg}}\right)^2\right)}{1-\theta_{agg}} \qquad (Eq.\ 7)$$

where θ_{agg} is the volume fraction of aggrecan, $r_{f,agg}$ is the average effective fiber radius of aggrecan in cartilage, and K is the partition coefficient of the solute. The solid volume fraction and effective fiber radius of aggrecan in healthy articular cartilage is about 0.08, and 0.475 nm, respectively[43,77,78,80]. Based on this Ogston model, solute partition coefficients are very sensitive to the size of the solute and aggrecan density[22].

Overall, for neutrally-charged, spherical solutes, the Ogston model (Eq. 7) was predictive of solute partition coefficient values previously reported (Figure 25). Across data for spherical solutes, the Ogston model exhibited a RMSE of 0.21, COV of 40%, and a R^2 of 0.63, assuming a solid volume fraction and effective fiber radius of aggrecan to be 0.08, and 0.475 nm, respectively. These literature-based parameters were within 10% of model parameters that were optimized for error minimization. As anticipated, partition coefficients of linear solutes were not well predicted by the Ogston model (Figure 25).

Discussion

This review consolidates over 50 years of cartilage transport data that has been collected using a wide variety of solutes, experimental techniques, and tissue types. The synthesis of this very large cohort of data enables us to make several important conclusions. First, linear molecules, such as dextrans, exhibited significantly higher diffusivities and partition coefficients compared to spherical solutes. Even though the study of linear solutes in cartilage is useful, they are clearly not good predictors of transport for similarly-sized proteins. Second, a simple power-law relationship fit all spherical solute data very well ($R^2 = 0.81$), spanning several orders of magnitude in molecular weight (7 Da – 200 kDa). Additionally, the relationship between solute diffusivity and solute size did not change with different experimental techniques, tissue species used, or tissue condition prior to use (fresh/frozen). This robust relationship, valid across several orders of magnitude in solute size, allows researchers to accurately predict solute transport in cartilage and design arthritis therapies that have optimized transport kinetics. Surprisingly, this power-law relationship holds beyond the average pore size of cartilage (~ 6 nm), which suggests that the tissue consists of a wider distribution of pore sizes than previously thought. This also opens the possibility that even larger (> 7.5 nm) molecules can penetrate cartilage. As such, nanoparticles, which can be functionalized with various therapeutics[83], could be a promising avenue for future arthritis therapies.

Despite many significant findings with the analysis of this large data set, several prominent knowledge gaps remain. With the discovery of a strong, simple empirical relationship between solute diffusivity and solute size, one would expect that

mechanistic transport models would also be predictive of solute diffusivities. Unfortunately, reported transport models were not consistent in their ability to predict solute diffusivities over a broad range of solute sizes. This is likely because all such models have been designed specifically for hydrogels with one fiber type, and may be too simple to describe cartilage. Additionally, these models clearly assume a very narrow distribution of pore sizes, and cannot account for the hierarchical pore structure that is evident in articular cartilage. While the best hydrogel-based transport model (Clague and Phillips[76]) was accurate (COV: 69%, R^2: 0.71) over the entire data range, development of a new transport model designed specifically for cartilage would be useful and could help predict transport locally within the tissue. The success of the Clague and Phillips model also indicates the importance of including both steric hindrance and frictional effects in future cartilage-based models.

The relationships in this review were assessed with transport data from healthy articular cartilage. However, clinical treatment of OA is usually administered after tissue damage has occurred. This tissue damage likely increases the ability of solutes to penetrate cartilage[30,84], but few studies have investigated this phenomenon[30,85–87]. As such, developing new relationships or mechanistic models that consider the local composition of the cartilage would be very helpful to develop new strategies for arthritis treatments with patients with late-stage OA.

Ultimately, we discovered a very strong empirical relationship between bulk diffusivity and solute size across a large range of solute radii (0.1 – 7.6 nm) and molecular weights

(10 Da – 200 kDa). This empirical relationship was more predictive of solute diffusivity than any published mechanistic model and was insensitive to the experimental method and tissue species used. Additionally, partitioning of solutes over this range was well predicted by an existing mechanistic model. This predictive power of these relationships is very useful for the design and customization of arthritis therapeutics with the most desirable transport kinetics into articular cartilage.

Supplementary Material:

Solute	Shape[a]	MW (Da)	Hydrodynamic Radius (nm)[b]	Diffusivity ($\mu m^2/s$)[c]	D_0 ($\mu m^2/s$)[d]	D/D_0	Partition Coefficient (K)[e]	Tissue Used[f]	Method to Obtain Diffusivity	Tissue Condition[g]	Reference	Notes
Li^+	Spherical	7	0.08	1423	2847	0.50	-	Immature bovine	Nuclear magnetic resonance (NMR)	Fresh	[39] Burstein 1993	1
Water	Spherical	18	0.10	1200	2327	0.52	1.00	Adult human	Diffusion cell (Radiolabel)	Frozen	[21] Maroudas 1968	
Water	Spherical	18	0.10	1396	2327	0.60	-	Immature bovine	Nuclear magnetic resonance (NMR)	Fresh	[39] Burstein 1993	
Na^+	Spherical	23	0.10	500	2327	0.21	1.50	Adult human	Diffusion cell (Radiolabel)	Frozen	[21] Maroudas 1968	12
Na^+	Spherical	23	0.10	1466	2327	0.63	-	Immature bovine	Nuclear magnetic resonance (NMR)	Fresh	[39] Burstein 1993	
Cl^-	Spherical	35	0.18	750	1293	0.58	0.75	Adult human	Diffusion cell (Radiolabel)	Frozen	[21] Maroudas 1968	11
K^+	Spherical	39	0.14	740	1724	0.43	-	Adult human	Diffusion cell (Radiolabel)	Frozen	[21] Maroudas 1968	12
Ca^+	Spherical	40	0.18	150	1270	0.10	3.00	Adult human	Diffusion cell (Radiolabel)	Frozen	[21] Maroudas 1976	12
Urea	Spherical	60	0.18	600	1293	0.46	1.00	Adult human	Diffusion cell (Radiolabel)	Frozen	[23] Maroudas 1970	
Sulfate	Spherical	96	0.24	300	962	0.31	0.60	Adult human	Diffusion cell (Radiolabel)	Frozen	[22] Maroudas 1976	11
Sulfate	Spherical	96	0.35	240	665	0.36	0.68	Mature bovine	Diffusion cell (Radiolabel)	Frozen	[25] Garcia 1996	11
Leucine	Spherical	139	0.33	169 (4°C)	372 (4°C)	0.45	-	Adult human (hip)	Diffusion cell (Radiolabel)	Frozen	[43] Nimer 2003	1
Sodium Iodide	Spherical	150	0.34	475	744	0.64	-	Mature bovine	Computed tomography (CT)	Fresh	[33] Kulmala 2010	1

Solute	Shape[a]	MW (Da)	Hydrodynamic Radius (nm)[b]	Diffusivity ($\mu m^2/s$)[c]	D_0 ($\mu m^2/s$)[d]	D/D_0	Partition Coefficient (K)[e]	Tissue Used[f]	Method to Obtain Diffusivity	Tissue Condition[g]	Reference	Notes
Sodium Iodide	Spherical	150	0.34	428	744	0.58	0.90	Mature bovine	Solute desorption (Fluorophore)	Frozen	[85] Chin 2013	1
Sodium Iodide	Spherical	150	0.34	475	744	0.64	0.70	Mature bovine	Computed tomography (CT)	Fresh	[35] Silvast 2013	1, 9, 12
Sodium Iodide	Spherical	150	0.34	474.7	1052	0.45	0.77	Mature bovine	Computed tomography (CT)	Fresh	[37] Kokkonen 2017	1, 9
Sodium Iodide	Spherical	150	0.34	838	744	1.13	0.74	Mature bovine	Solute desorption (Other)	Frozen	[88] Shafieyan 2014	1
Glucose	Spherical	180	0.37	608	894	0.68	0.72	Immature bovine	Solute desorption (Radiolabel)	Frozen	[89] Torzilli 1998	
Glucose	Spherical	180	0.37	403	894	0.45	0.76	Mature bovine	Solute desorption (Radiolabel)	Frozen	[90] Torzilli 1987	1
Glucose	Spherical	180	0.37	403	894	0.45	0.76	Mature bovine	Solute desorption (Radiolabel)	Frozen	[30] Torzilli 1997	
Glucose	Spherical	180	0.37	563	894	0.63	0.67	Mature bovine	Solute desorption (Radiolabel)	Frozen	[89] Torzilli 1998	
Glucose	Spherical	180	0.37	483 (37°C)	894 (37°C)	0.54	0.36	Mature equine and bovine	Solute desorption (Radiolabel)	Frozen	[91] Allhands 1984	15
Glucose	Spherical	180	0.37	220	632	0.35	0.90	Adult human	Diffusion cell (Radiolabel)	Frozen	[21] Maroudas 1968	
Thymidine	Spherical	242	0.46	320	506	0.63	0.78	Mature bovine	Diffusion cell (Radiolabel)	Frozen	[25] Garcia 1996	
Fluorescein	Spherical	332	0.49	-	477	-	0.7	Immature bovine	Fluorescence gradient	Frozen	[92] Albro 2011	1, 4

Solute	Shape[a]	MW (Da)	Hydrodynamic Radius (nm)[b]	Diffusivity ($\mu m^2/s$)[c]	D_0 ($\mu m^2/s$)[d]	D/D_0	Partition Coefficient (K)[e]	Tissue Used[f]	Method to Obtain Diffusivity	Tissue Condition[g]	Reference	Notes
Sucrose	Spherical	342.3	0.50	130	465	0.28	1.00	Adult human	Diffusion cell (Radiolabel)	Frozen	[23] Maroudas 1970	
Tetra-methyl-rhodamine (TMR)	Spherical	430	0.55	70	423	0.17	1.69	Mature bovine	Solute desorption (Fluorophore)	Frozen	[58] Quinn 2000	2, 7, 12
Tetra-methyl-rhodamine (TMR)	Spherical	430	0.55	52	423	0.12	1.71	Mature bovine	Solute desorption (Fluorophore)	Frozen	[93] Quinn 2001	3, 7, 12
Gadolinium-diethylenetriamine pentaacetic acid (DTPA)	Spherical	530	0.61	140	540	0.26	0.62	Mature bovine	Computed tomography (CT)	Fresh	[37] Kokkonen 2017	9, 11
Gadolinium-diethylenetriamine pentaacetic acid (DTPA)	Spherical	530	0.61	187	381	0.49	0.47	Mature bovine	Solute desorption (Other)	Frozen	[88] Shafieyan 2014	11
Gadolinium-diethylenetri-amine pentaacetic acid (DTPA)	Spherical	530	0.61	140	381	0.37	-	Immature bovine	Nuclear magnetic resonance (NMR)	Frozen	[26] Foy 2001	
Gadopentetate Dimeglumine	Spherical	548	0.62	254	378	0.67	-	Mature bovine	Computed tomography (CT)	Fresh	[33] Kulmala 2010	1
Gadodiamide	Spherical	574	0.63	161	370	0.44	-	Mature bovine	Computed tomography (CT)	Fresh	[33] Kulmala 2010	1
Raffinose	Spherical	594	0.56	290	416	0.70	0.48	Mature bovine	Diffusion cell (Radiolabel)	Frozen	[25] Garcia 1996	
Sodium Diatrizoate Hydrate	Spherical	636	0.66	145	353	0.41	0.39	Mature bovine	Solute desorption (Other)	Frozen	[88] Shafieyan 2014	1, 11

Solute	Shape[a]	MW (Da)	Hydrodynamic Radius (nm)[b]	Diffusivity ($\mu m^2/s$)[c]	D_0 ($\mu m^2/s$)[d]	D/D_0	Partition Coefficient (K)[e]	Tissue Used[f]	Method to Obtain Diffusivity	Tissue Condition[g]	Reference	Notes
Sodium Diatrizoate Hydrate	Spherical	636	0.66	475	499	0.95	0.70	Mature bovine	Computed tomography (CT)	Fresh	[37] Kokkonen 2017	1, 11
Pf-Pep	Spherical	760	0.62	100	375	0.27	3.00	Mature bovine	Diffusion cell (Radiolabel)	Fresh	[45] Byun 2010	12
Ioxaglate	Spherical	1269	0.91	143	256	0.56	-	Mature bovine	Computed tomography (CT)	Fresh	[33] Kulmala 2010	1
Ioxaglate	Spherical	1269	0.91	90	256	0.35	0.65	Mature bovine	Computed tomography (CT)	Fresh	[35] Silvast 2013	1, 9, 11
Iodixanol	Spherical	1550	1.00	20	234	0.09	-	Mature equine	Computed tomography (CT)	Frozen	[36]Arbabi 2015	1, 6
Inulin	Spherical	5000	1.52	97 (37°C)	217 (37°C)	0.45	0.62	Mature bovine	Solute desorption (Radiolabel)	Frozen	[90] Torzilli 1987	13
Inulin	Spherical	5000	1.52	93 (37°C)	217 (37°C)	0.43	0.62	Mature bovine	Solute desorption (Radiolabel)	Frozen	[30] Torzilli 1997	
Inulin	Spherical	5000	1.52	25	153	0.16	0.09	Adult human	Diffusion cell (Radiolabel)	Frozen	[23] Maroudas 1970	
Inulin	Spherical	5000	1.52	22	153	0.15	0.15	Adult human	Diffusion cell (Radiolabel)	Fresh	[94] Schneiderman 1995	
Insulin-like growth factor-1 (IGF-1)	Spherical	7650	2.09	26 (12°C)	81 (12°C)	0.32	1.39	Mature bovine	Diffusion cell (Radiolabel)	Fresh	[44] Garcia 2003	1, 12
Gadolinium-lysozyme	Spherical	14300	2.80	25	83	0.30	-	Immature bovine	Nuclear magnetic resonance (NMR)	Frozen	[26] Foy 2001	
Gadolinium-trypsinogen	Spherical	24000	4.70	5.0	50	0.10	-	Immature bovine	NMR	Frozen	[26] Foy 2001	

Solute	Shape[a]	MW (Da)	Hydrodynamic Radius (nm)[b]	Diffusivity ($\mu m^2/s$)[c]	D_0 ($\mu m^2/s$)[d]	D/D_0	Partition Coefficient (K)[e]	Tissue Used[f]	Method to Obtain Diffusivity	Tissue Condition[g]	Reference	Notes
Antibody Fragment (single chain fragment variable, scFv)	Spherical	25000	2.65	10 (37°C)	124 (37°C)	0.08	-	Immature bovine	Fluorescence gradient	Fresh	[31] DiDomenico 2017	5, 6
Tissue inhibitors of metalloproteinases (TIMP-1)	Spherical	28000	3.80	16	61	0.26	0.20	Mature bovine	Diffusion cell (Radiolabel)	Fresh	[95] Garcia 1998	1
Gadolinium-ovalbumin	Spherical	45000	3.50	4.0	66	0.06	-	Immature bovine	Nuclear magnetic resonance (NMR)	Frozen	[26] Foy 2001	
Antibody Fragment (antigen-binding, F_{ab})	Spherical	50000	3.03	9.3 (37°C)	109 (37°C)	0.09	-	Immature bovine	Fluorescence gradient	Fresh	[31] DiDomenico 2017	5, 6
Hemoglobin	Spherical	64500	3.18	13	73	0.17	0.04	Adult human	Diffusion cell (Radiolabel)	Frozen	[23] Maroudas 1970	
Serum Albumin	Spherical	66000	3.48	20	67	0.30	0.01	Adult human	Diffusion cell (Radiolabel)	Frozen	[22] Maroudas 1976	
Avidin	Spherical	66000	3.50	38 (37°C)	94 (37°C)	0.40	6.00	Immature bovine	Diffusion cell (Fluorophore)	Fresh	[46] Bajpayee 2014	8, 12
NeutraAvidin	Spherical	66000	3.50	38 (37°C)	94 (37°C)	0.40	0.44	Immature bovine	Diffusion cell (Fluorophore)	Fresh	[46] Bajpayee 2014	8
Transferrin	Spherical	80000	4.30	-	54	-	0.02	Immature bovine	Fluorescence gradient	Frozen	[92] Albro 2011	4
Antibody (IgG)	Spherical	150000	5.22	11	45	0.25	0.01	Adult human	Diffusion cell (Radiolabel)	Frozen	[22] Maroudas 1976	
Antibody (IgG)	Spherical	150000	5.22	8.4 (37°C)	63 (37°C)	0.13	-	Immature bovine	Fluorescence gradient	Fresh	[31] DiDomenico 2017	5, 6
Antibody (IgG)	Spherical	150000	5.22	4.2 (37°C)	63 (37°C)	0.07	-	Immature bovine	Fluorescence gradient	Frozen	[32] DiDomenico 2016	5, 7

Solute	Shape[a]	MW (Da)	Hydrodynamic Radius (nm)[b]	Diffusivity ($\mu m^2/s$)[c]	D_0 ($\mu m^2/s$)[d]	D/D_0	Partition Coefficient (K)[e]	Tissue Used[f]	Method to Obtain Diffusivity	Tissue Condition[g]	Reference	Notes
Antibody (IgG)	Spherical	150000	5.22	2.0 (37°C)	63 (37°C)	0.03	-	Mature equine	Fluorescence gradient	Frozen	[32] DiDomenico 2016	5, 7
Antibody (IgG)	Spherical	150000	5.22	4.5 (37°C)	63 (37°C)	0.07	-	Immature bovine	Fluorescence gradient	Fresh	[96] DiDomenico 2016	5, 7
Antibody (IgG, pI 5.9)	Spherical	150000	5.51	8.2 (37°C)	60 (37°C)	0.14	-	Immature bovine	Fluorescence gradient	Fresh	[97] DiDomenico 2017	5,6
Antibody (IgG, pI 5.4)	Spherical	150000	6.03	7.8 (37°C)	55 (37°C)	0.14	-	Immature bovine	Fluorescence gradient	Fresh	[97] DiDomenico 2017	5,6
Antibody (IgG, pI 4.7)	Spherical	150000	6.12	7.2 (37°C)	54 (37°C)	0.13	-	Immature bovine	Fluorescence gradient	Fresh	[97] DiDomenico 2017	5,6
Modified Antibody (dual variable domain, DVD)	Spherical	198000	7.59	7.8 (37°C)	43 (37°C)	0.18	-	Immature bovine	Fluorescence gradient	Fresh	[31] DiDomenico 2017	5,6

Solute	Shape[a]	MW (Da)	Hydrodynamic Radius (nm)[b]	Diffusivity ($\mu m^2/s$)[c]	D_0 ($\mu m^2/s$)[d]	D/D_0	Partition Coefficient (K)[e]	Tissue Used[f]	Method to Obtain Diffusivity	Tissue Condition[g]	Reference	Notes
Dextran 3K	Linear	3000	1.75	65	133	0.49	0.87	Mature bovine	Solute desorption (Fluorophore)	Frozen	[58] Quinn 2000	2, 7
Dextran 3K	Linear	3000	1.75	30	133	0.23	1.15	Mature bovine	Solute desorption (Fluorophore)	Frozen	[93] Quinn 2001	3, 7
Dextran 3K	Linear	3000	1.75	76	133	0.57	-	Mature porcine	Fluorescence recovery after photobleaching (FRAP)	Fresh	[28] Leddy 2003	6
Dextran 3K	Linear	3000	1.75	-	133	-	0.13	Immature bovine	Fluorescence gradient	Frozen	[92] Albro 2011	4
Dextran 4K	Linear	4000	1.54	31	151	0.21	0.30	Mature bovine	Solute desorption (Fluorophore)	Frozen	[85] Chin 2013	

Solute	Shape[a]	MW (Da)	Hydrodynamic Radius (nm)[b]	Diffusivity ($\mu m^2/s$)[c]	D_0 ($\mu m^2/s$)[d]	D/D_0	Partition Coefficient (K)[e]	Tissue Used[f]	Method to Obtain Diffusivity	Tissue Condition[g]	Reference	Notes
Dextran 10K	Linear	10000	2.36	267 (37°C)	139 (37°C)	1.92	0.65	Mature bovine	Solute desorption (Radiolabel)	Frozen	[90] Torzilli 1987	13
Dextran 10K	Linear	10000	2.36	374 (37°C)	139 (37°C)	2.68	0.57	Mature bovine	Solute desorption (Radiolabel)	Frozen	[89] Torzilli 1998	
Dextran 10K	Linear	10000	2.70	-	86	-	0.03	Immature bovine	Fluorescence gradient	Frozen	[92] Albro 2011	4
Chondroitin Sulfate	Linear	20000	3.25	89	71	1.24	0.23	Mature bovine	Solute desorption (Fluorophore)	Frozen	[85] Chin 2013	1
Dextran 20K	Linear	20000	3.26	158 (37°C)	101 (37°C)	1.56	0.26	Mature equine and bovine	Solute desorption (Radiolabel)	Frozen	[91] Allhands 1984	
Dextran 20K	Linear	20000	3.26	103 (37°C)	101 (37°C)	1.02	0.54	Mature bovine	Solute desorption (Radiolabel)	Frozen	[90] Torzilli 1987	13
Dextran 40K	Linear	40000	4.78	28	49	0.58	0.10	Mature bovine	Solute desorption (Fluorophore)	Frozen	[85] Chin 2013	
Dextran 40K	Linear	40000	4.78	40	49	0.82	0.36	Mature bovine	Solute desorption (Fluorophore)	Frozen	[58] Quinn 2000	2, 7
Dextran 40K	Linear	40000	4.78	19	49	0.39	0.16	Mature bovine	Solute desorption (Fluorophore)	Frozen	[93] Quinn 2001	3, 7
Dextran 40K	Linear	40000	4.78	58	49	1.19	-	Mature porcine	Fluorescence recovery after photobleaching (FRAP)	Fresh	[28] Leddy 2003	6
Dextran 70K	Linear	70000	5.80	37	40	0.92	-	Mature porcine	Fluorescence recovery after photobleaching (FRAP)	Fresh	[28] Leddy 2003	6

Solute	Shape[a]	MW (Da)	Hydrodynamic Radius (nm)[b]	Diffusivity ($\mu m^2/s$)[c]	D_0 ($\mu m^2/s$)[d]	D/D_0	Partition Coefficient (K)[e]	Tissue Used[f]	Method to Obtain Diffusivity	Tissue Condition[g]	Reference	Notes
Dextran 70K	Linear	70000	5.80	35	40	0.86	0.01	Adult human (ankle)	Fluorescence recovery after photobleaching (FRAP)	Frozen	[27] Fetter 2006	6
Dextran 70K	Linear	70000	5.80	35	40	0.88	0.02	Adult human	Fluorescence recovery after photobleaching (FRAP)	Frozen	[27] Fetter 2006	6
Dextran 70K	Linear	70000	5.80	40 (37°C)	57 (37°C)	0.70	0.38	Mature bovine	Solute desorption (Radiolabel)	Frozen	[30] Torzilli 1997	
Dextran 70K	Linear	70000	7.40	-	31	-	0.02	Immature bovine	Fluorescence gradient	Frozen	[92] Albro 2011	4
Dextran 500K	Linear	500000	15.90	9.0	15	0.61	-	Mature porcine	Fluorescence recovery after photobleaching (FRAP)	Fresh	[28] Leddy 2003	6

Superscripts:	
a	Chondroitin sulfate or dextran molecules were considered linear molecules; all others were considered spherical
b	All radii were taken from primary or secondary sources in the literature. If no size information was found on a solute, the empirical relation ($r_s = 0.0332MW^{0.463}$, [65]), was used where noted
c	All diffusivities are averages that were taken in a direction perpendicular to the articular surface and at zero tissue strain, unless otherwise noted
d	The Stoke's Einstein equation (Eq. 4) was used to calculate free diffusivity at 23°C, unless otherwise noted
e	Solute absorption/desorption technique used to calculate partition coefficient, unless otherwise noted
f	All tissue sources were from stifle or knee joints, unless otherwise noted
g	Denotes how the tissue was stored before experimentation took place

Notes:			
1	Empirical relationship ($r_s = 0.0332MW^{0.463}$, [65]) used to calculate hydrodynamic radius	10	Fluorescence gradient technique used to determine partition coefficient
2	Diffusivity taken at 0.05 strain	11	Negatively charged, excluded from partition coefficient analysis
3	Diffusivity taken at 0.08 strain	12	Positively charged, excluded from partition coefficient analysis
4	Diffusivity taken at 0.10 strain	13	Partition coefficient and diffusivity taken at t = 1 hr.
5	Diffusivity taken at 0.15 strain	14	Negatively charged, excluded from partition coefficient analysis
6	Average diffusivity through the depth of tissue	15	Positively charged, excluded from partition coefficient analysis
7	Diffusivity in direction parallel to articular surface	16	Partition coefficient and diffusivity taken at t = 1 hr.
8	Effective diffusivity cited		
9	Computed tomography (CT) technique used to determine partition coefficient		

REFERENCES

1. Hampel, U. *et al.* Chemokine and cytokine levels in osteoarthritis and rheumatoid arthritis synovial fluid. *J. Immunol. Methods* **396,** 134–139 (2013).
2. Marc Feldmann, Fionula M. Brennan, A. & Ravinder N. Maini. Role of Cytokines in Rheumatoid Arthritis. *Annu. Rev. Immunol.* **14,** 397–440 (1996).
3. Steiner, G. *et al.* Cytokine production by synovial T cells in rheumatoid arthritis. *Rheumatology* **38,** 202–213 (1999).
4. Feldmann, M. & Maini, R. N. Anti -TNFα Therapy of Rheumatoid Arthritis: What Have We Learned? *Annu Rev Immunol* **19,** 163–96 (2001).
5. McInnes, I. B., McInnes, I. B., Schett, G. & Schett, G. Cytokines in the pathogenesis of rheumatoid arthritis. *Nat. Rev. Immunol.* **7,** 429–42 (2007).
6. Moos, V., Fickert, S., Müller, B., Weber, U. & Sieper, J. Immunohistological analysis of cytokine expression in human osteoarthritic and healthy cartilage. *J. Rheumatol.* **26,** 870–879 (1999).
7. Fernandes, J. C., Martel-Pelletier, J. & Pelletier, J.-P. The role of cytokines in osteoarthritis pathophysiology. *Biorheology* **39,** 237–46 (2002).
8. Scanzello, C. R. *et al.* Local cytokine profiles in knee osteoarthritis: elevated synovial fluid interleukin-15 differentiates early from end-stage disease. *Osteoarthr. Cartil.* **17,** 1040–1048 (2009).
9. Evans, C. H., Kraus, V. B. & Setton, L. A. Progress in intra-articular therapy. *Nat. Rev. Rheumatol.* **10,** 11–22 (2013).
10. Evans, C. H. Drug delivery to chondrocytes. *Osteoarthritis and Cartilage* **24,** 1–3 (2016).

11. Bajpayee, A. G. & Grodzinsky, A. J. Cartilage-targeting drug delivery: can electrostatic interactions help? *Nat. Rev. Rheumatol.* **13,** 183–193 (2017).

12. Gerwin, N., Hops, C. & Lucke, A. Intraarticular drug delivery in osteoarthritis. *Adv. Drug Deliv. Rev.* **58,** 226–242 (2006).

13. McAlindon, T. E. *et al.* OARSI guidelines for the non-surgical management of knee osteoarthritis. *Osteoarthr. Cartil.* **22,** 363–388 (2014).

14. da Costa, B. R. *et al.* Effectiveness of non-steroidal anti-inflammatory drugs for the treatment of pain in knee and hip osteoarthritis: a network meta-analysis. *Lancet* **390,** e21–e33 (2017).

15. Urech, D. M. *et al.* Anti-inflammatory and cartilage-protecting effects of an intra-articularly injected anti-TNF{alpha} single-chain Fv antibody (ESBA105) designed for local therapeutic use. *Ann. Rheum. Dis.* **69,** 443–449 (2010).

16. Mow, V. C., Holmes, M. H. & Michael Lai, W. Fluid transport and mechanical properties of articular cartilage: A review. *J. Biomech.* **17,** 377–394 (1984).

17. Poole, A. R. *et al.* Composition and structure of articular cartilage: a template for tissue repair. *Clin. Orthop. Relat. Res.* **1,** S26–S33 (2001).

18. Maroudas, A. Biophysical chemistry of cartilaginous tissues with special reference to solute and fluid transport. *Biorheology`* **12,** 233–248 (1975).

19. Hwang, W. S. *et al.* Collagen fibril structure of normal, aging, and osteoarthritic cartilage. *J. Pathol.* **167,** 425–433 (1992).

20. Maroudas, A. & Bullough, P. Permeability of articular cartilage. *Nature* **219,** 1260–1261 (1968).

21. Maroudas, A. Physicochemical Properties of Cartilage in the Light of Ion

Exchange Theory. *Biophys. J.* **8,** 575–595 (1968).

22. Maroudas, A. Transport of solutes through cartilage: permeability to large molecules. *J. Anat.* **122,** 335–347 (1976).

23. Maroudas, A. Distribution and diffusion of solutes in articular cartilage. *Biophys. J.* **10,** 365–379 (1970).

24. Bonassar, L. J. *et al.* The effect of dynamic compression on the response of articular cartilage to insulin-like growth factor-I. *J. Orthop. Res.* **19,** 11–17 (2001).

25. Garcia, A. M., Frank, E. H., Grimshaw, P. E. & Grodzinsky, A. J. Contributions of Fluid Convection and Electrical Migration to Transport in Cartilage: Relevance to Loading. *Arch. Biochem. Biophys.* **333,** 317–325 (1996).

26. Foy, B. D. & Blake, J. Diffusion of paramagnetically labeled proteins in cartilage: enhancement of the 1-D NMR imaging technique. *J. Magn. Reson.* **148,** 126–134 (2001).

27. Fetter, N. L., Leddy, H. A., Guilak, F. & Nunley, J. A. Composition and transport properties of human ankle and knee cartilage. *J. Orthop. Res.* **24,** 211–219 (2006).

28. Leddy, H. A. & Guilak, F. Site-specific molecular diffusion in articular cartilage measured using fluorescence recovery after photobleaching. *Ann. Biomed. Eng.* **31,** 753–760 (2003).

29. Leddy, H. A., Haider, M. A. & Guilak, F. Diffusional anisotropy in collagenous tissues: fluorescence imaging of continuous point photobleaching. *Biophys. J.* **91,** 311–316 (2006).

30. Torzilli, P. A., Arduino, J. M., Gregory, J. D. & Bansal, M. Effect of proteoglycan removal on solute mobility in articular cartilage. *J. Biomech.* **30,** 895–902 (1997).

31. DiDomenico, C. D. *et al.* The Effect of Antibody Size and Mechanical Loading on Solute Diffusion Through the Articular Surface of Cartilage. *J. Biomech. Eng.* **139,** 091005 (2017).

32. DiDomenico, C. D., Xiang Wang, Z. & Bonassar, L. J. Cyclic Mechanical Loading Enhances Transport of Antibodies Into Articular Cartilage. *J. Biomech. Eng.* **139,** 011012 (2016).

33. Kulmala, K. A. M. *et al.* Diffusion coefficients of articular cartilage for different CT and MRI contrast agents. *Med. Eng. Phys.* **32,** 878–882 (2010).

34. Honkanen, J. T. J. *et al.* Cationic Contrast Agent Diffusion Differs Between Cartilage and Meniscus. *Ann. Biomed. Eng.* **44,** 2913–2921 (2016).

35. Silvast, T. S., Jurvelin, J. S., Tiitu, V., Quinn, T. M. & Töyräs, J. Bath Concentration of Anionic Contrast Agents Does Not Affect Their Diffusion and Distribution in Articular Cartilage In Vitro. *Cartilage* **4,** 42–51 (2013).

36. Arbabi, V., Pouran, B., Weinans, H. & Zadpoor, A. A. Transport of Neutral Solute Across Articular Cartilage: The Role of Zonal Diffusivities. *J. Biomech. Eng.* **137,** 071001 (2015).

37. Kokkonen, H. T., Chin, H. C., Töyräs, J., Jurvelin, J. S. & Quinn, T. M. Solute Transport of Negatively Charged Contrast Agents Across Articular Surface of Injured Cartilage. *Ann. Biomed. Eng.* **45,** 973–981 (2017).

38. Yin, Y., Zhao, C., Kuroki, S. & Ando, I. Diffusion of rodlike polypeptides with different main-chain lengths in the thermotropic liquid crystalline state as studied

by the field-gradient 1H NMR method. *Macromolecules* **35,** 2335–2338 (2002).

39. Burstein, D., Gray, M. L., Hartman, A. L., Gipe, R. & Foy, B. D. Diffusion of small solutes in cartilage as measured by nuclear magnetic resonance (NMR) spectroscopy and imaging. *J. Orthop. Res.* **11,** 465–478 (1993).

40. Bonassar, L. J., Grodzinsky, a J., Srinivasan, a, Davila, S. G. & Trippel, S. B. Mechanical and physicochemical regulation of the action of insulin-like growth factor-I on articular cartilage. *Arch. Biochem. Biophys.* **379,** 57–63 (2000).

41. Buschmann, M. D. *et al.* Stimulation of aggrecan synthesis in cartilage explants by cyclic loading is localized to regions of high interstitial fluid flow. *Arch. Biochem. Biophys.* **366,** 1–7 (1999).

42. Allen, K. D., Adams, S. B. & Setton, L. A. Evaluating intra-articular drug delivery for the treatment of osteoarthritis in a rat model. *Tissue Eng. Part B. Rev.* **16,** 81–92 (2010).

43. Nimer, E., Schneiderman, R. & Maroudas, A. Diffusion and partition of solutes in cartilage under static load. *Biophys. Chem.* **106,** 125–146 (2003).

44. Garcia, A. M. *et al.* Transport and binding of insulin-like growth factor I through articular cartilage. *Arch. Biochem. Biophys.* **415,** 69–79 (2003).

45. Byun, S. *et al.* Transport and equilibrium uptake of a peptide inhibitor of PACE4 into articular cartilage is dominated by electrostatic interactions. *Arch. Biochem. Biophys.* **499,** 32–39 (2010).

46. Bajpayee, A. G., Wong, C. R., Bawendi, M. G., Frank, E. H. & Grodzinsky, A. J. Avidin as a model for charge driven transport into cartilage and drug delivery for treating early stage post-traumatic osteoarthritis. *Biomaterials* **35,** 538–549

(2014).

47. Evans, R. C. & Quinn, T. M. Dynamic compression augments interstitial transport of a glucose-like solute in articular cartilage. *Biophys. J.* **91,** 1541–1547 (2006).

48. DiDomenico, C., Lintz, M. & Bonassar, L. J. Molecular transport in cartilage: What has a half century taught us? *Nat. Rev. Rheumatol.* **In press,** (2018).

49. Evans, R. C. & Quinn, T. M. Solute convection in dynamically compressed cartilage. *J. Biomech.* **39,** 1048–1055 (2006).

50. Yao, H. & Gu, W. Y. Convection and diffusion in charged hydrated soft tissues: A mixture theory approach. *Biomech. Model. Mechanobiol.* **6,** 63–72 (2007).

51. Ateshian, G. a, Maas, S. & Weiss, J. a. Multiphasic finite element framework for modeling hydrated mixtures with multiple neutral and charged solutes. *J. Biomech. Eng.* **135,** 111001 (2013).

52. Gu, W. Y., Lai, W. M. & Mow, V. C. Transport of fluid and ions through a porous-permeable charged-hydrated tissue, and streaming potential data on normal bovine articular cartilage. *J. Biomech.* **26,** 709–723 (1993).

53. Helfferich, F. G. *Ion Exchange*. (Courier Corporation, 1962).

54. Buschmann, M. D. & Grodzinsky, A. J. A Molecular Model of Electrostatic Forces in Cartilage Mechanics. *J. Biomech. Eng.* **1,** 179–192 (1995).

55. Truskey, G. A., Yuan, F. & Katz, D. F. *Transport Phenomena in Biological Systems*. (Pearson Education, 2010).

56. Zoppou, C. & Knight, J. H. Analytical Solutions for Advection and Advection-Diffusion Equations with Spatially Variable Coefficients. *J. Hydraul. Eng.* **123,**

144–148 (1997).

57. Crank, J. *The mathematics of diffusion*. *Oxford University Press* (Clarendon Press, 1975). doi:10.1016/0306-4549(77)90072-X

58. Quinn, T. M., Kocian, P. & Meister, J. J. Static compression is associated with decreased diffusivity of dextrans in cartilage explants. *Arch. Biochem. Biophys.* **384,** 327–334 (2000).

59. Nugent, L. J. & Jain, R. K. Extravascular Diffusion in Normal and Neoplastic Tissues. *Cancer Res.* **44,** 238–244 (1984).

60. Lebrun, L. & Junter, G. A. Diffusion of dextran through microporous membrane filters. *J. Memb. Sci.* **88,** 253–261 (1994).

61. Deen, W. M., Bohrer, M. P. & Epstein, N. B. Effects of molecular size and configuration on diffusion in microporous membranes. *AIChE J.* **27,** 952–959 (1981).

62. Swabb, E., Wei, J. & Gullino, P. Extravascular Diffusion in Normal and Neoplastic Tissues. *Cancer Res.* **34,** 2814–2822 (1974).

63. Pluen, A., Netti, P. A., Jain, R. K. & Berk, D. A. Diffusion of macromolecules in agarose gels: comparison of linear and globular configurations. *Biophys. J.* **77,** 542–52 (1999).

64. Deen, W. M. Hindered transport of large molecules in liquid-filled pores. *AIChE J.* **33,** 1409–1425 (1987).

65. Bert, J. L., Pearce, R. H., Mathieson, J. M. & Warner, S. J. Characterization of collagenous meshworks by volume exclusion of dextrans. *Biochem. J* **191,** 761–768 (1980).

66. Renkin, E. M. Filtration, diffusion, and molecular sieving through porous cellulose membranes. *J. Gen. Physiol.* **38,** 225–243 (1954).

67. Davidson, M. G., Suter, U. W. & Deen, W. M. Equilibrium Partitioning of Flexible Macromolecules between Bulk Solution and Cylindrical Pores. *Macromolecules* **20,** 1141–1146 (1987).

68. Adam, M., Delsanti, M., Adam, M. & Light, M. D. Light scattering by dilute solution of polystyrene in a good solvent. *J. Phys.* **37,** 1045–1049 (1976).

69. Sutherland, W. A dynamical theory of diffusion for non-electrolytes and the molecular mass of albumin. *Philos. Mag. Ser. 6* **9,** 781–785 (1905).

70. Cruickshank Miller, C. The Stokes-Einstein Law for Diffusion in Solution. *Math. Phys. Character* **106,** 724–749 (1924).

71. Beck, R. E. & Schultz, J. S. Hindered Diffusion in Microporous Membranes with Known Pore Geometry. *Science (80-.).* **170,** 1302–1305 (1970).

72. Amsden, B. Solute Diffusion within Hydrogels. Mechanisms and Models. *Macromolecules* **31,** 8382–8395 (1998).

73. Brinkman, H. C. A calculation of the viscous force exerted by a flowing fluid on a dense swarm of particles. *Flow, Turbul. Combust.* **1,** 27 (1949).

74. Gu, W. Y., Yao, H., Huang, C. Y. & Cheung, H. S. New insight into deformation-dependent hydraulic permeability of gels and cartilage, and dynamic behavior of agarose gels in confined compression. *J. Biomech.* **36,** 593–598 (2003).

75. Lai, W. M. & Mow, V. C. Drag-induced compression of articular cartilage during a permeation experiment. *Biorheology* **17,** 111–123 (1980).

76. Clague, D. S. & Phillips, R. J. Hindered diffusion of spherical macromolecules

through dilute fibrous media. *Phys. Fluids* **8,** 1720–1731 (1996).

77. Levick, J. R. Flow Through Interstitium and Other Fibrous Matrices. *Q. J. Exp. Physiol.* **72,** 409–437 (1987).

78. Maroudas, A., Bayliss, M. T. & Venn, M. F. Further studies on the composition of human femoral head cartilage. *Ann Rheum Dis* **39,** 514–523 (1980).

79. Parker, K. H., Winlove, C. P. & Maroudas, A. The theoretical distributions and diffusivities of small ions in chondroitin sulphate and hyaluronate. *Biophys. Chem.* **32,** 271–282 (1988).

80. Ogston, A. G., Preston, B. N. & Wells, J. D. On the Transport of Compact Particles Through Solutions of Chain-Polymers. *Proc. R. Soc. A Math. Phys. Eng. Sci.* **333,** 297–316 (1973).

81. Anderson, J. L. & Quinn, J. A. Restricted Transport in Small Pores. *Biophys. J.* **14,** 130–150 (1974).

82. Ogston, A. G. The spaces in a uniform random suspension of fibres. *Trans. Faraday Soc.* **54,** 1754 (1958).

83. Kim, S. E. *et al.* Ultrasmall nanoparticles induce ferroptosis in nutrient-deprived cancer cells and suppress tumour growth. *Nat. Nanotechnol.* **11,** 977–985 (2016).

84. Manning, H. B. *et al.* Detection of cartilage matrix degradation by autofluorescence lifetime. *Matrix Biol.* **32,** 32–38 (2013).

85. Chin, H. C., Moeini, M. & Quinn, T. M. Solute transport across the articular surface of injured cartilage. *Arch. Biochem. Biophys.* **535,** 241–247 (2013).

86. Moeini, M. *et al.* Decreased solute adsorption onto cracked surfaces of mechanically injured articular cartilage: Towards the design of cartilage-specific

functional contrast agents. *Biochim. Biophys. Acta - Gen. Subj.* **1840,** 605–614 (2014).

87. Decker, S. G. A., Moeini, M., Chin, H. C., Rosenzweig, D. H. & Quinn, T. M. Adsorption and distribution of fluorescent solutes near the articular surface of mechanically injured cartilage. *Biophys. J.* **105,** 2427–2436 (2013).

88. Shafieyan, Y., Khosravi, N., Moeini, M. & Quinn, T. M. Diffusion of MRI and CT contrast agents in articular cartilage under static compression. *Biophys. J.* **107,** 485–492 (2014).

89. Torzilli, P. A., Grande, D. A. & Arduino, J. M. Diffusive properties of immature articular cartilage. *J. Biomed. Mater. Res.* **40,** 132–138 (1998).

90. Torzilli, P. A., Adams, T. C. & Mis, R. J. Transient solute diffusion in articular cartilage. *J. Biomech.* **20,** 203–214 (1987).

91. Allhands, R. V, Torzilli, P. A. & Kallfelz, F. A. Measurement of diffusion of uncharged molecules in articular cartilage. *Cornell Vet.* **74,** 111–123 (1984).

92. Albro, M. B. *et al.* Dynamic loading of immature epiphyseal cartilage pumps nutrients out of vascular canals. *J. Biomech.* **44,** 1654–1659 (2011).

93. Quinn, T. M., Morel, V. & Meister, J. J. Static compression of articular cartilage can reduce solute diffusivity and partitioning: Implications for the chondrocyte biological response. *J. Biomech.* **34,** 1463–1469 (2001).

94. Schneiderman, R. *et al.* Insulin-like growth factor-I and its complexes in normal human articular cartilage: studies of partition and diffusion. *Arch. Biochem. Biophys.* **324,** 159–172 (1995).

95. Garcia, A. M., Lark, M. W., Trippel, S. B. & Grodzinsky, A. J. Transport of tissue

inhibitor of metalloproteinases-1 through cartilage: Contributions of fluid flow and electrical migration. *J. Orthop. Res.* **16,** 734–742 (1998).

96. DiDomenico, C. *et al.* Cyclic Mechanical Loading Enhances Transport of Antibodies Through Articular Cartilage. in *Orthopaedic Research Society* (2016).

97. DiDomenico, C. *et al.* Antibody Charge Affects Depth-Dependent Diffusion in Healthy Articular Cartilage. in *Orthopaedic Research Society* (2017).

CHAPTER 7

Conclusions and Future Directions

The goal of this dissertation was to investigate how large molecules, such as antibodies and antibody fragments, are transported through cartilage tissue. Long-term, this knowledge is valuable to the development of therapies that rely on transport of these types of drugs into cartilage. Before the turn of the 21st century, researchers in this field had assumed that any molecule larger than albumin (~ 4 nm) could not sufficiently penetrate cartilage to be useful as a therapeutic agent[1]. Even today, some argue that antibodies (~ 5.5 nm) are too large to enter cartilage, which is simply not true based on various evidence in this dissertation. One probable reason for this misconception is due to the small average pore size of cartilage (~ 5 nm). As such, there has been a focus on development of smaller drugs so that they could sufficiently penetrate the tissue. That sentiment is slowly changing. There are now several animal studies and clinical trials with much larger drugs, including antibodies and growth factors, which have been shown to sufficiently penetrate cartilage[2–4]. Even though these studies support that these large drugs can penetrate cartilage, very few studies have looked at local diffusion mechanics of these large proteins, critical components to fully understanding and developing new large arthritis therapeutics. As a result, current drug determinations are not based on a firm understanding on the transport kinetics of the molecule of interest. This is especially true because of the inherent heterogeneities of cartilage. These data in this dissertation therefore bridges this information gap and opens up new possibilities for arthritis treatments.

There are many arthritic diseases that interrupt the homeostasis of the joint space and cause a large societal and economic burden[5]. Many of these diseases precipitate the release of inflammatory factors that cause widespread joint degeneration, instability, and pain[6–8]. There are several main types of arthritis where drug penetration into articular cartilage can be beneficial to disease treatment. The two most common types of arthritis are rheumatoid arthritis (RA) and osteoarthritis (OA). In RA, systemic inflammation and increased levels of inflammatory cytokines leads to widespread joint destruction if left untreated. Because of the systemic nature of this disease, anti-inflammatory drugs, such as antibodies that are administered intra-muscularly, can dramatically reduce or halt disease progression and subsequent joint degeneration. Because of the systemic nature of administration, a small fraction of antibodies inevitably ends up in the joint synovial fluid, which results in the articular cartilage coming into direct contact with the drugs. Interestingly, there is relatively little information about how these drugs interact with the cartilage tissue during RA. Based on data solely from this dissertation, there is strong evidence that these drugs are able to diffuse through the cartilage matrix, and it is likely that they would exhibit some sort of anti-inflammatory effect on the chondrocytes in this disease. Because use of these anti-inflammatory drugs is so effective at halting RA progression, it seems like this effect would be relatively small compared to more systemic targets, such as the synovium. However, one cannot deny that this effect would be beneficial to the cartilage in the long-run as well.

Treating OA is another story. Because disease initiation is thought to originate in cartilage, administering drugs in a way that is efficacious is extremely difficult. Currently, intra-articular injections are the only way to administer efficacious number of drugs to the cartilage tissue. However, because of the high turnover rate of synovial fluid, most of the currently used smaller drugs, such as steroids, do not last in the joint space for more than 1 day, and their effects do not extend past several weeks after administration. Additionally, there is mixed evidence that intra-articular injections of either steroids or other small anti-inflammatory molecules are effective[3,4]. This has pushed the field toward use of larger molecules to try to increase drug half-lives in the joint.

Another treatment for early-stage OA is injection of high molecular weight hyaluronic acid into the joint. This highly viscous substance is able to reduce friction in the joint space by altering synovial fluid viscosity, which in turn will lower shear strains imparted on the chondrocytes in the cartilage and slow subsequent cartilage wear[4]. These injections have also been shown to last in the joint for many hours (days), which increases its therapeutic potential compared to shorter-lived therapeutic strategies. Unfortunately, these types treatment strategies have also been limited in effectiveness. As a result, the current focus of the field has now turned to relatively large therapeutics, such as growth factors and antibodies, which are large enough to have long half-lives, but not so large that they cannot fit into the pores of the cartilage matrix. As this dissertation shows, this brings a new host of challenges that need to be addressed.

Learning from decades of previous research, any new strategies to treat OA most likely need to have the following: (1) an extremely long joint half-life; (2) ability to get into the cartilage; (3) and ability to be retained within the cartilage matrix for a long time. The data from this dissertation allows researchers to be informed about how well antibodies and similarly-sized proteins move through the dense articular cartilage, a critical component in developing new therapeutics. Ultimately, there are several main findings to this dissertation.

Diffusion of antibodies is heterogeneous through the depth of cartilage due to changes in local cartilage composition (Chapter 3 and 5)

In these chapters, local molecular diffusion of a full-sized antibody molecule (150 kDa) was highly influenced by local matrix density in healthy and degraded articular cartilage. Overall, the diffusion kinetics of whole and fragmented antibodies were highly heterogeneous, with maximal diffusivities for both healthy and degraded samples occurring near 250 μm away from the articular surface of cartilage. This heterogeneous diffusion behavior are consistent with zonal diffusivities found from using 40 kDa and 70 kDa dextrans[9]. Thus, both linear (dextran) and spherical solutes (antibodies) within this size range (40 – 200 kDa), diffuse best between the highly organized, collagenous surface zone and the dense deeper zones.

These diffusion heterogeneities were found to be related to local composition ($0.3 < R^2 < 0.9$). Such correlations were strongest ($R^2 > 0.8$) for samples that underwent collagen damage, and these samples exhibited higher local diffusivities at the surface, compared

to trypsin-degraded or healthy samples. Therefore, our data supports that the highly organized collagenous surface zone acts as a selective barrier to large solutes, which agrees with research looking at diffusional anisotropy through the surface zone of cartilage tissue for linear dextran molecules[10]. In OA, this organized surface layer is often disrupted[11], and therefore diseased cartilage would not hinder large solutes as much as healthy tissue. Ultimately, our studies confirm a strong link between local diffusion kinetics and local composition, and that the highly organized surface collagen significantly slows diffusion of large solutes, such as antibodies.

The fact that large molecules are substantially affected by both cartilage structure and composition is not entirely surprising. Because of the small effective pore size of cartilage (~5 nm), molecules close to this pore size will likely be very sensitive to changes in collagen structure and/or composition. Additionally, the effective pore size of cartilage is thought to decrease significantly through the depth of cartilage, which will in turn affect diffusion of molecules approaching the local pore size.

Future directions

Even though these data were produced using degraded cartilage, which is sought to mimic compositional and structural changes that would be evident from disease *in vivo*, it would be beneficial to complete these types of experiments again with osteoarthritic tissue. With diseased human tissue, one can relate diffusion to stages of OA, which would hold great clinical significance.

Based on the steep slopes on our diffusivity/aggrecan correlations, diffusion is extremely sensitive to aggrecan changes. Because of this, it is hypothesized that there are percolation thresholds (minimum concentration values) for aggrecan in relation to local diffusivity. The development of a percolation model (and/or other similar FE transport models) that would be able to explain changes in diffusive behavior as a function of composition, and perhaps solute size, would be helpful further to pinpoint changes in transport of various therapeutics.

Convective transport during cyclic loading significantly increases overall transport (Chapter 2 and 3)

Convective contributions from cyclic loading for a 150 kDa antibody were found to be maximal at 1 Hz and 5% cyclic strain, for a variety of cartilage tissue obtained from different animal species[12]. In these chapters, bulk solute transport in the radial direction in loaded samples was 2-3 times higher than transport in passive samples. Additionally, local transport of variously sized solutes (25-200 kDa) was enhanced (2-4 fold) up to 400 μm from the articular surface. Areas of local transport enhancement were highest near the sample periphery (and near the articular surface[13]), where fluid velocity was highest. These data support the idea that obtaining the best combination of fluid velocity and fluid penetration depth is important to maximizing solute transport enhancement[12].

Ultimately, cyclic mechanical loading of cartilage leads to a significant enhancement (up to 3-fold) of solute transport at physiologic strain amplitudes (1 – 5%) and

frequencies (0.1 – 2 Hz). These data support that joint movement is very important for sufficient penetration of arthritis therapeutics *in vivo.*

Future Directions

These loading-based enhancements were found primarily using healthy articular cartilage. Because degradation of cartilage will lead to significant gains in diffusivities, it is unclear how much mechanical loading would help transport (both diffusivity and partition coefficient) *in vivo*. The complex loading conditions and geometries of cartilage *in vivo* make this a very difficult transport problem, but finite element models could prove useful in elucidating some of the finer details in relation to convective transport in cartilage. Additionally, it would be useful to perform similar experiments with degraded and/or diseased cartilage to see if changes in composition play a large role in convective transport.

Solute charge aids local transport (Chapter 4)

In Chapter 4, solute charge was shown to alter local diffusion mechanics for antibody molecules (150 kDa) within 125 – 300 μm from the articular surface of the cartilage[14]. In this region, a 5.9 pI antibody exhibited a 20% increase in diffusivity compared to that of a pI 4.7 molecule. Within this range of isoelectric points, its seems that charge interactions between matrix and solute were only significant at certain aggrecan concentrations that were present in this region.

Thus, increasing positive solute charge is associated with higher local diffusivities. Positively charged solutes also are retained in the cartilage tissue for longer periods of time[2]. Thus, relying on reversible binding of positively charged solutes can be used to increase effectiveness of future drug therapies. These effects are ultimately linked to strong electrostatic interactions between the solute and the negatively charged cartilage matrix. These data support that isoelectric point represents another tunable property that could be changed to optimize macromolecular transport within cartilage.

Future directions

Despite a local difference in diffusivity of these charged solutes, it would be very interesting to investigate how large changes of pI relates to local diffusivity and local partition coefficients. The field already is aware of the benefits to bulk partition coefficient by using positively charged molecules, but local changes are still not well-understood. Elucidating these local changes can lead to advances in localized, targeted therapies that target specific regions of the cartilage.

Solute transport in articular cartilage can be accurately predicted based on molecular size (Chapter 6)

In Chapter 6, over a wide solute size range (0.1 – 7.6 nm), solute diffusivity in articular cartilage was accurately predicted with an empirical relationship that was not dependent on experimental procedure, tissue species, or tissue age. For spherical solutes, such as antibodies, the relationship between solute diffusivity and molecular weight or hydrodynamic radius was well-described by a power-law relationship (R^2 = 0.81).

Diffusivities of linear solutes, such as dextran, were not well-described by a power-law (R^2 = 0.25) and its diffusivity/size relationship deviated significantly from spherical solutes. It is ultimately unclear whether another metric other than hydrodynamic radius would be a better predictor of linear solute diffusion, such as persistence length of these molecules.

The strong empirical relationship reported herein strongly supports that diffusivity for spherical solutes can be accurately predicted in cartilage regardless of the experimental parameters used in individual experiments. Additionally, the disparity between spherical and linear solute data supports that linear solutes exhibit fundamentally different transport mechanics in cartilage, possibly due to their ability to change conformation while in the cartilage matrix. While further understanding the diffusion mechanics of linear solutes in cartilage would be helpful, our data supports that they are overestimate transport kinetics for similarly-sized spherical solutes. On the other hand, potential therapeutic, spherical molecules, such as antibodies and large drug-carrying nanoparticles, hold more clinical importance and should be the focus of future study.

Future Directions

Based on literature data, even solutes larger than the effective pore size of cartilage can diffuse through the entire depth of the tissue. This raises some interesting opportunities for macromolecular therapeutic design. For instance, nanoparticles ($r_s \geq 3$ nm) have been used to deliver customizable effects to cancer cells[15], but these particles have never been used to target cartilage chondrocytes directly. These molecules can easily be

customized to bind to collagen in the cartilage matrix and be functionalized with various therapeutics, likely giving these molecules extremely long joint half-lives and great therapeutic potential. Preliminary data shows that these nanoparticles diffuse as expected by their molecular size (see Appendix). A nanoparticle of radius 3.2 nm had a diffusivity through the articular surface of around 9 $\mu m^2/s$, which is similar to that of a 2.75 nm antibody fragment. Significantly changing the charge or binding characteristics would be the next steps for this project.

Similarly, we have also investigated the diffusion properties of very large aggrecan mimetics, which aim to replenish areas of depleted native aggrecan in cartilage. Collaborators at Drexel University have shown the healing properties of these large molecules in a mouse model[16]. The healing potential of these molecules are thought to be from their ability to sufficiently diffuse (although slowly) and bind in the surface regions of the cartilage tissue, which our data supports (see Appendix). Because these aggrecan mimetics can be modified heavily in size and shape, further understanding how these changes affect the diffusive properties is clinically important.

Likewise, delivery of antibodies using microspheres and delivery of large (r_s ~ 25 nm) viral vectors to modify diseased chondrocytes remains unstudied for arthritis therapy[4,17]. Even though these macromolecules would diffuse slowly through cartilage, they could be modified with binding domains to maximize joint residence times, which could make their development more feasible. Furthermore, it would be interesting to determine an

upper threshold for molecular size for solutes that can penetrate both healthy and degraded cartilage.

Additionally, Chapter 6 investigated current mechanistic transport models and noted that they were inconsistent in predicting solute diffusivity in cartilage. Mechanistic transport models can include two different types of solute interactions with the matrix: steric hindrance and hydrodynamic (frictional) effects. Both the Brinkman (hydrodynamic) and Renkin (steric) models only include one type of solute/matrix interaction. The Clague and Phillips model includes both steric and hydrodynamic solute interactions, and is likely why this model outperformed the others. However, all current transport models were developed specifically for hydrogels with only one fiber species, which may not be appropriate for cartilage. Thus, cartilage-specific models that include both steric and hydrodynamic solute/matrix effects should be developed in the future.

Clinical Interpretations

Because of the double network formed from aggrecan and collagen within cartilage, this network gives way to two sets of different pores through which solutes can diffuse. One set of pores, between GAG chains (~5 nm), give the tissue a small average pore size because of the high density of GAGs within the tissue. On the other hand, spaces in between collagen fibrils result in pores that are much larger (~50 nm). These larger pores are likely more important to diffusion in regions of relatively low GAG content, such as near the articular surface. These larger spaces inevitably help even 16 nm

molecules (500 kDa dextran) penetrate the full depth of the tissue, albeit slowly[9,10]. These facts open the field to new arthritis therapeutic strategies.

Furthermore, arthritic cartilage will likely have significantly larger pores than healthy, which will cause larger amounts of macromolecular transport within the tissue in these cases. Thus, data from this dissertation likely underestimates macromolecular diffusion in degraded cartilage. Additionally, the data from Chapter 6 likely underestimates transport, because the vast majority of transport data collected from the literature has been from healthy articular cartilage. Indeed, this dissertation shows the effect of degradation on transport (Chapter 5), with an increase in diffusivity of large molecules up to an order of magnitude in highly degraded regions (e.g. surface). Surprisingly, these dramatic increases were only due to moderate degradation of the articular cartilage. Based on histological images of aggrecan (Safrinin-O), these degradation protocols present in Chapter 5 would only result as Grade 1 or 2 osteoarthritis on the OARSI scale in humans [18].

These dramatic increases in cartilage transport based only early-moderate stages of OA have other implications. The strong power-law relationship found in Chapter 6 would likely shift upwards as cartilage degradation progresses to later stages of OA. Whether this would be a uniform shift at all sizes of molecules is less clear. There is evidence that degradation affects smaller molecules less so than larger ones[19]. Thus, it is possible that degradation of cartilage would lead to a flattening of the curve found in Chapter 6, with the most drastic increase in diffusivity for the largest molecules. This intrinsically

makes sense, since dramatically increasing the pore size of the tissue would likely have bigger effects on molecules that already "struggle" to fit into them.

Despite this deep understanding of transport, this dissertation seemingly supports that these drugs would probably not make the best treatments, because of their slow diffusion rates in cartilage. Even though OA cartilage would likely increase the transport rate of these drugs, it is very likely that unmodified variations of these drugs would not persist in the joint space and/or cartilage for long enough to be effective at changing the behavior of the native or diseased chondrocytes in the long-term. We have not yet found a drug that can achieve this goal. However, because of the size of these drugs, these drugs are more able to be retained within the matrix, which is a crucial factor in drug efficacy. Additionally, because of their size and customizability, these macromolecules can be heavily modified to further resist leaving the tissue, such as increasing solute charge[3,4]. With transport information obtained from our experiments, the field should focus on modifying these large molecules so they can sufficiently bind to the cartilage matrix and obtain the longest possible intra-articular half-life. Encapsulation of these drugs in microspheres, attaching them to nanoparticles, and/or increasing their charge could lead us to a better solution to treat cartilage disease. Ultimately, these molecules are promising therapeutics as long as we can make sure that they reside in the joint and cartilage tissue for as long as possible.

Significance

Because OA is so prevalent and often debilitating, understanding how to better treat and alleviate symptoms of OA would have far-reaching effects to many people. Since the introduction of antibody treatments for RA, such as AbbVie's Humira®, have surfaced, hundreds of thousands of people have experienced significant prognosis improvement. If a similar treatment for OA was developed, it would likely have a similar impact. Treatments would help with mobility and quality of life of the patient, leading to increased productivity and decreased future medical costs. This dissertation and its findings are a step in the right direction to develop OA treatments that are firmly grounded in an understanding of macromolecular transport.

REFERENCES

1. Maroudas, A. Distribution and diffusion of solutes in articular cartilage. *Biophys. J.* **10,** 365–379 (1970).
2. Bajpayee, A. G. & Grodzinsky, A. J. Cartilage-targeting drug delivery: can electrostatic interactions help? *Nat. Rev. Rheumatol.* **13,** 183–193 (2017).
3. Evans, C. H. Drug delivery to chondrocytes. *Osteoarthritis and Cartilage* **24,** 1–3 (2016).
4. Evans, C. H., Kraus, V. B. & Setton, L. A. Progress in intra-articular therapy. *Nat. Rev. Rheumatol.* **10,** 11–22 (2013).
5. Ma, V. Y., Chan, L. & Carruthers, K. J. Incidence, prevalence, costs, and impact on disability of common conditions requiring rehabilitation in the united states: Stroke, spinal cord injury, traumatic brain injury, multiple sclerosis, osteoarthritis, rheumatoid arthritis, limb loss, and back pa. *Archives of Physical Medicine and Rehabilitation* **95,** 986–995.e1 (2014).
6. Marc Feldmann, Fionula M. Brennan, A. & Ravinder N. Maini. Role of Cytokines in Rheumatoid Arthritis. *Annu. Rev. Immunol.* **14,** 397–440 (1996).
7. Shimizu, Y. & Ohta, M. Influence of plaque stiffness on deformation and blood flow patterns in models of stenosis. *Biorheology* **52,** 171–182 (2015).
8. Van Kuijk, A. W. R. & Tak, P. P. Synovitis in psoriatic arthritis: Immunohistochemistry, comparisons with rheumatoid arthritis, and effects of therapy. *Curr. Rheumatol. Rep.* **13,** 353–359 (2011).
9. Leddy, H. A. & Guilak, F. Site-specific molecular diffusion in articular cartilage measured using fluorescence recovery after photobleaching. *Ann. Biomed. Eng.*

31, 753–760 (2003).

10. Leddy, H. A., Haider, M. A. & Guilak, F. Diffusional anisotropy in collagenous tissues: fluorescence imaging of continuous point photobleaching. *Biophys. J.* **91,** 311–316 (2006).
11. Bank, R. A., Soudry, M., Maroudas, A., Mizrahi, J. & Tekoppele, J. M. The increased swelling and instantaneous deformation of osteoarthritic cartilage is highly correlated with collagen degradation. *Arthritis Rheum.* **43,** 2202–2210 (2000).
12. DiDomenico, C. D., Xiang Wang, Z. & Bonassar, L. J. Cyclic Mechanical Loading Enhances Transport of Antibodies Into Articular Cartilage. *J. Biomech. Eng.* **139,** 011012 (2016).
13. DiDomenico, C. D. *et al.* The Effect of Antibody Size and Mechanical Loading on Solute Diffusion Through the Articular Surface of Cartilage. *J. Biomech. Eng.* **139,** 091005 (2017).
14. DiDomenico, C. *et al.* Antibody Charge Affects Depth-Dependent Diffusion in Healthy Articular Cartilage. in *Orthopaedic Research Society* (2017).
15. Kim, S. E. *et al.* Ultrasmall nanoparticles induce ferroptosis in nutrient-deprived cancer cells and suppress tumour growth. *Nat. Nanotechnol.* **11,** 977–985 (2016).
16. Evan, P. *et al.* Biomimetic aggrecan molecularly engineers articular cartilage following intra-articular injection in an OA rabbit model in vivo: a pilot study. *Front. Bioeng. Biotechnol.* **4,** (2016).
17. Champion, J. A., Walker, A. & Mitragotri, S. Role of Particle Size in Phagocytosis of Polymeric Microspheres. *Pharm. Res.* **25,** 1815–1821 (2008).

18. Pritzker, K. P. H. *et al*. Osteoarthritis cartilage histopathology: Grading and staging. *Osteoarthr. Cartil.* **14,** 13–29 (2006).

19. Torzilli, P. A., Arduino, J. M., Gregory, J. D. & Bansal, M. Effect of proteoglycan removal on solute mobility in articular cartilage. *J. Biomech.* **30,** 895–902 (1997).

APPENDIX:

Cyclic loading based enhancement based on molecular size (using historic data):

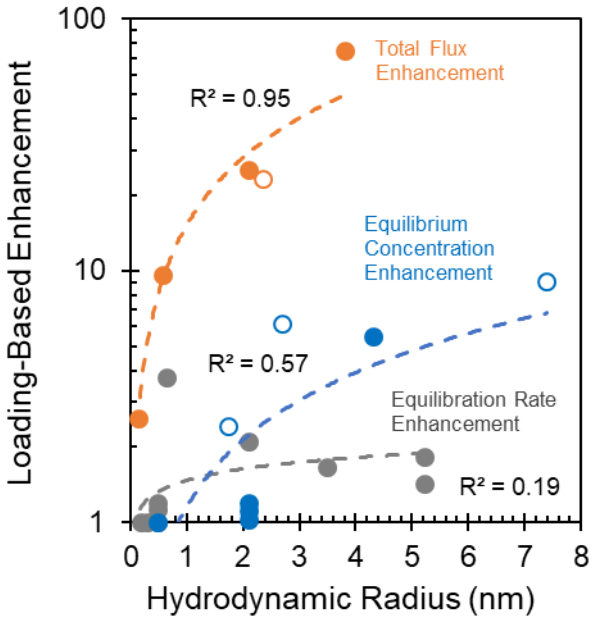

Convective transport enhancement increases drastically with solute size. Previous studies on the effects of loading or fluid convection on overall solute transport were examined for trends (summarized below). Data from convection studies were grouped into three categories that quantified solute transport enhancement in distinct ways: total flux enhancement (from 3 studies), equilibrium concentration enhancement (from 2 studies), and equilibration rate enhancement (from 5 studies). Total flux enhancement was defined as the ratio of total solute flux (convection and diffusion) to solute diffusive flux. Solute equilibrium concentration enhancement was defined as an equilibrium concentration ratio between samples undergoing mechanical loading and non-loaded samples. Studies that quantified solute diffusivities, solute equilibration times, or desorption rates between loaded and non-loaded samples were defined as the equilibration rate enhancement group. These specific data groupings included many different loading regimes that were used across the 10 total studies. Nevertheless, total flux, equilibrium concentration, and equilibration rate enhancements generally increased as the size of both linear (open points) and spherical (filled points) solutes increased (R^2: 0.19 - 0.95, power-law fit to log-transformed data).

Summary of convective transport of solutes:

Solute	MW (Da)	Radius (nm)	Frequency Loading (Hz)	Cyclic Loading Applied	Timeframe	Transport Metric	References
Equilibrium Concentration Enhancement						*Equilibrium Concentration Enhancement*	
Fluorescein	332	0.49*	0.2	10%	20 hr	1.0	[29] Albro 2011
Dextran 3K	3000	1.75	0.2	10%	20 hr	2.4	
Dextran 10K	10000	2.70	0.2	10%	20 hr	6.1	
Dextran 70K	70000	7.40	0.2	10%	20 hr	9.0	
Transferrin	80000	4.30	0.2	10%	20 hr	5.5	
Insulin-like growth factor 1 (IGF-1)	7650	2.09*	0.01-1	2%	5 hr	1.02-1.04	[117] Zhang 2007
Insulin-like growth factor 1 (IGF-1)	7650	2.09*	0.01-1	6%	5 hr	1.07-1.16	
Insulin-like growth factor 1 (IGF-1)	7650	2.09*	0.01-1	10%	5 hr	1.12-1.28	
Equilibration Rate Enhancement						*Enhancement in Desorption Rate*	
2-NBDG	342	0.49*	0.0006	5-50%	0.5 hr	0.9-1.07	[58] Evans 2006
2-NBDG	342	0.49*	0.01	5-50%	0.5 hr	1.07-1.18	
2-NBDG	342	0.49*	0.1	5-50%	0.5 hr	1.05-1.35	
Urea	60	0.18	1	2.8 MPa	1 hr	~1.0	[59] Ohara 1990
Sodium Iodide	127	0.31*	1	2.8 MPa	1 hr	~1.0	
Serum Albumin	66000	3.48	1	2.8 MPa	1 hr	1.3-2.0	
						Diffusivity Enhancement	
Antibody (IgG)	150000	5.22	1	0.25-5%	3 hr	1.23-2.40	[140] DiDomenico 2016
Antibody (IgG)	150000	5.22	0.25-2.6	2.50%	3 hr	0.95-1.91	
						Enhancement in Equilibrium Time Constant	
Iothalamate	613	0.65*	1	10%	1 hr	3.75	[119] Entezari 2014
Insulin-like growth factor 1 (IGF-1)	7650	2.09*	0.1	2%	6 hr	2.1	[42] Bonassar 2001
Total Flux Enhancement						*Total Flux Enhancement*	
$^3H_20$	18	0.13*	N/A	26 mA/cm^2 (current density)	2 hr	2.6	[31] Garcia 1996
Raffinose	594	0.57	N/A	26 mA/cm^2	2 hr	9.6	[31] Garcia 1996
Insulin-like growth factor 1 (IGF-1)	7650	2.09*	N/A	26 mA/cm^2	2 hr	25	[54] Garcia 2003
Dextran 10K	10000	2.36	N/A	26 mA/cm^2	2 hr	23	[31] Garcia 1996
Tissue inhibitor of metalloproteinases (TIMP-1)	28000	3.80*	N/A	17.4 mA/cm^2	2 hr	75	[120] Garcia 1998

*: empirical relationship ($r_s = 0.0332MW^{0.463}$, [138]), was used to estimate hydrodynamic radius.

Diffusion of variously-sized aggrecan mimetics (Drexel University Collaboration):

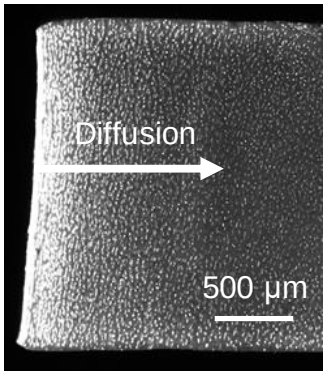

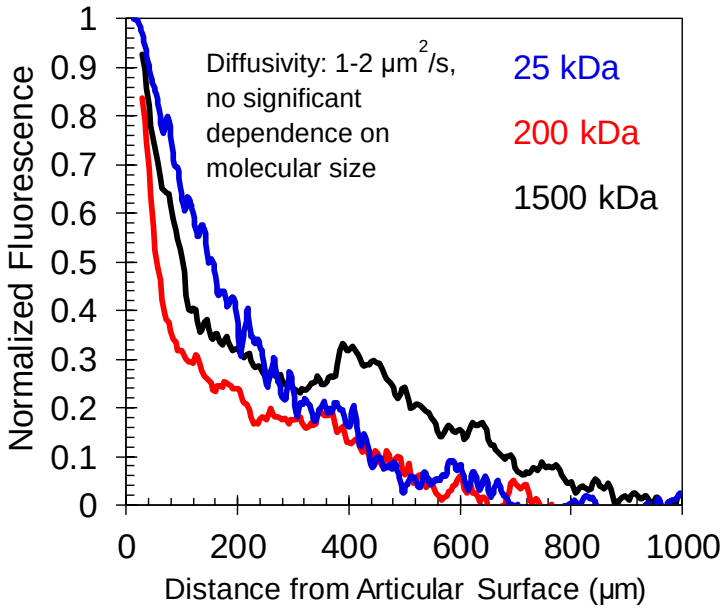

Diffusion of nanoparticles (Material Science Collaboration):

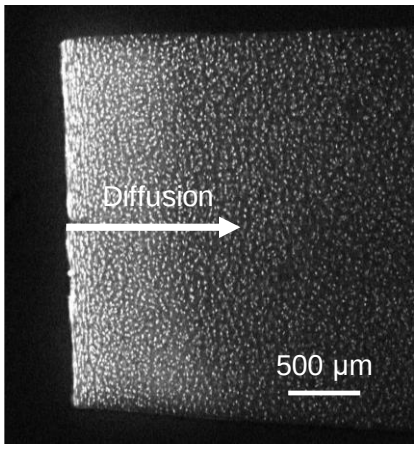

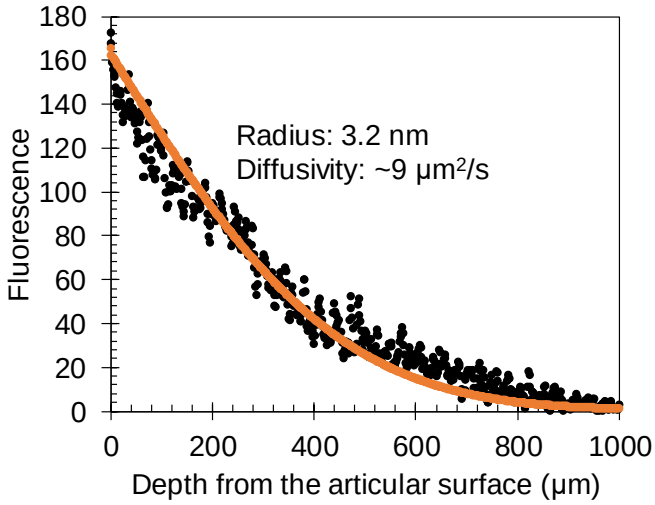

Multi-layer diffusion code for Matlab:

```
function [ucorrected,sumsquarederror] =
ModifiedMultDiff(m,kappa,l0,lm,l,u0,Lbnd,Rbnd,tspan,interface,varargi
n)
% MULTDIFF Solves the one-dimensional multilayer diffusion problem
using a
%                 Semi-Analytic method.
```

```
%
%   MULTDIFF solves the transient diffusion equation in a one-
dimensional
%   composite slab of finite length consisting of multiple layers.
The code
%   is applicable to both perfect and imperfect contact at the
interfaces
%   between adjacent layers and either Dirichlet, Neumann or Robin
boundary
%   conditions at the ends of the slab.
%
%   MULTDIFF is an implementation of the semi-analytic method
%   proposed by Carr and Turner based on the Laplace Transform and an
%   orthogonal eigenfunction expansion.
%
%   Full details can be found in the paper:
%   E. J. Carr and I. W. Turner.
%
%   Description:
%   ------------------------------------------------------------------
------
%   MULTDIFF solves the standard diffusion equation in each layer
%   (l(i-1) < x < l(i)):
%
%      du_(i)/dt = d/dx * (kappa(i) * du_(i)/dx),   i = 1,...,m,
%
%   subject to the following initial and external boundary
conditions:
%
%      u_(i)(x,t) = u0(x)                              at t = 0
%      aL * u_(1)(x,t) + bL * du_(1)/dx(x,t) = cL   at x = l0
%      aR * u_(m)(x,t) + bR * du_(m)/dx(x,t) = cR   at x = lm
%
%   where u_(i) is the solution in layer i, kappa(i) is the
diffusivity in
%   layer i (constant) and aL, bL, cL, aR, bR and cR are constants.
%
%   Either perfect or imperfect contact is imposed at the interfaces
%   between adajacent layers (at x = l(i), i = 1,...,m-1):
%
%    - Perfect contact
%       u_(i)(x,t) = u_(i+1)(x,t)
%       kappa(i) * u_(i)(x,t) = kappa(i+1) * u_(i+1)(x,t)
%
%    - Imperfect contact
%       kappa(i) * du_(i)/dx(x,t) = H(i) * (u_(i+1)(x,t) -
u_(i)(x,t))
%       kappa(i+1) * du_(i+1)/dx(x,t) = H(i) * (u_(i+1)(x,t) -
u_(i)(x,t))
%
%   Usage:
%   ------------------------------------------------------------------
------
%   [U,X] = multdiff(m,kappa,l0,lM,l,u0,bcs,tspan,'Perfect')
%   [U,X] = multdiff(m,kappa,l0,lM,l,u0,bcs,tspan,'Perfect',options)
```

```
%   [U,X] = multdiff(m,kappa,l0,lM,l,u0,bcs,tspan,'Imperfect',H)
%   [U,X] =
multdiff(m,kappa,l0,lM,l,u0,bcs,tspan,'Imperfect',H,options)
%
%   Input Arguments:
%   ----------------------------------------------------------------
------
%   m           Number of layers. Must be an integer greater than or
equal
%               to 3.
%   kappa       A vector of length M containing the diffusivity
values
%               in each layer such that the diffusivity in Layer i is
given
%               by kappa(i) (i = 1,...,m).
%   l0          x coordinate of the left boundary of the slab
%   lm          x coordinate of the right boundary of the slab
%   l           A vector of length M-1 containing the locations of
the
%               interfaces between adjacent layers such that the
interface
%               between Layer i and Layer i+1 is located at L(i)
%               (i = 1,...,m-1).
%   u0          A function handle specifying the initial condition.
The
%               function uint = u0(X) should accept a vector argument
x and
%               return a vector result uint. Use array operators .*,
./ and
%               .^ in the definition of u0 so that it can be
evaluated with
%               a vector argument.
%   Lbnd        A cell array specifying the boundary condition at the
x=l0.
%               Lbnd takes the form {type,aL,bL,cL}, where type is
one of
%                    'Dirichlet': aL ~= 0 and bL = 0
%                    'Neumann':   aL = 0 and bL ~= 0
%                    'Robin':     aL ~= 0 and bL ~= 0
%   Rbnd        A cell array specifying the boundary condition at the
x=lm.
%               Rbnd takes the form {type,aR,bR,cR}, where type is
one of
%                    'Dirichlet': aR ~= 0 and bR = 0
%                    'Neumann':   aR = 0 and bR ~= 0
%                    'Robin':     aR ~= 0 and bR ~= 0
%   tspan       A vector specifying the times at which a solution is
%               requested. To obtain solutions at specific times
%               t0,t1,...,tf, use TSPAN = [t0,t1,...,tf].
%   interface   Internal boundary conditions at interfaces between
adjacent
%               layers. inteface can be either 'Perfect' or
'Imperfect'.
%   H           A vector of length m-1 containing the contact
```

```
%               transfer coeffecients at the interfaces between
adjacent
%               layers such that the coefficient between layer i and
%               layer i+1 is given by H(i) (i = 1,..,m-1).
%               * Applicable to imperfect contant only.
%   options     An (optional) set of solver options. Fields in the
%               structure options are
%                - N    number of eigenvalues to use in expansions
%                       [N = 50 by default]
%                - NX   number of divisions within each slab. U(:,j)
gives
%                       the solution at x = l(i-1):(l(i)-l(i-
1))/NX:l(i)
%                       and t = tspan(j).
%                       [NX = 50 by default]
%                - NZ   number of poles in CF method (see cf.m)
%                       [NZ = 14 by default]
%                - Hp   value of contact transfer coefficient to
%                       approximate perfect contact condition
%                       [Hp = 1e6 by default]
%
%   Output Arugments:
%   -----------------------------------------------------------------
------
%   u   Matrix of solution values. u(:,j) gives the solution on the
entire
%       slab (l0 <= x <= lm) at time t = tspan(j) and at the grid
points
%       returned in the output vector x.
%   x   Vector of grid points at which solution is given. x is a
vector
%       taking the form x = [x1,x2,...,xm]', where:
%          x1 = l0:(l(1)-l0)/NX:l(1)
%          xi = l(i-1):(l(i)-l(i-1))/NX:l(i), i = 2,..,m-1
%          xm = l(m-1):(lm-l(m-1))/NX:lm
%
%   Example:
%   -----------------------------------------------------------------
------
%   u0 = @(x) zeros(size(x));
%   [u,x] = multdiff(3,[1,0.1,1],0.0,1.0,[0.3,0.7],u0,...
%          {'Dirichlet',1.0,0.0,1.0},{'Dirichlet',1.0,0.0,0.5},...
%          [0.02,0.05,0.1,0.2,0.5,1.0],'Perfect');
%

% Default values
AbsTol = 1e-10;
RelTol = 1e-6;

% AbsTol = 1e-14;
% RelTol = 1e-10;

% -----------------------------------------------------------------
------
% Check inputs
```

```
% ------------------------------------------------------------------
------
if nargin < 10
    error('Not enough input arguments.');
elseif nargin == 10
    if strcmp(interface,'Imperfect')
        error('H must be specified for imperfect contact at
interfaces.');
    end
    options = struct;
elseif nargin == 11
    if strcmp(interface,'Perfect')
        options = varargin{1};
    elseif strcmp(interface,'Imperfect')
        H = varargin{1};
        options = struct;
    end
elseif nargin == 12
    if strcmp(interface,'Perfect')
        error('Too many input arguments for interface =
''Perfect''.');
    elseif strcmp(interface,'Imperfect')
        H = varargin{1};
        options = varargin{2};
    end
else
    error('Too many input arguments.');
end

% Number of layers
if round(m) ~= m || m < 3
    error('m must be an integer greater than or equal to 3.')
end

% Diffusivities
if length(kappa) ~= m || sum(kappa > 0) ~= m
    error('kappa must be a vector of length m with kappa(i)>0.')
end

% Slab left and right boundary
if l0 > lm
    error('l0 must be less than lm.')
end

% Interfaces
if length(l) ~= m-1 || sum(diff(l)>0) ~= m-2
    error('l must be a vector of length m-1 with with increasing
values.')
elseif l(1) <= l0 || l(m-1) >= lm
    error('l(1) must be greater than l0 and l(m-1) must be less than
lm.');
end

% Initial condition
```

```
if ~isa(u0,'function_handle') || nargin(u0) ~= 1
    error('u0 must be a function handle of the form uint = u0(x).');
end

% Boundary conditions
if ~isa(Lbnd,'cell') || length(Lbnd) ~= 4
    error(['Lbnd must be a cell array of length 4.']);
end
if ~isa(Rbnd,'cell') || length(Rbnd) ~= 4
    error(['Rbnd must be a cell array of length 4.']);
end

% Time vector
tlength = length(tspan);
if sum(tspan > 0) ~= tlength
    error('tspan must have entries that are greater than or equal to
0.')
end

% Internal boundary conditions at interfaces
if strcmp(interface,'Perfect') || strcmp(interface,'Imperfect')
else
    error('interface must be either ''Perfect'' or ''Imperfect''.')
end

% Check options structure
if ~isa(options,'struct')
    error('options must be a structure.')
end
Names = {'N','NX','NZ','Hp'};
fn = fieldnames(options);
for i = 1:length(fn)
    j = strcmp(fn(i),Names);
    if sum(j) == 0
        error('Invalid option ''%s''.',fn{i});
    end
end
% Number of eigenvalues to use in expansions
if isfield(options,'N')
    N = options.N;
    if round(N) ~= N && N < 1
        error('options.N must be an integer greater than or equal to
1.')
    end
else
    N = 50; % Default
end
% Number of divisions within each slab
if isfield(options,'NX')
    NX = options.NX;
    if round(NX) ~= NX && NX < 1
        error('options.NX must be an integer greater than or equal to
1.')
    end
else
```

```
    NX = 250; % Default
end
% Number of poles in CF method (see cf.m)
if isfield(options,'NZ'),
    NZ = options.NZ;
    if round(NZ) ~= NZ && NX < 1
        error('options.NZ must be an integer greater than or equal to
1.')
    end
else
    NZ = 14; % Default
end
% Value of contact transfer coefficient to approximate perfect
contact
% condition
if isfield(options,'Hp')
    if strcmp(interface,'Perfect')
        Hp = options.Hp;
        if Hp < 0
            error('options.Hp must be greater than or equal to 0.')
        end
    else
        warning('options.Hp is specified but not used.')
    end
else
    Hp = 1.0e6; % Default
end
if strcmp(interface,'Perfect')
    H = Hp*ones(m-1,m);
end

% Get boundary condition constants
Ltype = Lbnd{1};
Rtype = Rbnd{1};
aL    = Lbnd{2};
bL    = Lbnd{3};
cL    = Lbnd{4};
aR    = Rbnd{2};
bR    = Rbnd{3};
cR    = Rbnd{4};

% Check boundary conditions are implemented correctly
if sum(strcmp(Ltype,{'Dirichlet','Neumann','Robin'})) == 0
    error(['Boundary condition at left boundary must be one of
either',...
        ' ''Dirichlet'', ''Neumann'' or ''Robin''.']);
end
if sum(strcmp(Rtype,{'Dirichlet','Neumann','Robin'})) == 0
    error(['Boundary condition at right boundary must be one of
either',...
        ' ''Dirichlet'', ''Neumann'' or ''Robin''.']);
end
if aL == 0 && strcmp(Ltype,'Dirichlet')
    error('Dirichlet condition at left boundary cannot have aL =
0.');
```

```
end
if bL == 0 && strcmp(Ltype,'Neumann')
    error('Neumann condition at left boundary cannot have bL = 0.');
end
if aR == 0 && strcmp(Rtype,'Dirichlet')
    error('Dirichlet condition at right boundary cannot have aR =
0.');
end
if bR == 0 && strcmp(Rtype,'Neumann')
    error('Neumann condtion at right boundary cannot have bR = 0.');
end
if strcmp(Ltype,'Dirichlet') && bL ~= 0
    error('Dirichlet condition at left boundary cannot have bL =
0.');
end
if strcmp(Rtype,'Dirichlet') && bR ~= 0
    error('Dirichlet condition at right boundary cannot have bR =
0.');
end
if strcmp(Ltype,'Neumann') && aL ~= 0
    error('Neumann condition at left boundary cannot have aL = 0.');
end
if strcmp(Rtype,'Neumann') && aR ~= 0
    error('Neumann condition at right boundary cannot have aR = 0.');
end
if (aL == 0 || bL == 0) && strcmp(Ltype,'Robin')
    error('Robin condition at left boundary cannot have aL = 0 or bL
= 0');
end
if (aR == 0 || bR == 0) && strcmp(Rtype,'Robin')
    error('Robin condition at left boundary cannot have aR = 0 or bR
= 0');
end
if strcmp(Ltype,'Robin') && aL/bL < 0
    warning('Robin condition at left boundary must have aL/bL > 0.');
end
if strcmp(Rtype,'Robin') && aR/bR < 0
    warning('Robin condition at right boundary must have aR/bR >
0.');
end
if aL == 0 && bL == 0
    error('Boundary condition is incorrect at left boundary (aL = bL
= 0).')
end
if aR == 0 && bR == 0
    error('Boundary condition is incorrect at left boundary (aR = bR
= 0).')
end

if strcmp(Ltype,'Neumann') && strcmp(Rtype,'Neumann') && ...
        (kappa(1)*bR*cL + kappa(m)*bL*cR) ~= 0
    error(['If Neumann boundary conditions are applied at both ends
then ', ...
        'kappa(1)*bR*cL + kappa(m)*bL*cR must be equal to zero.'])
end
```

```
% ------------------------------------------------------------------
------
% Compute function w(x) that satisfies non-homogeneous BCs
%
% Slab 1:
% w1(x) = w(1) + w(2)*x            for Dirichlet, Robin
% w1(x) = w(1)*x + w(2)*x^2        for Neumann
%
% Slab i = 2,..,m-1:
% wi(x) = w(2*i-1) + w(2*i)*x      for Dirichlet, Robin, Neumann
%
% Slab m:
% wm(x) = w(2*m-1) + w(2*m)*x      for Dirichlet, Robin
% wm(x) = w(2*m-1)*x + w(2*m)*x^2  for Neumann
%
% So we want to solve the linear system of equations:
%
%  kappa(1)*w_(1)'(l(1)) = H(1)*(w_(2)(l(1)) - w_(1)(l(1))
%  kappa(1)*w_(1)'(l(1)) = kappa(2)w_(2)'(l(1))
%                     .
%                     .
%                     .
%  kappa(m-1)*w_(m-1)'(l(m-1)) = H(m-1)*(w_(m)'(l(m-1))-w_(m-1)'(l(m-
1)))
%  kappa(m-1)*w_(m-1)'(l(m-1)) = kappa(m) * w_(m)'(l(m-1))
%  aL * w_(1)(l0) + bL * w_(1)'(l0) = cL
%  aR * w_(m)(lm) + bR * w_(m)'(lm) = cR
% ------------------------------------------------------------------
------

A = zeros(2*m,2*m);
b = zeros(2*m,1);

% if strcmp(Ltype,'Neumann') && strcmp(Rtype,'Neumann')
%
%     % Interface conditions
%     for i = 1:m-1
%         A(2*i-1,2*i-1) = l(i)+1/H(i)*kappa(i);
%         A(2*i-1,2*i)   = 2*kappa(i)*l(i)/H(i)+l(i)^2;
%         A(2*i-1,2*i+1) = -l(i);
%         A(2*i-1,2*i+2) = -l(i)^2;
%         b(2*i-1) = 0;
%
%         A(2*i,2*i-1) = kappa(i);
%         A(2*i,2*i) = 2*kappa(i)*l(i);
%         A(2*i,2*i+1) = -kappa(i+1);
%         A(2*i,2*i+2) = -2*kappa(i+1)*l(i);
%         b(2*i) = 0;
%     end
%
%     % Right boundary condition
%     A(2*m-1,2*m)   = 2*bR*lm;
%     A(2*m-1,2*m-1) = bR;
```

```
%     b(2*m-1)       = cR;
%
%     % Left boundary condition
%     A(2*m,1) = bL;
%     b(2*m)   = cL;


% else

    % Interface conditions
    for i = 1:m-1
        A(2*i-1,2*i-1) = 1.0;
        A(2*i-1,2*i)   = (kappa(i)/H(i)) + l(i);
        A(2*i-1,2*i+1) = -1.0;
        A(2*i-1,2*i+2) = -l(i);
        b(2*i-1)       = 0.0;

        A(2*i,2*i)   = kappa(i);
        A(2*i,2*i+2) = -kappa(i+1);
        b(2*i)       = 0.0;
    end

    % Right boundary condition
    A(2*m-1,2*m)   = bR+aR*lm;
    A(2*m-1,2*m-1) = aR;
    b(2*m-1)       = cR;

    % Left boundary condition
    A(2*m,1) = aL;
    A(2*m,2) = -bL+aL*l0;
    b(2*m)   = cL;

% end

if strcmp(Ltype,'Neumann') && strcmp(Rtype,'Neumann')
    i = 1;
    A(2*m+1,2*i-1) = l(1) - l0;
    A(2*m+1,2*i)   = (l(1)^2-l0^2)/2;
    b(2*m+1)       =
integral(u0,l0,l(1),'AbsTol',AbsTol,'RelTol',RelTol);
    for i = 2:m-1
        A(2*m+1,2*i-1) = l(i)-l(i-1);
        A(2*m+1,2*i)   = (l(i)^2-l(i-1)^2)/2;
        b(2*m+1)       = b(2*m+1) + integral(u0,l(i-
1),l(i),'AbsTol',AbsTol,'RelTol',RelTol);
    end
    i = m;
    A(2*m+1,2*i-1) = lm-l(m-1);
    A(2*m+1,2*i)   = (lm^2-l(m-1)^2)/2;
    b(2*m+1)       = b(2*m+1) + integral(u0,l(m-
1),lm,'AbsTol',AbsTol,'RelTol',RelTol);
end
```

```
w = A\b;
% pause;
% w = 0.5*ones(size(w))
% pause;

% ------------------------------------------------------------------------
------
% Eigenvalues
% ------------------------------------------------------------------------
------
eigs = zeros(N,m);

% Slab 1 (First slab)
switch Ltype
    case 'Dirichlet'
        eigs(:,1) = (2*[0:N-1]+1)'*pi/(2*(l(1)-l0));
    case 'Neumann'
        eigs(:,1) = [0:N-1]'*pi/(l(1)-l0);
    case 'Robin'
        eigs(:,1) = eigvals(l(1),l0,aL/bL,N);
end

% Slab 2,..., m-1 (Middle slabs)
for i = 2:m-1
    eigs(:,i) = [0:N-1]'*pi/(l(i)-l(i-1));
end

% Slab m (End slab)
switch Rtype
    case 'Dirichlet'
        eigs(:,m) = (2*[0:N-1]+1)'*pi/(2*(lm-l(m-1)));
    case 'Neumann'
        eigs(:,m) = [0:N-1]'*pi/(lm-l(m-1));
    case 'Robin'
        eigs(:,m) = eigvals(lm,l(m-1),aR/bR,N);
end

% ------------------------------------------------------------------------
------
% Eigenfunction normalisation constants
% ------------------------------------------------------------------------
------
eigs_norm = zeros(N,m);

% Slab 1 (First slab)
for n = 1:N

    if strcmp(Ltype,'Dirichlet')
        eigs_norm(n,1) = sqrt(2/(l(1)-l0));
    elseif strcmp(Ltype,'Neumann')
        if n == 1
            eigs_norm(n,1) = sqrt(1/(l(1)-l0));
        else
```

```
            eigs_norm(n,1) = sqrt(2/(l(1)-l0));
        end
    elseif strcmp(Ltype,'Robin')
        lambda = eigs(n,1);
        eigs_norm(n,1) = sqrt((2*(1+(bL^2/aL^2)*lambda^2))/...
            ((bL/aL)+(l(1)-l0)*(1+(bL^2/aL^2)*lambda^2)));
    end

end

% Slab 2,..., m-1 (Middle slabs)
for i = 2:m-1
    eigs_norm(1,i) = sqrt(1/(l(i)-l(i-1)));
    for n = 2:N
        eigs_norm(n,i) = sqrt(2/(l(i)-l(i-1)));
    end
end

% Slab m (End slab)
for n = 1:N

    if strcmp(Rtype,'Dirichlet')
        eigs_norm(n,m) = sqrt(2/(lm-l(m-1)));
    elseif strcmp(Rtype,'Neumann')
        if n == 1
            eigs_norm(n,m) = sqrt(1/(lm-l(m-1)));
        else
            eigs_norm(n,m) = sqrt(2/(lm-l(m-1)));
        end
    elseif strcmp(Rtype,'Robin')
        lambda = eigs(n,m);
        eigs_norm(n,m) = sqrt((2*(1+(bR^2/aR^2)*lambda^2))/...
            ((bR/aR)+(lm-l(m-1))*(1+(bR^2/aR^2)*lambda^2)));
    end

end

% eigs_norm

% ------------------------------------------------------------------
------
% Grid spacing within each slab
% ------------------------------------------------------------------
------
xgrid = zeros(NX+1,m);

% Slab 1 (First slab)
xgrid(:,1) = l0:(l(1)-l0)/NX:l(1);

% Slabs 2,...,m
for i = 2:m-1
    xgrid(:,i) = l(i-1):(l(i)-l(i-1))/NX:l(i);
end
```

```
% Slab m (First slab)
xgrid(:,m) = l(m-1):(lm-l(m-1))/NX:lm;

% ------------------------------------------------------------------
------
% Initial conditions - expand in terms of eigenfunctions
% ------------------------------------------------------------------
------
c = zeros(N,m); % Coefficients

% Slab 1 (First slab)
for n = 1:N
    lambda = eigs(n,1);
    prod = @(x) (u0(x)-wfunc(1,Ltype,Rtype,x,m,w)) .* ...
        eigfunc(lambda,1,Ltype,Rtype,x,m,l0,lm,l);
    c(n,1) =
eigs_norm(n,1)*integral(prod,l0,l(1),'AbsTol',AbsTol,'RelTol',RelTol)
;
end

% Slabs 2,...,m
for i = 2:m-1
    for n = 1:N
        lambda = eigs(n,i);
        prod = @(x) (u0(x)-wfunc(i,Ltype,Rtype,x,m,w)) .* ...
            eigfunc(lambda,i,Ltype,Rtype,x,m,l0,lm,l);
        c(n,i) = eigs_norm(n,i)*integral(prod,l(i-
1),l(i),'AbsTol',AbsTol,'RelTol',RelTol);
    end
end

% Slab m
for n = 1:N
    lambda = eigs(n,m);
    prod = @(x) (u0(x)-wfunc(m,Ltype,Rtype,x,m,w)) .* ...
        eigfunc(lambda,m,Ltype,Rtype,x,m,l0,lm,l);
    c(n,m) = eigs_norm(n,m)*integral(prod,l(m-
1),lm,'AbsTol',AbsTol,'RelTol',RelTol);
end
% wfunc(1,Ltype,Rtype,x,m,w)
% wfunc(m,Ltype,Rtype,x,m,w)
% c

% Plot initial condition
u = zeros(NX+1,m);
for n = 1:N
    for i = 1:m
        lambda = eigs(n,i);
        u(:,i) = u(:,i)+c(n,i)*...
            eigs_norm(n,i)*...
            eigfunc(lambda,i,Ltype,Rtype,xgrid(:,i),m,l0,lm,l);
    end
end
```

```
usoln = reshape(u,(NX+1)*m,1);
x = reshape(xgrid,(NX+1)*m,1);

% % % figure;
% % % % for i = 1:m
% % % %     uint(:,i) = u0(xgrid(:,i))-
wfunc(i,Ltype,Rtype,xgrid(:,i),m,w);
% % % % end
% % % % for i = 1:m
% % % %     u(:,i) = u(:,i) + wfunc(i,Ltype,Rtype,xgrid(:,i),m,w);
% % % % end
% % % usoln = reshape(u,(NX+1)*m,1);
% % % plot(x,usoln,'r')
% % % % hold on
% % % %plot(x,reshape(uint,(NX+1)*m,1),'b')
% % % drawnow
% % % hold off
% % % % pause;

% eigs
% pause;

% norm(u(end,1)-u(1,2),inf)
% pause;

% Get weights and poles for use in inverse transform
[zk,ck] = cf(NZ);

usoln = zeros((NX+1)*m,tlength);

% Time loop
for j = 1:tlength

    t = tspan(j);

    % Solution (at given time)
    u = zeros(NX+1,m);

    for i = 1:m
        u(:,i) = wfunc(i,Ltype,Rtype,xgrid(:,i),m,w);
    end

%     if strcmp(Ltype,'Neumann') && strcmp(Rtype,'Neumann')
%         u(:,1) = u(:,1)+2*kappa(1)*w(2)*sqrt(l(1)-l0)*t;
%         for i = 2:m-1
%             u(:,i) = u(:,i)+2*kappa(i)*w(2*i)*sqrt(l(i)-l(i-1))*t;
%         end
%         u(:,m) = u(:,m)+2*kappa(m)*w(2*m)*sqrt(lm-l(m-1))*t;
%     end

    % Compute inverse Laplace transform of interface functions
    vbar = zeros(m-1,NZ/2);
```

```
    for k = 1:NZ/2

        A    = zeros(m-1,m-1);
        vr   = zeros(m-1,1);
        b    = zeros(m-1,1);

        poles = 2*k-1;
        s = zk(poles)/t;

%         if strcmp(Ltype,'Neumann') && strcmp(Rtype,'Neumann')
%             b(1) =  2*kappa(2)*w(4)*sqrt(l(2)-l(1))/s^2 ...
%                 -2*kappa(1)*w(2)*sqrt(l(1)-l0)/s^2;
%             for i = 2:m-2
%                 b(i) = 2*kappa(i+1)*w(2*(i+1))*sqrt(l(i+1)-
l(i))/s^2 ...
%                     -2*kappa(i)*w(2*i)*sqrt(l(i)-l(i-1))/s^2;
%             end
%             b(m-1) = 2*kappa(m)*w(2*m)*sqrt(lm-l(m-1))/s^2 ...
%                -2*kappa(m-1)*w(2*(m-1))*sqrt(l(m-1)-l(m-2))/s^2;
%         end

        for n = 1:N

            % Interface 1 (between layers 1 and 2)
            lambda = eigs(n,1);
            phin_r = eigfunc(lambda,1,Ltype,Rtype,l(1),m,l0,lm,l);
            s1     = s+kappa(1)*lambda^2;
            A(1,1) = A(1,1)+eigs_norm(n,1)^2*phin_r*phin_r/s1;
            b(1)   = b(1)-c(n,1)*eigs_norm(n,1)*phin_r/s1;

            lambda = eigs(n,2);
            phin_l = eigfunc(lambda,2,Ltype,Rtype,l(1),m,l0,lm,l);
            phin_r = eigfunc(lambda,2,Ltype,Rtype,l(2),m,l0,lm,l);
            s2     = s+kappa(2)*lambda^2;
            A(1,1) = A(1,1)+eigs_norm(n,2)^2*phin_l*phin_l/s2;
            A(1,2) = A(1,2)-eigs_norm(n,2)^2*phin_l*phin_r/s2;
            b(1)   = b(1)+c(n,2)*eigs_norm(n,2)*phin_l/s2;

            % Middle interfaces
            for i = 2:m-2
                lambda   = eigs(n,i);
                phin_l   = cos(lambda*(l(i)-l(i-1)));
                phin_r   = 1.0;
                s1       = s+kappa(i)*lambda^2;
                A(i,i-1) = A(i,i-1)-
eigs_norm(n,i)^2*phin_l*phin_r/s1;
                A(i,i)   = A(i,i)+eigs_norm(n,i)^2*phin_r*phin_r/s1;
                b(i)     = b(i)-c(n,i)*eigs_norm(n,i)*phin_r/s1;

                lambda   = eigs(n,i+1);
                phin_l   = cos(lambda*(l(i+1)-l(i)));
                phin_r   = 1.0;
                s2       = s+kappa(i+1)*lambda^2;
```

```
                A(i,i)   =
A(i,i)+eigs_norm(n,i+1)^2*phin_l*phin_l/s2;
                A(i,i+1) = A(i,i+1)-
eigs_norm(n,i+1)^2*phin_r*phin_l/s2;
                b(i)     = b(i)+c(n,i+1)*eigs_norm(n,i+1)*phin_l/s2;
            end

            % Interface m (between layers m and m-1)
            lambda     = eigs(n,m-1);
            phin_l     = eigfunc(lambda,m-1,Ltype,Rtype,l(m-
2),m,l0,lm,l);
            phin_r     = eigfunc(lambda,m-1,Ltype,Rtype,l(m-
1),m,l0,lm,l);
            s2         = s+kappa(m-1)*lambda^2;
            A(m-1,m-2) = A(m-1,m-2)-eigs_norm(n,m-
1)^2*phin_l*phin_r/s2;
            A(m-1,m-1) = A(m-1,m-1)+eigs_norm(n,m-
1)^2*phin_r*phin_r/s2;
            b(m-1)     = b(m-1)-c(n,m-1)*eigs_norm(n,m-1)*phin_r/s2;

            lambda     = eigs(n,m);
            phin_l     = eigfunc(lambda,m,Ltype,Rtype,l(m-
1),m,l0,lm,l);
            s1         = s+kappa(m)*lambda^2;
            A(m-1,m-1) = A(m-1,m-
1)+eigs_norm(n,m)^2*phin_l*phin_l/s1;
            b(m-1)     = b(m-1)+c(n,m)*eigs_norm(n,m)*phin_l/s1;

        end

        for i = 1:m-1
            A(i,i) = A(i,i)+(1.0/H(i));
        end

        % Laplace transform of v evaluated at zk(poles)/t
        vbar(:,k) = A\b;
%         norm(b - A*vbar(:,k),'inf');
%         pause;
        %vbar(:,k) = zeros(size(b));

    end

    % Form the sums corresponding to interfaces
    for n = 1:N

        % Compute inverse Laplace transform of
v(1)/(s+kappa*lambda^2)
        lambda = eigs(n,1);
        vr(1) = 0;
        for k = 1:NZ/2
            poles = 2*k-1;
            s = zk(poles)/t;
            vr(1) = vr(1)-...
                ck(poles)*vbar(1,k)/(t*(s+kappa(1)*lambda^2));
```

```
        end
        vr(1) = 2*real(vr(1));
        u(:,1)  = u(:,1)+eigs_norm(n,1)^2*vr(1)*...
            eigfunc(lambda,1,Ltype,Rtype,l(1),m,l0,lm,l)*...
            eigfunc(lambda,1,Ltype,Rtype,xgrid(:,1),m,l0,lm,l);
%         n
%         abs(eigs_norm(n,1)^2*vr(1)*...
%             eigfunc(lambda,1,Ltype,Rtype,l(1),m,l0,lm,l)*...
%             eigfunc(lambda,1,Ltype,Rtype,xgrid(:,1),m,l0,lm,l))
%         pause;

        for i = 2:m-1
            lambda = eigs(n,i);
            vr(i-1) = 0;
            for k = 1:NZ/2
                poles = 2*k-1;
                s = zk(poles)/t;
                vr(i-1) = vr(i-1)-...
                    ck(poles)*vbar(i-1,k)/(t*(s+kappa(i)*lambda^2));
            end
            vr(i-1) = 2*real(vr(i-1));
            u(:,i) = u(:,i)-eigs_norm(n,i)^2*vr(i-1)*...
                eigfunc(lambda,i,Ltype,Rtype,l(i-1),m,l0,lm,l)*...
                eigfunc(lambda,i,Ltype,Rtype,xgrid(:,i),m,l0,lm,l);
            vr(i) = 0;
            for k = 1:NZ/2
                poles = 2*k-1;
                s = zk(poles)/t;
                vr(i) = vr(i)-ck(poles)*...
                    vbar(i,k)/(t*(s+kappa(i)*lambda^2));
            end
            vr(i) = 2*real(vr(i));
            u(:,i) = u(:,i)+eigs_norm(n,i)^2*vr(i)*...
                eigfunc(lambda,i,Ltype,Rtype,l(i),m,l0,lm,l)*...
                eigfunc(lambda,i,Ltype,Rtype,xgrid(:,i),m,l0,lm,l);
        end

        % Compute inverse Laplace transform of v(m-
1)/(s+kappa*lambda^2)
        lambda = eigs(n,m);
        vr(m-1) = 0;
        for k = 1:NZ/2
            poles = 2*k-1;
            s = zk(poles)/t;
            vr(m-1) = vr(m-1)-ck(poles)*...
                vbar(m-1,k)/(t*(s+kappa(m)*lambda^2));
        end
        vr(m-1) = 2*real(vr(m-1));
        u(:,m) = u(:,m)-eigs_norm(n,m)^2*vr(m-1)*...
            eigfunc(lambda,m,Ltype,Rtype,l(m-1),m,l0,lm,l)*...
            eigfunc(lambda,m,Ltype,Rtype,xgrid(:,m),m,l0,lm,l);
    end

%     u = zeros(size(u));
    % Form the sums corresponding to initial condition
```

```
    for n = 1:N
        % Slabs 1,..,m
        for i = 1:m
            lambda = eigs(n,i);
            u(:,i) = u(:,i)+exp(-t*kappa(i)*lambda^2)*c(n,i)*...
                eigs_norm(n,i)*...
                eigfunc(lambda,i,Ltype,Rtype,xgrid(:,i),m,l0,lm,l);
%             if i == 1
%                 n
%                 exp(-t*kappa(i)*lambda^2)*c(n,i)*...
%                 eigs_norm(n,i)*...
%                 eigfunc(lambda,i,Ltype,Rtype,xgrid(:,i),m,l0,lm,l)
%                 pause;
%             end
        end
    end

    usoln(:,j) = reshape(u,(NX+1)*m,1);

end
global ASDIFFCORRECTED sumsquarederror ErrorBro ucorrected
u = usoln;
x = reshape(xgrid,(NX+1)*m,1);


% n = numel(u);
% ucorrected = interp1(1:n, u, linspace(1,n, 1000/numel(u)*n),
'nearest');
%
% hh = size(ucorrected);
% for i=1:hh(2)
%     ErrorBro(1,i) = (abs(ucorrected(i) - ASDIFFCORRECTED(i))).^2;
% end
% sumsquarederror = sum(ErrorBro);
% plot(ucorrected)
% hold on
% plot(ASDIFFCORRECTED)
```

```
function [zk,ck] = cf(n)
% Computes the poles zk and residues ck by the Caratheodory-Fejer
method
% for the type (n,n) best approximation to exp(z) on the negative
real
% line.
%
% For full details see:
% J. A. C. Weideman L. N. Trefethen and T. Schmelzer (2006) Talbot
% quadratures and rational approximations. BIT Numer. Math., 46:653-
670.
%
% The following code is given in Figure 4.1 of the above paper.

K = 75;                     % no of Cheb coeffs
nf = 1024;                  % no of pts for FFT
w = exp(2i*pi*(0:nf-1)/nf); % roots of unity
t = real(w);                % Cheb pts (twice over)
scl = 9;                    % scale factor for stability
F = exp(scl*(t-1)./(t+1+1e-16)); % exp(x) transpl. to [-1,1]
c = real(fft(F))/nf;        % Cheb coeffs of F
f = polyval(c(K+1:-1:1),w); % analytic part f of F
[U,S,V] = svd(hankel(c(2:K+1))); % SVD of Hankel matrix
s = S(n+1,n+1);             % singular value
u = U(K:-1:1,n+1)'; v = V(:,n+1)'; % singular vector
zz = zeros(1,nf-K);         % zeros for padding
b = fft([u zz])./fft([v zz]); % finite Blaschke product
rt = f-s*w.^K.*b;           % extended function r-tilde
rtc = real(fft(rt))/nf;     % its Laurent coeffs
zr = roots(v); qk = zr(abs(zr)>1); % poles
qc = poly(qk);              % coeffs of denominator
pt = rt.*polyval(qc,w);     % numerator
ptc = real(fft(pt)/nf);     % coeffs of numerator
ptc = ptc(n+1:-1:1); ck = 0*qk;

for k = 1:n                 % calculate residues
    q = qk(k); q2 = poly(qk(qk~=q));
    ck(k) = polyval(ptc,q)/polyval(q2,q);
end

zk = scl*(qk-1).^2./(qk+1).^2; % poles in z-plane
ck = 4*ck.*zk./(qk.^2-1);   % residues in z-plane
```

```
function eig_func = eigfunc(lambda,i,Ltype,Rtype,x,m,l0,lm,l)
% Defines the eigenfunctions for the different layers and boundary
% conditions.

if i == 1
    switch Ltype
        case 'Dirichlet'
            eig_func = sin(lambda*(x-l0));
        case 'Neumann'
            eig_func = cos(lambda*(x-l0));
        case 'Robin'
            eig_func = cos(lambda*(l(1)-x));
    end
elseif i == m
    switch Rtype
        case 'Dirichlet'
            eig_func = sin(lambda*(lm - x));
        case 'Neumann'
            eig_func = cos(lambda*(lm - x));
        case 'Robin'
            eig_func = cos(lambda*(x-l(m-1)));
    end
else
    eig_func = cos(lambda*(l(i)-x));
end
```

```
function eigs = eigvals(a,b,c,N)
% Solves the nonlinear equation:
%
% f(lambda) = lambda * tan(lambda*(a-b)) = c
%
% numerically for the first N non-negative values of lambda, using a
% combination of the bisection method and Newton's method.
%
% Solution to this equation is required to compute the eigenvalues
when
% Robin conditions are applied at either the left or right
boundaries.

f = @(lambda) lambda * sin(lambda*(a-b)) - c*cos(lambda*(a-b));
for i = 1:10
    g = chebfun(f,[0,10^i]);
    r = roots(g);
    numroots = length(r);
    if numroots >= N
        r = r(1:N);
        break;
    end
end
eigs = r;

% pause;
%
% MaxIters = 20;
% tol      = 1e-8;
% eigs     = zeros(N,1);
%
% if c > 0
%     n = 0;
%     converged = false;
%
%     lambda_left  = 0.0;
%     lambda_right = (2*n+1) * pi / (2 * (a-b));
%
%     % Initial guess (midpoint)
%     lambda = (lambda_left+lambda_right)/2;
%
%     f = compute_func(lambda,a,b,c);
%     absf0 = abs(f);
%
%     for k = 1:MaxIters
%         fdash = compute_fdash(lambda,a,b,c);
%         lambda = lambda - f / fdash;
%         f = compute_func(lambda,a,b,c);
%         if abs(f)/absf0 < tol
%             converged = true;
%             break;
%         end
%     end
%
%     if converged == true
```

```
%         eigs(1) = lambda;
%     else
%         warning('Failed to converge when finding eigenvalue
(n=%i)\n',n+1);
%     end
%
% end
%
% nu = 0;
% n = 0;
% while nu < N
%
%     n = n + 1;
%
%     converged = false;
%
%     if c < 0
%         lambda_left  = max((2*n+1) * pi / (2 * (a-b)),0.0);
%         lambda_right = (2*(n+1)+1) * pi / (2 * (a-b));
%     else
%         lambda_left  = max((2*(n-1)+1) * pi / (2 * (a-b)),0.0);
%         lambda_right = (2*n+1) * pi / (2 * (a-b));
%     end
%
%     % Initial guess (midpoint)
%     lambda = (lambda_left + lambda_right)/2;
%
%     f = compute_func(lambda,a,b,c);
%     for k = 1:MaxIters
%         fdash = compute_fdash(lambda,a,b,c);
%         lambda = lambda - f / fdash;
%         f = compute_func(lambda,a,b,c);
%         if abs(f) < tol
%             converged = true;
%             break;
%         end
%     end
%
%     if converged == true
%         unique_eig = true;
%         for i = 0:nu-1
%             if abs(lambda - eigs(i+1)) < 1e-4*eigs(i+1)
%                 unique_eig = false;
%                 break;
%             end
%         end
%         if unique_eig
%             eigs(nu+1) = lambda;
%             nu = nu + 1; % Unique eigenvalue counter
%             if nu == N
%                 break;
%             end
%         end
%     else
```

```
%         warning('Failed to converge when finding eigenvalue
(n=%i)\n',n+1);
%     end
%
% end
%
% eigs = sort(eigs);
%
% end
%
% % Sub-functions
% % Compute function f(lambda)
% function f = compute_func(lambda,a,b,c)
% f = lambda * sin(lambda*(a-b)) - c*cos(lambda*(a-b));
% end
% % Compute derivative f'(lambda)
% function fdash = compute_fdash(lambda,a,b,c)
% fdash = sin(lambda*(a-b)) + ...
%     lambda*cos(lambda*(a-b))*(a-b)+c*sin(lambda*(a-b))*(a-b);
% end
```

```
function w = steady_state(m,kappa,l0,lm,l,Lbnd,Rbnd)

aL = Lbnd{2};
bL = Lbnd{3};
cL = Lbnd{4};
aR = Rbnd{2};
bR = Rbnd{3};
cR = Rbnd{4};

H = 1e16*ones(m-1,1);

A = zeros(2*m,2*m);
b = zeros(2*m,1);

% Interface conditions
for i = 1:m-1
    A(2*i-1,2*i-1) = 1.0;
    A(2*i-1,2*i)   = (kappa(i)/H(i)) + l(i);
    A(2*i-1,2*i+1) = -1.0;
    A(2*i-1,2*i+2) = -l(i);
    b(2*i-1)       = 0.0;

    A(2*i,2*i)   = kappa(i);
    A(2*i,2*i+2) = -kappa(i+1);
    b(2*i)       = 0.0;
end

% Right boundary condition
A(2*m-1,2*m)   = bR+aR*lm;
A(2*m-1,2*m-1) = aR;
b(2*m-1)       = cR;

% Left boundary condition
A(2*m,1) = aL;
A(2*m,2) = -bL+aL*l0;
b(2*m)   = cL;

w = A\b;
```

```
function wfunc = wfunc(i,Ltype,Rtype,x,m,w)
% Form of the non-transient component of the solution
% (steady state if it exists)

% if strcmp(Ltype,'Neumann') && strcmp(Rtype,'Neumann')
%     if i == 1
%         wfunc = w(1)*x + w(2)*x.^2;
%     elseif i == m
%         wfunc = w(2*m-1)*x + w(2*m)*x.^2;
%     else
%         wfunc = w(2*i-1)*x + w(2*i)*x.^2;
%     end
% else
    wfunc = w(2*i-1) + w(2*i)*x;
% end
```

Matlab code to be used to input into multi-layer code:

```
clear
close all

global u0 m kappa l0 lm l tspan Rbnd Lbnd interface ASDIFFCORRECTED

load('AbbExp01072016.mat') % change to reflect workspace for
experiment
h=figure;
hold on
FileS = ['C403P1.tif']; % change to reflect picture relevant to data
being analyzed
%FileSave = 'ProCon1Loaded2'; % change to reflect test to be analyzed
(will be file name saved for excel)
FileSave2 = 'C403P1';
File = C403P1; % change to reflect test to analyze (check workspace)
MicronPerPixel = 1.6605; % change based on picture size and pixel
size (check in Zeiss)

imshow(FileS)
[Col, Row] = ginput(4); % go around sample picking the corners of the
desired area in a clockwise motion, starting at the top left corner
for k = round(min(Col)):floor(max(Col))
    gradLoaded(k-round(min(Col))+1) =
sum(File(round(min(Row)):floor(max(Row)),k)); % currently sums over
the Widths in the image to get the sume of brightness for that
Lengthumn
end

% for k = round(min(Length)):round(max(Length))
%     gradLoadedaxial(k) =
sum(File(round(min(Width)):round(max(Width), k))); % currently sums
over the Widths in the image to get the sume of brightness for that
Lengthumn
% end

% Old way where everything is used
% for k = 1:round(max(Length)) - round(min(Length))
%     gradLoaded(k) = sum(File(:,k)); % currently sums over the
Widths in the image to get the sume of brightness for that Lengthumn
% end

% Background_Noise_From_Negative_Loaded_Control = x; to be added
later
% Background_Noise_From_Negative_Unloaded_Control = x; to be added
later

while mod(length(gradLoaded),2) == 1 % checks to make sure vector is
even numbered, adds an element if it is not
    gradLoaded = horzcat(gradLoaded,zeros(1,1));
end
```

```
Background_Baseline = mean(mean(File(1:100,1:100))); % finds the
background noise to be subtracted later
XZero = find(gradLoaded ==
max(gradLoaded(1:length(gradLoaded)/2)),1); % makes y-zero the first
brightness peak
LoadedX1 = [([round(min(Col)):round(max(Col))]-
(XZero+round(min(Col)))) .* MicronPerPixel]; % corrects x axis to
mean radial depth in microns
gradLoadedscaledCol = gradLoaded./(round(max(Row)) - round(min(Row)))
- Background_Baseline; % corrects y axis to be average brigtness
% gradLoadedscaledY = gradLoadedaxial./(round(max(Width)) -
round(min(Width)));

while mod(length(gradLoadedscaledCol),2) == 1 &&
mod(length(LoadedX1),2) == 1 % checks to make sure vector is even
numbered, adds an element if it is not
    gradLoadedscaledCol = horzcat(gradLoaded,zeros(1,1));
    LoadedX1 = horzcat(LoadedX1,zeros(1,1));
end

while length(gradLoadedscaledCol)>length (LoadedX1) % checks to make
sure vector is even numbered, adds an element if it is not
    LoadedX1 = horzcat(LoadedX1,zeros(1,1));
end

while length(LoadedX1) > length(gradLoadedscaledCol) % checks to make
sure vector is even numbered, adds an element if it is not
    gradLoadedscaledCol = horzcat(gradLoadedscaledCol,zeros(1,1));
end

CorrectedMat = [LoadedX1; gradLoadedscaledCol]; % holds the correct x
position (microns) and corresponding average brightness values
High1 = max(gradLoadedscaledCol(1:length(gradLoadedscaledCol)/2)); %
brightness value of first peak (might have to change this to make it
better);might not end in the center of sample))
High2 =
max(gradLoadedscaledCol(length(gradLoadedscaledCol)/2:length(gradLoad
edscaledCol))); % brightness value of second peak (might have to
change this to make it  better); might not end in the center of
sample))
Baseline =
mean(gradLoadedscaledCol(length(gradLoadedscaledCol)/2+XZero-
100:length(gradLoadedscaledCol)/2+XZero+100)); % brightness value in
middle (or close to it, might want to change this later)
Difference1 = High1 - Baseline;
Difference2 = High2 - Baseline;
FindHighCorrected1 = CorrectedMat(1,find(CorrectedMat(2,:) ==
High1)); % correct x position of first peak
FindHighCorrected2 = CorrectedMat(1,find(CorrectedMat(2,:) ==
High2));

% subplot(2,1,1), imshow('Exp 3 Non Loaded 4.tif'), subplot(2,1,2),
plot(LoadedX1, gradLoadedscaledX), axis([0 4250 0
max(gradLoadedscaledX)*1.1])
```

```
%plot(LoadedX1, gradLoadedscaledX, 'g', axis([0
CorrectedMat(1,find(CorrectedMat(2,:) == High2)) 0
max(gradLoadedscaledX)*1.1]));

subplot(2,1,1), imshow(FileS), subplot(2,1,2), plot(LoadedX1,
gradLoadedscaledCol), axis([0 4250 0 max(gradLoadedscaledCol)*1.1])
plot(LoadedX1, gradLoadedscaledCol, 'g'),axis([0
CorrectedMat(1,find(CorrectedMat(2,:) == High2,1)) 0
max(gradLoadedscaledCol)*1.1]);
hold on

gradLoadedscaledCol = gradLoadedscaledCol - Baseline;
gradLoadedscaledCol = gradLoadedscaledCol(1:1000);
Max = find(gradLoadedscaledCol == (High1 - Baseline));
% plot(LoadedX1(Max:1000), gradLoadedscaledCol(Max:1000))
ASDIFF = gradLoadedscaledCol(Max:1000)./High1;
plot(LoadedX1(Max:1000), ASDIFF)

% dlmwrite(FileSave, [(find(gradLoadedscaledCol ==
High1):find(gradLoadedscaledCol == High2))',
(gradLoadedscaledCol(find(gradLoadedscaledCol ==
High1):find(gradLoadedscaledCol == High2)))'])
dlmwrite(FileSave2, [LoadedX1(1:1000)', gradLoadedscaledCol']);

n = numel(ASDIFF);


%%%%%LJ%LJLKFJLD


u0 = @(x) zeros(size(x));
m = 3;
kappa = [3,10,7];
l0 = 0;
lm = 1000;
l = [100, 400];
tspan = 10800;
Rbnd = {'Dirichlet',1.0,0.0,0};
Lbnd = {'Dirichlet',1.0,0.0,1.0};
interface = 'Perfect';
ASDIFFCORRECTED = interp1(1:n, ASDIFF, linspace(1, n, 1.66*n),
'nearest');

[u, x] = multdiff(m,kappa,l0,lm,l,u0,Lbnd,Rbnd, tspan, interface);
figure
plot(x,u,LoadedX1(Max:1000),ASDIFF)
```